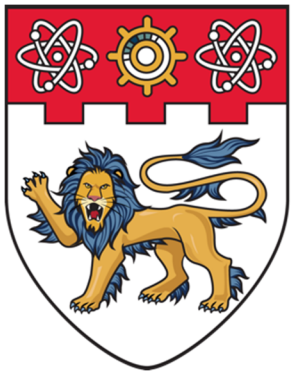

NANYANG TECHNOLOGICAL UNIVERSITY
SINGAPORE

# SYNTHESES AND CHARACTERIZATIONS OF UNCONVENTIONAL AZAARENES WITH NONLINEAR SHAPES AND NOVEL FUNCTIONAL GROUPS

**ZHAO KEXIANG**

**SCHOOL OF MATERIALS SCIENCE AND ENGINEERING**

**2019**

# SYNTHESES AND CHARACTERIZATIONS OF UNCONVENTIONAL AZAARENES WITH NONLINEAR SHAPES AND NOVEL FUNCTIONAL GROUPS

**ZHAO KEXIANG**

SCHOOL OF MATERIALS SCIENCE AND ENGINEERING

A thesis submitted to the Nanyang Technological University
in partial fulfilment of the requirement for the degree of
Doctor of Philosophy

**2019**

## Statement of Originality

I hereby certify that the work embodied in this thesis is the result of original research, is free of plagiarised materials, and has not been submitted for a higher degree to any other University or Institution.

. . . 05/Aug/2019 . . .
Date

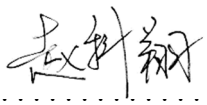

. . . . . .
Zhao Kexiang

## Supervisor Declaration Statement

I have reviewed the content and presentation style of this thesis and declare it is free of plagiarism and of sufficient grammatical clarity to be examined. To the best of my knowledge, the research and writing are those of the candidate except as acknowledged in the Author Attribution Statement. I confirm that the investigations were conducted in accord with the ethics policies and integrity standards of Nanyang Technological University and that the research data are presented honestly and without prejudice.

. . . 05/Aug/2019 . . .
Date

. . . . . .
Zhang Qichun

# Authorship Attribution Statement

This thesis contains material from a paper published in the following peer-reviewed journal where I was the first author.

Chapter 4 is published as Wang, N., Zhao, K., Ding, T., Liu, W., Ahmed, A. S., Wang, Z. R., Tian, M., Sun, X. W., Zhang, Q. C., *Adv. Energy Mater*. 2017, 7, 1700522. DOI:10.1002/aenm.201700522.

The contributions of the co-authors are as follows:

- A/Prof Zhang Qichun provided the initial project direction and edited the manuscript drafts.
- Dr. Wang Ning and I prepared the manuscript drafts. The manuscript was revised by Prof. Sun Xiaowei.
- I co-designed the study with A/Prof Zhang Qichun and performed all the organic synthesis at the School of Materials Science and Engineering.
- I measured the NMR spectra, UV-Vis spectrum and cyclic voltammetry curve of HATNT.
- SEM were conducted by me in the Facility for Analysis, Characterization, Testing and Simulation.
- Dr. Wang Ning fabricated the OPV devices and conducted performance-related characterizations.
- Mr. Ding Tao, Mr. Liu Wenbo, Mr. Ali Said Ahmed and Ms. Tian Miaomiao also assisted in the device fabrication.
- Dr Wang Zongrui assisted in the measurement of mobilities of HATNT.

. . . 05/Aug/2019 . . .
Date

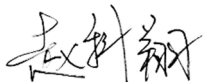

. . . . . .
Zhao Kexiang

## Abstract

This thesis aims to address the lack of azaarenes with nonlinear backbone and novel functional groups. Further study on the electronic and optical properties was conducted in order to grasp the structure-property relationship of unconventional azaarenes. Star-shape and U-shape were selected as the nonlinear backbones. Imide and thiadiazole were chosen as the functional groups.

In the first result, thiadiazole-fused star-shaped azaarene was synthesized and characterized by NMR, HRMS, UV-Vis and cyclic voltammetry. It was applied in the Perovskite solar cells as electron-transporting material with electron mobility up to $1.73 \times 10^{-2}$ $cm^2V^{-1}s^{-1}$. A high power conversion efficiency of 18.1% is achieved, which is fully comparable with the efficiency from the control device fabricated with $PC_{61}BM$ as ETL.

In the second result, a series of U-shaped helical azaarenes were synthesized and characterized by NMR, HRMS, UV-Vis and cyclic voltammetry. Crystal structures of helical azaarenes were obtained, and the solid-state structures unequivocally exhibited the helicity. Its electronic and optical properties were measured and compared with that of Z-shaped azaarenes.

In the third result, a series of novel imide-fused diazatetracenes were synthesized via Buchwald-Hartwig C-N coupling with a highly active palladium source. The obtained diazatetracenes were characterized by NMR, HRMS, UV-Vis and cyclic voltammetry. Its electronic and optical properties were measured and compared with that of unsubstituted diazatetracene. By changing the alkyl chains of the new diazatetracenes, different solid-state packings were achieved.

In conclusion, unconventional azaarenes with nonlinear backbone and novel functional groups were successfully acquired. Along with the syntheses, electronic and optical properties were also investigated. Moreover, from all the successful and failed attempts new strategies for more unconventional azaarenes were discovered.

## Lay Summary

The past few decades have witnessed the bloom of organic electronics. The old silicon-based electronics could no longer satisfy the increasing demand for thinner and flexible devices with lower cost. Hence, organic electronics were developed. In order to achieve higher performance and fabricate versatile devices, scientists start to explore novel organic semiconductors. Acenes are among the first batch of organic semiconductors which have been well investigated. However, most of the acenes are p-type material. More electron-negative atom, $sp^2$-nitrogen, was incorporated into the acene backbone. The obtained azaacenes displayed n-type performance.

Azaacenes, which refer to linearly-fused nitrogen-containing acenes, belong to the azaarene family. Although azaacenes have been applied as good n-type semiconductors, the nonlinear azaarenes are rarely investigated. Moreover, functional groups other than halogens and pseudohalogens are seldomly attached to azaacenes. This thesis tries to address the lack of azaarenes with nonlinear backbone and novel functional groups. Further investigation on the electronic and optical properties might reveal the structure-property relationship of unconventional azaarenes. Thus, unconventional azaarenes with nonlinear shapes and versatile functional groups are highly desirable.

In this thesis, star-shape and U-shape were selected as the nonlinear backbones. Imide and thiadiazole group were chosen as the functional groups. A series of novel azaarenes were successfully obtained. The thiadiazole-fused star-shaped azaarene HATNT is an excellent electron transporting material in perovskite solar cells. A high power conversion efficiency of 18.1% was achieved. The second result involves the helical azaarenes. If the pure enantiomer was separated by chiral column, there is a chance to fabricate the CPL emitting OLED devices which are rare for the azaarenes. For the last result, novel imide-fused diazatetracenes were synthesized in high yield. These diazatetracenes could be easily further modified to finely tune the LUMO and HOMO levels as well as optical properties. This marks the beginning of a class of new imide-fused azaarenes.

## Acknowledgements

This dissertation would not have been possible without the NTU research scholarship.

I would like to express my gratitude to my supervisor Associate Professor Zhang Qichun for his support and guidance during the period of this project.

Special thanks to Prof. Michinobu from Tokyo Institute of Technology who offered me the opportunity to visit his group. I am indebted to his kind assistance and guidance during my stay in Japan.

A debt of gratitude is owed to Dr. Yu Fei for his assistance in acquiring single crystal structures. I would also like to thank Dr. Long Guankui for his theoretical calculations.

I also wish to thank Dr. Gu Peiyang, Dr. Wang Zilong, Dr. Wang Zongrui, Dr. Liu Guangfeng, Dr. Nie Lina, Dr. Huang Yinjuan, Mr. Ali Said Ahmed, Mr. Liu Wenbo and all the other group members from whom I learned a lot of valuable knowledge and skills which would benefit me for the following academic career.

Finally, I would like to thank my family, especially my mother Mrs. Zhao Yan, who have supported me for all these years. Without their support, I would not be able to pursue the doctoral degree.

# Table of Contents

**Abstract** ..... i

**Lay Summary** ..... iii

**Acknowledgements** ..... v

**Table of Contents** ..... vii

**Table Captions** ..... xi

**Figure Captions** ..... xiii

**Abbreviations** ..... xix

**Chapter 1 Introduction** ..... **1**

1.1 Hypothesis ..... 2

1.2 Objectives and Scope ..... 3

1.3 Dissertation Overview ..... 3

1.4 Findings and Outcomes/Originality ..... 4

References ..... 5

**Chapter 2 Literature Review** ..... **7**

2.1 Quantum Chemical Calculation ..... 8

2.2 Synthetic Approaches Towards N-Heteroacenes ..... 10

2.2.1 Condensation ..... 10

2.2.2 Nucleophilic Amination....14
2.2.3 Other synthetic routes....20
2.3 PhD in context of literature....21
References....22

**Chapter 3 Experimental Methodology....25**
3.1 Rationale for selection....26
3.2 Synthetic Methodology....26
3.2.1 Extraction....26
3.2.2 Recrystallization....27
3.2.3 Distillation....28
3.2.4 Chromatography....33
3.3 Characterization Methodology....35
3.3.1 Infrared Spectroscopy....35
3.3.2 Ultraviolet–Visible Spectroscopy....36
3.3.3 Fluorescence Spectroscopy....38
3.3.4 Nuclear Magnetic Resonance (NMR)....39
3.3.5 Mass Spectrometry....44
3.3.5 Cyclic Voltammetry (CV)....46
3.3.5 X-ray Crystallography....48
3.4 Overview of methodologies....49
References....50

**Chapter 4 First Results Chapter....51**
4.1 Introduction....52

4.2 Experimental ..... 53
4.2.1 Device fabrication ..... 53
4.2.2 Synthesis ..... 54
4.3 Results and Discussion ..... 55
4.3.1 Characterization ..... 55
4.3.2 Properties and PSC Performance ..... 57
4.4 Conclusions ..... 61
References ..... 62

**Chapter 5 Second Results Chapter ..... 63**
5.1 Introduction ..... 64
5.2 Synthesis ..... 64
5.3 Results and Discussion ..... 67
5.3.1 Characterization ..... 67
5.3.2 Optical and Electrochemical Properties ..... 76
5.3.3 Single Crystal X-ray Structures ..... 78
5.4 Conclusion ..... 79
References ..... 81

**Chapter 6 Third Results Chapter ..... 83**
6.1 Introduction ..... 84
6.2 Synthesis ..... 84
6.3 Results and Discussion ..... 87
6.3.1 Characterization ..... 87
6.3.2 Optical and Electronic Properties ..... 104

6.3.2 Single Crystal X-ray Structures ..... 106
6.4 Conclusions ..... 107
References ..... 108

**Chapter 7 Discussion and Future Work ..... 109**
7.1 General Discussion ..... 110
7.1.1 Thiadiazole-fused star-shaped azaacene ..... 110
7.1.2 U-shaped helical azaarenes ..... 113
7.1.3 Imide-fused diazatetracenes ..... 117
7.2 Summary ..... 120
References ..... 121

**Appendix** ..... 123

# Table Captions

**Table 3.1** Common recrystallization solvents.

**Table 3.2** Selection of different column sizes.

**Table 3.3** NMR-active nuclei.

**Table 4.3.1** Devcie parameters of the perovskite solar cells with different thickness of HATNT.

**Table 5.3.1** Optical properties of U7, U9, U11 and its isomers.

**Table 5.3.2** Electronic properties of U7, U9, U11 and its isomers.

**Table 6.3.1** Optical properties of compounds 5 - 9.

**Table 6.3.2** Electronic properties of compounds 5 - 9.

**Table A.1** Material parameters for HATNT.

**Table A.2** Dihedral angles of U7, U9 and U11.

## Figure Captions

**Figure 2.1.1** Theoretical calculations of promising N-heteroacenes in organic electronics by Chao *et al*.

**Figure 2.1.2** Theoretical calculations of promising N-heteroacenes in organic electronics by Winkler and Houk.

**Figure 2.1.3** Calculated FMO levels of selected dihydroazaacenes by Shuai and co-workers.

**Figure 2.2.1** Synthesis of N-heteroacene through the condensation of o-dihydroxy compound and o-diamine compound.

**Figure 2.2.2** Syntheses of halogenated TAPs.

**Figure 2.2.3** A series of hexazapentacene compounds synthesized by Zhang et al.

**Figure 2.2.4** 7.7 nm long pyrene-fused N-heteroacenes and giant star-shaped N-heteroacenes

**Figure 2.2.5** A series of novel fluorinated tetraazaacenes synthesized by Bunz et al.

**Figure 2.2.6** Synthesis of highly electron-deficient hexaazapentacene.

**Figure 2.2.7** Syntheses of azapentacenes via palladium catalyzed C-N coupling.

**Figure 2.2.8** Syntheses of azahexacenes via palladium catalyzed C-N coupling.

**Figure 2.2.9** Microwave-assisted coupling reactions of o-diamine with inactive o-dihalide using Pd catalyst.

**Figure 2.2.10** Synthesis of azaheptacenes.

**Figure 2.2.11** Coupling reactions without microwave using RuPhos Pd G2 as catalyst.

**Figure 2.2.12** Influence of side chains on the reactivity of 2,3-diaminonaphthalene.

**Figure 2.2.13** Difference in reactivity of various TIPS substituted diamines.

**Figure 2.2.14** Difference in reactivity of various dihalides.

**Figure 2.2.15** Synthesis of quinoxalines through [4+2] annulation.

**Figure 2.2.16** Condensation reaction of o-dialdehyde and hydrazine.

**Figure 2.2.17** Synthesis of cinnoline-containing acene.

**Figure 3.1** a) Separating funnel; b) Venting excess pressure.

**Figure 3.2** Illustration of simple distillation process.

**Figure 3.3** Distillation at atmospheric pressure.

**Figure 3.4** Vacuum distillation.

**Figure 3.5** Fractional distillation.

**Figure 3.6** Thin layer chromatography.

**Figure 3.7** Column chromatography (gravity elution).

**Figure 3.8** List of main IR spectroscopy bands.

**Figure 3.9** various kinds of electronic excitation that may occur in organic molecules.

**Figure 3.10** Jablonski diagram.

**Figure 3.11** Simple illustration of general principle of NMR.

**Figure 3.12** Illustration of T1 and T2 relaxation.

**Figure 3.13** Regions in proton NMR spectrum.

**Figure 3.14** 500 MHz 1H-NMR spectrum of 1-chloropropane in CDCl3 at room temperature.

**Figure 3.15** Spin-spin couplings in 1-chloropropane.

**Figure 3.16** Overview of mass spectrometer.

**Figure 3.17** Ionization of analyte in MALDI-TOF mass spectrometry.

**Figure 3.18** Overview of cyclic voltammetry.

**Figure 3.19** Typical cyclic voltammogram of a reversible electrochemical reaction.

**Figure 3.20** Bragg diffraction.

**Figure 4.2.1** Synthesis of HATNT.

**Figure 4.3.1** 1H NMR spectrum of HATNT in $CDCl_3$.

**Figure 4.3.2** $^{13}C$ NMR spectrum of HATNT in $CDCl_3$.

**Figure 4.3.3** HRMS spectrum of HATNT.

**Figure 4.3.4** a) Device architecture of PSC used in this work. b) Corresponding energy level diagram of a) using HATNT as ETL. c) CV curve of HATNT. d) Optical absorption characteristic of HATNT in THF solution in the visible region.

**Figure 4.3.5** a) J-V curves of the PSCs with different thickness HATNT as ETL. b) PCE distribution characteristic based on 36 devices fabricated in one batch. The line indicates the Gaussian fitting. c) Best-performing J-V curve of the PSC with HATNT as ETL. d) The corresponding IPCE spectrum of c) and integrated current plots. e) Stable output

curves of current density and efficiency for the PSC at the maximum power point. f) Hysteresis behavior of the PSC device with HATNT as ETL under different scanning directions. For reverse and forward scan, the parameters are a step of 25 mV with a delay time of 200 ms.

**Figure 5.1** Synthesis of helical azaarenes U7, U9 and U11.

**Figure 5.3.1** $^{1}$H NMR spectrum of 2 in Acetone-$d_6$.

**Figure 5.3.2** $^{13}$C NMR spectrum of 2 in DMSO-$d_6$.

**Figure 5.3.4** HRMS spectrum of 2.

**Figure 5.3.5** $^{1}$H NMR spectrum of 3 in THF-$d_8$.

**Figure 5.3.6** HRMS spectrum of 3.

**Figure 5.3.7** $^{1}$H NMR spectrum of U7 in $CDCl_3$.

**Figure 5.3.8** $^{13}$C NMR spectrum of U7 in $CDCl_3$.

**Figure 5.3.9** HRMS spectrum of U7.

**Figure 5.3.10** $^{1}$H NMR spectrum of U9 in $CDCl_3$.

**Figure 5.3.11** $^{13}$C NMR spectrum of U9 in $CDCl_3$.

**Figure 5.3.12** HRMS spectrum of U9.

**Figure 5.3.13** $^{1}$H NMR spectrum of U11 in $CDCl_3$.

**Figure 5.3.14** $^{13}$C NMR spectrum of U11 in $CDCl_3$.

**Figure 5.3.15** HRMS spectrum of U11.

**Figure 5.3.16** Normalized absorption spectra of U7, U9 and U11 in dichloromethane.

**Figure 5.3.17** Z-shaped constitutional isomers of U7, U9 and U11.

**Figure 5.3.18** Crystal structures and packing of U7 (top left), U9 (top right) and U11 (bottom left).

**Figure 6.2.1** Synthesis of imide-containing diazatetracenes via palladium catalyzed coupling; EH = ethylhexyl.

**Figure 6.3.1** $^{1}$H NMR spectrum of **2** in $CDCl_3$.

**Figure 6.3.2** $^{13}$C NMR spectrum of **2** in $CDCl_3$.

**Figure 6.3.3** $^{1}$H NMR spectrum of **3** in Acetone-$d_6$.

**Figure 6.3.4** $^{13}$C NMR spectrum of **3** in $CDCl_3$.

**Figure 6.3.5** $^{1}$H NMR spectrum of **4b** in $CDCl_3$.

**Figure 6.3.6** $^{13}$C NMR spectrum of **4b** in $CDCl_3$.

**Figure 6.3.7** $^{1}H$ NMR spectrum of **5** in $CDCl_3$.

**Figure 6.3.8** $^{13}C$ NMR spectrum of **5** in $CDCl_3$.

**Figure 6.3.9** $^{1}H$ NMR spectrum of **6** in $CDCl_3$.

**Figure 6.3.10** $^{13}C$ NMR spectrum of **6** in $CDCl_3$.

**Figure 6.3.11** $^{1}H$ NMR spectrum of **7** in $CDCl_3$.

**Figure 6.3.12** $^{13}C$ NMR spectrum of **7** in $CDCl_3$.

**Figure 6.3.13** $^{1}H$ NMR spectrum of **8** in $CDCl_3$.

**Figure 6.3.14** $^{13}C$ NMR spectrum of **8** in $CDCl_3$.

**Figure 6.3.15** HRMS spectrum of 2.

**Figure 6.3.16** HRMS spectrum of 3.

**Figure 6.3.17** HRMS spectrum of 4b.

**Figure 6.3.18** HRMS spectrum of 5.

**Figure 6.3.19** HRMS spectrum of 6.

**Figure 6.3.20** HRMS spectrum of 7.

**Figure 6.3.21** HRMS spectrum of 8.

**Figure 6.3.22** Normalized absorption spectra of 6 and 8 in dichloromethane.

**Figure 6.3.23** Crystal structures and packing of 5 (top left), 7 (bottom left) and 8 (bottom right).

**Figure 7.1** Various alkylated o-diamines which have been used to react with hexaketocyclohexane.

**Figure 7.2** Linear-fused quinone-containing twofold condensation product (left) and star-shaped threefold condensation product (right).

**Figure 7.3** Synthetic route towards 7.

**Figure 7.4** Attempt to synthesize large star-shaped azaarenes.

**Figure 7.5** Proposed synthetic route towards phenazine-branched star-shaped azaarenes.

**Figure 7.6** Reported synthetic route towards *o*-quinones.

**Figure 7.7** Attempted syntheses of *o*-quinones using BSA.

**Figure 7.8** Proposed new synthetic route towards naphthalene-1,2,7,8-tetraone using BSA.

**Figure 7.9** Possible synthetic route towards large nitrogen-containing macrocycle.

**Figure 7.10** Proposed synthetic route towards azaarene with multiple helicity.

**Figure 7.11** Initially proposed synthetic route towards imide-fused diazatetracenes.

**Figure 7.12** Synthetic route towards imide-fused diazatetracenes. i) Pd Ruphos G4, $Cs_2CO_3$, toluene and *t*-BuOH; ii) Excessive $MnO_2$, DCM.

**Figure 7.13** Attempted synthesis of imide-fused tetraazatetracenes.

**Figure 7.14** Possible imide-fused diazatetracenes with deeper LUMO via side chain engineering.

**Figure 7.15** Possible malononitrile containing diazatetracenes.

**Figure 7.16** Possible halogenated imide-fused diazatetracenes.

**Figure 7.17** Possible imide-fused azaacenes with different π-backbone.

**Figure A.1** Atomic force microscope images of HATNT under different annealing temperatures.

**Figure A.2** Scanning electron microscope images of the pure perovskite (a) and the bilayer perovskite/HATNT (55 nm) thin films (b). c) Cross-section image of the Glass/ITO/Perovskite, the inset shows the optical photograph of the device.

**Figure A.3** Device efficiency distribution characteristic of the 32 PCBM-based perovskite solar cells fabricated within on batch.

**Figure A.4** J-V curve for the electron-only device with a structure of glass/ITO/$Cs_2CO_3$/HATNT/Ca/Al.

**Figure A.5** Normalized emission spectra of U7, U9 and U11 in DCM.

**Figure A.6** Interplane angle of U7.

**Figure A.7** Interplane angle of U9.

**Figure A.8** Interplane angle of U11.

**Figure A.9** Atom labeling of U7, U9 and U11. The calculations of torsional angles of U7, U9 and U11 start from C2, C4 and C5 respectively.

**Figure A.10** CV curves of Ferrocene, U7, U9 and U11.

**Figure A.11** Quantum-chemical calculations of frontier molecular orbitals (FMOs).

**Figure A.12** CV curves of imide-fused diazatetracenes and unmodified TIPS-DAT.

**Figure A.13** Normalized emission spectra of imide-fused TIPS-DATs and DAT in DCM.

**Figure A.14** Normalized absorption spectra of N-methyl imide-fused DATs in DCM.

## Abbreviations

| | |
|---|---|
| NMR | Nuclear Magnetic Resonance |
| HRMS | High Resolution Mass Spectrometry |
| UV-Vis | Ultraviolet-Visible |
| FTIR | Fourier Transform Infrared Spectroscopy |
| CV | Cyclic Voltammetry |
| ETL | Electron Transporting Layer |
| CPL | Circular Polarized Luminescence |
| OLED | Organic Light Emitting Diode |
| LUMO | Lowest Unoccupied Molecular Orbit |
| HOMO | Highest Occupied Molecular Orbit |
| OTFT | Organic Thin Film Transistor |
| OPV | Organic Photovoltaics |
| SEM | Scanning Electron Microscopy |
| EA | Electron Affinity |
| OFET | Organic Field Effect Transistor |
| TIPS | Triisopropylsilyl |
| TAP | Tetraazapentacene |
| AcOH | Acetic Acid |
| DMF | N,N-Dimethylformamide |
| NICS | Nucleus Independent Chemical Shift |
| DDQ | 2,3-Dichloro-5,6-dicyano-1,4-benzoquinone |
| TLC | Thin Layer Chromatography |
| CC | Column Chromatography |
| IUPAC | International Union of Pure and Applied Chemistry |
| PSC | Perovskite Solar Cell |
| PCE | Power Conversion Efficiency |
| DCM | Dichloromethane |
| ITO | Indium Tin Oxide |
| THF | Tetrahydrofuran |

| | |
|---|---|
| ppm | Parts per million |
| BSA | Benzeneseleninic Acid Anhydride |
| DMSO | Dimethyl Sulfoxide |
| EH | Ethylhexyl |
| COF | Covalent Organic Framework |
| IBX | 2-Iodoxybenzoic acid |
| TMS | Trimethylsilyl |
| HPLC | High Pressure Liquid Chromatography |
| NDI | Naphthalene Diimide |
| PDI | Perylene Diimide |
| *t*-BuOH | tert-Butanol |

# Chapter 1

# Introduction

*In this chapter, the historical background of azaacenes is briefly introduced and the goal and scope of this thesis are presented. The thesis tries to address the lack of azaarenes molecules with nonlinear backbone and novel functional groups. Major findings are also summarized.*

## 1.1 Hypothesis

The rapid development of organic electronics over the past few decades has prompted the researchers around the world to explore novel organic semiconductors.[1] Acenes have been intensively studied over the last 30 years as a good class of p-type materials in organic electronics.[1a] The ability to replace its inorganic counterpart as semiconductors enables lower manufacturing cost and devices built on flexible and lightweight substrates over considerably large areas. Among all acenes, some molecules, like pentacene and rubrene, show outstanding electronic properties with hole mobility reaching 40 $cm^2/(V \cdot s)$.[2] Although acenes have shown promising p-type performance, they also suffer from poor ambient stability. Pentacene, for example, is highly sensitive to light. Moreover, n-type organic semiconductors are also needed to form pure organic p-n junctions in organic electronics.

Azaacenes, which have been known for more than one century, are arguably one of the most investigated n-type semiconductors in organic electronics.[3] Compared to its hydrocarbon counterpart, azaacenes show much better long-term stability and environmental robustness as a result of their deeper LUMO levels.[4] By altering the number, position and valence state of nitrogen atoms, it is convenient to adjust the HOMO-LUMO position as well as the band gap of N-heteroacenes.[5] Recently, through the surface engineering of OTFT device, the electron mobility of azaacenes reached a surprising value of 27.8 $cm^2/(V \cdot s)$, which is comparable to the single crystal device of pentacene.[6]

However, azaacene is only a member of azaarene family that adopts the linear configuration, and seldomly are any additional functional groups attached to the azaacenes backbone other than halogens and pseudohalogens.[7] Thus, it is of great necessity to synthesize non-linear azaarenes and azaacenes with additional functional groups. Through the study of electronic and optical properties of unconventional azaarenes, more insight could be gained into the structure-property relationship and substituent-property relationship, which could further lead to the guidelines of rational design of azaarenes towards the applications in organic electronics. Thus, unconventional azaarenes with

nonlinear shapes and versatile functional groups are highly desirable. This thesis focuses on exploring the syntheses of unconventional azaarenes and investigating their electronic and optical properties.

## 1.2 Objectives and Scope

1. To design and synthesize unconventional azaarenes with novel shapes and functional groups.
2. To test the electronic and optical properties of unconventional azaarenes.
3. To seek for potential applications in organic electronics based on electronic and optical properties of unconventional azaarenes.

## 1.3 Dissertation Overview

The thesis tries to address the lack of azaarenes molecules with nonlinear backbone and novel functional groups. Further study on the electronic and optical properties revealed the structure-property relationship of unconventional azaarenes.

*Chapter 1* provides a rationale for the research and outlines the goals and scope.

*Chapter 2* reviews the literature concerning the synthetic methods and current development of azaarenes.

*Chapter 3* discuss the principles underlying the synthesis and characterization of azaarenes. Purification methods, including recrystallization, distillation, extraction and chromatography, are illustrated. Fundamentals of characterization methods, such as UV-Vis spectroscopy, fluorescence spectroscopy, nuclear magnetic resonance spectroscopy, mass spectrum and single crystal X-ray analysis, are discussed.

*Chapter 4* elaborates the first major set of results. In this chapter, star-shaped azaacene, HATNT, was synthesized and characterized. Its application as electron transporting

material in Perovskite solar cells was investigated.

*Chapter 5* elaborates the second major set of results. In this chapter, a series of U-shaped helical azaarenes were synthesized and fully characterized. Crystal structures of helical azaarenes were obtained, and the solid-state structures were investigated. Its electronic and optical properties were measured and compared with that of Z-shaped azaarenes.

*Chapter 6* elaborates the third major set of results. In this chapter, a series of imide-fused diazatetracenes were synthesized and fully characterized. Their solid-state structures and electronic as well as optical properties were investigated.

*Chapter 7* includes the unsuccessful attempts and implications of the previous three chapters. The extent to which the hypothesis was proven is also discussed. After concluding the thesis, new strategies towards unconventional azaarenes with nonlinear backbones or various functional groups could be obtained, which provides the opportunities for the synthesis of a wide range of novel azaarenes.

## 1.4 Findings and Outcomes/Originality

This research led to several novel outcomes:

1. Thiadiazole-fused star-shaped azaacene was first applied in the Perovskite solar cells as electron-transporting material and showed a superior performance compared with commonly used $P_{61}$CBM.
2. Pyrazine-containing helical azaarenes were first synthesized and characterized. Electronic and optical properties were studied and compared with that of angular analogue. Solid-state structures were further investigated, and the helicity was unequivocally exhibited.
3. A series of novel imide-fused diazatetracenes were synthesized via Buchwald-Hartwig C-N coupling. By changing the alkyl chains of the diazatetracenes, different solid-state packings were achieved.

## References

[1] a) J. E. Anthony, *Chem. Rev.* **2006**, *106*; b) J. E. Anthony, A. Facchetti, M. Heeney, S. R. Marder, X. Zhan, *Adv. Mater.* **2010**, *22*, 3876-3892; c) C. Wang, H. Dong, W. Hu, Y. Liu, D. Zhu, *Chem. Rev.* **2012**, *112*, 2208-2267.

[2] T. Hasegawa, J. Takeya, *Science and Technology of Advanced Materials* **2009**, *10*.

[3] a) Q. Miao, *Adv. Mater.* **2014**, *26*, 5541-5549; b) J. Li, Q. Zhang, *ACS Appl. Mater. Interfaces* **2015**, *7*, 28049-28062.

[4] Q. Miao, T. Q. Nguyen, T. Someya, G. B. Blanchet, C. Nuckolls, *J. Am. Chem. Soc.* **2003**, *125*, 10284-10287.

[5] Q. Miao, *Adv. Mater.* **2014**, *26*, 5541-5549.

[6] M. Chu, J.-X. Fan, S. Yang, D. Liu, C. F. Ng, H. Dong, A.-M. Ren, Q. Miao, *Adv. Mater.* **2018**, *30*, 1803467.

[7] U. H. Bunz, *Acc Chem Res* **2015**, *48*, 1676-1686.

# Chapter 2

# Literature Review

*In this chapter, literatures regarding the quantum chemical calculations and synthetic methods of azaarenes have been reviewed. In the calculation part, reorganization energy (λ) and electron affinity (EA) are considered as fundamental parameters to evaluate the performance and stability of n-type organic semiconductors. It has been proven that azaarenes hold the potential of being suitable n-type materials for OFETs. Synthetic approaches towards azaarenes have been summarized. Condensation is the most frequently used method and the most reliable one. The other widely used method is the Buchwald-Hartwig type C-N coupling, which provides a very useful alternative for the synthesis of novel azaarenes.*

## 2.1 Quantum chemical calculation

By studying the perfluorinated pentacene, it is found that the internal reorganization energy (λ) of electron/hole hopping is doubled. This explains why perfuorinated pentacene has a much lower hole mobility compared with pristine pentacene, since carrier mobility will be reduced if λ increases. Reducing λ value is of great importance for material scientists to design functional materials. Chen and Chao proposed several N-functionalized pentacenes with low λ (0.15-0.2 eV), compared with perfluorinated pentacene, and desirable ionization potentials.[1] Based on their calculation, these N-heteroacenes hold the potential of being suitable n-type material for OFETs.

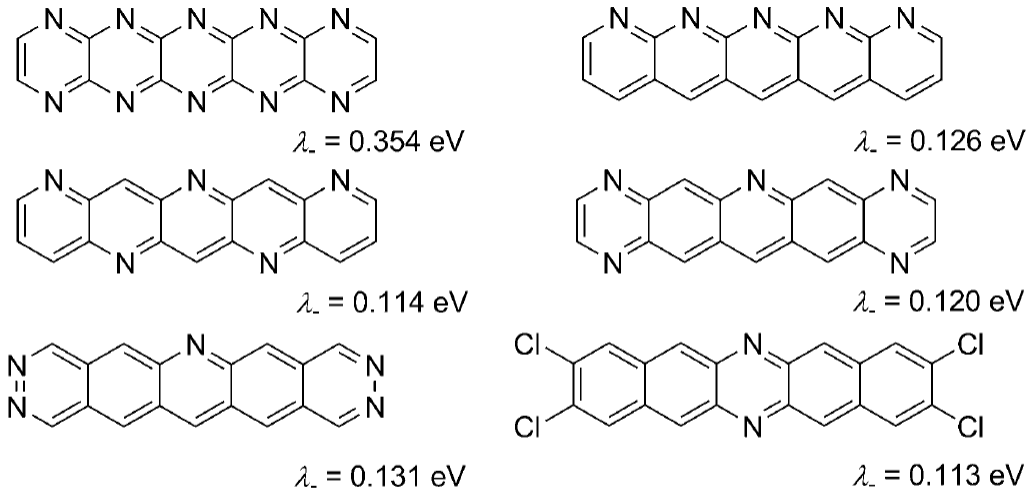


**Figure 2.1.1** Theoretical calculations of promising N-heteroacenes in organic electronics by Chao et al.

Winkler and Houk further investigated a series of nitrile substituted N-heteroacenes in detail.[2] According to their work, several promising N-heteroacenes as n-type semiconductors in OFET are proposed. The incorporation of at least seven N atoms will increase the electron affinity (EA) to a desired level. The nitrile substituents will promote self-assembly as well as air stability.

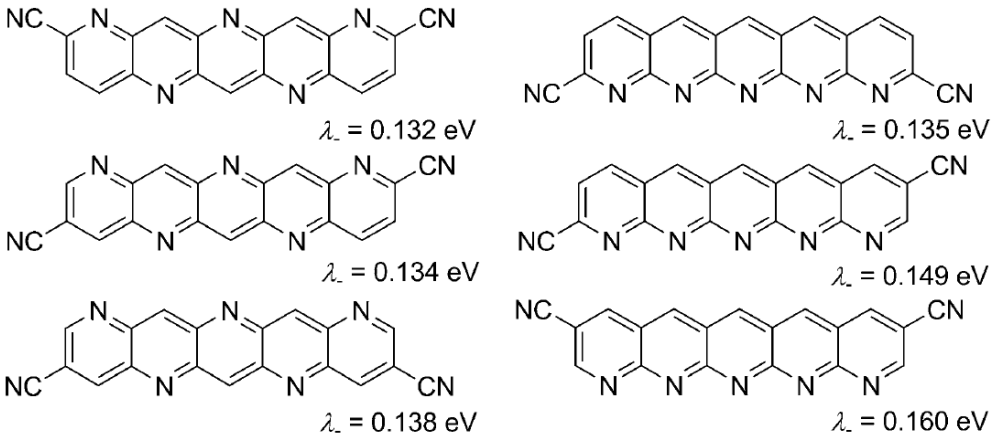


**Figure 2.1.2** Theoretical calculations of promising N-heteroacenes in organic electronics by Winkler and Houk.

Shuai *et al*. compared the HOMO-LUMO positions between N-heteroacenes and its N,N'-dihydro reduced forms.[3] It is found that the oxidization of N,N'-dihydro compound will lead to a lower LUMO level, hence favoring the electron injection. Moreover, the LUMO level would be affected to a greater extent than HOMO level if oxidization occurs. Meanwhile, λ values in oxidized N-heteroacenes are nearly unaffected by where the N atoms is located.

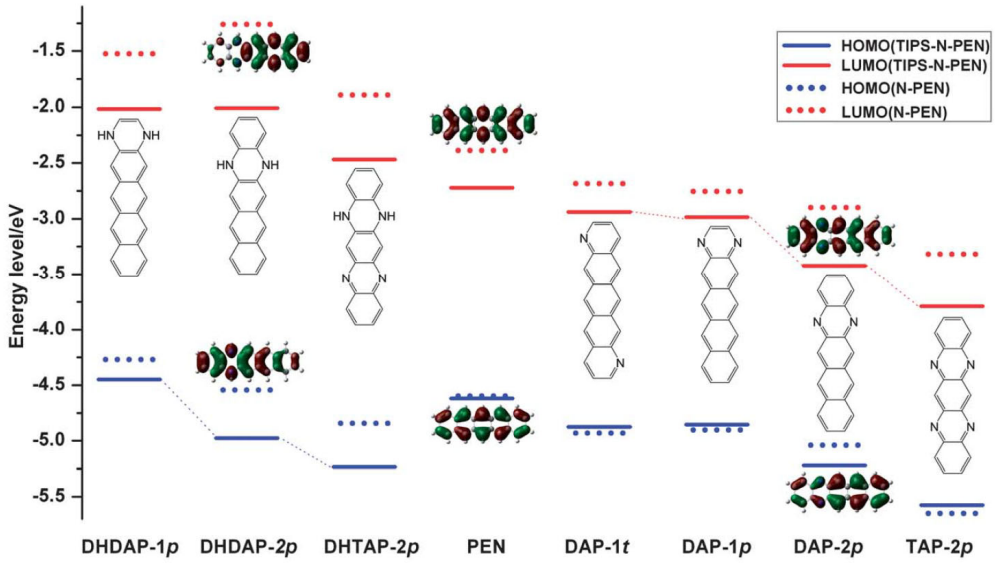


**Figure 2.1.3** Calculated FMO levels of selected dihydroazaacenes by Shuai and co-workers.

Quantum chemical calculations from different groups showed that N-heteroacenes could be a promising class of n-type materials. But one must be aware of that these calculations are based on simplified ideal physical models. It is still difficult to predict good n-type materials using quantum chemical calculations alone. However, calculations do point out an overall direction towards better n-type organic semiconductors.

Although a significant number of promising N-heteroacenes have been suggested, the lack of proper synthetic approaches hinders the development of N-heteroacenes in organic electronics. The following part will focus on the synthetic approaches.

## 2.2 Synthetic approaches towards N-heteroacenes

Although most of the aforementioned N-heteroacenes contain pyridine rings, there is no available synthetic routes towards such fused pyridine systems. The scope of this part will be limited to fused pyrazine systems which are easier to synthesize.

Generally, the synthetic approaches could be divided into two categories. One is the condensation reaction between *o*-diamine and *o*-quinone/*o*-dihydroxy compounds. The other is the nucleophilic amination between *o*-diamine and *o*-dihalogen compounds.

### 2.2.1 Condensation

One traditional and widely used method to synthesize N-heteroacenes is the condensation reaction. Hinsberg[4] as well as Fischer and Hepp[5] reported the preparation and basic properties of a series of N,N'-dihydroazacenes. **3**-$H_2$ is synthesized through the condensation between **1** and **2**. This kind of condensation often gives good to excellent yield. However, this condition usually does not work for the substituted species. By oxidizing **3**-$H_2$ with chloranil, dizazpentacene is obtained.

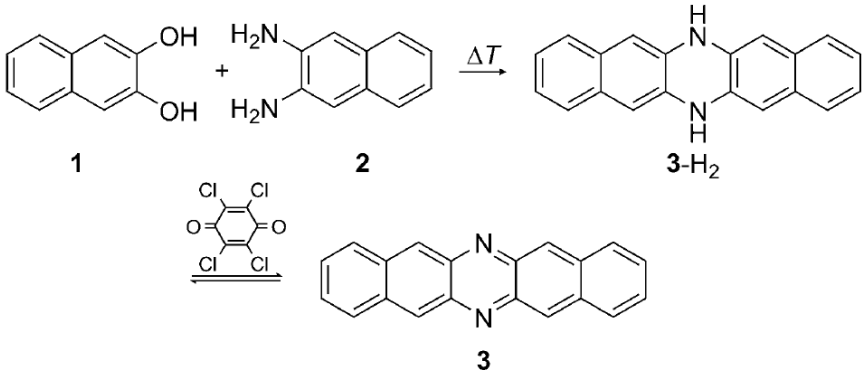


**Figure 2.2.1** Synthesis of N-heteroacene through the condensation of *o*-dihydroxy compound and *o*-diamine compound.

Recently, Miao *et al*. reported a serial of halogen substituted TIPS-TAPs, which showed excellent performance in OFET, breaking the record of the highest electron mobility among n-type materials.[6] Mono-halogenated and di-halogenated quinone intermediates **5a-d** were obtained through the condensation reaction between dihydroxy **4a-d** and *o*-phenylenediamine in moderate yields. This method is typically used in the syntheses of TAP with TIPS groups substituted at 6,13 positions.[7]

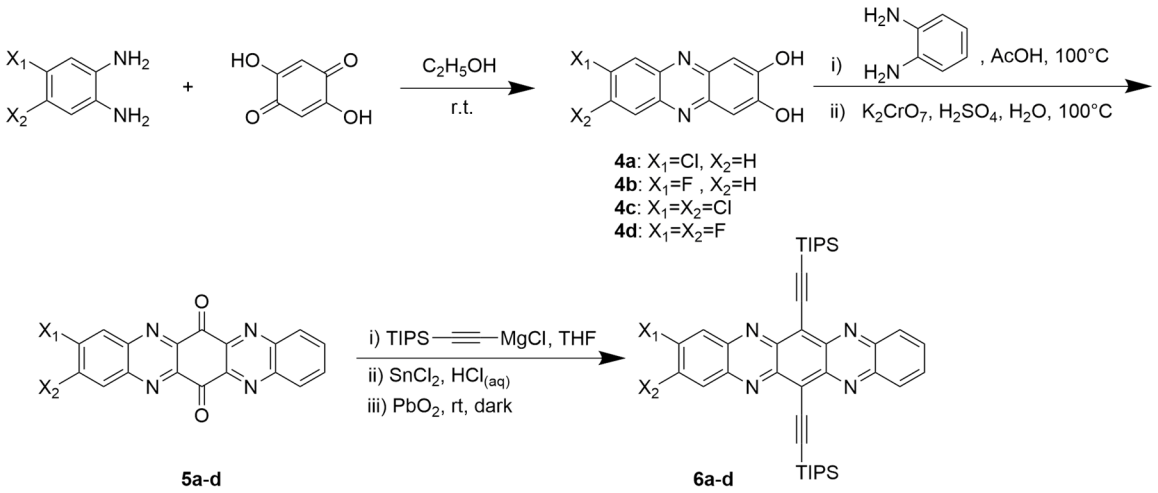


**Figure 2.2.2** Syntheses of halogenated TAPs.

Similarly, ortho-quinones were used to synthesize N-heteroacenes. Due to its higher reactivity than dihydroxy compounds, the reaction requires less harsh conditions and can be carried out in solution. In 2012, Zhang *et al*. first synthesized a series of

hexazapentacenes **8-11** via the condensation reaction between tetraaminophenazine and various diketones.[8] However, without bulky solubilizing substituents, these hexazapentacenes are only sparsely soluble in DMF and insoluble in common solvents such as hexane and dichloromethane.

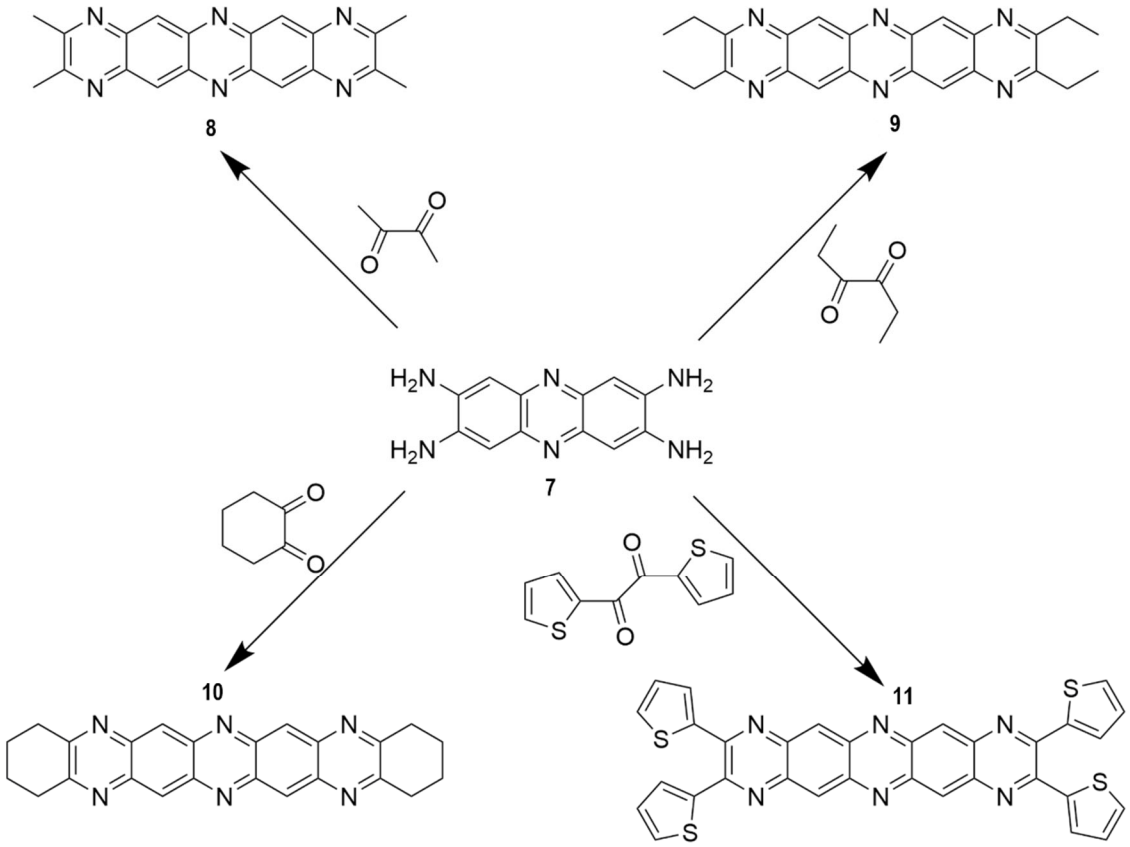


**Figure 2.2.3** A series of hexazapentacene compounds synthesized by Zhang et al.

Unlike its hydrocarbon counterpart, N-heteroacenes are generally air-stable and resistant to oxidation. However, dimerizations through Diels-Alder reaction are often observed in long linear N-heteroacenes, such as azahexacenes[9] and azaheptacenes[10]. It could give well-defined dimerized products or unidentifiable mixtures. To avoid such problem, pyrene units, which act as spacer units to break the fully conjugated azaacenes into isolated units, are introduced by utilizing pyrene ketones[11]. With the incorporation of spacer units, N-heteroacenes could be extended to a surprisingly 7.7 nm in length through repeatedly condensation reactions between *o*-quinone and *o*-diamine.[12] Besides the linear shape, the nanosized N-heteroacenes could also be made star-shaped and three-dimensional by adopting hexaaminozenzene core and hexaaminotriptycene core respectively followed by

repeatedly condensations.[13] Although pyrene-fused N-heteroacenes could be extended into staggering sizes, it is worth pointing out that, after a few rounds of condensations, these giant molecules almost bear the same electrochemical properties as the less fused intermediates. Additionally, NICS calculations also showed low aromaticity in pyrene units.[14]

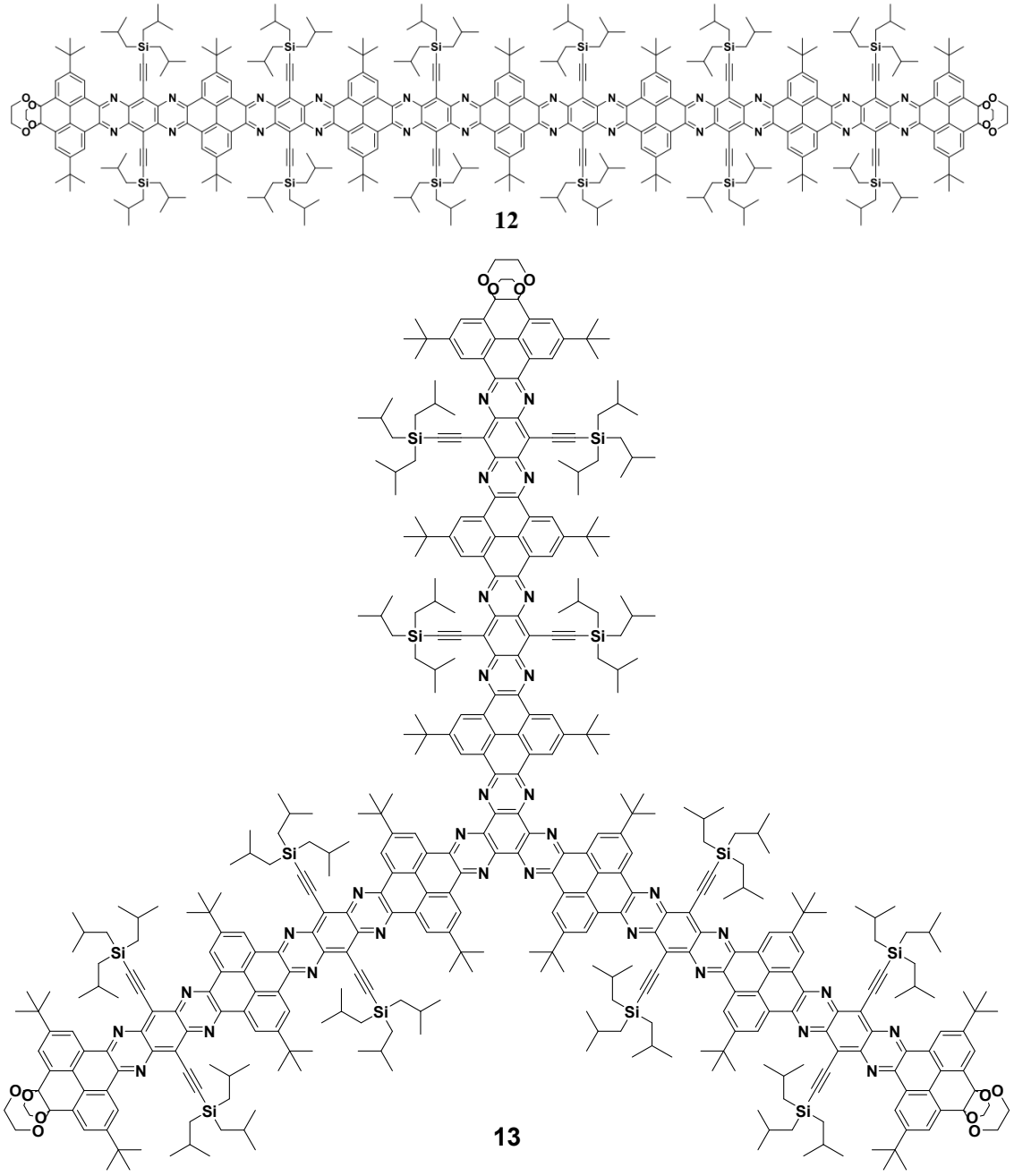

**Figure 2.2.4** 7.7 nm long pyrene-fused N-heteroacenes and giant star-shaped N-heteroacenes.

### 2.2.2 Nucleophilic amination

In 2013, Bunz *et al*. reported the nucleophilic aminations between fluoroaromatic compounds and diamine.[9c] By treating phenazine diamine with fluorinated aromatic compounds in the presence of sodium hydride, a series of novel fluorinated tetraazaacenes (**15-18**) were obtained.

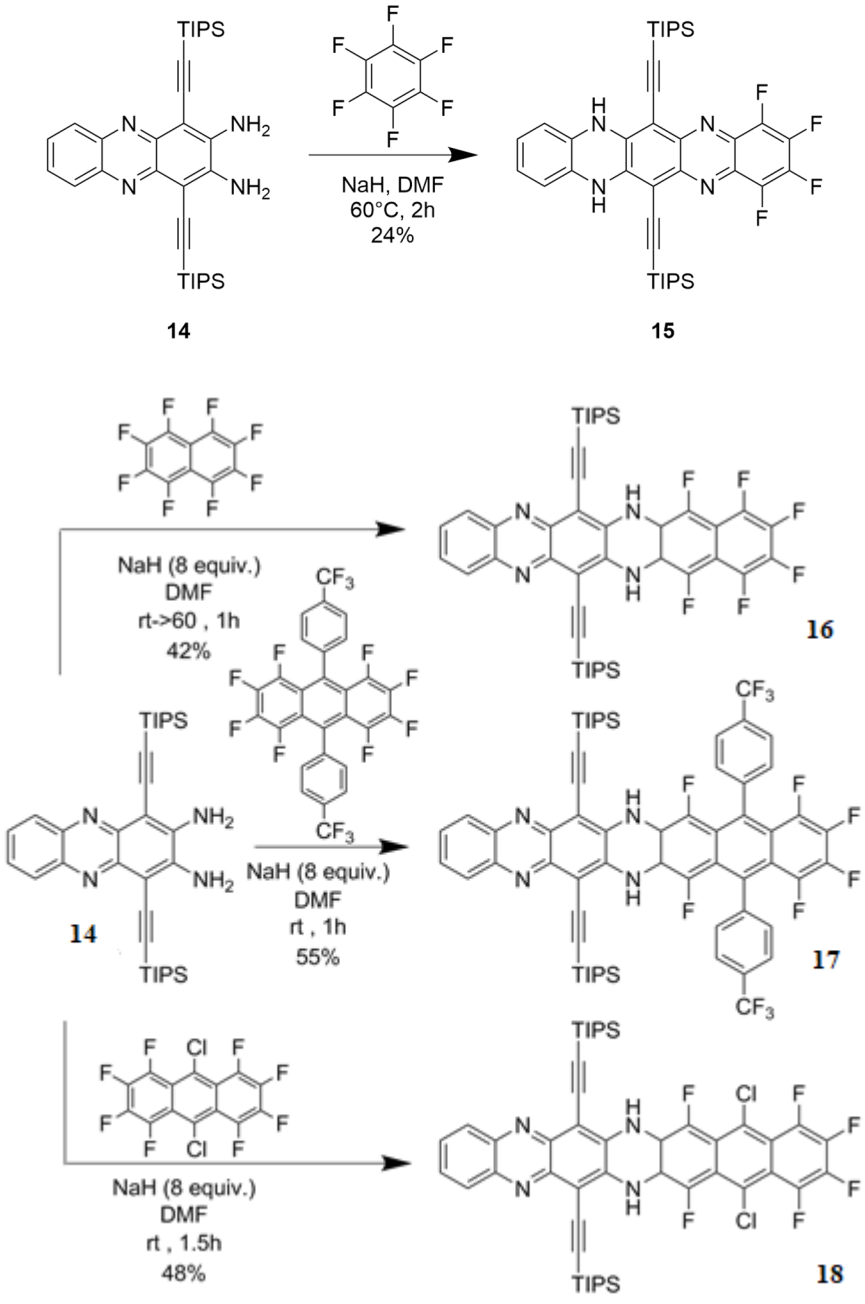


**Figure 2.2.5** A series of novel fluorinated tetraazaacenes synthesized by Bunz *et al*.

However, only **15** could be oxidized into the fully conjugated acene, whereas the oxidation of **16-18** either gave unidentifiable mixtures or dimerized products.

Miao *et al*. reported highly electron-deficient hexaazapentacenes through the nucleophilic amination between cyanide substituted compounds and *o*-diamines.[15] The yields of such reactions are very good due to the high reactivity of **19**. Because of the presence of three fused pyrazine rings, **23** is so electron-deficient that common oxidizer, such as $MnO_2$, chloranil and DDQ, cannot oxidize **22**. Finally, $PbO_2$ was proven to be an effective oxidizer, which rendered **23** in excellent yield. Although high electron-deficiency means high electron affinity which could make **23** a promising n-type material in OFET, the very low-lying LUMO level actually compromises the ambient stability of **23** and turns it into a potent oxidizer.

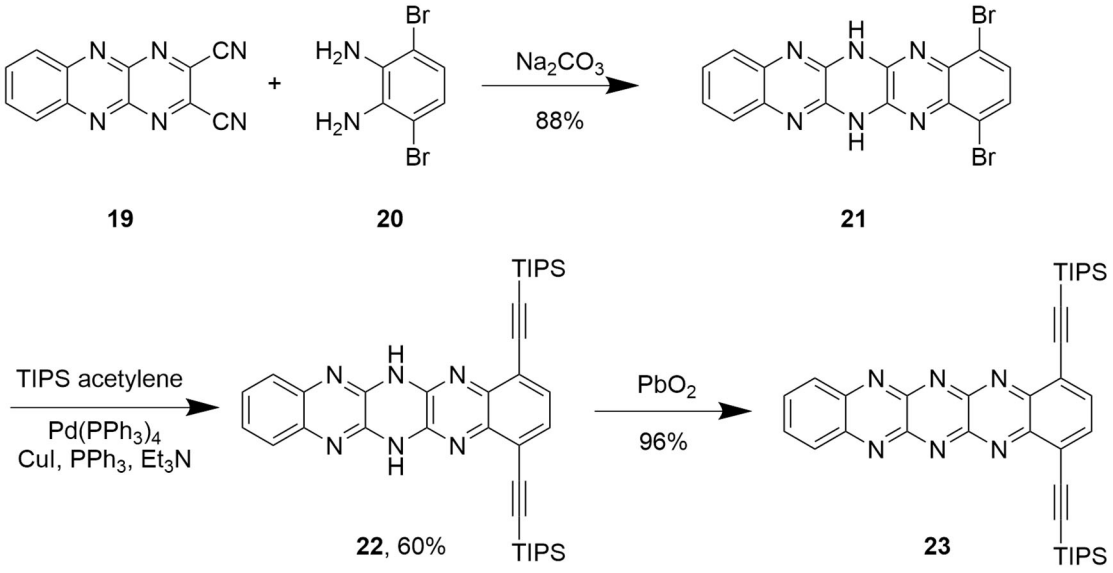


**Figure 2.2.6** Synthesis of highly electron-deficient hexaazapentacene.

The previous two examples are just rare cases, where the palladium catalysts are not involved in the nucleophilic aminations. In order to achieve the catalyst free nucleophilic amination, the halogenated reactants should be electron-deficient whereas the *o*-phenyldiamines should be electron-rich. This could be easily explained by the nucleophilic nature of the reaction that the electron-deficiency of halogenated reactants favors the nucleophilic attack of electron-rich amino groups. In the synthesis of **21**, reactant **19** is quite electron-deficient and **20** does not bear any strong electron-withdrawing groups. As

a result, this reaction only requires weak base and furnishes **23** in very good yield. In comparison, in the syntheses of fluorinated tetraazacenes, a less electron-rich diamine **14** is used, and the C-F bond is quite strong. Consequently, a much stronger base (NaH) was employed, and the yields were just mediocre.

To improve the applicability of nucleophilic amination, palladium catalysts are utilized. Bunz and co-workers first reported the C-N activation method to synthesize azapentacenes (**26a-c**).[16] Using $Pd(dba)_2$ as palladium source and RuPhos as ligand, the coupling reaction between 1,2-dichloroquinoxaline and TIPS substituted diamine in Hünig base gives the desired compound in good to excellent yield. This opened a new path towards the synthesis of large azaacenes.

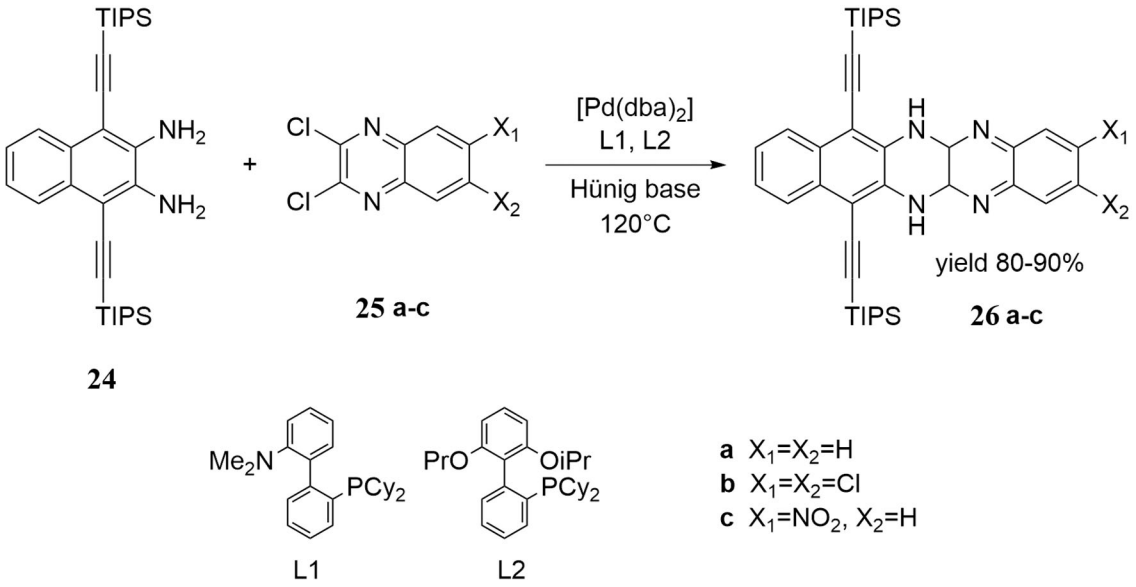


**Figure 2.2.7** Syntheses of azapentacenes via palladium catalyzed C-N coupling.

Shortly after, stable tetraazahexacenes were obtained using the same method and larger diamines. [9a] Although at this point this palladium way to synthesize azaacenes seems to be fairly useful, one must be aware of the fact that the dihalides used in these reactions are still electron-deficient species. Moreover, there are certain drawbacks of this method as well. Firstly, inactive halogen compounds, such as 1,2-dibromobenzene, do not react with ortho diamines under the reported condition. Secondly, if the reactants or the products are reductive or oxidative, it could lead to the reductive or oxidative poisoning of palladium catalysts.

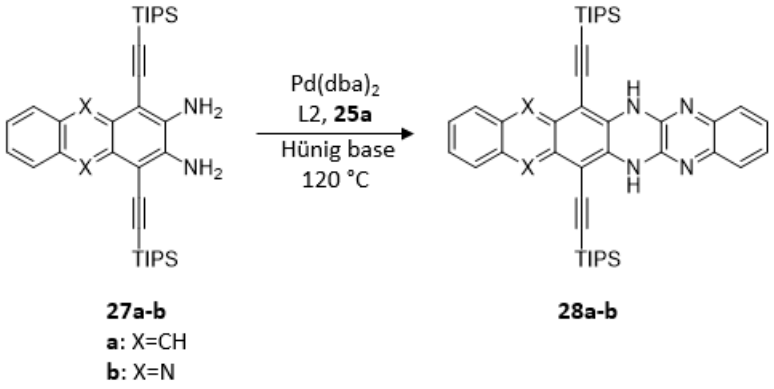


**Figure 2.2.8** Syntheses of azahexacenes via palladium catalyzed C-N coupling.

To further expand the scope of palladium catalyzed nucleophilic amination, Bunz *et al*. proposed that microwave is needed to promote reaction between inactive dihalides and diamines to achieve moderate yield.[9b] More active palladium source, RuPhos Pd G1 precatalyst, was also used.

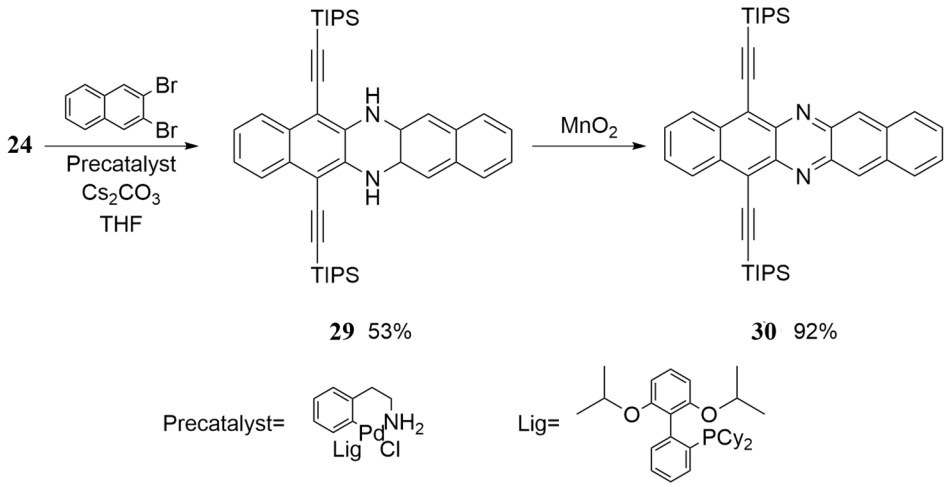


**Figure 2.2.9** Microwave-assisted coupling reactions of *o*-diamine with inactive *o*-dihalide using Pd catalyst.

Following the success of microwave-assisted C-N coupling, azaheptacenes were synthesized.[10b] Like its hydrocarbon analogues, azaheptacenes are unstable and susceptible to dimerization. Therefore, bulky solubilizing side chains are introduced to weaken the π-π interaction and enlarge the distance between azaheptacene molecules. Proton NMR shows that **34a** is not stable in solution. Dimerized products could be

observed after merely 2 min in solution. In comparison, **34b** is stable in solution for one hour, which is attributed to the larger sec-butyl side chains.

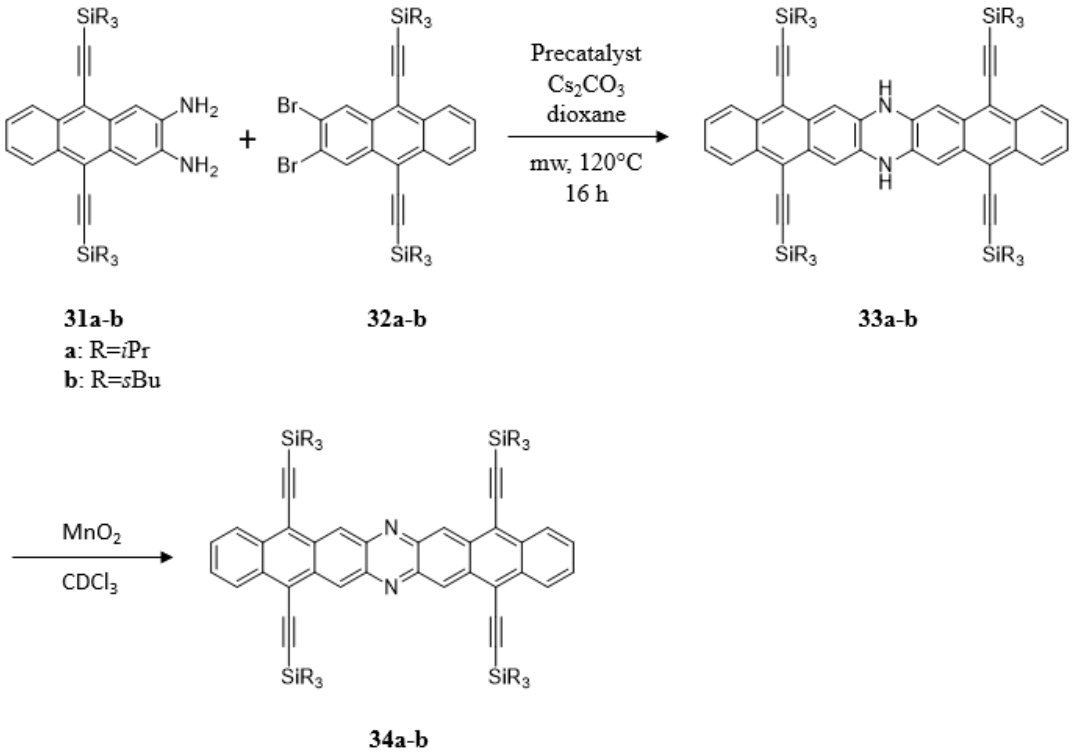


**Figure 2.2.10** Synthesis of azaheptacenes.

Recently, Koert *et al*. reported the coupling of inactive dibromo compounds and 2,3-diaminonaphthalene using RuPhos Pd G2 as catalyst.[17] This method does not require microwave probably due to the increased reactivity of palladium catalyst and unsubstituted 2,3-diaminonaphthalene. The yield of this method could even reach 90%.

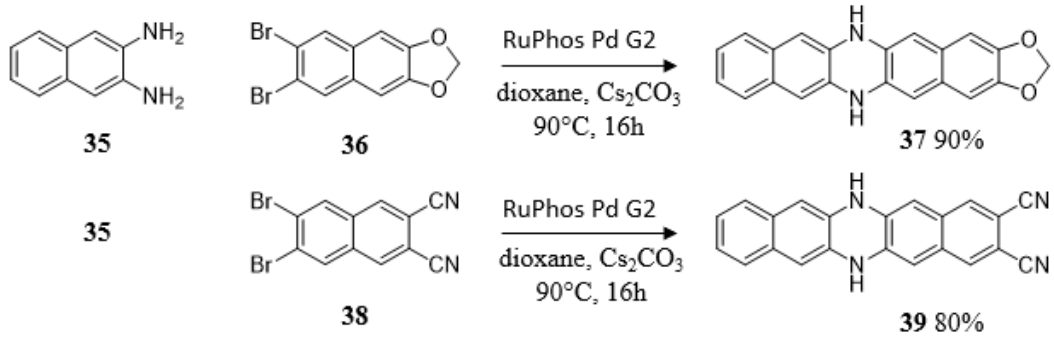


**Figure 2.2.11** Coupling reactions without microwave using RuPhos Pd G2 as catalyst.

Palladium catalyzed C-N activation has been systematically studied over the years. However, the reactivities of various diamines and dihalides have never been compared. Herein, the reactivities of commonly used reactants in palladium catalyzed nucleophilic amination are summarized.

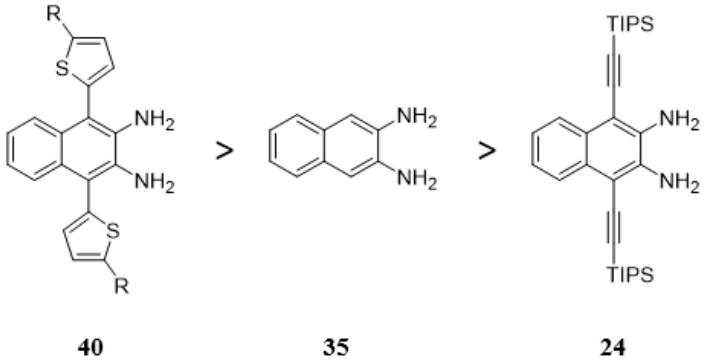


**Figure 2.2.12** Influence of side chains on the reactivity of 2,3-diaminonaphthalene.

As shown in the figure above, electron-donating groups could increase the reactivity of diamines due to the higher electron density on amino groups, whereas the slightly electron-withdrawing acetylene groups have the negative effect.

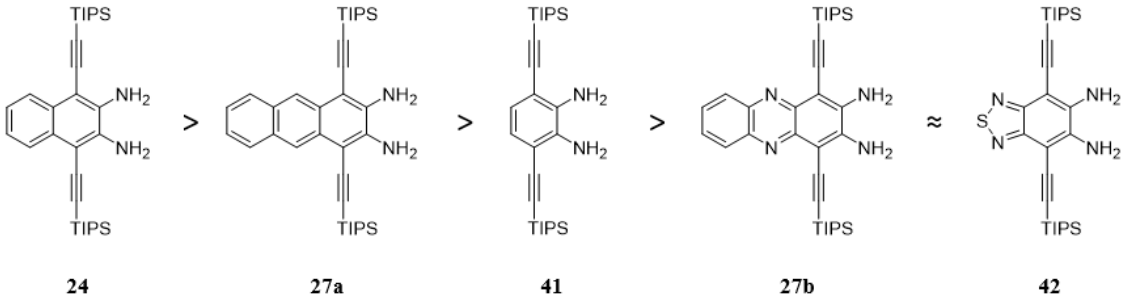


**Figure 2.2.13** Difference in reactivity of various TIPS substituted diamines.

Since the center benzene ring of anthracene has higher electron density than the peripheral benzene, the anthracene diamine has a lower reactivity compared with naphthalene diamine. Experiments are also in accordance with this ranking. In the microwave-assisted syntheses of azaacenes reported by Bunz *et al*., when anthracene diamine is reactant strong base sodium tert-butoxide is used in order to achieve a moderate yield. But for naphthalene diamine, weaker base cesium carbonate could be applied to reach a similar yield. For the phenylene diamine, unpaired electrons of amino groups are delocalized to a greater extend

due to the high aromaticity of benzene ring. Hence, the electron density on amino groups of phenylene diamine is low. With the electron-withdrawing moiety, **27b** and **42** have significantly decreased reactivities. Thus, the reactions between **27b** and inactive dihalides could not yield the desired closed-ring compounds.

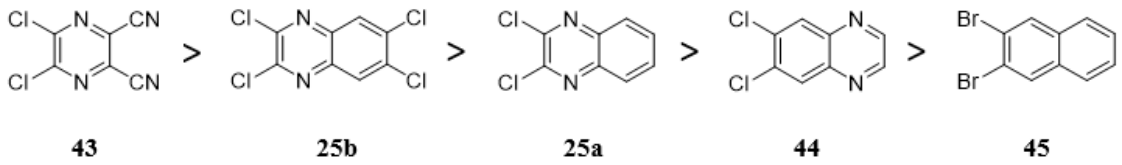


**43** **25b** **25a** **44** **45**

**Figure 2.2.14** Difference in reactivity of various dihalides.

On the contrary to diamines, electron-withdrawing moieties enhance the reactivity of dihalides. *o*-Phenylenediamine could react with **43** without any palladium catalyst and base as a result of highly electron-negative pyrazine ring. However, if halogen is attached onto benzene ring instead of electron-deficient pyrazine ring, there will be a substantial drop of reactivity. For dihalides **45**, no electron-withdrawing moiety is present at the aromatic ring resulting in the poor reactivity towards diamines. Microwave has to be applied to achieve moderate yield of nucleophilic amination.

### 2.2.3 Other synthetic routes

In 2013, Satoshi et.al reported a novel synthesis of quinoxalines.[18] Hypervalent iodine (III) was used to induce this oxidative [4+2] annulation. Unlike the traditional synthesis of quinoxalines through condensation of diamine and diketone, this method allows a quick access to electron deficient quinoxalines using alkynes.

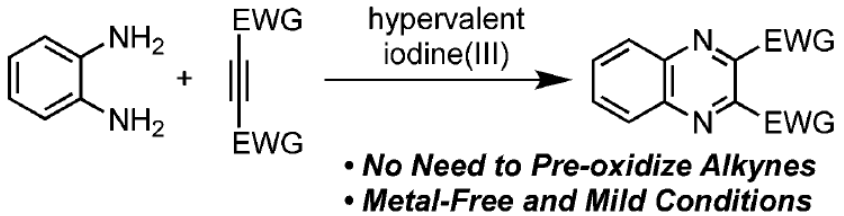


**Figure 2.2.15** Synthesis of quinoxalines through [4+2] annulation.

Another way to incorporate N atoms to the aromatic system is to introduce pyridazine rings. As shown in the scheme, the introduction of phthalazine unit is achieved by the condensation between ortho-dialdehyde and hydrazine.

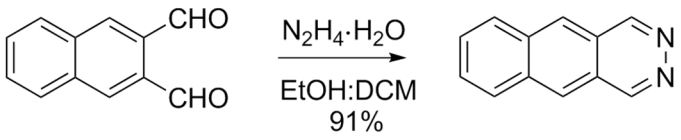


**Figure 2.2.16** Condensation reaction of o-dialdehyde and hydrazine.

Instead of phthalazine unit, cinnoline could also be incorporated. Haley et.al reported the cinnoline-containing azaacenes, which is the first example of large cinnoline system[19].

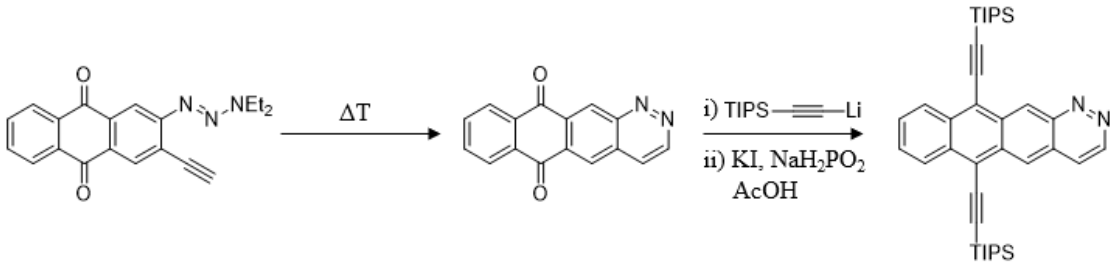


**Figure 2.2.17** Synthesis of cinnoline-containing acene.

## 2.3 PhD in context of literature

In this chapter, the literature regarding the theoretical calculations and synthetic methods of N-heteroarenes are discussed. Multiple examples of theoretical calculations showed that azaacenes are competitive candidates of excellent n-type semiconductors. From the theoretical point of view, electron affinity, reorganization energy and band positions are useful parameters to evaluate the n-type semiconductor properties, which also provides theoretical guidelines for the design of azaacenes. Shortly after, thanks to the great efforts made by organic chemists, various azaacenes were synthesized and applied in organic electronics. As expected, some of these azaarenes exhibited surprisingly high n-type mobilities. Synthetic methods are divided into two categories. One is the condensation reaction between *o*-quinones and *o*-diamines. The other is the nucleophilic amination between *o*-diamines and *o*-dihalides. Condensation is the most widely used method due to its ease of operation and high efficiency. However, the need to synthesize versatile

azaacenes and the difficulty to obtain *o*-quinones prompted chemists to develop new method. Palladium-catalyzed nucleophilic amination was then successfully applied in the synthesis of tetraazaacenes.

For the unconventional azaarenes with nonlinear shapes and novel functional groups, there is a lack of related literature concerning the theoretical calculations, yet, still the parameters used to evaluate azaacenes could be applied. For the synthesis, both condensation and nucleophilic amination could be adopted. But new building blocks are apparently required.

**References**

[1] H. Y. Chen, I. Chao, *Chemphyschem* **2006**, *7*, 2003-2007.

[2] M. Winkler, K. N. Houk, *J. Am. Chem. Soc.* **2007**, *129*, 1805-1815.

[3] X.-D. Tang, Y. Liao, H. Geng, Z.-G. Shuai, *J. Mater. Chem.* **2012**, *22*, 18181.

[4] O. Hinsberg, *Justus Liebigs Annalen der Chemie* **1901**, *319*, 257-286.

[5] O. Fischer, E. Hepp, *Berichte der deutschen chemischen Gesellschaft* **1890**, *23*, 2789-2793.

[6] M. Chu, J.-X. Fan, S. Yang, D. Liu, C. F. Ng, H. Dong, A.-M. Ren, Q. Miao, *Adv. Mater.* **2018**, *30*, 1803467.

[7] a) S. Miao, A. L. Appleton, N. Berger, S. Barlow, S. R. Marder, K. I. Hardcastle, U. H. F. Bunz, *Chem. Eur. J.* **2009**, *15*, 4990-4993; b) J. U. Engelhart, F. Paulus, M. Schaffroth, V. Vasilenko, O. Tverskoy, F. Rominger, U. H. F. Bunz, *J. Org. Chem.* **2016**, *81*, 1198-1205.

[8] G. Li, Y. C. Wu, J. K. Gao, C. Y. Wang, J. B. Li, H. C. Zhang, Y. Zhao, Y. L. Zhao, Q. C. Zhang, *J. Am. Chem. Soc.* **2012**, *134*, 20298-20301.

[9] a) B. D. Lindner, J. U. Engelhart, O. Tverskoy, A. L. Appleton, F. Rominger, A. Peters, H.-J. Himmel, U. H. F. Bunz, *Angew. Chem. Int. Ed.* **2011**, *50*, 8588-8591; b) J. U. Engelhart, B. D. Lindner, O. Tverskoy, F. Rominger, U. H. F. Bunz, *Chem. Eur. J.* **2013**, *19*, 15089-15092; c) J. U. Engelhart, B. D. Lindner, O. Tverskoy, F. Rominger, U. H. F. Bunz, *J. Org. Chem.* **2013**, *78*, 10832-10839.

[10] a) A. L. Appleton, S. Barlow, S. R. Marder, K. I. Hardcastle, U. H. F. Bunz, *Synlett* **2011**, *22*, 1983-1986; b) J. U. Engelhart, O. Tverskoy, U. H. F. Bunz, *J. Am. Chem. Soc.* **2014**, *136*, 15166-15169.

[11] S. More, R. Bhosale, S. Choudhary, A. Mateo-Alonso, *Org. Lett.* **2012**, *14*, 4170-4173.

[12] D. Cortizo-Lacalle, J. P. Mora-Fuentes, K. Strutyński, A. Saeki, M. Melle-Franco, A. Mateo-Alonso, *Angew. Chem. Int. Ed.* **2018**, *57*, 703-708.

[13] J. P. Mora-Fuentes, A. Riaño, D. Cortizo-Lacalle, A. Saeki, M. Melle-Franco, A. Mateo-Alonso, *Angew. Chem. Int. Ed.* **2019**, *58*, 552-556.

[14] a) Z. Wang, J. Miao, G. Long, P. Gu, J. Li, N. Aratani, H. Yamada, B. Liu, Q. Zhang, *Chem. Asain. J.* **2016**, *11*, 482-485; b) W. Chen, X. Li, G. Long, Y. Li, R. Ganguly, M. Zhang, N. Aratani, H. Yamada, M. Liu, Q. Zhang, *Angew. Chem. Int. Ed.* **2018**, *57*, 13555-13559.

[15] Z. He, R. Mao, D. Liu, Q. Miao, *Org. Lett.* **2012**, *14*, 4190-4193.

[16] O. Tverskoy, F. Rominger, A. Peters, H.-J. Himmel, U. H. F. Bunz, *Angew. Chem. Int. Ed.* **2011**, *50*, 3557-3560.

[17] J. Schwaben, N. Münster, M. Klues, T. Breuer, P. Hofmann, K. Harms, G. Witte, U. Koert, *Chem. Eur. J.* **2015**, *21*, 13758-13771.

[18] S. Okumura, Y. Takeda, K. Kiyokawa, S. Minakata, *Chem. Commun.* **2013**, *49*, 9266-9268.

[19] B. S. Young, J. L. Marshall, E. MacDonald, C. L. Vonnegut, M. M. Haley, *Chem. Commun.* **2012**, *48*, 5166-5168.

# Chapter 3

# Experimental Methodology

*Chapter 3 discusses the principles underlying the synthesis and characterization of azaacenes. Purification methods, including recrystallization, distillation, extraction and chromatography, are illustrated. Fundamentals of characterization methods, such as UV-Vis spectroscopy, fluorescence spectroscopy, nuclear magnetic resonance spectroscopy, mass spectrum and single crystal X-ray analysis are discussed.*

## 3.1 Rationale for selection

This thesis mainly focuses on the synthesis and characterizations of azaarenes. General experimental techniques of organic synthesis, such as extraction, distillation and chromatography, have to be introduced. Characterizations in this thesis serve two purposes. One is the determination of structures. The other is the investigation of properties. For the structure determination, NMR, HRMS, FTIR and X-ray crystallography are discussed. For the property investigation, UV-Vis spectroscopy and fluorescence spectroscopy are used to obtain optical properties of azaarenes, whereas cyclic voltammetry is applied to test the electrochemical properties.

## 3.2 Synthetic methodology

### 3.2.1 Extraction

Extraction is one of the most frequently used work-up procedures in organic lab. It is usually carried out in a separating funnel. The general steps are as followed:

1) Two solutions (not immiscible) are added to the funnel. Normally, one is organic solution, and the other is aqueous solution.
2) Shake the funnel to mix the two phases thoroughly.
3) The mixture is allowed to stand to give two layers again.
4) Drain the lower layer into a container and pour out the upper layer into another container.

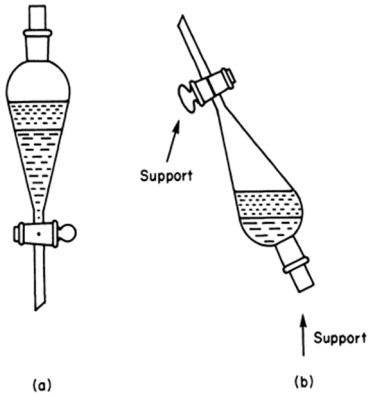


**Figure 3.1** a) Separating funnel; b) Venting excess pressure. (Copied from Ref [1])

### 3.2.2 Recrystallization

Generally, the crude product obtained from one organic reaction is not pure and often contaminated with byproduct, unreacted starting material or catalysts. The most efficient way to purify the solid crude product is the recrystallization using appropriate solvent or solvent mixture. The general steps are as followed:

1) Dissolve the crude product into proper solvent at the boiling point to obtain the near saturated solution. If the melting point of crude product ($T_m$) is lower than the boiling point of solvent ($T_b$), then the solution should not be heated to a temperature higher than $T_m$.
2) If the solution contains colored impurities, activated charcoal could be added to absorb them.
3) Filter the solution while hot to remove insoluble impurities and activated charcoal.
4) Cool the filtrate slowly so that crystals of desired product would form while soluble impurities remain in the solution.
5) Isolate the crystals by suction filtration and wash it with small amount of solvent to remove the mother liquor. Test the melting point of the obtained crystal. If the purity could not meet the standard, repeat the above steps until the purity is good enough.

Solubility of solid organic compounds in solvents is closely related to temperature. Normally, as temperature increases, the solubility increases as well. When organic solids are dissolved in hot solvent to give a near saturated solution, once the solution is cooled, it will become oversaturated. Ideally, the organic solids will crystallize out of the solution and the impurities remain in the solution. Obviously, recrystallization is a technique which takes advantage of changes in solubility at different temperatures. So, finding a proper solvent or solvent mixture is the key to successful recrystallization. The ideal solvent should meet the following requirements:

1) Does not react with the desired product.
2) The solubility changes between high temperature and low temperature should be as large as possible.
3) Impurities should have a very good or very poor solubility in the solution.

4) Easy to evaporate (low boiling point) so that solvent could be removed with ease.
5) Product could form nice crystals instead of fine powder.
6) No or low toxicity.

**Table 3.1** Common recrystallization solvents

| Solvent | Boiling point/°C | Melting point/°C | Miscibility with water | Flammability |
|---|---|---|---|---|
| Water | 100 | 0 | + | 0 |
| Methanol | 65 | <0 | + | + |
| 95% Ethanol | 78 | <0 | + | ++ |
| Acetic acid | 118 | 16.7 | + | + |
| Acetone | 56 | <0 | + | +++ |
| Diethyl ether | 34.5 | <0 | - | ++++ |
| Hexanes | 50-70 | <0 | - | ++++ |
| Ethyl acetate | 78 | <0 | - | ++ |
| Chloroform | 62 | <0 | - | 0 |
| Benzene | 80 | <0 | - | 0 |

### 3.2.3 Distillation

Like recrystallization, distillation is another efficient technique to purify crude product. The difference is that distillation is widely used to purify or separate organic liquids. A simple distillation typically involves heating the liquid to its boiling point to generate vapor and condensation of the vapor to yield desired liquid product. If the difference in boiling point between two components is larger than 30°C, simple distillation could be adopted. However, when the difference is less than 30°C, fractional distillation should be used, which requires more complicated apparatus. For high boiling point liquids, distillation at atmospheric pressure is often difficult and might cause the decomposition of desired product. In this case, distillation should be conducted at reduced pressure to lower the

boiling point thus preventing the liquid from decomposition. This technique is generally known as vacuum distillation.

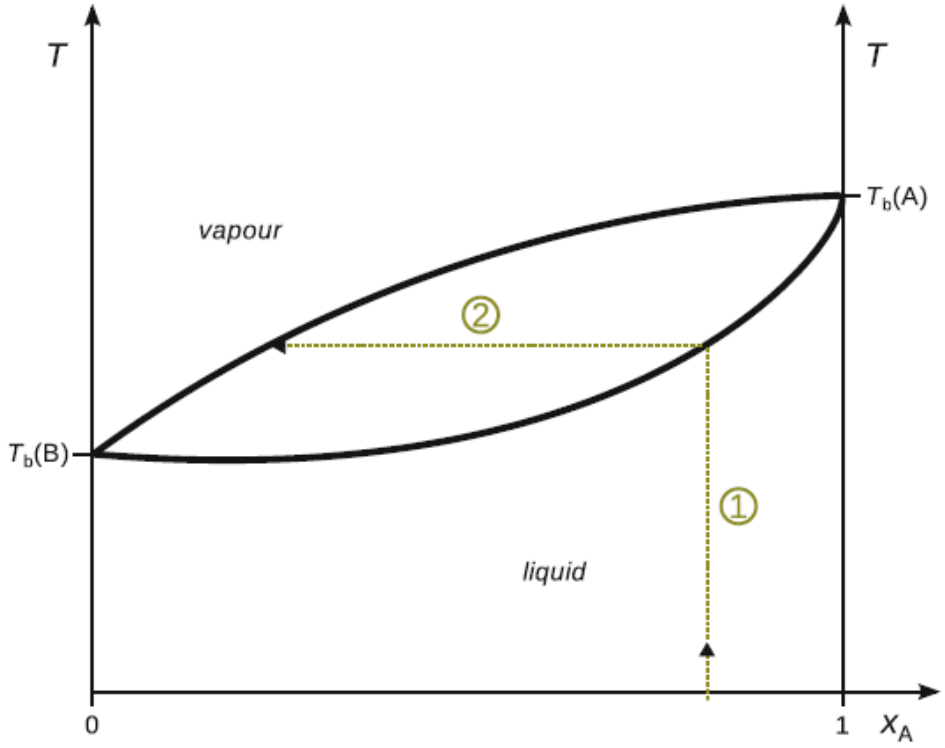


**Figure 3.2** Illustration of simple distillation process. (Copied from Ref [2])

In the simple distillation apparatus, a liquid mixture of highly volatile B and less volatile A could be separated to some extent. As shown in Figure 3.1, the initial ratio of A is around 80%. In the arrow 1, as the temperature increases, the mixture reach the bubbling point where it starts to boil. If the temperature remains constant at the bubbling point, the ratio of A in the vapor phase will be less than that of B. Since more B is continuously removed from the mixture by condensation, the ratio of A in the whole mixture would decrease as depicted in arrow 2. During arrow 1 and 2, there is more B being removed than A, which means the ratio of B in the distillate is larger than A. Apparently, this process dose not give the 100% pure product, and it is only useful when the difference in boiling point between two components is larger than 30°C.

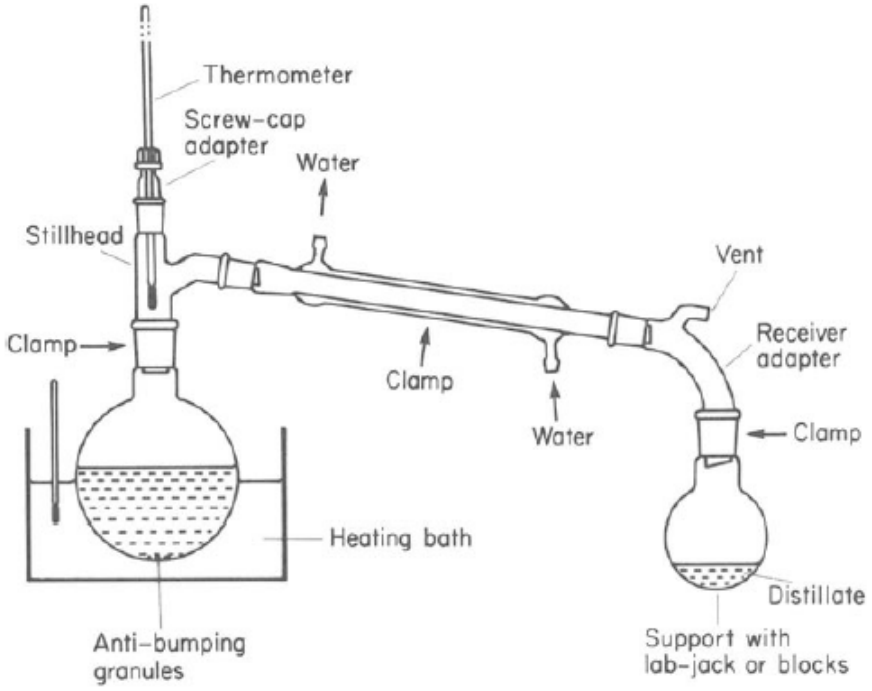


**Figure 3.3** Distillation at atmospheric pressure. (Copied from Ref [1])

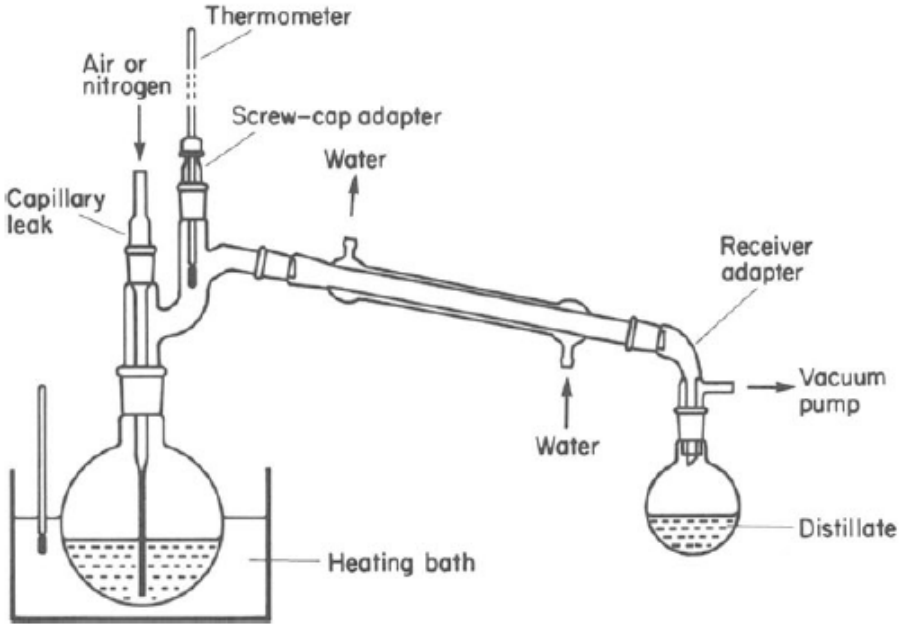


**Figure 3.4** Vacuum distillation. (Copied from Ref [1])

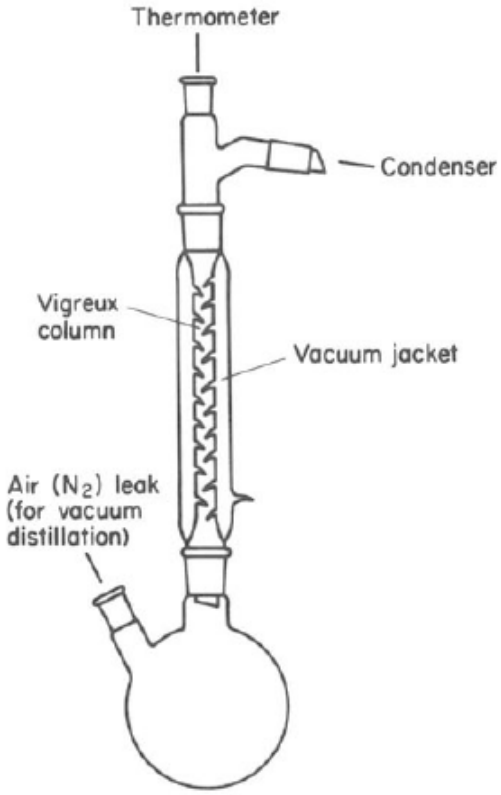


**Figure 3.5** Fractional distillation. (Copied from Ref [1])

### 3.2.4 Chromatography

Chromatography is one of the most important and widely used methods to separate, purify and identify organic compounds. The basic idea of chromatography is to take advantage of the distribution law. The mixture is firstly dissolved in solvent and absorbed by the stationary phase (typically silica gel or alumina). Then mobile phase is added to elute the mixture. Since different components have different distribution coefficient between stationary phase and mobile phase, during the elution process, the mixture could be separated. For component having lowest distribution in stationary phase, it will be eluted

out first. For component having the highest distribution in stationary phase, it will be eluted out last. In the modern organic laboratory, there are generally two types of chromatography:

1) small-scale, analytical chromatography.
2) large-scale, preparative chromatography.

In this thesis, thin layer chromatography (TLC) and column chromatography (CC) will be introduced.

**a) Thin layer chromatography (TLC)**

Thin layer chromatography is known for quick qualitative analysis of mixtures. It is usually used to monitor organic reactions and determine the polarity of eluent in preparative column chromatography. TLC generally involves the following procedures:

1) Prepare sample solution with proper concentration. The ideal solvent should be volatile and nonpolar.
2) Apply the sample to TLC plate using a capillary dropper. The sample spot should never be immersed in the developing solvent.
3) Run the TLC in developing solvent with proper polarity in a suitable developing jar.
4) Examine the TLC plate under an UV lamp.

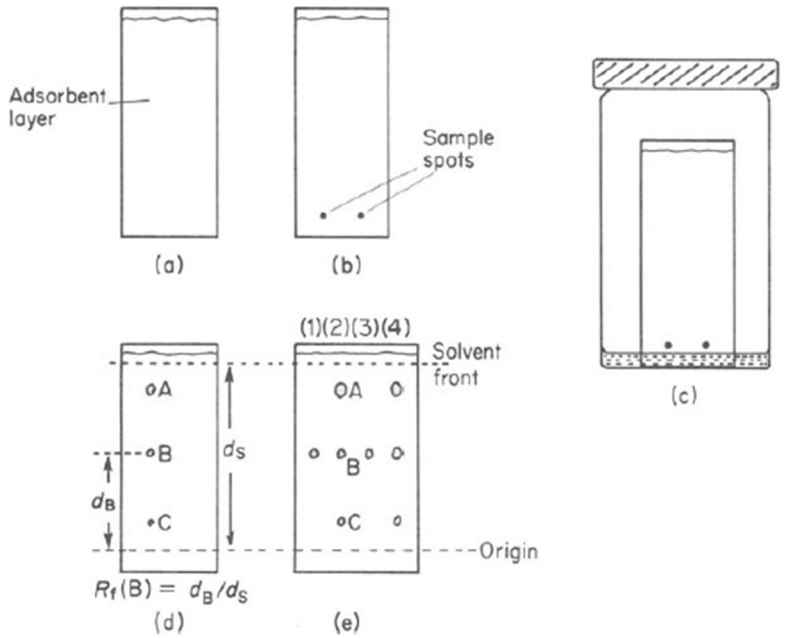


**Figure 3.6** Thin layer chromatography. (Copied from Ref [1])

**b) Column chromatography**

Column chromatography (CC) is the most important tool to separate mixtures on a preparative scale. For the CC, the following steps are involved:

1) Select proper eluting solvent. This could be done by a preliminary TLC to find out the suitable polarity of the solvent mixture. Generally, hexane/ethyl acetate solvent mixture is recommended since it covers a wide range of polarity and has low toxicity. For compounds not soluble in hexane and ethyl acetate, dichloromethane/hexane could be used.
2) Pack the column. Depending on the quantity of mixtures, a column of proper size could be selected accordingly (Table 3.2). Columns with fritted glass pad are preferred. To the column, a small volume of eluent is added in order to soak the glass pad. Before the addition of silica gel paste, make sure there is 5 cm high solvent in the column. To a beaker, silica gel is added followed by the addition of eluent so that silica gel is fully immersed. Stir the mixture to form silica gel paste. At this point, there should not be any bubbles in the paste. Then transfer the paste to column using an addition funnel. Rinse the funnel with eluent and apply pressure to drive off excessive eluent. Never let the column run dry.
3)

**Table 3.2** Selection of different column sizes

| Column diameter (mm) | Volume of eluent (ml) | Typical sample loading (mg) | | Typical fraction size (ml) |
|---|---|---|---|---|
| | | $\Delta R_f \geq 0.2$ | $\Delta R_f \geq 0.1$ | |
| 10 | 100 | 100 | 40 | 5 |
| 20 | 200 | 400 | 160 | 10 |
| 30 | 400 | 900 | 360 | 20 |
| 40 | 600 | 1600 | 600 | 30 |
| 50 | 1000 | 2500 | 1000 | 50 |

4) Load the sample. Prepare a concentrated solution of mixture. Add the solution onto the absorbent bed carefully. Do not disrupt the surface of absorbent bed. Push the solution

into the silica gel by applying pressure. Wash the walls with a small amount of eluent and push washings into the absorbent bed. Add sand onto the top of the silica gel.

5) Elute the column. Fill the column and reservoir with eluent and connect the column with pressurizing pump. Collect the eluate with a rack of test tubes and determine the purity and composition of each fraction by TLC.

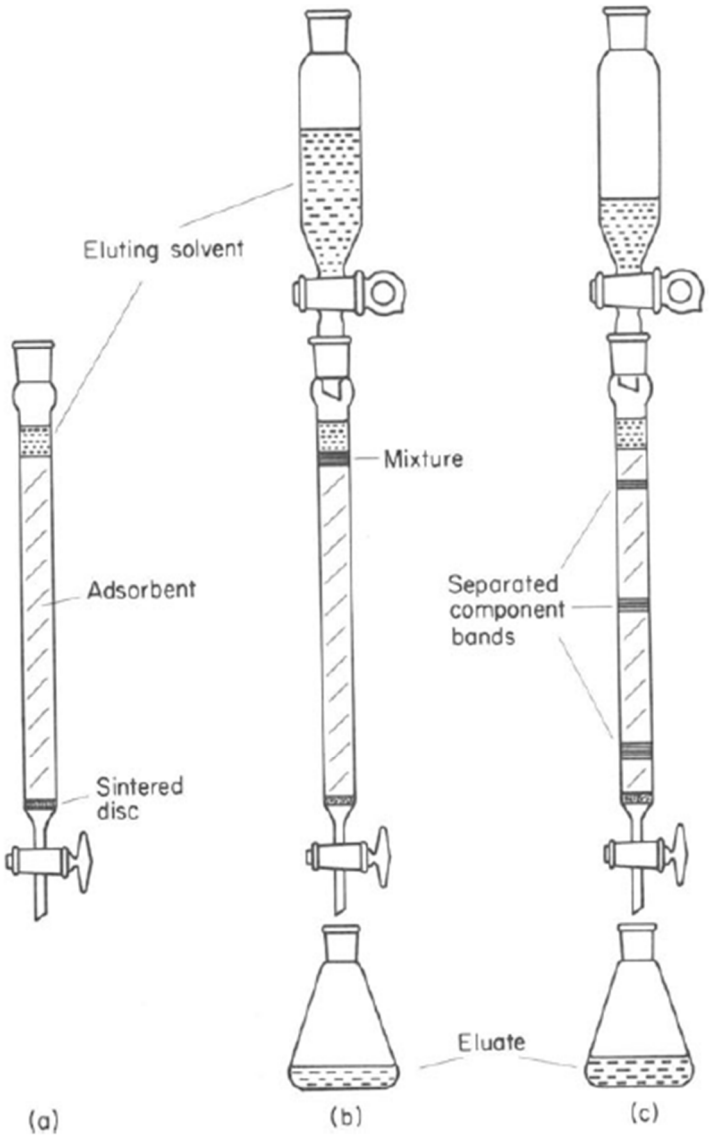


**Figure 3.7** Column chromatography (gravity elution). (Copied from Ref [1])

## 3.2 Characterization methodology

### 3.3.1 Infrared spectroscopy

Although nowadays NMR is the most powerful tool for organic chemists to determine the structure of an unknown product, infrared spectroscopy still plays an important role for the following reasons:

1) Facile determination of some functional groups, especially polar functional groups, such as carbonyl group and hydroxyl group.
2) Excellent applicability. Able to test samples in solid, liquid or gaseous state. The price of an infrared spectroscopy is way cheaper than NMR or mass spectroscopy.
3) Ability to differentiate inorganic compounds from organic compounds.

The infrared spectrum origins from the absorption of infrared light. The wavenumber of absorbance corresponds to rotational and vibrational frequency of sample molecule. Certain functional groups have their characteristic absorption wavenumber. Therefore, infrared spectroscopy is often used to determine the existence of certain functional groups.

By adopting the spring module, wavenumber of absorbance *v* can be calculated:

$$v = \frac{1}{2\pi c}\sqrt{\frac{k}{\mu}}$$

Where k is the spring constant for the bond, c is the speed of light, and $\mu$ is the reduced mass of the A-B system:

$$\mu = \frac{m_a m_b}{m_a + m_b}$$

For molecules without dipole momentum, there will be no rotational absorption. If the binary system consists of homonuclear two-atomic molecule, there will be no vibrational absorption neither. In this case, infrared spectroscopy is no longer applicable.

An infrared spectrum generally consists of two regions:

1) Functional group region ($v$≥1500 $cm^{-1}$).

2) Fingerprint region ($\nu$<1500 $cm^{-1}$).

In the IR spectrum, functional groups will have their characteristic bands in terms of frequency and intensity, which is very important to identify the unknown structures. Therefore, the functional group region is quite useful when determining a new structure. In the fingerprint region, there are so many troughs that it is difficult to interpret all the information accurately. Consequently, the fingerprint region is usually used to compare with a known compound.

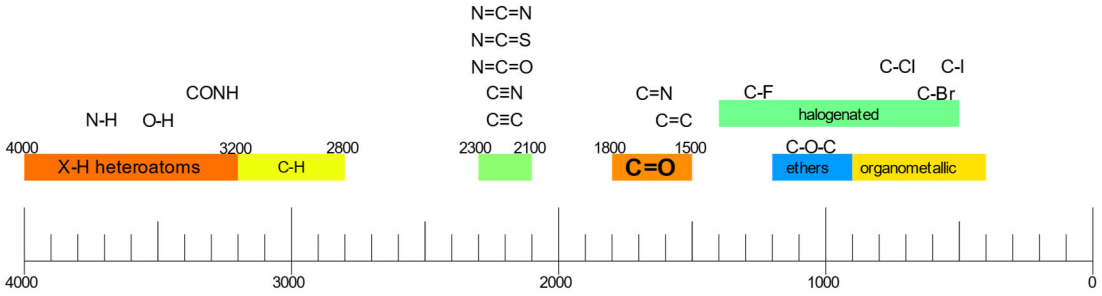


**Figure 3.8** List of main IR spectroscopy bands. (Retrieved from https://en.wikipedia.org/wiki/Infrared_spectroscopy

### 3.3.2 Ultraviolet–visible spectroscopy

The range of the UV-Vis spectrum is usually between 200 and 800 nm, whereas 200-400 nm is the UV part, and 400-800 nm is the visible part. Accordingly, the energy of UV and Vis light could be calculated to be 670-314 kJ/mol and 314-155 kJ/mol respectively. Since not all the excitation energy falls into the energy range of UV-Vis, only some of the organic compounds have UV-Vis absorption spectra.

In most organic compounds, atoms are connected by covalent bonds. There are two major covalent bonds. A Single bond is usually a σ bond. For the double bond and triple bond, beside the σ bond, there are π bonds. According to molecular orbital theory, there are σ-bonding orbital and π-bonding orbital. For each bonding orbital, there will be a corresponding anti-bonding orbital ($\sigma^*$ and $\pi^*$).

During the formation of σ bonds and π bonds, a large amount of energy is released. As a result, the bonding electrons of stable molecules always locate at the bonding orbitals, which have lower energy compared with anti-bonding orbitals.

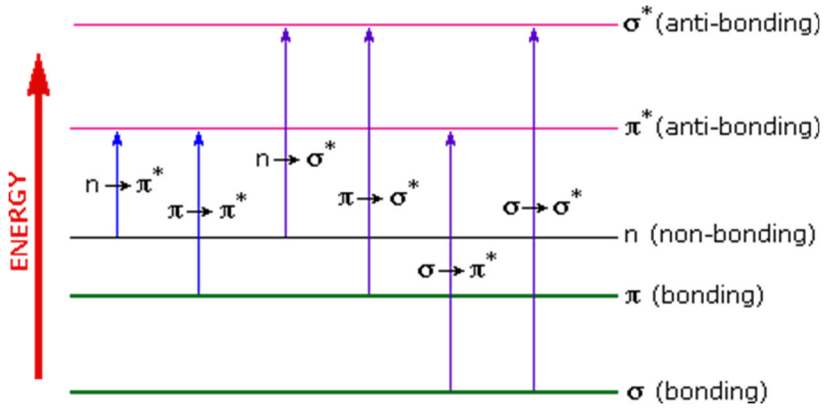


**Figure 3.9** Electronic excitations that may occur in organic molecules. (Retrieved from https://chem.libretexts.org/Bookshelves/Organic_Chemistry/Map%3A_Organic_Chemistry_(Vollhardt_and_Schore)/14%3A_Delocalized_Pi_Systems%3A_Investigation_by_Ultraviolet_and_Visible_Spectroscopy/14.11%3A_%09Electronic_Spectra%3A__Ultraviolet_and__Visible__Spectroscopy)

In Figure 3.9, there are 6 types of energy level transitions, among which the n- $\pi^*$ and π- $\pi^*$ require lowest energy. The energy needed for the transition could be roughly calculated by the equation below:

$$\Delta E = \frac{hc}{\lambda} = \frac{28600}{\lambda} \text{ kJ/mol}$$

where $\lambda$ is the wavelength. Using the equation, it is apparent that only n- $\pi^*$ transition absorb near-UV light. However, if a conjugated molecule contains two or more conjugated double bonds, the excitation energy of π- $\pi^*$ transition will be much lower, thus enabling it to absorb UV or even visible light.

Molecules, which are used in the organic electronics as semiconductors, usually contain π-electrons. Ultraviolet or visible light can be absorbed by these molecules. The absorption of light results in the excitation of the π-electrons to higher anti-bonding molecular orbitals. By measure the absorption curve of UV-vis, optical bandgap can be calculated.

### 3.3.3 Fluorescence spectroscopy

After the absorption of UV-Vis light, some organic molecules can give a spontaneous emission, which is known as fluorescence. In order to better understand the mechanism, Jablonski diagram is needed to illustrate the various electronic states and the transition between them.

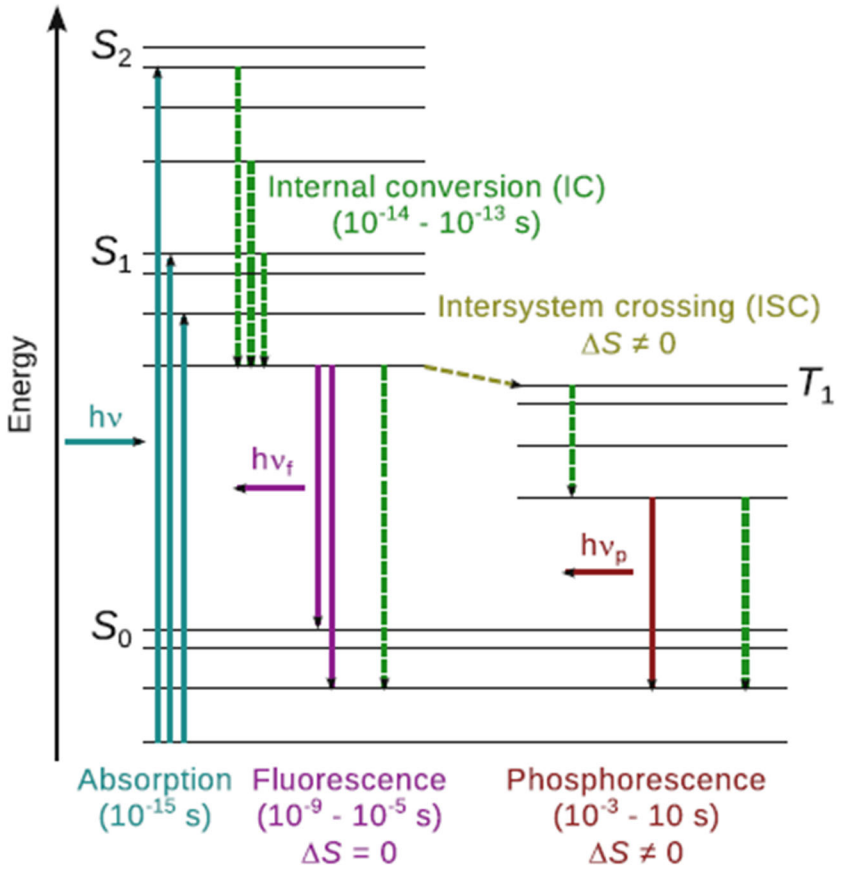


**Figure 3.10** Jablonski diagram. (Copied from Ref [2])

When a molecule absorbs light, it could reach various excited electronic states depending on the energy of that light and energy difference between excited states and ground states. If vibrational states are not considered, there would be only one excited state. However, since the molecules have different vibrational states, both ground states and excited states contain various vibrational states. After the molecule reached excited vibrational state ($S_1v_i$), it will eventually relax into the vibrational ground state ($S_1v_0$) through internal

conversion (IC) by dissipate the extra energy in the form of heat. Then the molecule returns to electronic ground state ($S_0v_i$) and give a light emission simultaneously. But in some cases, the molecule would go through another internal conversion without the emission of photons.

One important parameter to show the efficiency of the fluorescence process is quantum yield Φ:

$$\phi = \frac{\text{Number of protons emitted}}{\text{Number of protons absorbed}}$$

Typically, fluorescent molecules would emit less protons than they absorbed since the excited states could be deactivated by other processes:

1) Internal conversion;
2) Intersystem crossing;
3) Photoreaction;
4) Resonance energy transfer.

Fluorescence spectroscopy is one of the basic characterization tools in organic electronics and biomaterials. Fluorescent properties of molecules are closely related to applications in devices such as OLED and solar cells.

### 3.3.4 Nuclear Magnetic Resonance (NMR)

The modern organic chemistry is built on the development of NMR spectroscopy. The occurrence of NMR made it so much easier for organic chemists to determine the structures of new molecules. Today, NMR is the most widely used characterization method for organic compounds.

In a typical NMR test, NMR sample is placed in a strong constant magnetic field, then the magnetic signal of the sample is recorded. After Fourier transformation of the raw data, an NMR spectrum is obtained. The magnetic signal is produced by NMR active nuclei. Examples of frequently used nuclei are listed in the table below:

**Table 3.3** NMR-active nuclei.

| Nucleus | Spin | Natural abundance (%) | Frequency relative to $^{1}H$ |
|---|---|---|---|
| $^{1}H$ | ½ | 99.985 | 1.00000 |
| $^{13}C$ | ½ | 1.108 | 0.25145 |
| $^{15}N$ | ½ | 0.37 | 0.10137 |
| $^{19}F$ | ½ | 100 | 0.94094 |
| $^{31}P$ | ½ | 100 | 0.40481 |
| $^{2}H$ | 1 | 0.015 | 0.15351 |

Whether a nucleus is NMR-active is dictated by the nuclear spin quantum number *I*. Unlike the electron spin quantum number *s*, which has a set value of ½, the value of nuclear spin quantum number *I* cannot be predicted based on the number of protons and neutrons within an atom. It could only be roughly estimated using the following rules:

1) If the number of protons (Z) and the number of neutrons (N) are both even. Then the spin quantum number *I* is 0. In this case, the nucleus is not NMR-active.
2) If one of Z and N is even, and the other is odd, then *I* is half-integral.
3) If both Z and N are odd, then *I* is integral.

In 2) and 3), the nuclei are NMR-active. When the nuclear spin quantum number is not equal to 0, in a strong homogenous magnetic field, the nuclei will flip into higher-energy alignment. In the following time T, the nuclei will restore to their original states along with the emission of radio frequency signal, which is called free induction decay (FID).

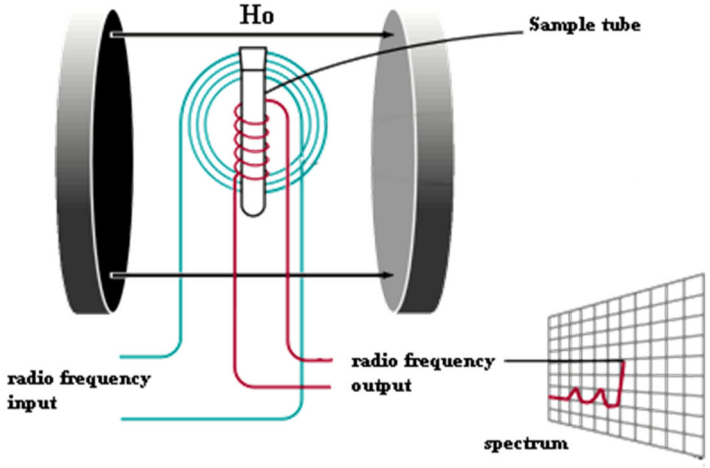


**Figure 3.11** Simple illustration of general principle of NMR. (Retrieved from http://www.chem.ucalgary.ca/courses/350/Carey5th/Ch13/ch13-nmr-1b.html)

In Figure 3.12, T1 or longitudinal relaxation result in a decrease of the magnetization anti-parallel to the external magnetic field. T2 or transversal relaxation lead to the decrease of magnetization perpendicular to the external magnetic field. ΔE is the energy gap between ground state and excited state. ΔE can be calculated by the following equations:

$$\Delta E = \Upsilon B_0$$

and

$$\Delta E = h\nu$$

γ is the gyromagnetic ratio; $B_0$ is the strength of applied magnetic field; h is the plank constant; $\nu$ is frequency.

The NMR frequency $\nu$ could be calculated:

$$\nu = \frac{\Upsilon B_0}{h}$$

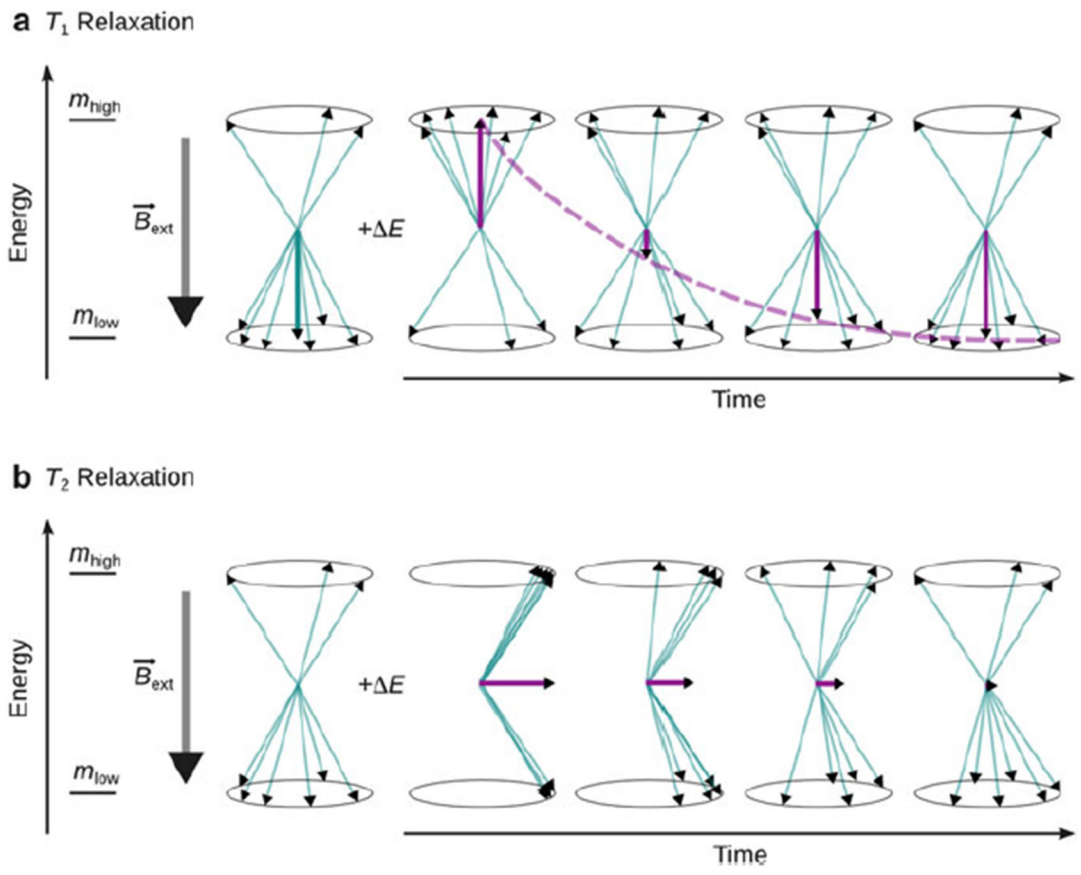


**Figure 3.12** Illustration of $T_1$ and $T_2$ relaxation. (Copied from Ref [5])

There are 4 major parameters in NMR spectrum: chemical shift, peak area, peak splitting and spin-spin coupling constant J. Chemical shift is caused by the resistance of electron cloud to the external magnetic field. It could give the information on the electron density around the nucleus. More electrons in the vicinity of nucleus, more resistance there will be. Based on chemical shift, chemical environment of nuclei could be deduced.

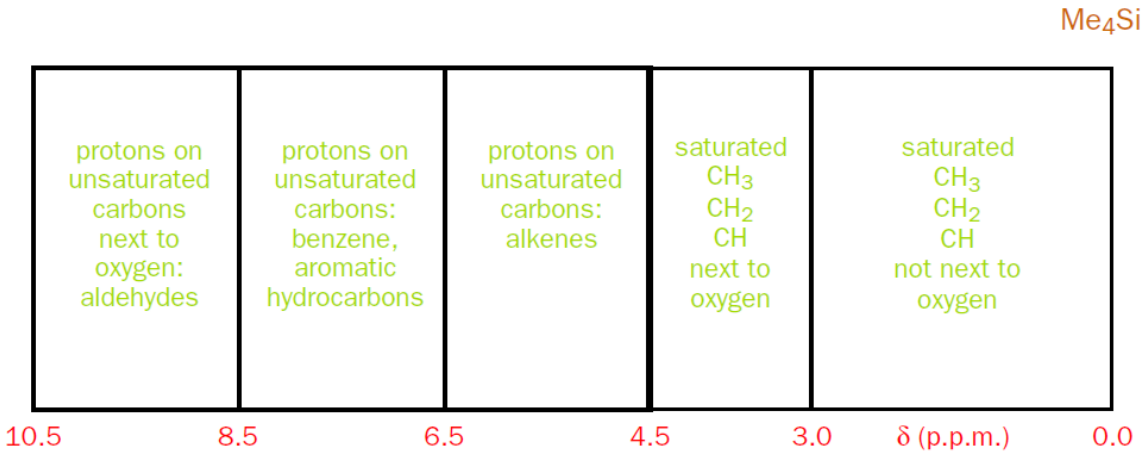


**Figure 3.13** Regions in proton NMR spectrum. (Copied from Ref [4])

Peak area of 1H-NMR is proportional to the number of H atoms in each peak. According to the integration, the total number of H atoms in one molecule could be obtained, which is very important when determining the structure. Peak splitting and spin-spin coupling constant could tell us the information about the nuclei near that nucleus. Take 1-chloropropane as an example.

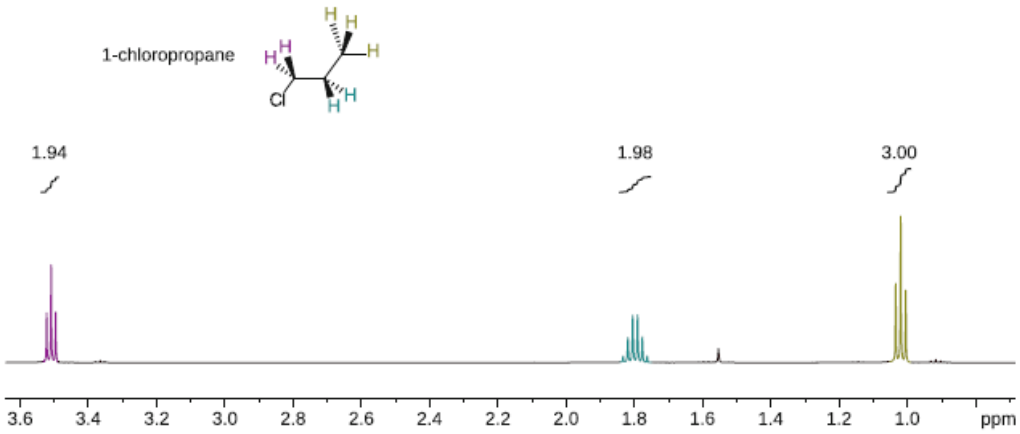


**Figure 3.14** 500 MHz $^{1}$H-NMR spectrum of 1-chloropropane in $CDCl_3$ at room temperature. (Copied from Ref [4])

There are 3 sets of peaks in the spectrum, and those peaks are all splitting due to the spin-spin coupling. The number of splitting N depends on how many coupling nuclei (n) around the nucleus. When the coupling constant is the same for the nuclei around, the relation between N and n is as followed:

$$N = n+1$$

For example, the methyl group in 1-chloropropane has 2 coupling H atoms. As a result, in the spectrum, the methyl peak is a triplet.

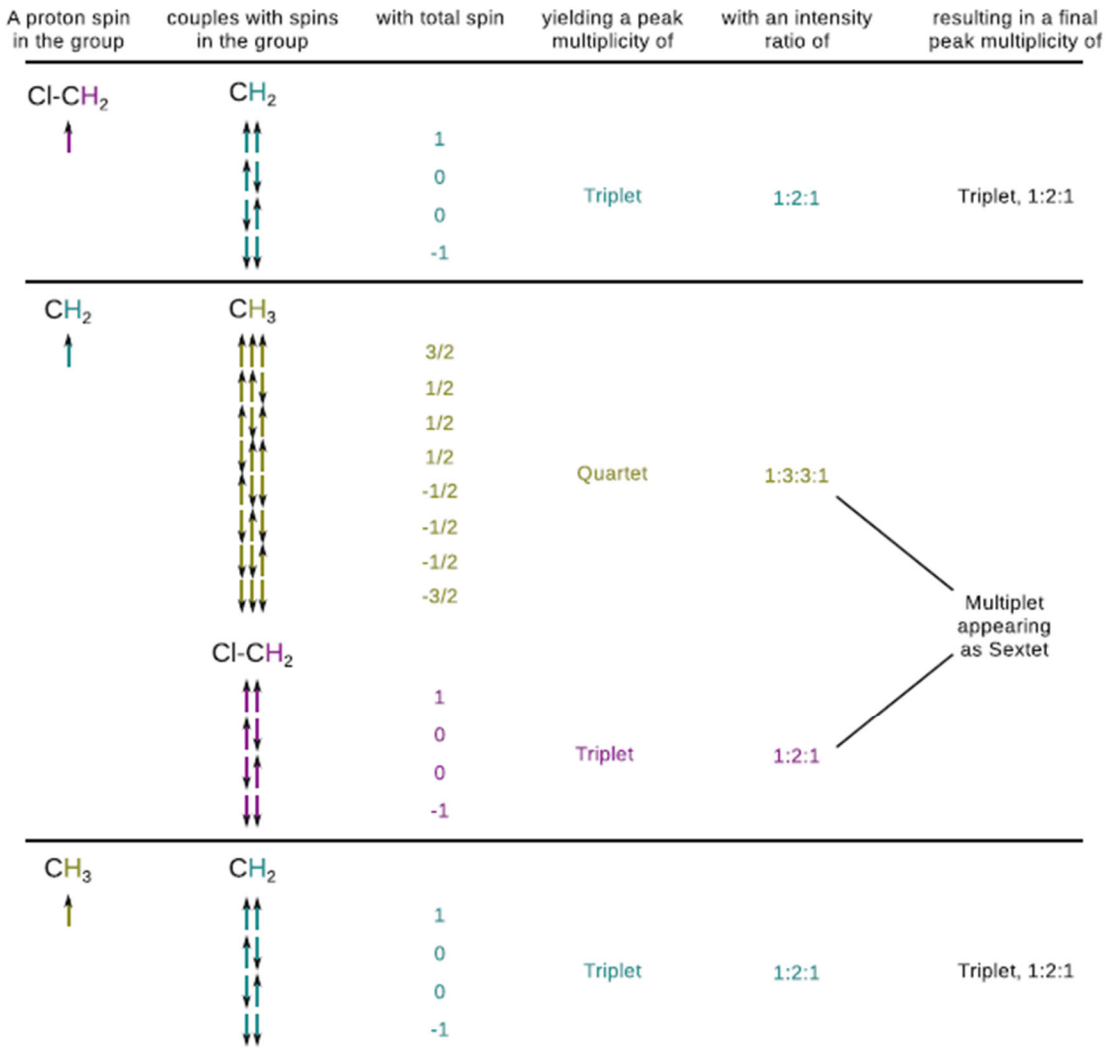


**Figure 3.15** Spin-spin couplings in 1-chloropropane. (Copied from Ref [4])

When analyzing the NMR spectrum, there are several typical steps:

1) Distinguish the impurities and solvent peaks;
2) Calculate the degree of unsaturation;
3) Confirm the number of protons of each set of peaks;
4) Confirm the functional groups;
5) Analyze the spin-spin couplings.

To fully confirm the structure of an unknown organic compound, more characterizations are required, such as mass spectrum, elemental analysis, IR and even x-ray crystallography.

### 3.3.5 Mass Spectrometry

Mass spectrometry is the only way to obtain information on molecular weight of an unknow compound. It is an essential tool to characterize new organic compounds. The ordinary MS consists of 5 parts. The first part is the sample injection system. Samples are usually made into solutions and injected to the sample chamber through syringe. The second part is ion source. In this part, samples are ionized by various methods, such as electrospray ionization. The third part is mass analyzer. Ions pass through this part being separated by m/z. After ions are separated, the detector will count the number of ions for each m/z then send signal to the computer.

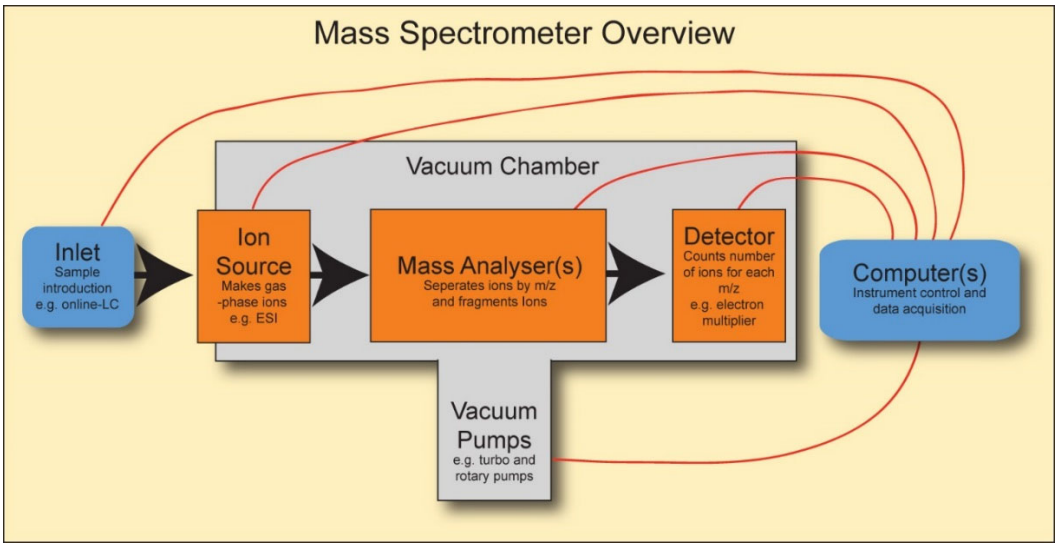


**Figure 3.16** Overview of mass spectrometer. (Retrieved from https://www.pinterest.jp/pin/388224430356469936/?lp=true)

In the traditional MS, an m/z is calculated only as an integer which is known as nominal mass. As a result, traditional MS usually have 1 Da resolution. For example, it is possible to tell one ion lights up as 89. However, the resolution cannot reach any finer level. If molecule A and B have the same nominal masses 89, normal MS cannot show the difference in molecular weight. Unlike the traditional mass spectrometry, which can only measure nominal masses, the high-resolution mass spectrometry can measure the exact masses. Although the nominal mass is the same, it is unlikely for 2 molecules with different formulas have the same exact mass. Hence, HRMS is particularly useful to differentiate between molecular formulas with the same nominal masses.

The traditional ionization methods of MS usually give a large sum of fragmentations. For molecules which are difficult to vaporize (usually polymers) or biomolecules which fragment readily, MALDI-TOF is used as a soft-ionization method with little to no fragmentation. Its ability to ionize polymers and large biomolecules makes it a vital characterization tool to organic chemists and biologists.

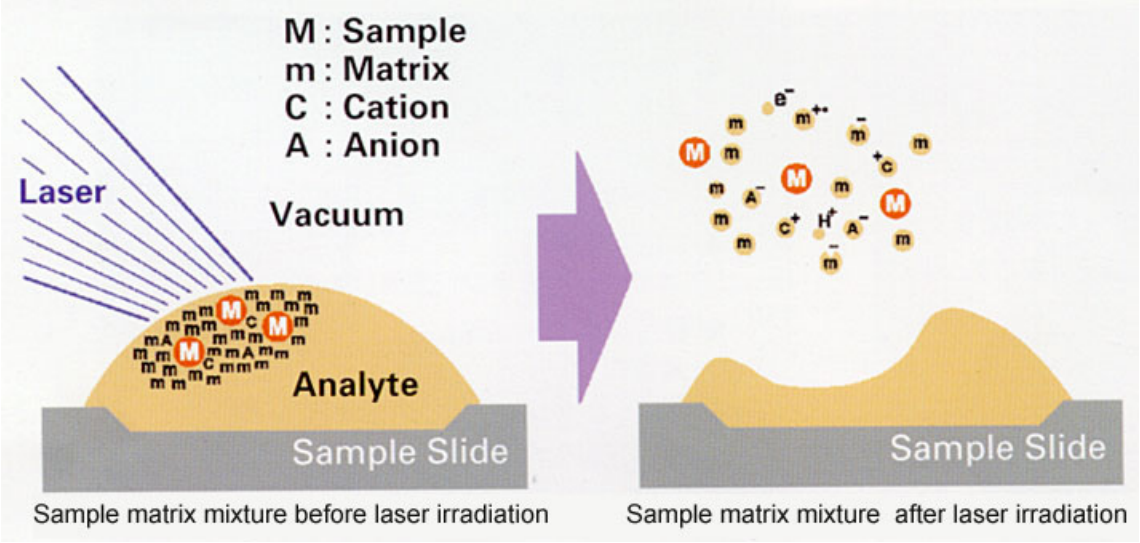


**Figure 3.17** Ionization of analyte in MALDI-TOF mass spectrometry. (Retrieved from https://www.shimadzu.com/an/lifescience/maldi/princpl1.html)

In the MALDI-TOF test, analyte is mixed with matrix and placed on the sample slide. After load the sample plate, the sample spot is irradiated with UV laser. Heat is generated, and the analyte is vaporized with the matrix.

### 3.3.6 Cyclic voltammetry (CV)

Cyclic voltammetry is generally used to study the electrochemical properties of compounds. In the area of organic electronics, cyclic voltammetry is usually used to determine the energy levels of organic semiconductors. In other words, it can measure the HOMO and LUMO position of organic semiconductors. The energy level is an essential parameter of organic semiconductors since it determines whether an organic semiconductor could act as an acceptor or a donor in the organic electronic devices.

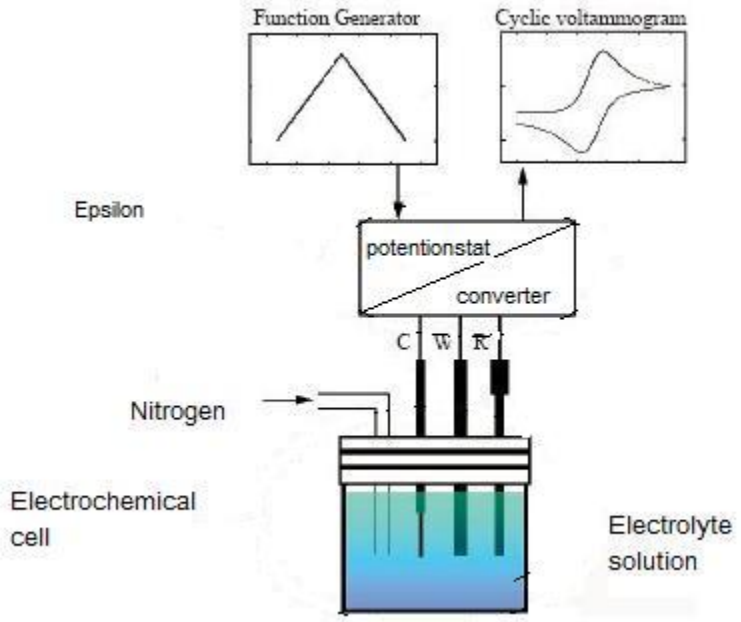


**Figure 3.18** Overview of cyclic voltammetry. (Adapted from D. K. Gosser, Jr., Cyclic Voltammetry Simulation and Analysis of Reaction Mechanisms, Wiley-VCH, NewYork, (1993).)

For most of the cyclic voltammetry, a three-electrode configuration is adopted, namely counter electrode, working electrode and reference electrode. The analyte and electrolyte are dissolved in an anhydrous and degassed solvent. During the test, the solution is remained undisturbed.

Working electrode is where the electrochemical reactions take place. It could be mercury, platinum, gold, graphite and glassy carbon. Among the various electrodes, glassy carbon is the most frequently used working electrode material for the study of electrochemical properties of organic compounds due to its wide potential window in both anodic and

cathodic sides. Apart from this, working electrodes could be made into different shapes, such as disk, rod, spherical and hemispherical.

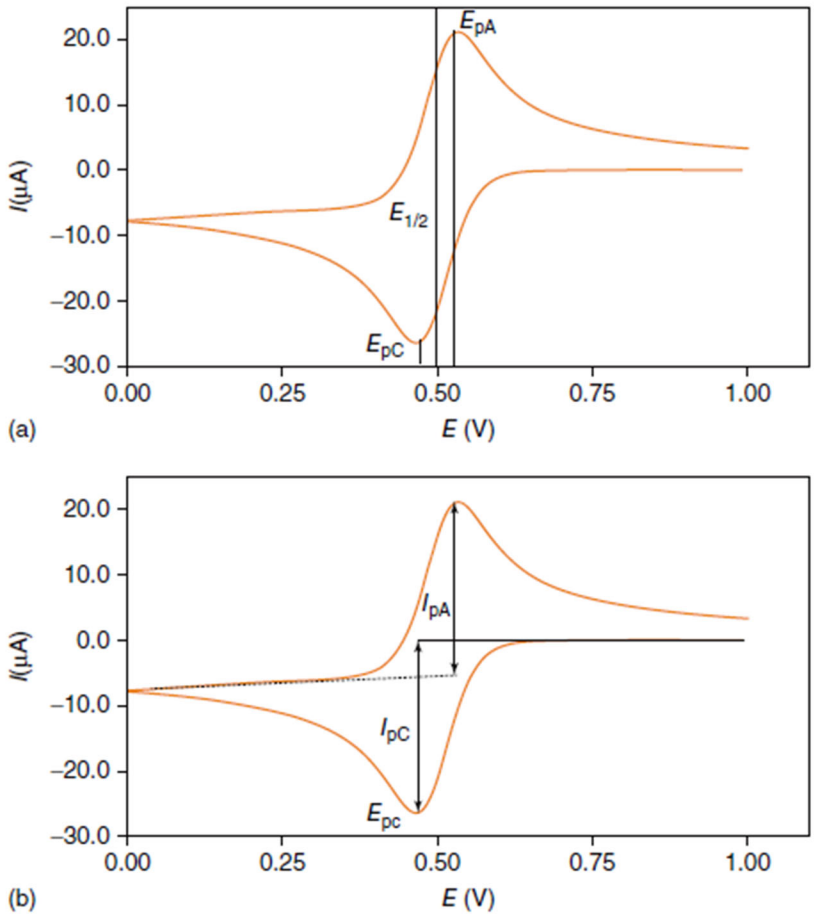


**Figure 3.19** Typical cyclic voltammogram of a reversible electrochemical reaction. (Copied from Ref [3])

The reference electrode works as a reference and gives a fixed potential against the working electrode potential. Generally, there are three kinds of reference electrodes, namely aqueous reference electrode, nonaqueous reference electrode, and quasi-reference electrode. In the early age of cyclic voltammetry, the standard hydrogen electrode (SHE) was used as reference electrode, which displays a potential of zero. However, SHE is difficult to set up due to the usage of hydrogen gas. Nowadays, silver/silver chloride electrode (Ag/AgCl) and saturated calomel electrode (SCE) are the two commonly used aqueous reference electrodes. But when dealing with organic compounds, nonaqueous reference electrodes are required. Silver-silver ion ($Ag/Ag^+$) electrode is the most widely

used reference electrode for nonaqueous systems. But the stability of $Ag/Ag^+$ electrode is not good enough, which could lead to the poor reproducibility. Consequently, IUPAC suggests the employment of ferrocene redox couple ($Fc/Fc^+$) as a reference redox system where $Fc/Fc^+$ acts as an internal standard. Since $Fc/Fc^+$ is applied, the reference electrodes could actually be replaced with inert electrodes, such as platinum, gold and silver. In this case, those inert electrodes are called quasi-reference electrodes or pseudo-reference electrodes.

LUMO and HOMO positions are important and characteristic property of organic semiconductors. The energy of LUMO is related to the electron affinity whereas the energy of HOMO is related to minimum energy required to remove an electron from molecule in gaseous phase. In cyclic voltammetry, reduction/oxidation potentials are measured, which is related to ionization potentials in vacuum. By exploiting such correlation, HOMO/LUMO energies could be obtained. However, it needs to be clarified that, unlike the solution-based reduction/oxidation potentials, the HOMO/LUMO energies are scaled in vacuum. As a result, the correlations might not be very precise. The most frequently adopted equation to calculate the HOMO/LUMO energies is as followed:

$$E_{HOMO} = -(E_{[onset,ox\ vs\ Fc^+/Fc]} + 5.1)(eV)$$

$$E_{LUMO} = -(E_{[onset,red\ vs\ Fc^+/Fc]} + 5.1)(eV)$$

### 3.3.7 X-ray crystallography

X-ray crystallography is the most direct method and the last resort to determine the structures of organic compounds. Many large biomolecules are characterized by this method, including DNA and various proteins. Although it is very powerful, the process of growing crystals could be quite difficult. There are many proteins that could not form crystals which is large enough for X-ray crystallography. Protein crystals could be smaller than one-millimeter cross. But for the conjugated organic semiconductors, growing crystals is much easier. In addition, some organic semiconductors have a limited number of hydrogen atoms and repeating units. It is difficult to determine the structures of such

molecules using NMR and MS. Therefore, X-ray crystallography is a commonly used and most straightforward method to determine the structures of organic semiconductors.

Bragg's law is the foundation of X-ray crystallography. In the crystals, there are planes consisting of orderly arranged atoms. The superposition of light scattering from individual atoms gives rise to the diffraction. As shown in figure 3.20, the lower beam travels an extra distance of 2dsinθ. When 2dsinθ is equal to an integer multiple of the wavelength of the radiation nλ, constructive interference will occur, which gives the Bragg diffraction. By recording the angles and intensities of the diffracted beams, a three-dimensional picture of the density of electrons within the crystal could be obtained. Further analysis of the electron density lead to the mean positions of the atoms in the crystal, as well as their chemical bonds. Using that information, the 3D structure of a molecule could be determined.

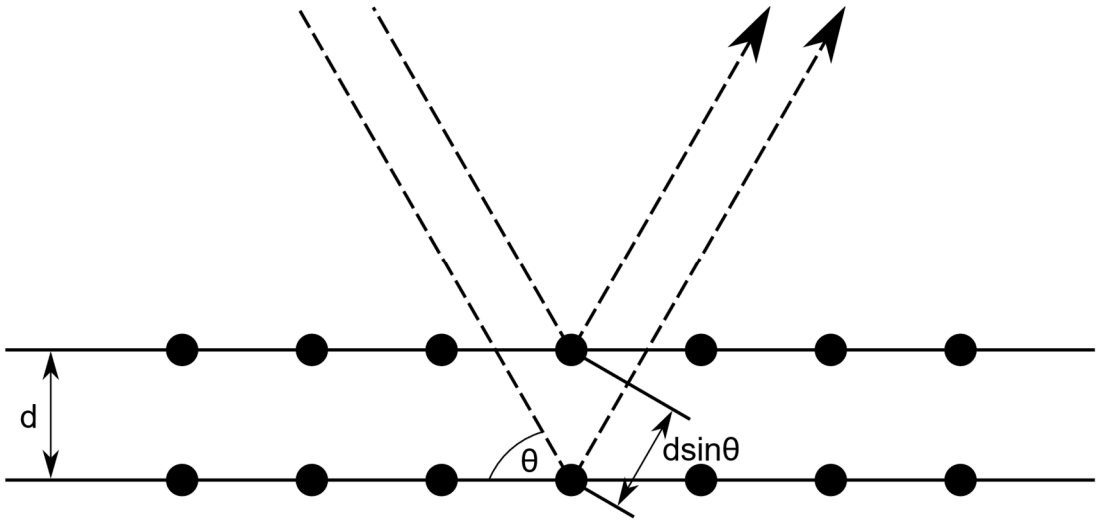


**Figure 3.20** Bragg diffraction.

## 3.4 Overview of methodologies

In summary, this chapter discusses the basic principles of experimental techniques of organic synthesis and characterization methods of small molecule organic semiconductors. In detail, purification methods (extraction, recrystallization and column chromatography), analysis method (thin layer chromatography), structure determination methods (NMR,

HRMS, FTIR and X-ray crystallography) and property investigation methods (UV-Vis spectroscopy, fluorescence spectroscopy and cyclic voltammetry) are illustrated.

**References**

[1] J. T. Sharp, I. Gosney and A. G. Rowley. *Practical Organic Chemistry*. **1989**, 57-59, 91-99, 114, 154.

[2] A. Hofmann. *Physical Chemistry Essentials*. **2018**, 92, 370-373, 390-394, 398.

[3] L. Khalafi, M. Rafiee. *Cyclic Voltammetry. In Encyclopedia of Physical Organic Chemistry*. **2017**, 3-4, 9.

[4] J. Clayden, N. Greeves, and S. Warren. *Organic Chemistry*. **2001**, 246-272.

[5] J. H. Simpson. *Organic Structure Determination Using 2-D NMR Spectroscopy*. **2008**,2.

[6] https://archive.cnx.org/contents/50cd332c-b40e-4538-b80d-19acc17db704@1/introduction-to-cyclic-voltammetry-measurements

[7] https://en.wikipedia.org/wiki/Infrared_spectroscopy

[8] https://chem.libretexts.org/

[9] http://www.chem.ucalgary.ca/courses/350/Carey5th/Carey.html

# Chapter 4*

# Synthesis of Thiadiazole-fused Star-shaped Azaarene and Its Application in Perovskite Solar Cells as ETL

*In this chapter, star-shaped azaarene, HATNT, was synthesized and characterized. Thiadiazole-fused star-shaped azaarene was first applied in the Perovskite solar cells as electron-transporting material with electron mobility up to 1.73 × $10^{-2}$ $cm^2V^{-1}s^{-1}$. A high power conversion efficiency of 18.1% is achieved, which is fully comparable with the efficiency from the control device fabricated with $PC_{61}BM$ as ETL.*

*This section published substantially as Ning Wang, Kexiang Zhao, Tao Ding, Wenbo Liu, Ali Said Ahmed, Zongrui Wang, Miaomiao Tian, Xiao Wei Sun,* Qichun Zhang*, "Improving Interfacial Charge Recombination in Planar Heterojunction Perovskite Photovoltaics with Small Molecule as Electron Transport Layer", Adv. Energy Mater. 2017, 7(18), 1700522.

## 4.1 Introduction

The extravagant usage of fossil fuels in the past century leads to the drastic increase of carbon dioxide concentration in the atmosphere and serious global environmental issues, such as global warming.[1] Moreover, crude oil and coal are not sustainable and likely to run out in the 21st century.[2] It is urgent to replace fossil fuels with sustainable energy sources. Solar cell is one of the most promising green energy sources. Different from the traditional silicon-based solar cells, perovskite solar cells (PSCs) have received immense attention due to the ease of fabrication and outstanding thin-film photovoltaic performance. To date, most state-of-the-art PSCs utilize organic materials and metal oxides as hole and electron transport layer (ETL), respectively. In general, high-temperature annealing process is necessary to prepare these metal oxides, which will hinder the low-temperature and solution-processed fabrication of PSCs, especially in the case of large-scale R2R technique for flexible substrates.

To address such problem, n-type small organic molecules are adopted as ETLs. The most frequently used species is fullerene derivatives.[3] Although there are many fullerene derivatives, such as ICBA and $PC_{71}BM$, only $PC_{61}BM$-based PSCs could achieve high performance. However, $PC_{61}BM$ is very expensive and the poor morphological controllability of $PC_{61}BM$ under annealing conditions could result in different device performance of solar cells.[4] Hence, it is of great importance to design and synthesize new n-type organic semiconductors which could act as ETL in PSCs.

Unlike its linear counterpart, star-shaped azaarene is a less extensively studied class of N-heteroarene. The first star-shaped azaarene, 1,4,5,8,9,12-hexaazatriphenylene (HAT), was synthesized in 1981 as a metal ligand.[5] The presence of electron-deficient pyrazine rings results in the electron-acceptor properties of HAT derivatives. Along with the rapid development in organic electronics, there is an increasing demand for n-type organic semiconductors. The charge-carrier mobility of HAT derivatives is then investigated. The first reported electron mobility of a HAT derivatives is 0.08 $cm^2V^{-1}s^{-1}$ in both liquid crystalline and crystal phases.[6] Following this good result, 5,6,11,12,17,18-

hexaazatrinaphthylene derivative was synthesized and showed a much higher electron mobility of 0.9 $cm^2V^{-1}s^{-1}$ in crystal phase.[7] Those results showed that HAT derivatives could be a promising candidate of ETL material in PSCs.

Herein, a novel star-shaped small molecule hexaazatrinaphtho[2,3-c][1,2,5]thiadiazole, **HATNT**, is proposed, which has high electron mobility and suitable band gap. By employing thiophene side chains and incorporating thiadiazole moieties into the HAT backbone, sulfur atoms are introduced, which are believed to greatly improve the interfacial interaction between the perovskite and the ETL via S-I or S-Pb bonding.[8] Employing this **HATNT** as ETL in low-temperature and solution-processed planar heterojunction PSCs, a high PCE of 18.1% is obtained under standard AM 1.5G illumination, which is fully comparable with that (16.2%) from traditionally $PC_{61}BM$-based device. More importantly, this **HATNT** shows more effective suppression of photogenerated charge recombination at the perovskite/ETL interface.

## 4.2 Experimental

### 4.2.1 Device Fabrication

The pre-patterned ITO patterned glass was cleaned ultrasonically with an alconox (detergent) solution, followed by sonication in sequence with deionized water, acetone, and isopropyl alcohol for 15 min each, then the substrates were dried using blowing nitrogen gas. The ITO glasses are then UV-ozone treated for 20 mins prior to the deposition of other layers. A 35 nm thickness of poly(3,4-ethylenedioxythiophene) polystyrene sulfonate (PEDOT:PSS) hole transport layer was spun on the top of indium tin oxide (ITO) glass substrate at 3000 rpm for 60 s in ambient conditions, following an annealing treatment at 130 °C for 30 min in air. A ~350 nm-thick perovskite ($CH_3NH_3PbI_3$) layer was spun on PEDOT:PSS hole transport layer in glove box using 40 wt.% precursor with equal molar $CH_3NH_3I$ and $PbI_2$ in DMF solution. The as-spun perovskite layer was annealed at 100 °C for 5 min to drive off solvent and form the perovskite phase. Different thickness of HATNT was spun on top of perovskite layer using a solution of HATNT in 1,2-dichlorobenzene.

The thickness of HATNT was carefully carried out using Alpha-Step D-600 Stylus Profiler (KLA-Tencor Corporation). The device (active area: 3.2 mm × 3.2 mm) was completed by the thermal evaporation of the LiF (1 nm)/Al (100 nm) electrode on the top.

### 4.2.2 Synthesis

Thiophene substituted benzo[c][1,2,5]thiadiazole-5,6-diamine was synthesized according to the previous literature[9]. As depicted in Figure 4.2.1, HATNT was prepared through the threefold condensation reaction between 4,7-bis(5-(2-ethylhexyl)thiophen-2-yl)benzo[c][1,2,5]thiadiazole-5,6-diamine and hexaketocyclohexane followed by the oxidation of *p*-chloranil.

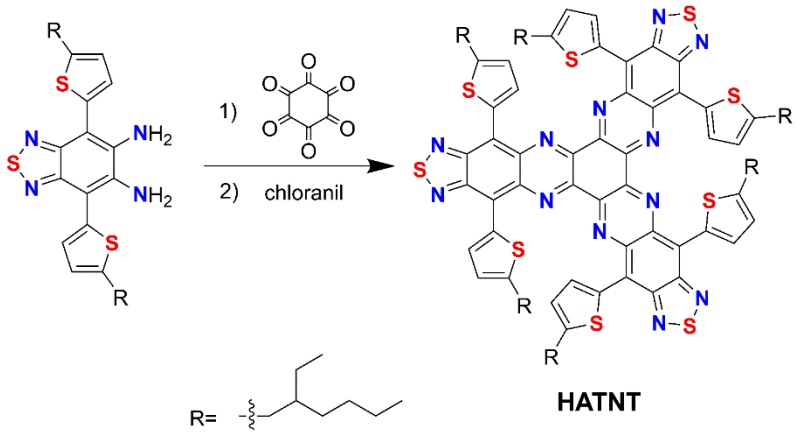


**Figure 4.2.1** Synthesis of HATNT.

Synthesis of **HATNT**: A mixture of 4,7-bis(5-(2-ethylhexyl)thiophen-2-yl)benzo[c][1,2,5]thiadiazole-5,6-diamine (284 mg, 0.51 mmol) and hexaketocyclohexane octahydrate (53.3 mg, 0.17 mmol) in acetic acid (20 mL) was stirred at 100 °C for 1 d. After cooling to room temperature, the solvent was removed under reduced pressure. The residue was washed with methanol and further purified by column chromatography on silica gel using a Hexane/DCM (v/v, 4:1) solvent mixture. The first two green fractions were collected and dried in vacuo. The mixture was dissolved in THF (20 mL) and an excess of chloranil (492 mg, 2 mmol) was added to the solution. The solution was stirred at room temperature for 1 h. Then the excessive chloranil was removed by filtration and the filtrate was collected and dried in vacuo. This crude product was further purified by

column chromatography on silica gel using a Hexane/DCM (v/v, 4:1) solvent mixture. The desired product (54.2 mg, 18% yield, two steps) was obtained as a black solid.

## 4.3 Results and Discussion

### 4.3.1 Chacracterization

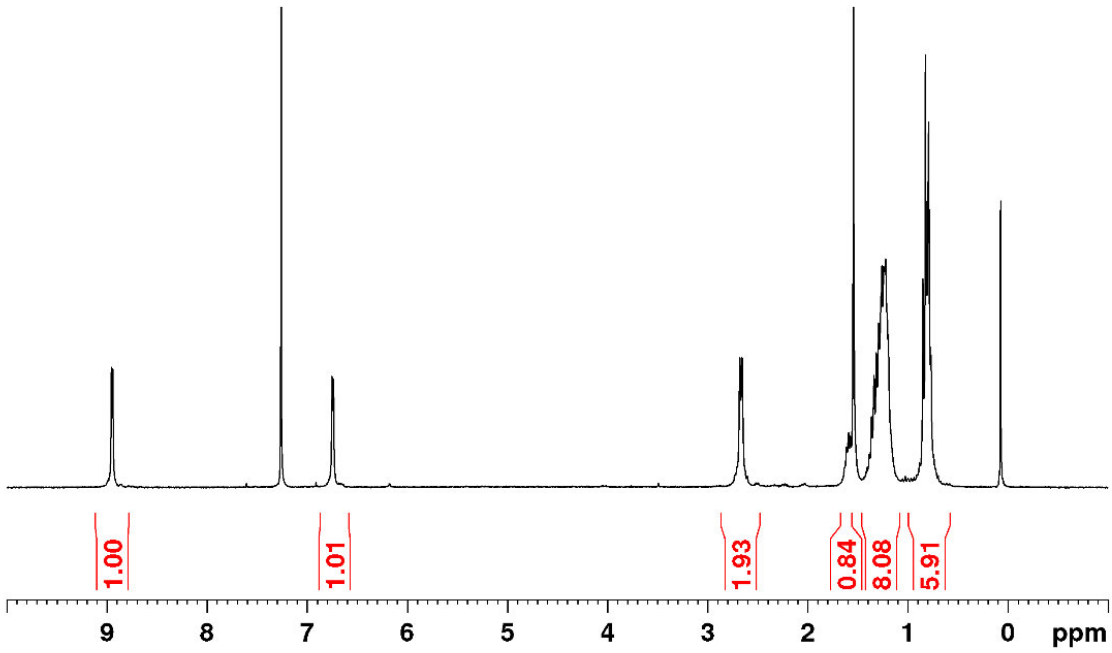


**Figure 4.3.1** $^{1}$H NMR spectrum of HATNT in $CDCl_3$.

$^{1}$H NMR (300 MHz, $CDCl_3$) δ 8.95 (d, J = 3.78 Hz, 6H), 6.74 (d, J = 3.75 Hz,6H), 2.66 (d, 12H), 1.59 (m, 6H), 1.36 – 1.19 (m, 48H), 0.84 – 0.77 (m, 36H).

There are two peaks in the aromatic area, which are ascribed to thiophene ring. Doublet at 2.66 ppm belongs to the -$CH_2$ group attached to thiophene ring. The peak area matches with the total number of H atoms in HATNT. The result is in good accordance with the predicted spectrum.

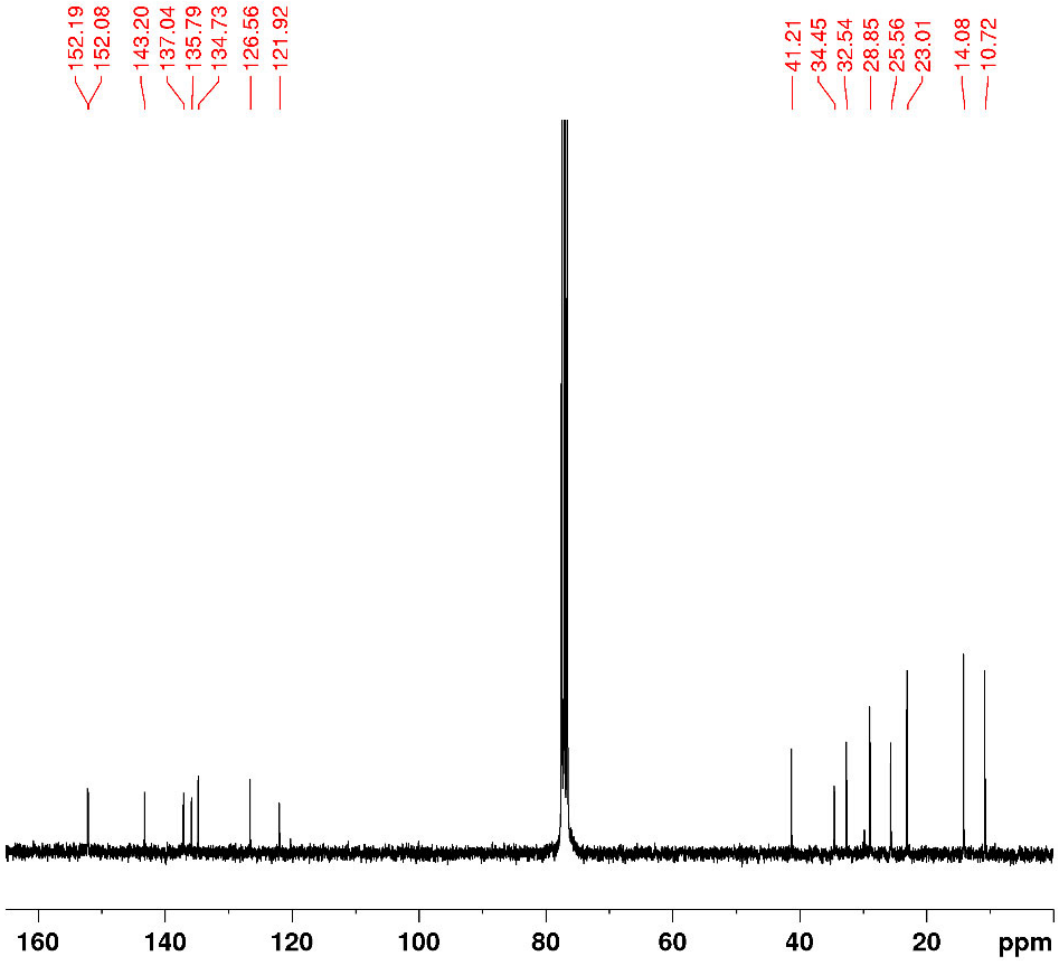


**Figure 4.3.2** $^{13}C$ NMR spectrum of HATNT in $CDCl_3$.

$^{13}C$ NMR (75 MHz, $CDCl_3$) δ 152.2, 152.1, 143.2, 137.0, 135.8, 134.7, 126.6, 121.9, 41.2, 34.4, 32.5, 28.8, 25.6, 23.0, 14.1, 10.7.

There are 16 peaks in the spectrum, which represent the 16 kinds of carbon atoms in HATNT. The result is in good accordance with the predicted spectrum.

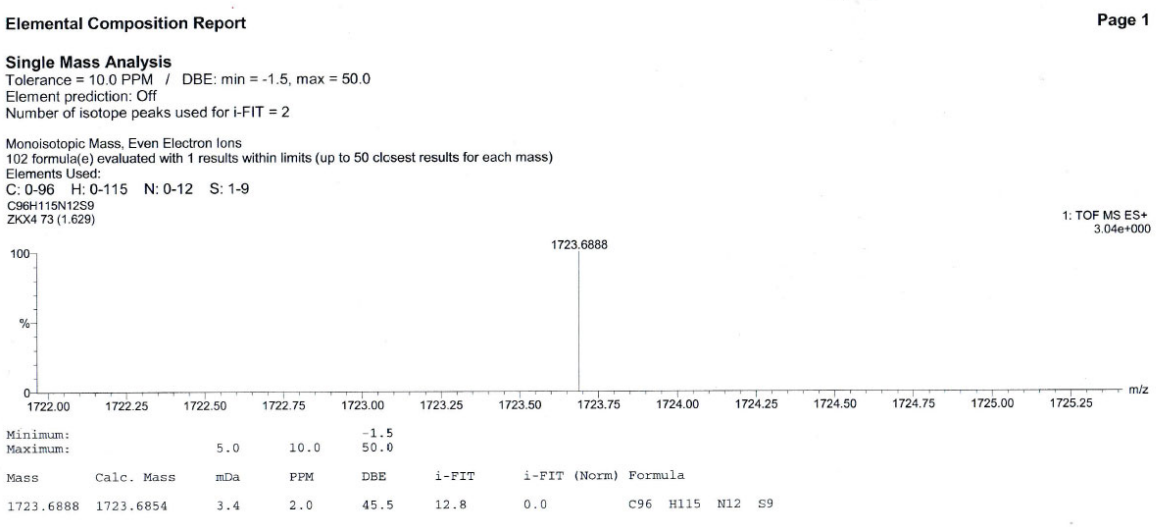


**Figure 4.3.3** HRMS spectrum of HATNT.

HRMS, calcd for $C_{96}H_{115}N_{12}S_9$, 1723.6854; found, 1723.6888. The result is in good accordance with the exact mass of HATNT.

### 4.3.2 Properties and PSC Performance

The device configuration of the **HATNT**-based perovskite solar cell is depicted in Figure 4.3.4a. It is comprised of glass/ITO/PEDOT:PSS/perovskite ($MAPbI_3$)/HATNT/LiF/Al, in which the PEDOT:PSS acts as hole transport layers and **HATNT** acts as electron transport layers. The corresponding energy band diagram is depicted in Figure 4.3.4b. Under solar light illumination, the excitons are generated, separated and diffused within the perovskite layer. The electrons and holes are then transported and collected by the counter electrode, PEDOT:PSS/ITO and HATNT/LiF/Al subsequently.

Figure 4.3.4c shows cyclic voltammetry (CV) of **HATNT** in dichloromethane solution, indicating a reversible reductive wave. From this CV measurement, LUMO energy level of **HATNT** was calculated to be 4.0 eV. In Figure 4.3.4d, the UV-Vis absorption spectrum of **HATNT** in dichloromethane solution shows two absorption bands. One is around 300-500 nm and the other is around 500-770 nm. The two absorption bands stem from the [1,2,5]thiadiazolo[3,4-g]quinoxaline segment and charge transfer from the dithienylbenzothiadiazole skeleton branch to the hexaaza core. The absorption edge of

HATNT extends to ~ 765 nm, from which the optical band gap is estimated to be 1.62 eV. The suitable optical band gap and perfect match of the energy levels of **HATNT** between $MAPbI_3$ and aluminum suggest that HATNT might be an excellent ETL candidate in perovskite solar cells.

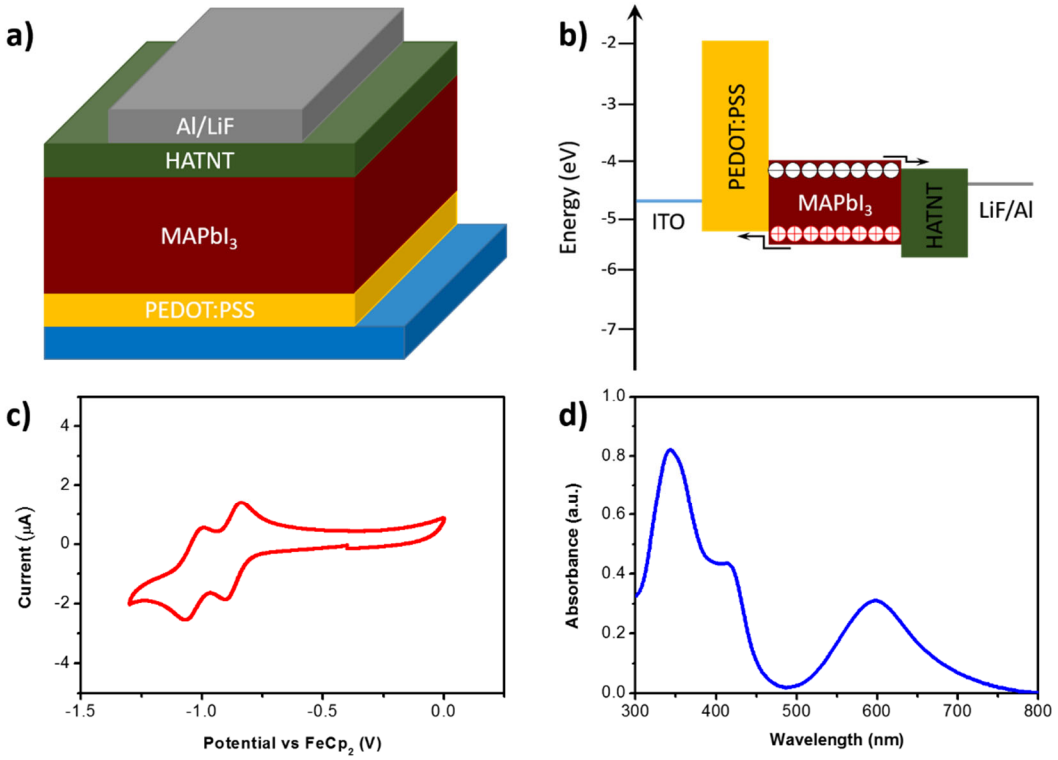


**Figure 4.3.4** a) Device architecture of PSC used in this work. b) Corresponding energy level diagram of a) using HATNT as ETL. c) CV curve of HATNT. d) Optical absorption characteristic of HATNT in THF solution in the visible region.

Based on the high electron mobility of **HATNT** and the simulated optoelectronic results, high device performance can be expected. The dependence of device performance on **HATNT** thickness was carried out. The corresponding J-V curves and detailed device parameters are shown in Figure 4.3.5a and table respectively. It can be found that when the **HATNT** thickness is too thin, the device shows leakage current behavior, leading to a low open-circuit voltage ($V_{OC}$), poor current density ($J_{SC}$) and fill factor (FF). This should be attributed to the poor coverage of **HATNT** on the perovskite layer, which will result in low shunt resistance and affect device performance. When the **HATNT** thickness is too high (for example, 55 nm), it will increase the series resistance, which will reduce the fill factor.

An optimized device performance was obtained when the **HATNT** thickness is about 35 nm, although the device with 45-nm **HATNT** achieved better FF.

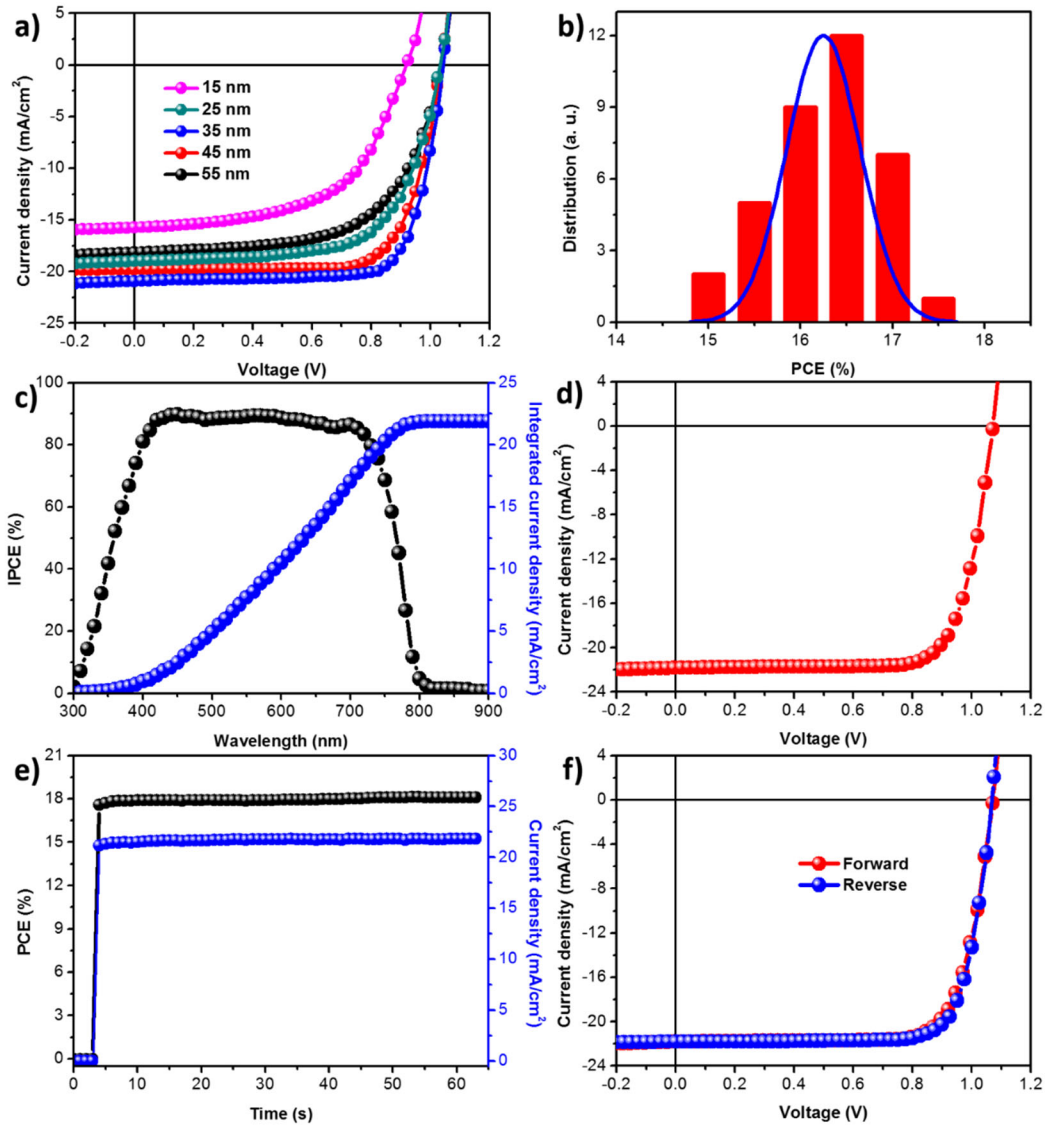


**Figure 4.3.5** a) J-V curves of the PSCs with different thickness HATNT as ETL. b) PCE distribution characteristic based on 36 devices fabricated in one batch. The line indicates the Gaussian fitting. c) Best-performing J-V curve of the PSC with HATNT as ETL. d) The corresponding IPCE spectrum of c) and integrated current plots. e) Stable output curves of current density and efficiency for the PSC at the maximum power point. f) Hysteresis behavior of the PSC device with HATNT as ETL under different scanning directions. For reverse and forward scan, the parameters are a step of 25 mV with a delay time of 200 ms.

An important aspect of perovskite solar cell research and development is the efficiency reproducibility without large variations within one batch. Device performance distributions are shown in Figure 4.3.5b. All 32 devices were fabricated with identical parameters in one batch. Although the PCE distributions show some variation, it is clear that our devices show good reproducibility and a high average PCE around 16.4%. Figure 4.3.5d shows the best-performing J-V curve for the **HATNT** based solar cell, performing a $V_{OC}$ of 1.07 V, a $J_{SC}$ of 21.83 mA/cm2, and an FF of 77.8%, leading to a high device efficiency of 18.1%. As comparison, the control device was also fabricated using $PC_{61}BM$ as ETL. This $PC_{61}BM$-based device produced a device efficiency of 16.2% with a $V_{OC}$ of 1.03 V, a $J_{SC}$ of 20.9 mA $cm^{-2}$, and an FF of 75.3%. With the same device architecture and perovskite layer, the **HATNT**-based device harvests higher open-circuit voltage and current density comparing to the device with $PC_{61}BM$ as ETL. This high open-circuit voltage should be ascribed to the more favorable band alignment between the $MAPbI_3$ film and electron transport layer, where the LUMO levels of **HATNT** and $PC_{61}BM$ are 4.0 and 4.2 eV, respectively. The shallower LUMO level of the **HATNT** tend to achieve better electrically contact with the $MAPbI_3$ layer, thus increasing the potential difference between electron and hole transport layers.

**Table 4.3.1** Devcie parameters of the perovskite solar cells with different thickness of HATNT.

| Device No. | Thickness of HATNT | $V_{OC}$ (V) | $J_{SC}$ (mA $cm^{-2}$) | FF (%) | PCE (%) |
|---|---|---|---|---|---|
| 1# | 15 | 0.93 | 15.73 | 56.2 | 8.18 |
| 2# | 25 | 1.03 | 18.98 | 66.6 | 13.01 |
| 3# | 35 | 1.04 | 20.91 | 75.4 | 16.39 |
| 4# | 45 | 1.03 | 19.81 | 74.2 | 15.13 |
| 5# | 55 | 1.03 | 18.15 | 62.2 | 11.62 |

The obviously higher electron mobility ($1.73 \times 10^{-2}$ $cm^2$ $V^{-1}$ $s^{-1}$) of **HATNT** could be an important factor for the preferable current density in comparison with the $PC_{61}BM$-based device. Moreover, the possibly interfacial interaction between the perovskite and the **HATNT** via S-I or S-Pb bonding should be beneficial to this preferable device performance. The incident photo-to-electron conversion efficiency (IPCE) spectrum of the best-performing **HATNT**-based solar cell is shown in Figure 4.3.5c. The integrated current

gives a $J_{SC}$ value of 21.76 mA $cm^{-2}$, which is in good accordance with the measured J-V result. Figure 4.3.5e shows the stable output curve of the **HATNT**-based device using maximum power point tracking model, indicating a stable output characteristic within 60 seconds. The J-V curves of the **HATNT**-based solar cell with forward and reverse scan directions are shown in Figure 4.3.5f, in which a slight hysteresis phenomenon is observed. The control $PC_{61}BM$-based device also shows slight hysteresis curves. Similarly, some slight hysteresis behaviors had been also observed in perovskite solar cells with nonmetallic oxide or organic small molecules as ETLs. Although there are many different opinions on the origin of hysteresis in perovskite photovoltaics, more and more papers have proposed that the hysteresis is due to the ion motion within the perovskite layer.[10] For our p-i-n planar heterojunction device, the possible reason is that the $PC_{61}BM$/HATNT molecule clusters and the perovskite cannot easily penetrate into each other.[11] This will cause imperfect suppression of the ion motion in the perovskite and thus slight hysteresis.

## 4.4 Conclusion

In summary, a novel organic small molecule **HATNT** with suitable optical bandgap has been designed and synthesized. This **HATNT** possesses good electron mobility up to 1.73 $\times 10^{-2}$ $cm^2$ $V^{-1}$ $s^{-1}$, making it favorable serve as ETL in metal oxide-free perovskite solar cells. In comparison with the traditional ETL materials $PC_{61}BM$, **HATNT** is easier to be synthetized and its cost is cheaper. The champion device based on **HATNT** has demonstrated a high PCE of 18.1% with a $V_{OC}$ of 1.07 V, an FF of 77.8%, and a $J_{SC}$ of 21.83 mA/$cm^2$. This efficiency is fully comparable with the perovskite solar cell using $PC_{61}BM$ as ETL, an efficiency of 16.2% in the latter has been achieved. This high efficiency can be primarily attributed to the higher electron mobility and the lower $R_{ec}$, which suppress the recombination of photogenerated charges at the $MAPbI_3$/HATNT interface, thus facilitating electron transfer and extraction in the device.

**References**

[1] S. Solomon, D. Qin, M. Manning, Z. Chen, M. Marquis, K.B. Averyt, M.Tignor and H.L. Miller (eds.), *IPCC, 2007: Climate Change 2007: The Physical Science Basis. Contribution of Working Group I to the Fourth Assessment Report of the Intergovernmental Panel on Climate Change*, Cambridge University Press, Cambridge, United Kingdom and New York, NY, USA, **2007**.

[2] EIA, *International Energy Outlook 2018*, Energy Information Administration, Office of Integrated Analysis and Forecasting, U.S. Department of Energy, **2018**.

[3] J.-Y. Jeng, Y.-F. Chiang, M.-H. Lee, S.-R. Peng, T.-F. Guo, P. Chen, T.-C. Wen, *Adv. Mater.* **2013**, *25*, 3727-3732.

[4] Y. Shao, Y. Yuan, J. Huang, *Nature Energy* **2016**, *1*, 15001.

[5] R. Nasielski-Hinkens, M. Benedek-Vamos, D. Maetens, J. Nasielski, *J. Organomet. Chem.* **1981**, *217*, 179-182.

[6] R. I. Gearba, M. Lehmann, J. Levin, D. A. Ivanov, M. H. J. Koch, J. Barberá, M. G. Debije, J. Piris, Y. H. Geerts, *Adv. Mater.* **2003**, *15*, 1614-1618.

[7] M. Lehmann, G. Kestemont, R. Gómez Aspe, C. Buess-Herman, M. H. J. Koch, M. G. Debije, J. Piris, M. P. de Haas, J. M. Warman, M. D. Watson, V. Lemaur, J. Cornil, Y. H. Geerts, R. Gearba, D. A. Ivanov, *Chem. Eur. J.* **2005**, *11*, 3349-3362.

[8] a) M. Saliba, S. Orlandi, T. Matsui, S. Aghazada, M. Cavazzini, J.-P. Correa-Baena, P. Gao, R. Scopelliti, E. Mosconi, K.-H. Dahmen, F. De Angelis, A. Abate, A. Hagfeldt, G. Pozzi, M. Graetzel, M. K. Nazeeruddin, *Nature Energy* **2016**, *1*, 15017; b) N. K. Noel, A. Abate, S. D. Stranks, E. S. Parrott, V. M. Burlakov, A. Goriely, H. J. Snaith, *Acs Nano* **2014**, *8*, 9815-9821.

[9] P. Y. Gu, J. Zhang, G. K. Long, Z. L. Wang, Q. C. Zhang, *J. Mater. Chem. C* **2016**, *4*, 3809-3814.

[10] Y. Shao, Z. Xiao, C. Bi, Y. Yuan, J. Huang, *Nature Communications* **2014**, *5*, 5784.

[11] J. Xu, A. Buin, A. H. Ip, W. Li, O. Voznyy, R. Comin, M. Yuan, S. Jeon, Z. Ning, J. J. McDowell, P. Kanjanaboos, J.-P. Sun, X. Lan, L. N. Quan, D. H. Kim, I. G. Hill, P. Maksymovych, E. H. Sargent, *Nature Communications* **2015**, *6*, 7081.

# Chapter 5

# Synthesis, Characterizations and Crystal Structures of U-shaped Helical Azaarenes

*In this chapter, a series of U-shaped helical azaarenes were synthesized and characterized by NMR, MS, UV-Vis and cyclic voltammetry. Crystal structures of helical azaarenes were obtained, and the solid-state structures unequivocally exhibited the helicity. Their electronic and optical properties were measured and compared with that of Z-shaped azaarenes.*

## 5.1 Introduction

The past few decades have witnessed the rapid development of N-heteroarenes in organic electronics,[1] especially in organic field effect transistors (OFETs).[2] However, most of the N-heteroarenes are synthesized in the linear shape due to the lack of suitable building blocks to construct non-linear backbones. Consequently, the majority of non-linear N-heteroarenes are HAT (1,4,5,8,9,12-hexaazatriphenylene)-based star-shaped azaarenes employing the commercially available hexaketocyclohexane as building block.[3] Among the existing non-linear N-heteroarenes, helical azaarenes are seldomly reported compared with star-shaped analogues.[4]

Currently, the majority of helical azaarenes are azahelicenes. Although azahelicenes were synthesized prior to carbohelicenes, the latter has received more attention because of its good functionality and the versatile synthetic approaches towards it. Until recently, more interesting properties have been observed in azahelicenes.[5] The incorporation of nitrogen atoms could alter the electronic structure and allow the fine tuning of optoelectrical properties. Based on the nitrogen-containing heterocycles, azahelicenes could be classified into several types: pyridine-containing[6], pyrrole[7], pyridazine derivatives[8], etc. It is noteworthy that pyrazine-containing azahelicenes are extremely rare.[9] Such gap prompts us to synthesize novel pyrazine-containing helical azaarenes.

In this chapter, a series of pyrazine-containing helical azaarenes (**U7**, **U9**, **U11**) were synthesized in good yields. Optical and structural properties of these helical azaarenes are presented and compared with previous reported analogues.

## 5.2 Synthesis

Starting from 2,7-dimethoxyanthracene **1**[10], demethylation using $BBr_3$ in boiling dichloromethane furnishes **2** in quantitative yield; followed by oxidizing **2** with benzeneseleninic acid anhydride (BSA), tetraketone **3** is obtained in 71% yield. The

twofold condensation between tetraketone **3** and diamine **4**, **5** and **6** gives the helical azaarenes in moderate to good yields.

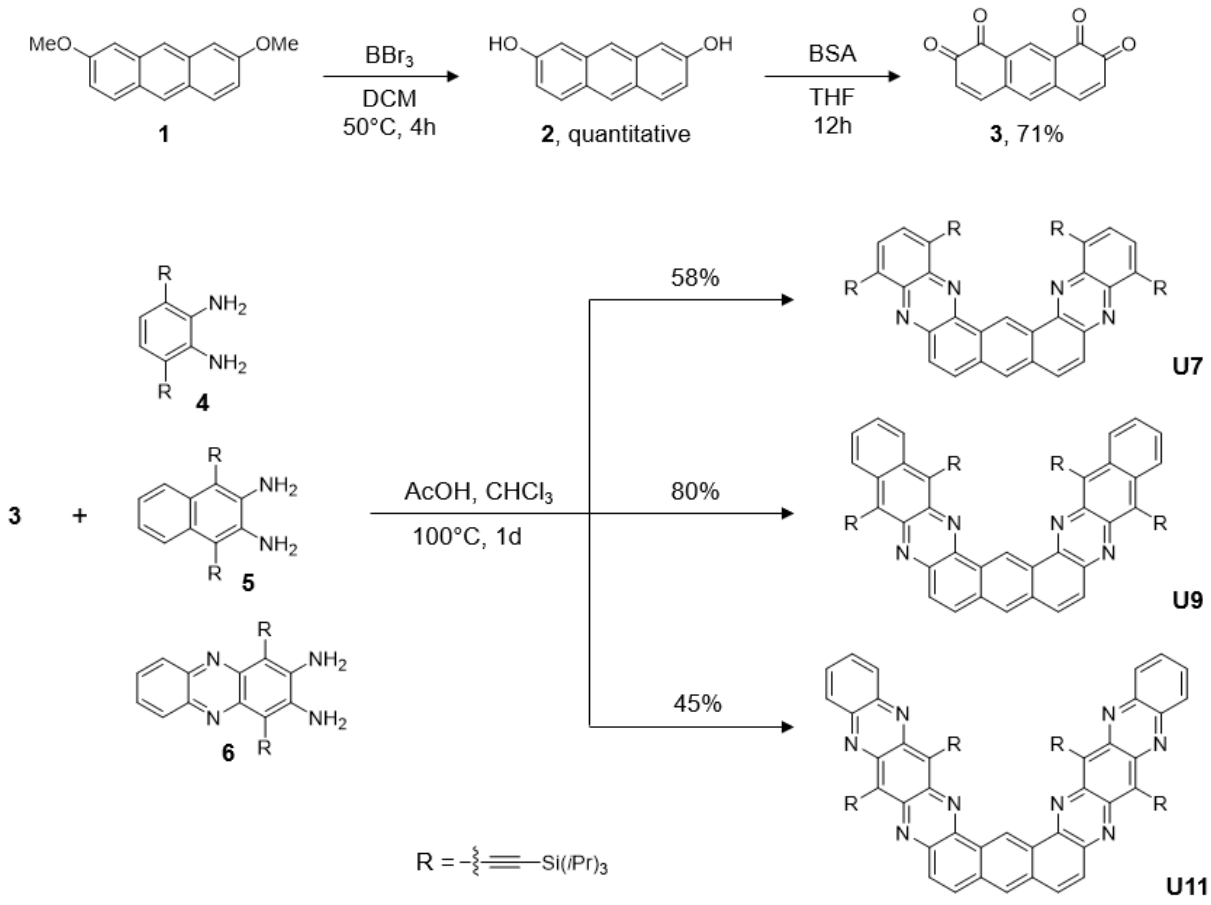


**Figure 5.1** Synthesis of helical azaarenes **U7**, **U9** and **U11**.

Synthesis of 2,7-dihydroxyanthracene **2**: In a heatgun-dried Schlenk flask purged with argon, **1** (477 mg, 2 mmol, 1 eq) was dispersed in dry DCM (30 ml). The suspension was cooled to 0 °C followed by the dropwise addition of $BBr_3$ (1 ml, 5 eq). Then the cooling bath was removed, and the mixture was heated to reflux for 4h. After being cooled to 0 °C again, ice-cold water was carefully added to the mixture to quench the unreacted $BBr_3$. The resulting slurry was extracted with diethyl ether (3 x 50 ml), and the organic phase was combined and dried with sodium sulfate. The removal of solvent under reduced pressure gave **2** as light brown solid (420 mg, quant.).

Synthesis of anthracene-1,2,7,8-tetraone **3**: In a heatgun-dried round bottom flask, benzeneseleninic acid anhydride (1.8 g, 5 mmol) was suspended in dry THF (80 ml) under argon. To the stirring suspension a solution of **2** (0.5 g, 2.38 mmol) in dry THF (40 ml) was added dropwise at 50 °C. After the addition, heat was turned off, and the resulting deep red solution was allowed to stand overnight. Upon the completion of reaction, solvent was removed *in vacuo*. The residual was washed with hot diethyl ether (15 ml), methanol (10 ml) and finally DCM (10 ml) then dried *in vacuo*. The product was obtained as deep reddish brown solid (403 mg, 71%).

General procedure for condensation reaction: To a round bottom flask equipped with condenser **3** (20 mg, 0.084 mmol) and diamine (0.2 mmol) were dissolved in a 3:1 solvent mixture of chloroform (5 ml) and acetic acid (15 ml). The stirring solution was heated to 100 °C for 1 d. The mixture was cooled to RT, and the solvent was removed *in vacuo*. This crude product was further purified by column chromatography on silica gel using a Hexane/DCM solvent mixture.

Synthesis of **U7**: The general procedure was applied to **3** (20 mg) and **4** (94 mg). Column chromatography (Hexane/DCM = 5:1) yielded **U7** as a yellow crystalline solid (54 mg, 58 %).

Synthesis of **U9**: The general procedure was applied to **3** (20 mg) and **5** (104 mg). Column chromatography (Hexane/DCM = 4:1) yielded **U9** as a red crystalline solid (81 mg, 80 %).

Synthesis of **U11**: The general procedure was applied to **3** (20 mg) and **6** (114 mg). Column chromatography (Hexane/DCM = 2:1) yielded **U11** as a dark purple crystalline solid (49 mg, 45 %).

## 5.3 Results and discussion

### 5.3.1 Characterization

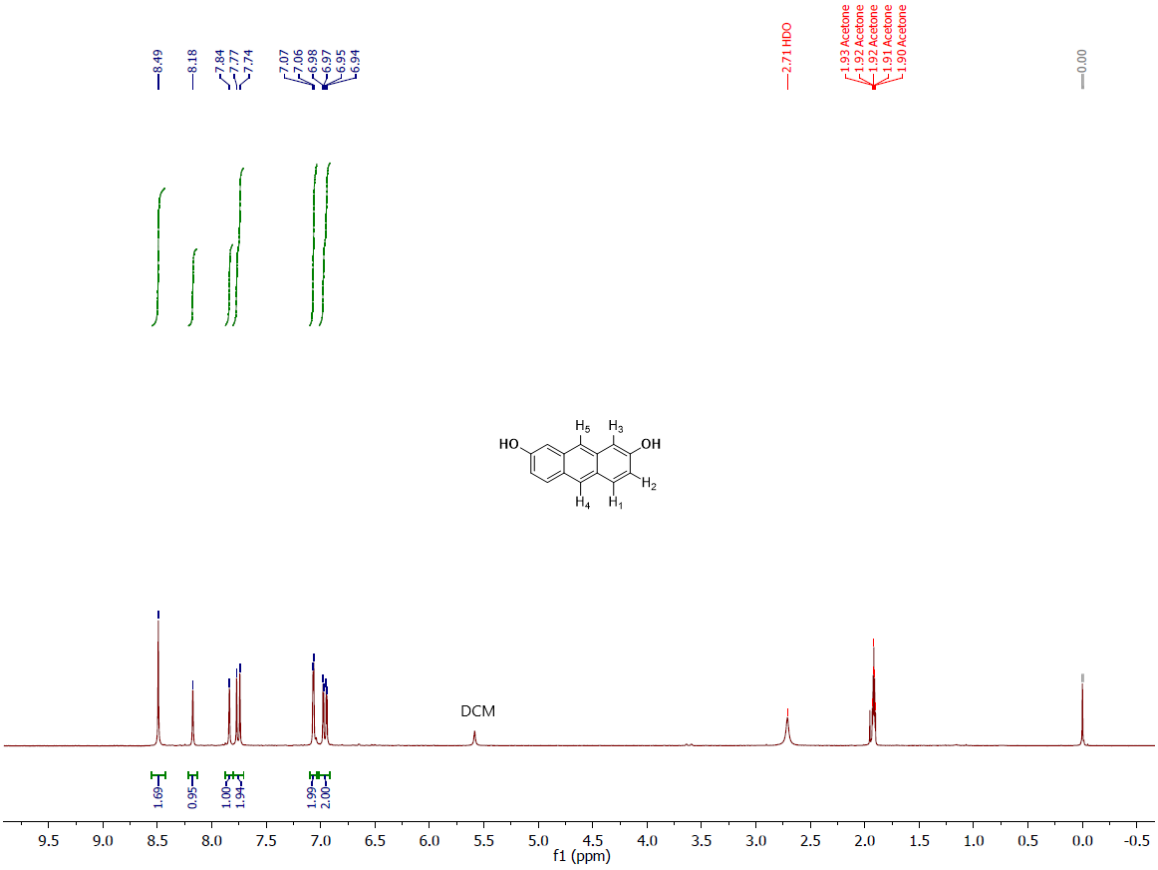


**Figure 5.3.1** $^{1}$H NMR spectrum of **2** in Acetone-$d_6$.

$^{1}$H NMR (300 MHz, Acetone-$d_6$) δ 8.49 (s, 2H), 8.18 (s, 1H), 7.84 (s, 1H), 7.76 (d, J = 9.1 Hz, 2H), 7.07 (d, J = 2.3 Hz, 2H), 6.96 (dd, J = 9.1, 2.4 Hz, 2H).

The single peak at 8.49 ppm corresponds to the hydroxy proton indicating the successful demethylation. The double-double peak at 6.96 ppm belongs to $H_1$ due to the presence of $^{3}$J coupling to $H_2$ and $^{4}$J coupling to $H_4$. Two single peaks at 8.18 ppm and 7.84 ppm belongs to $H_5$ and $H_4$ respectively. The doublet at 7.07 ppm has a coupling constant of 2.3 Hz which is attributed to $^{4}$J coupling. This doublet belongs to $H_3$. Doublet at 7.76 ppm has the same $^{3}$J coupling constant with $H_1$, which indicates $H_2$ is the corresponding proton. The peak area matches with the total number of H atoms in **2**. The result is in good accordance with the predicted spectrum.

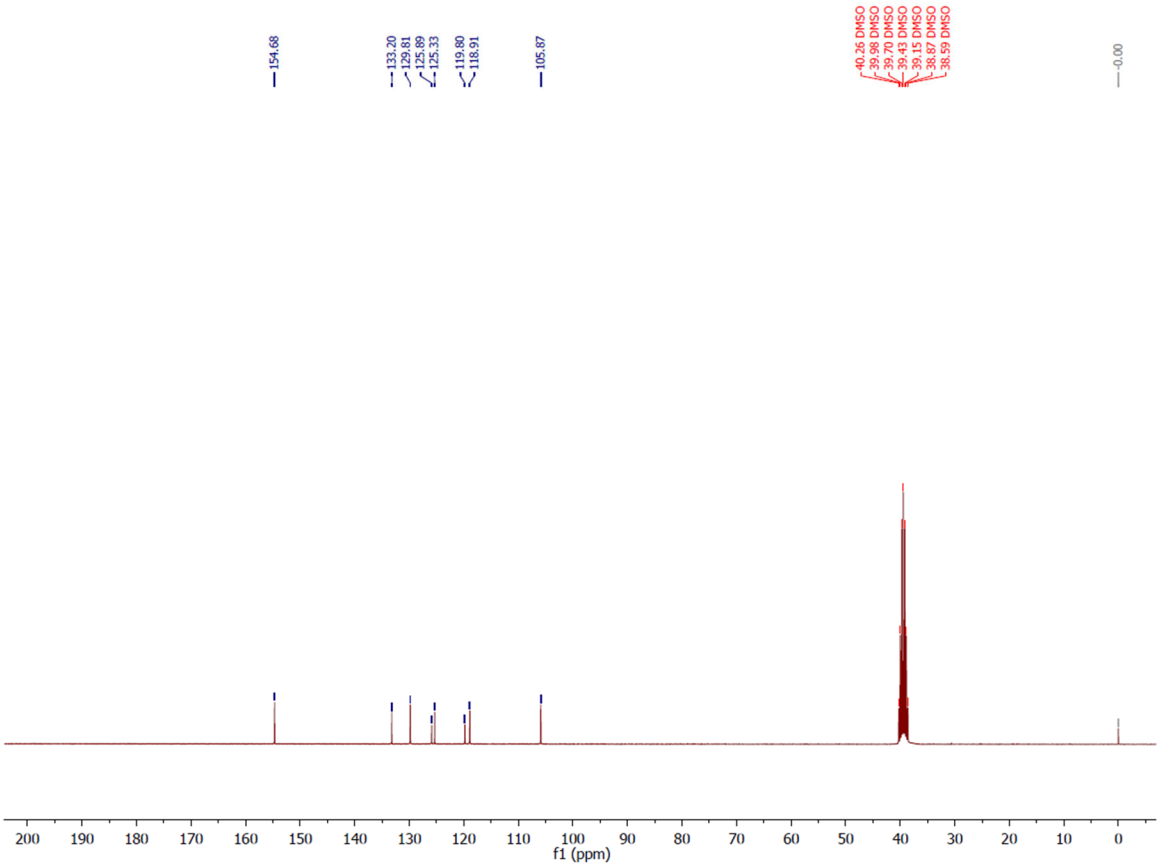


**Figure 5.3.2** $^{13}$C NMR spectrum of **2** in DMSO-$d_6$.

$^{13}$C NMR (75 MHz, DMSO-$d_6$) δ 154.68, 133.20, 129.81, 125.89, 125.33, 119.80, 118.91, 105.87.

There are 8 peaks in the spectrum which represent the 8 kinds of carbon atoms in **2**. The result is in good accordance with the predicted spectrum.

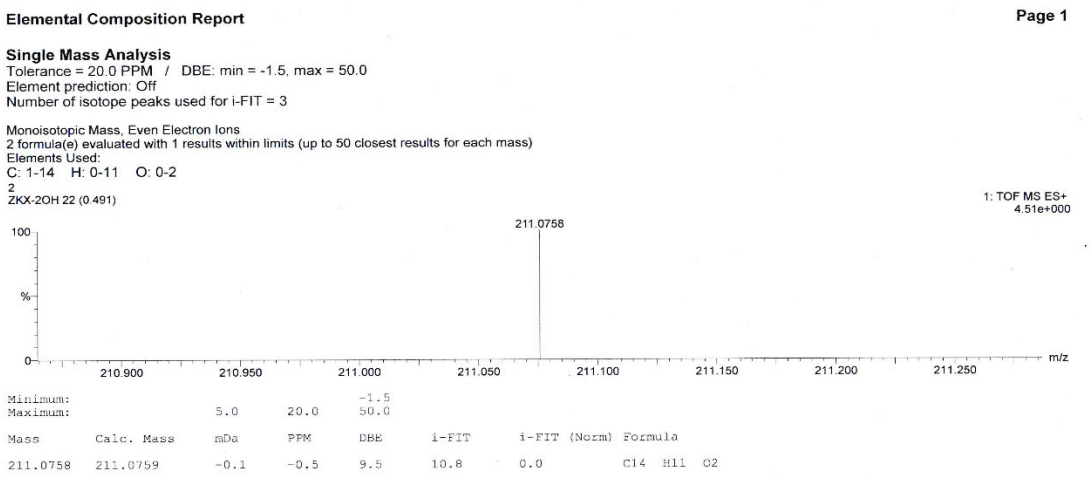


**Figure 5.3.4** HRMS spectrum of **2**.

HRMS, calcd for $C_{14}H_{11}O_2$, 211.0759; found, 211.0758. The result is in good accordance with the exact mass of **2**.

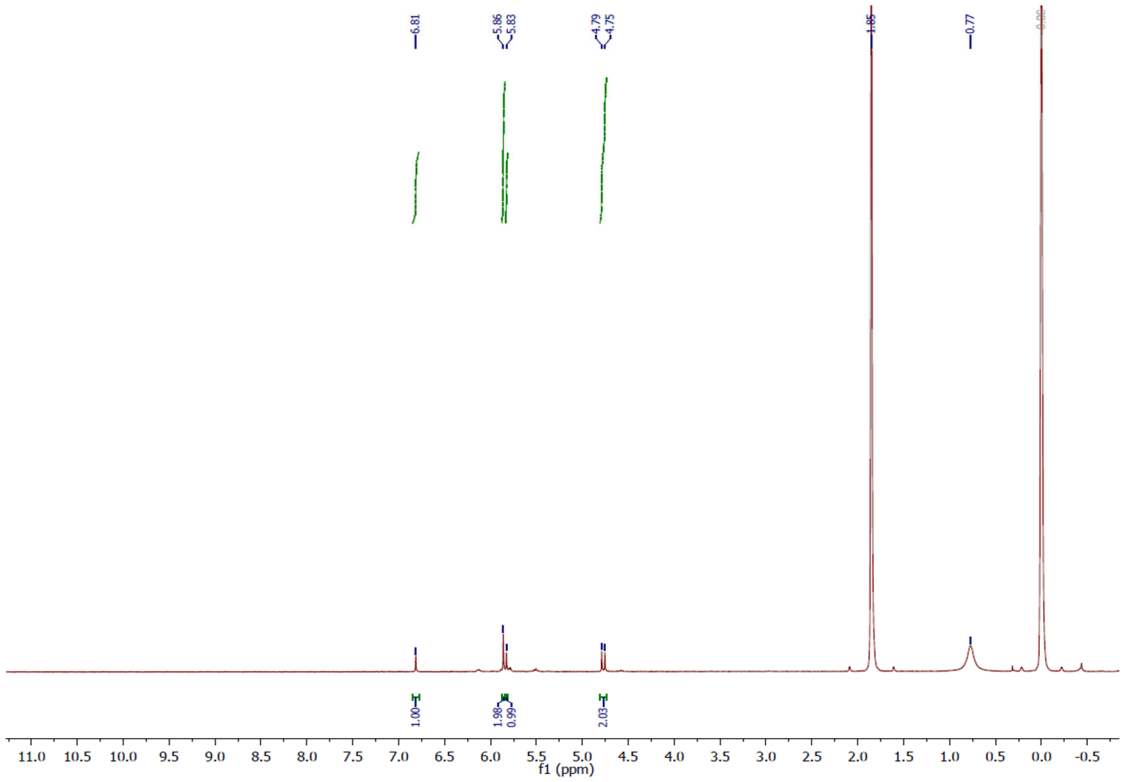


**Figure 5.3.5** $^1$H NMR spectrum of **3** in THF-$d_8$.

$^1$H NMR (300 MHz, THF-$d_8$) δ 6.81 (s, 1H), 5.86 (s, 2H), 5.83 (s, 1H), 4.77 (d, J = 10.2 Hz, 2H).

The peak area matches with the total number of H atoms in **3**. The result is in good accordance with the predicted spectrum. $^{13}$C NMR was not taken due to the poor solubility of **3** in common solvents.

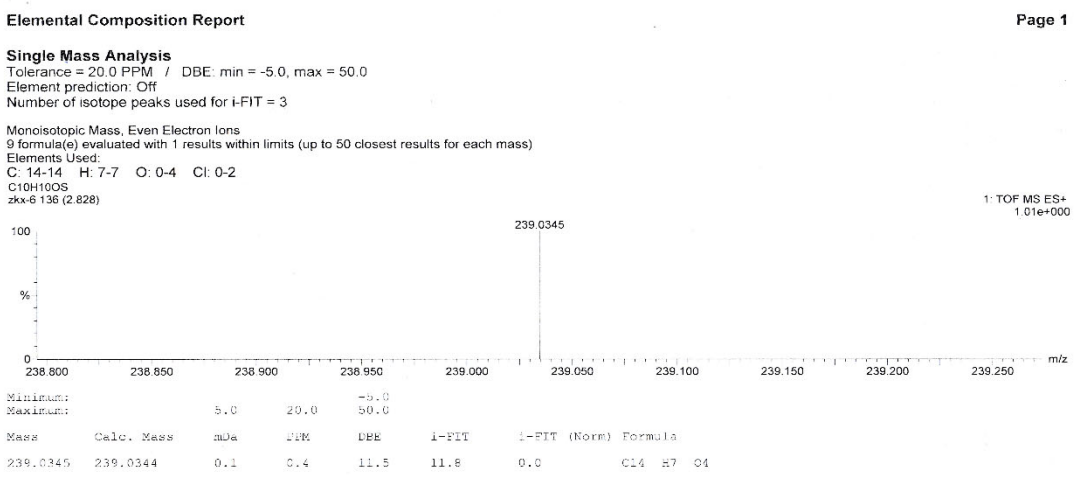


**Figure 5.3.6** HRMS spectrum of **3**.

HRMS, calcd for $C_{14}H_7O_4$, 239.0344; found, 239.0345. The result is in good accordance with the exact mass of **3**.

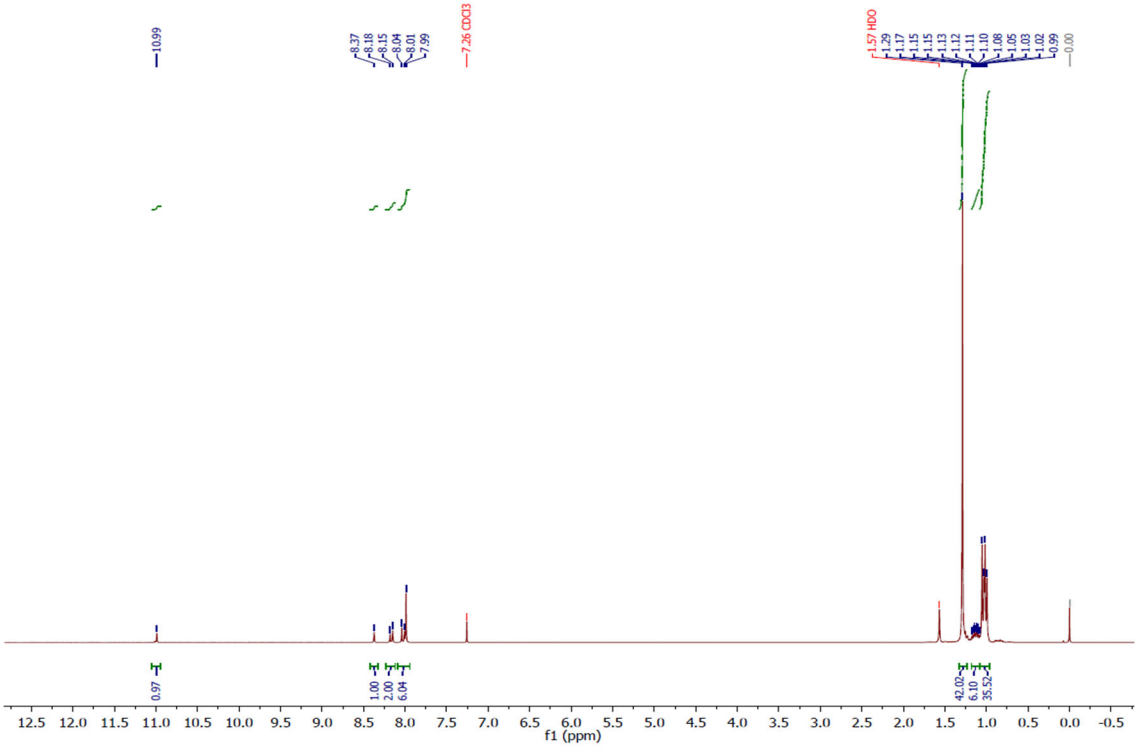


**Figure 5.3.7** $^1$H NMR spectrum of **U7** in $CDCl_3$.

$^{1}$H NMR (300 MHz, Chloroform-d) δ 10.99 (s, 1H), 8.37 (s, 1H), 8.17 (d, J = 9.3 Hz, 2H), 8.02 (d, J = 9.3 Hz, 2H), 7.99 (s, 4H), 1.29 (s, 42H), 1.23 – 1.14 (m, 6H), 1.02 (dd, J = 10.8, 6.9 Hz, 36H).

The proton at 9 position of anthracene unit showed a significant downfield shift of 2.81 ppm compared to that of **2**. This is caused by the introduction of two electron-withdrawing pyrazine units.

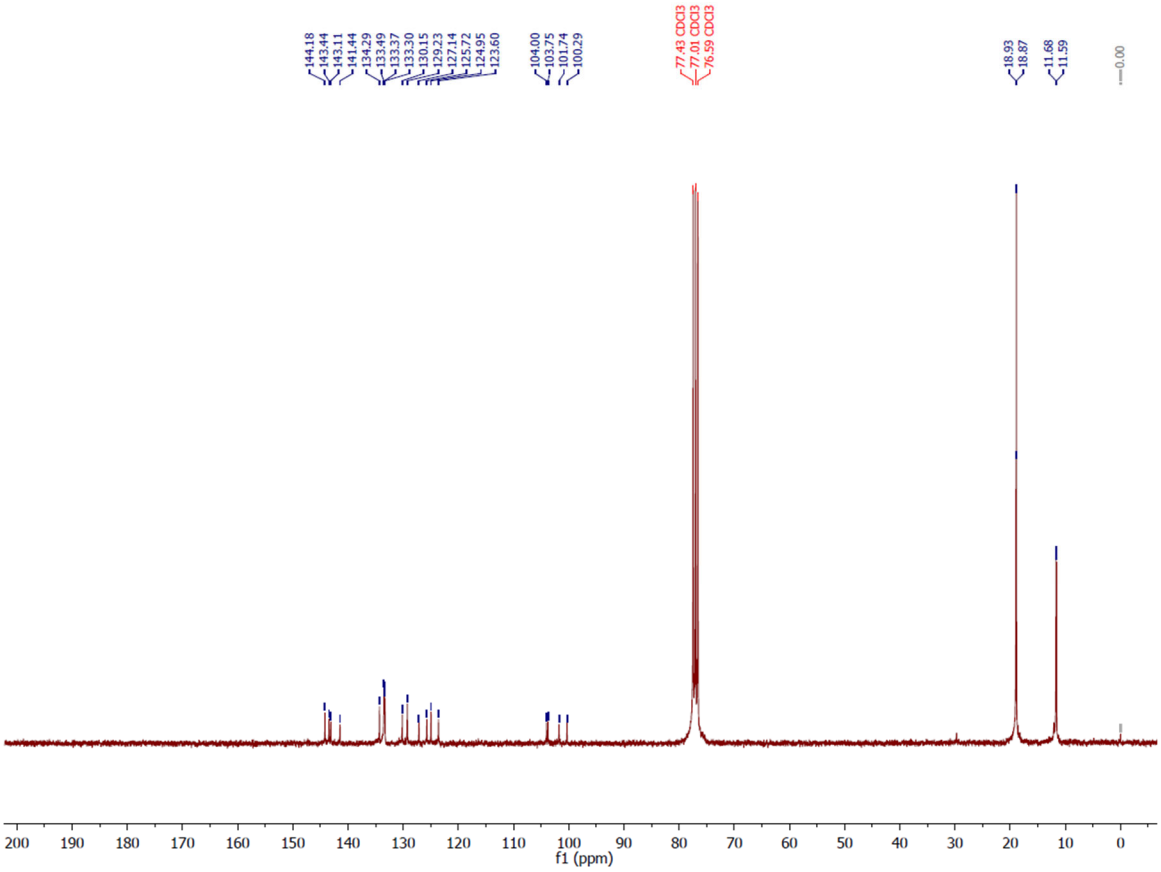


**Figure 5.3.8** $^{13}$C NMR spectrum of **U7** in $CDCl_3$.

$^{13}$C NMR (75 MHz, $CDCl_3$) δ 144.18, 143.44, 143.11, 141.44, 134.29, 133.49, 133.37, 133.30, 130.15, 129.23, 127.14, 125.72, 124.95, 123.60, 104.00, 103.75, 101.74, 100.29, 18.93, 18.87, 11.68, 11.59.

Unlike the proton NMR, $^{13}$C NMR clearly showed the unsymmetrical nature of **U7**. There are two set of TIPS peaks, which means the TIPS substituents at inner and outer helix are chemically different. Overall, there are 22 peaks in the spectrum, which represent the 22 kinds of carbon atoms in **U7**. The result is in good accordance with the predicted spectrum.

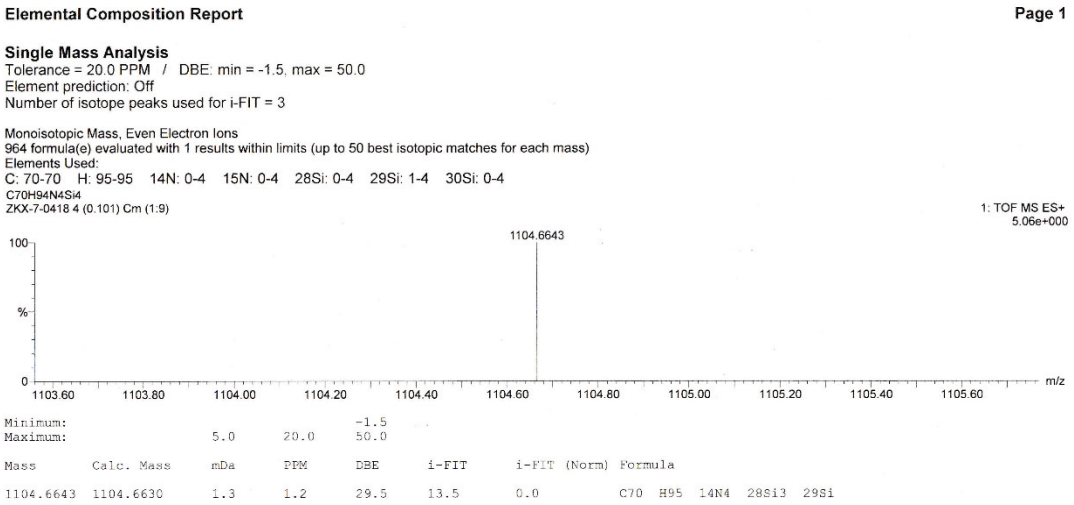


**Figure 5.3.9** HRMS spectrum of **U7**.

HRMS, calcd for $C_{70}H_{95}N_4Si_4$, 1104.6630; found, 1104.6643. The result is in good accordance with the exact mass of **U7**.

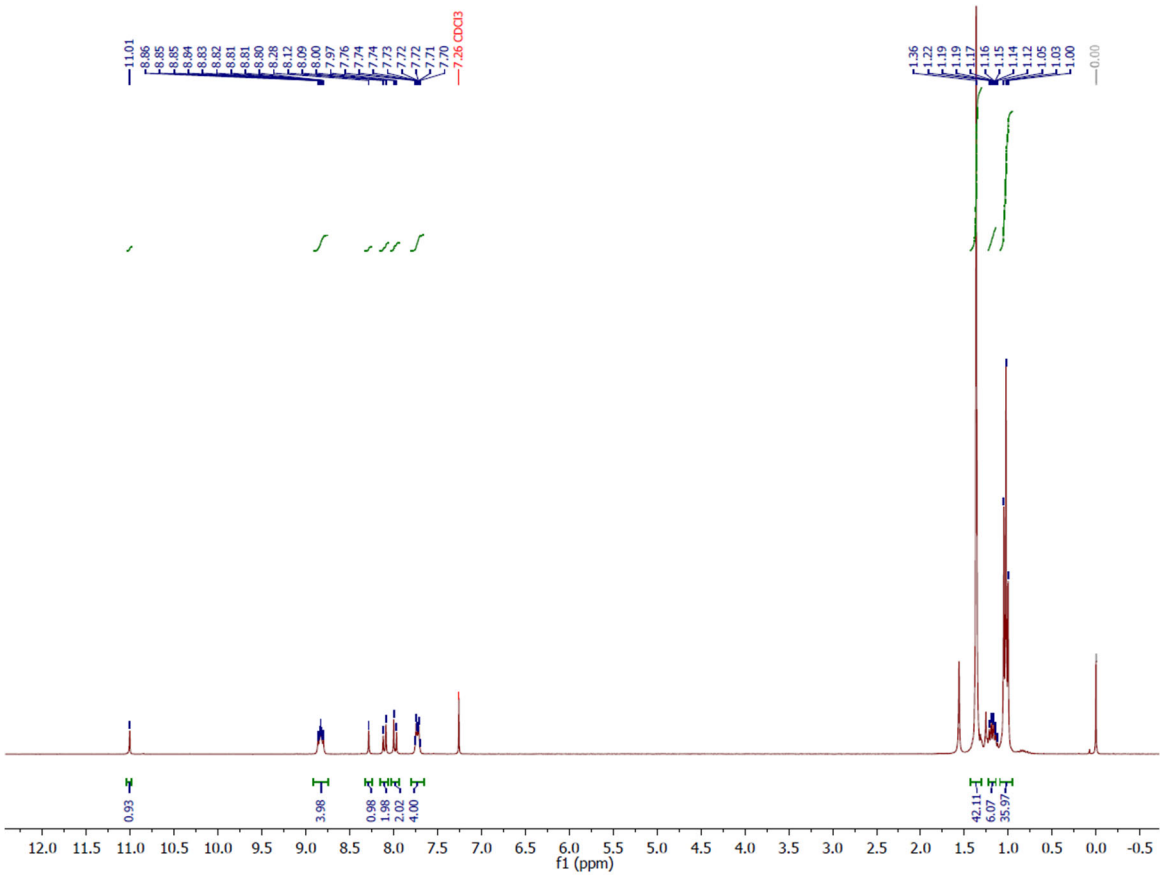


**Figure 5.3.10** $^1$H NMR spectrum of **U9** in $CDCl_3$.

$^{1}$H NMR (300 MHz, $CDCl_3$) δ 11.01 (s, 1H), 8.91 – 8.74 (m, 4H), 8.28 (s, 1H), 8.10 (d, J = 9.4 Hz, 2H), 7.98 (d, J = 9.4 Hz, 2H), 7.80 – 7.66 (m, 4H), 1.36 (s, 42H), 1.23 – 1.14 (m, 6H), 1.03 (t, J = 7.3 Hz, 36H).

The two multiplets are good indication of naphthalene unit of **U9**. The single peak at 11.01 ppm is similar to that of **U7**, which is attributed to proton at 9 position of anthracene unit. The peak area matches with the total number of H atoms in **U9**. The result is in good accordance with the predicted spectrum.

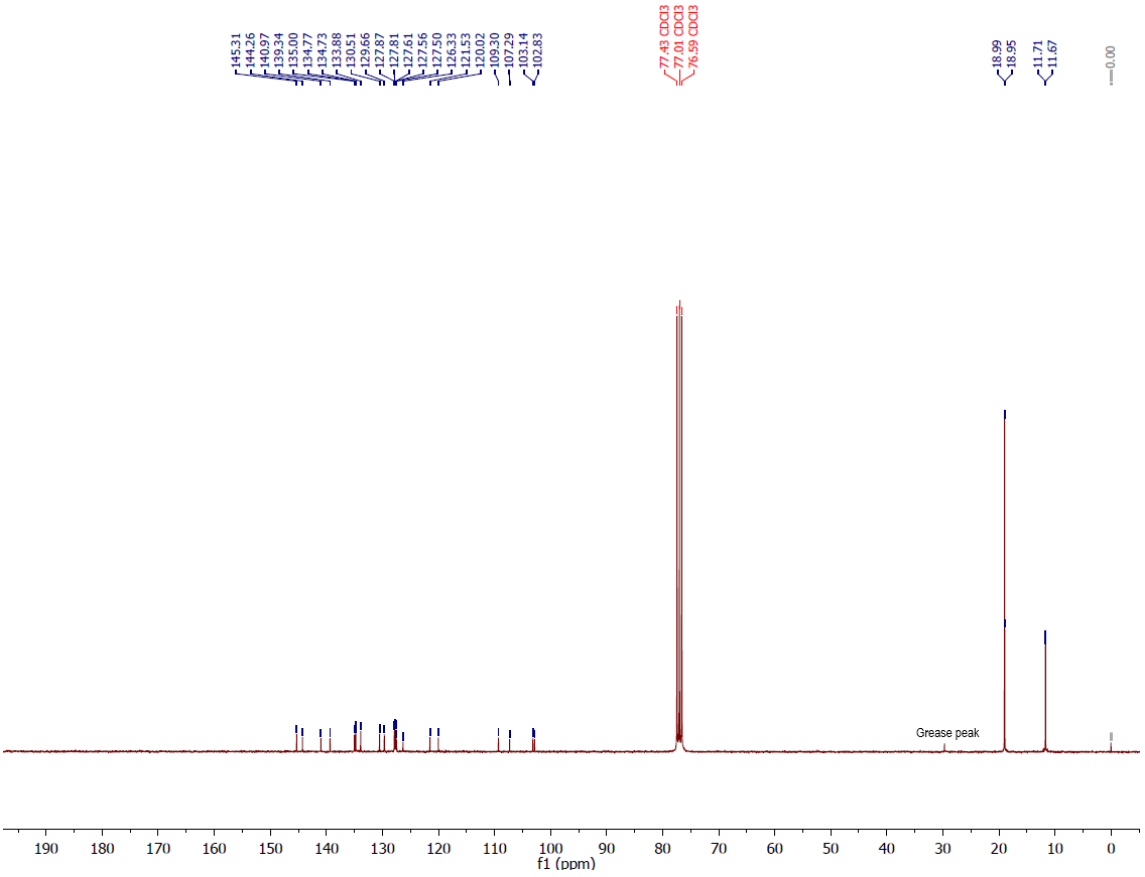


**Figure 5.3.11** $^{13}$C NMR spectrum of **U9** in $CDCl_3$.

$^{13}$C NMR (75 MHz, $CDCl_3$) δ 145.31, 144.26, 140.97, 139.34, 135.00, 134.77, 134.73, 133.88, 130.51, 129.66, 127.87, 127.81, 127.61, 127.56, 127.50, 126.33, 121.53, 120.02, 109.30, 107.29, 103.14, 102.83, 18.99, 18.95, 11.71, 11.67.

There are 26 peaks in the spectrum, which represent the 26 kinds of carbon atoms in **U9**. The result is in good accordance with the predicted spectrum.

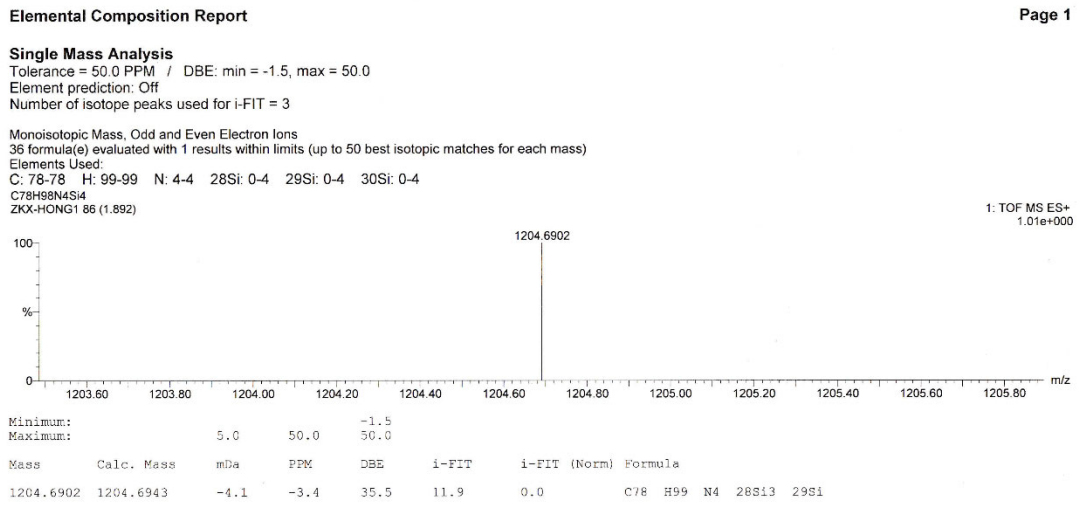


**Figure 5.3.12** HRMS spectrum of **U9**.

HRMS, calcd for $C_{78}H_{99}N_4Si_4$, 1204.6943; found, 1204.6902. The result is in good accordance with the exact mass of **U9**.

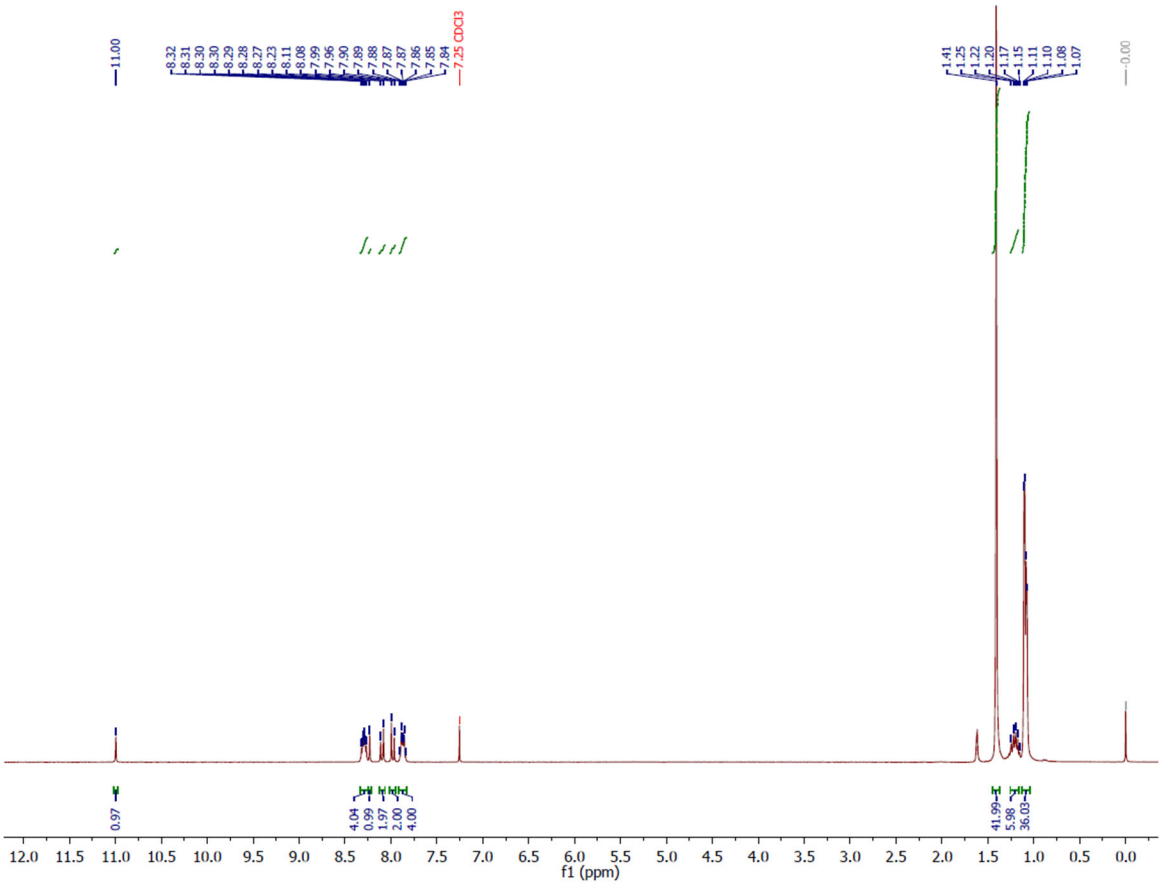


**Figure 5.3.13** $^1$H NMR spectrum of **U11** in $CDCl_3$.

$^{1}$H NMR (300 MHz, $CDCl_3$) δ 11.00 (s, 1H), 8.34 – 8.25 (m, 4H), 8.23 (s, 1H), 8.10 (d, J = 9.4 Hz, 2H), 7.98 (d, J = 9.4 Hz, 2H), 7.91 – 7.83 (m, 4H), 1.41 (s, 42H), 1.26 – 1.17 (m, 6H), 1.09 (dd, J = 7.0, 2.9 Hz, 36H).

The single peak at 11.0 ppm is characteristic of this type of helical azaarenes. The peak area matches with the total number of H atoms in **U11**. The result is in good accordance with the predicted spectrum.

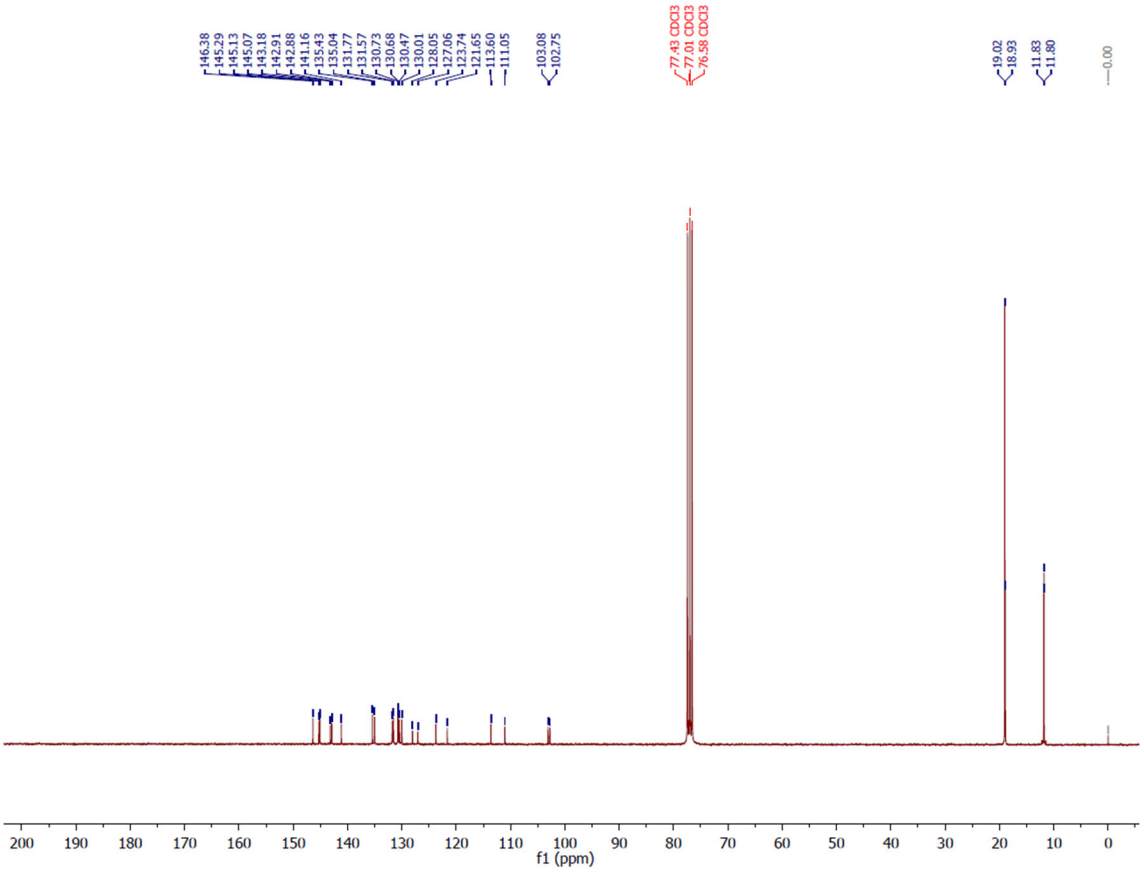


**Figure 5.3.14** $^{13}$C NMR spectrum of **U11** in $CDCl_3$.

$^{13}$C NMR (75 MHz, $CDCl_3$) δ 146.38, 145.29, 145.13, 145.07, 143.18, 142.91, 142.88, 141.16, 135.43, 135.04, 131.77, 131.57, 130.73, 130.68, 130.47, 130.01, 128.05, 127.06, 123.74, 121.65, 113.60, 111.05, 103.08, 102.75, 19.02, 18.93, 11.83, 11.80.

There are 28 peaks in the spectrum which represent the 28 kinds of carbon atoms in **U11**. The result is in good accordance with the predicted spectrum.

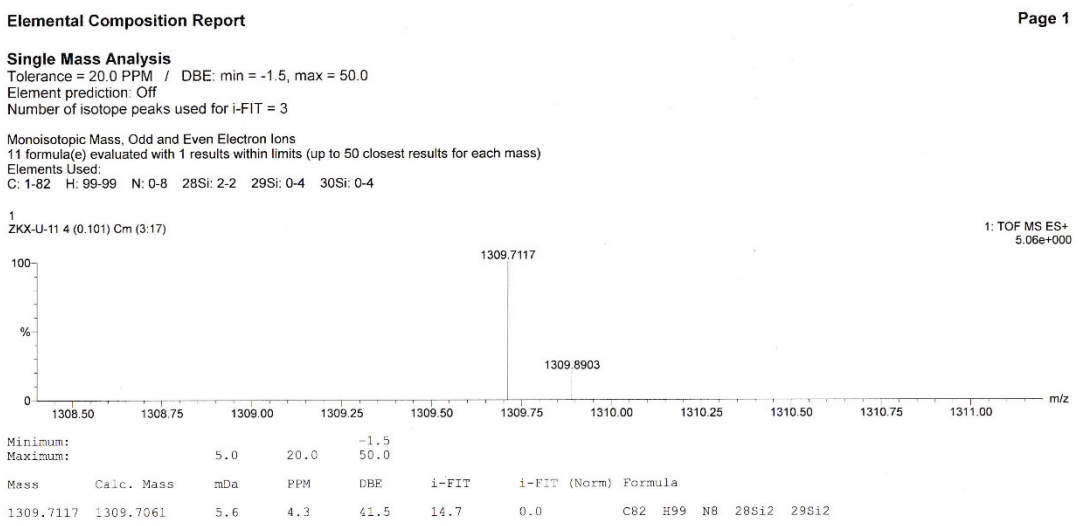


**Figure 5.3.15** HRMS spectrum of **U11**.

HRMS, calcd for $C_{82}H_{99}N_8{}^{28}Si_2{}^{29}Si_2$, 1309.7061; found, 1309.7117. The result is in good accordance with the exact mass of **U11**.

### 5.3.2 Optical and electrochemical properties

Figure 5.3.16 shows the normalized absorption spectra of **U7**, **U9** and **U11**. There is an obvious increase in $\lambda_{max}$ from **U7** to **U11**, which indicates the size-dependent bathochromic shift in the absorption. Compared with the reported Z-shape counterparts[11], **U7** and **U9** show small hypsochromic shifts (around 10 nm) in $\lambda_{max}$. For **U11**, due to the presence of a shoulder peak in the absorption spectrum of **Z11**, the hypsochromic shift in $\lambda_{max}$ is larger (48 nm). It is worth mentioning that the helical azaarenes have almost identical optical band gaps to their constitutional isomers, which indicates the similarity in their optical properties. Unlike the constitutional isomers, cyclic voltammetry of helical azaarenes was performed in DCM at room temperature due to the much better solubility. The measured LUMOs of helical azaarenes are apparently shallower than that of Z-shaped isomers, which means the helical azaarenes are more easily to reduce. Calculated results show the same trend. Calculated LUMOs of helical azaarenes are around 0.4 ev shallower than that of Z-shaped isomers. This could be ascribed to its twisted helical structure. The two pyrazine units near the center are highly distorted because of the torsional strain of the helix. Hence,

the conjugation in these two pyrazine units is rather weak resulting in smaller π-systems compared to Z-shaped azaarenes, which further leads to the shallower LUMOs. Table 5.3.1 and table 5.3.2 summarize the photophysical and electronic properties of helical azaarenes and its constitutional isomers.

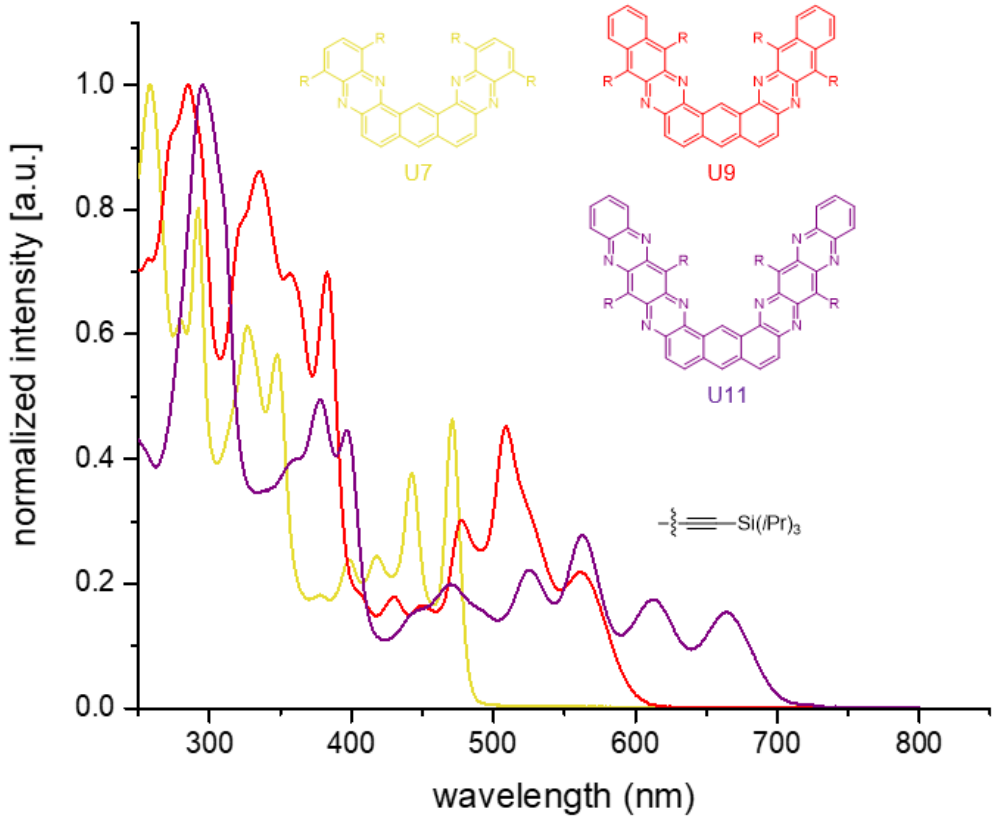


**Figure 5.3.16** Normalized absorption spectra of **U7**, **U9** and **U11** in dichloromethane.

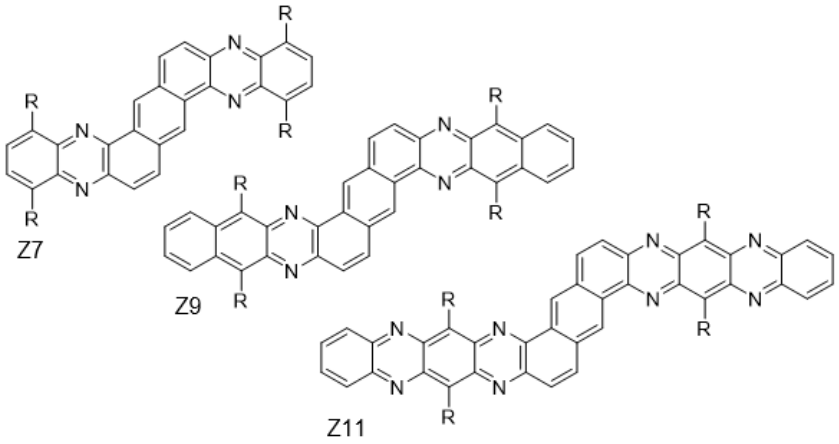


**Figure 5.3.17** Z-shaped constitutional isomers of **U7**, **U9** and **U11**.

**Table 5.3.1** Optical properties of **U7**, **U9**, **U11** and its isomers.

| Compound | $\lambda_{max, abs.}$ [nm] | $\lambda_{onset}$ [nm] | $\lambda_{max, ems.}$ [nm] |
|---|---|---|---|
| U7 | 471 | 482 | 478 |
| U9 | 561 | 594 | 602 |
| U11 | 664 | 701 | 692 |
| Z7 | 480 | 495 | 491 |
| Z9 | 575 | 599 | 597 |
| Z11 | 712 | 744 | 688 |

**Table 5.3.2** Electronic properties of **U7**, **U9**, **U11** and its isomers.

| Compound | LUMO [ev] [a]meas./[b]calcd | HOMO [ev] [c]meas./[b]calcd | gap [ev] [d]meas./[b]calcd |
|---|---|---|---|
| U7 | -3.08/-2.82 | -5.65/-5.68 | 2.57/2.86 |
| U9 | -3.27/-3.07 | -5.36/-5.25 | 2.09/2.18 |
| U11 | -3.77/-3.53 | -5.54/-5.31 | 1.77/1.78 |
| Z7 | -3.38/-3.20 | -5.88/-5.97 | 2.50/2.77 |
| Z9 | -3.60/-3.44 | -5.67/-5.56 | 2.07/2.12 |
| Z11 | -4.29/-3.93 | -6.04/-5.63 | 1.75/1.70 |

[a] $LUMO_{meas}$= - ($E_{red(onset)}$ + 4.8) (eV);

[b] DFT calculations (B3LYP/6-31G*) using Gaussian 09; TMS groups were used instead of TIPS;

[c] $E_{HOMO}$=$E_{LUMO(CV)}$ - $E_{gap(opt)}$ (eV);

[d] $gap_{meas}$ was calculated from 1240nm/$\lambda_{onset}$.

Data for **Z7**, **Z9** and **Z11** were taken from reference [9].

### 5.3.3 Single crystal X-ray structures

The crystals suitable for X-ray analysis were obtained via slow evaporation of methanol into the chlorobenzene solutions of helical azaarenes. The solid-state structures and stacking patterns are shown in the figure 5.3.18. All hydrogen atoms and solvent molecules are omitted for clarity. From the crystal structures, it could be pointed out that the helicity

of the obtained azaacenes is evidently caused by the steric hindrance between the two inner TIPS groups. Moreover, it is obvious that all the three racemates are racemic compounds, which means the *P* and *M*-isomers are both present in the crystal in an ordered 1:1 ratio. The packing motifs of **U7**, **U9** and **U11** are similar. *P* and *M*-isomers pack in pairs which are positioned such that the arms of the helix are on top of each other to different extents in an inverted manner. **U9** has the largest overlapping area and longest stack distance, whereas **U11** possesses the smallest overlapping area but the shortest stack distance. **U7**, on the other hand, bears intermediate overlapping area and stack distance. The TIPS groups strongly hinder the π–π stacking due to its bulkiness, and the helical backbone further obstructs the effective π–π stacking. Consequently, helical azaarenes possess much improved solubility compared with their Z-shaped isomers, and they could be easily dissolved in chlorinated solvents and other common solvents, such as dichloromethane, hexane, THF, DMF and toluene.

The interplane angles of **U7**, **U9** and **U11** are 38.9º, 48.2º and 39.7º respectively. The sum of torsional angels increases from 52.7º to 82.0º as the size of helical skeleton becomes larger. Unlike the common helicenes, where all the aromatic rings are fused inward encircling the axis, there are only two phenanthrene segments folding inward in the obtained helical azaarene molecules. Thus, although the interplane angle of **U9** is significantly larger than that of **U7**, there is little difference in the sum of their torsional angles. Upon close inspection on their torsional angles, it is found that the largest torsional angles of **U7**, **U9** and **U11** are almost identical. More interestingly, those largest torsional angles all belong to the phenanthrene segments, which substantiate the similarity in helical skeletons among the obtained helical azaarenes.

## 5.4 Conclusion

In conclusion, a series of novel helical azaarenes have been prepared by the condensation reactions between **3** and diamines **4** – **6**. The optical and electronic properties of obtained compounds were investigated and compared with their Z-shaped constitutional isomers. Helical skeletons of

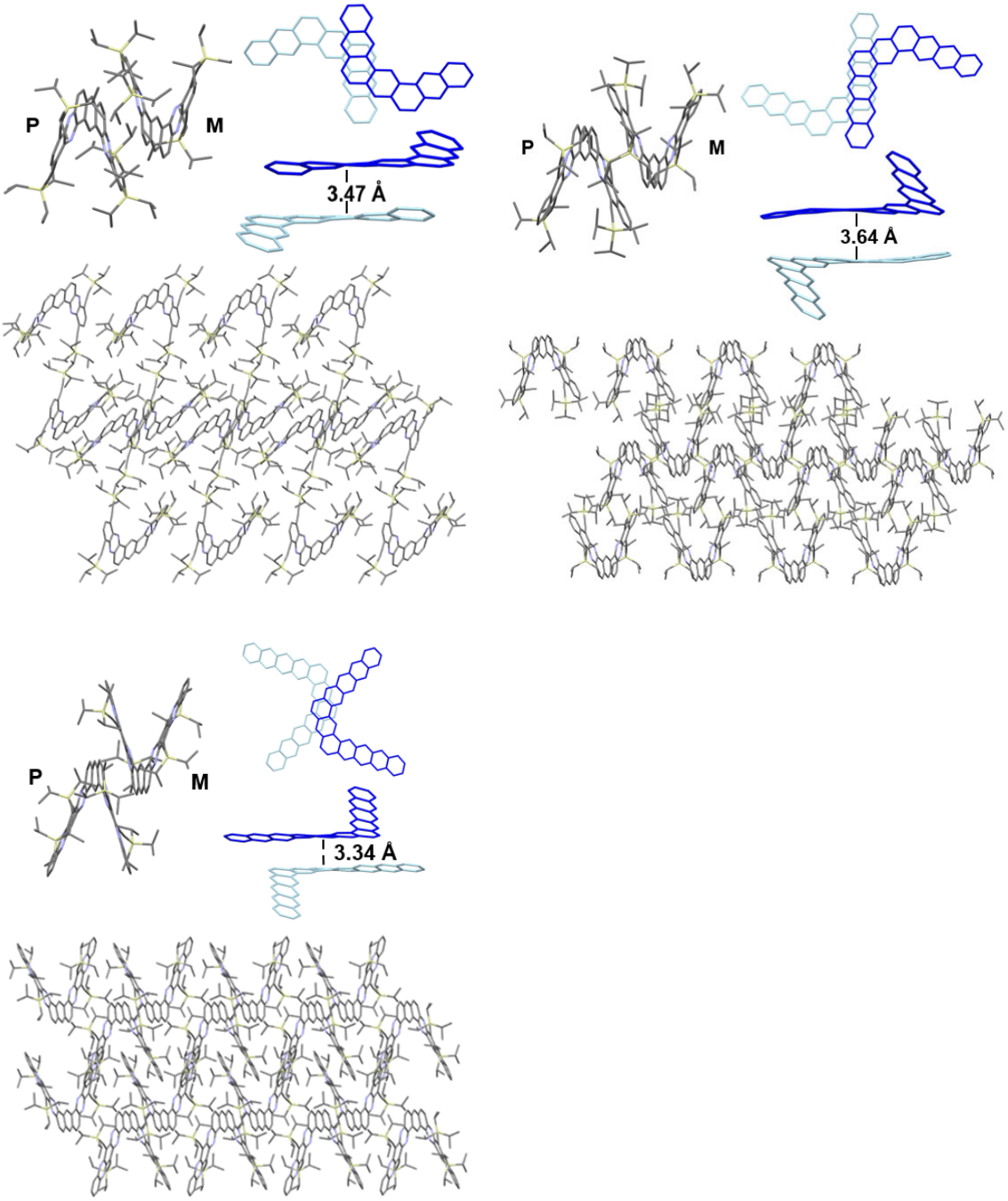


**Figure 5.3.18** Crystal structures and packing of **U7** (top left), **U9** (top right) and **U11 (**bottom left).

those helical azaarenes were unequivocally revealed by the single crystal X-ray analysis. Further elongation of the helical backbone could give rise to multi-helical azaarenes.

**References**

[1] a) J. Li, Q. Zhang, *ACS Appl. Mater. Interfaces* **2015**, *7*, 28049-28062; b) U. H. F. Bunz, *Acc. Chem. Res.* **2015**, *48*, 1676-1686; c) J. E. Anthony, *Chem. Rev.* **2006**, *106*; d) B. Kohl, F. Rominger, M. Mastalerz, *Angew. Chem. Int. Ed.* **2015**, *54*, 6051-6056; e) J. P. Mora-Fuentes, A. Riaño, D. Cortizo-Lacalle, A. Saeki, M. Melle-Franco, A. Mateo-Alonso, *Angew. Chem. Int. Ed.* **2019**, *58*, 552-556; f) B.-L. Hu, C. An, M. Wagner, G. Ivanova, A. Ivanova, M. Baumgarten, *J. Am. Chem. Soc.* **2019**, *141*, 5130-5134.

[2] Q. Miao, *Adv. Mater.* **2014**, *26*, 5541-5549.

[3] R. Juárez, M. M. Oliva, M. Ramos, J. L. Segura, C. Alemán, F. Rodríguez-Ropero, D. Curcó, F. Montilla, V. Coropceanu, J. L. Brédas, Y. Qi, A. Kahn, M. C. Ruiz Delgado, J. Casado, J. T. López Navarrete, *Chem. Eur. J.* **2011**, *17*, 10312-10322.

[4] Y. Shen, C. F. Chen, *Chem. Rev.* **2012**, *112*, 1463-1535.

[5] a) G. M. Upadhyay, H. R. Talele, A. V. Bedekar, *J. Org. Chem.* **2016**, *81*, 7751-7759; b) M. Ben Braiek, F. Aloui, B. Ben Hassine, *Tetrahedron Lett.* **2016**, *57*, 2763-2766.

[6] S. Abbate, C. Bazzini, T. Caronna, F. Fontana, C. Gambarotti, F. Gangemi, G. Longhi, A. Mele, I. N. Sora, W. Panzeri, *Tetrahedron* **2006**, *62*, 139-148.

[7] J. Meisenheimer, K. Witte, *Berichte der deutschen chemischen Gesellschaft* **1903**, *36*, 4153-4164.

[8] T. Caronna, F. Fontana, A. Mele, I. N. Sora, W. Panzeri, L. Viganò, *Synthesis* **2008**, *2008*, 413-416.

[9] H. Sakai, S. Shinto, Y. Araki, T. Wada, T. Sakanoue, T. Takenobu, T. Hasobe, *Chem. Eur. J.* **2014**, *20*, 10099-10109.

[10] K. V. Domasevitch, P. V. Solntsev, H. Krautscheid, I. S. Zhylenko, E. B. Rusanov, A. N. Chernega, *Chem. Commun.* **2012**, *48*, 5847-5849.

[11] S. Hahn, S. Koser, M. Hodecker, O. Tverskoy, F. Rominger, A. Dreuw, U. H. F. Bunz, *Chem. Eur. J.* **2017**, *23*, 8148-8151.

# Chapter 6

## Synthesis, Characterizations and Crystal Structures of Novel Imide-fused Diazatetracenes

*In this chapter, a series of novel imide-fused diazatetracenes were synthesized via Buchwald-Hartwig C-N coupling with a highly active palladium source. The obtained diazatetracenes were characterized by NMR, HRMS, UV-Vis and cyclic voltammetry. By changing the alkyl chains of the diazatetracenes, different solid-state packings were achieved.*

## 6.1 Introduction

Azaacenes, which have a long-standing history, are promising n-type semiconductors in organic electronics.[1] Since the first instance of applying dihydro-azapentacene in thin film transistor[2], great effort has been channeled into the syntheses of azapentacene derivatives and investigation of their performance in OFET devices.[3] In contrast to the numerous azapentacene family, there are only a handful of reports on the azatetracene derivatives.[4] The relatively shallower LUMO and less effective charge injection of azatetracenes make it less competitive in organic electronics compared to the azapentacene analogue. It is essential to lower the LUMO energy level of azatetracenes to achieve better device performance.[5]

From the synthetic perspective, the introduction of electron-withdrawing units could evidently deepen the LUMO of azatetracenes.[4a, 4e] Mark *et al*. reported a series of anthracenedicarboximides, where two imide groups were linearly fused to anthracene unit.[6] The attachment of imide groups successfully turned the anthracene into an air-stable n-type semiconductor. Thus, it is assumed that the incorporation of imide units to azatetracenes backbone should lower the LUMO energy level and improve the performance in organic electronics.[7]

In this chapter, the synthesis of a series of novel imide-containing diazatetracenes **3** via Buchwald-Hartwig C-N coupling is reported. Optical and electronic properties are investigated and compared with unsubstituted diazatetarcenes. The electron-withdrawing imide segment effectively lowers the LUMO of obtained diazatetracenes.

## 6.2 Synthesis

The synthetic route to imide-fused diazatetracenes is shown in Figure 6.2.1. Starting from **1**, the stille coupling in refluxing toluene gives the diamine precursor **2** in 89% yield. Further reduction of the thiadiazole unit furnishes the thiophene-substituted naphthalene diamine **3a** quantitatively. Imide-fused diazatetracenes **5-8** are obtained through the

Buchwald-Hartwig coupling of diamines **3a-b** and dihalides **4a-b**. It is noteworthy that **4a-b** are not reactive dihalides spices especially when the halogen is chloride. However, the usage of highly active Pd source enables the good coupling yields which range from 65-81 %.

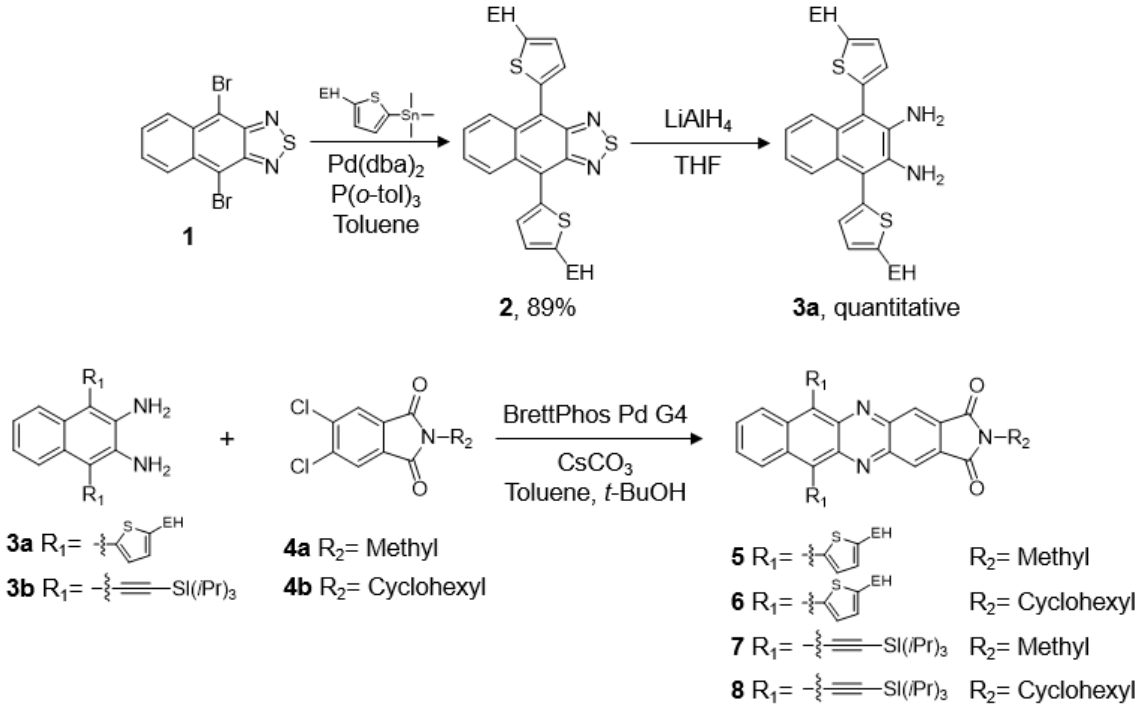


**Figure 6.2.1** Synthesis of imide-containing diazatetracenes via palladium catalyzed coupling; EH = ethylhexyl.

Synthesis of **2**: In a heatgun-dried Schlenk flask, **1** (344 mg, 1 mmol) and tin reagent (1.08 g, 3 mmol) were dissolved in 10 ml dry toluene. After the solution was purged with argon for 15 min, $Pd(dba)_2$ (28.8 mg, 5 mol%) and P(*o*-tol)$_3$ (15.2 mg, 5 mol%) were added. The mixture was purged for 5 more min and then heated to reflux for 1 d. After cooling to room temperature, solvent was removed *in vacuo*. The residue was purified by column chromatography on silica gel using a Hexane/DCM (v/v, 4:1) solvent mixture. The product was obtained as a dark purple highly viscous liquid (515 mg, 89.5 %).

Synthesis of **3a**: In a heatgun-dried round bottom flask, **2** (500 mg, 0.87 mmol) was dissolved in 10 ml dry THF under argon. After the solution was cooled to 0 °C, 2M $LiAlH_4$

solution in THF (3.5 ml, 7mmol, 8 eq) was added dropwise. Then the solution was warmed to room temperature and stirred for 12 h. The mixture was cooled again to 0 °C and carefully quenched with saturated $NH_4Cl_{(aq)}$. Afterwards, the mixture was extracted with diethyl ether (20 ml x 3), and the organic phase was combined and dried over sodium sulphate. Flash column chromatography on silica gel using hexane/ethyl acetate (v/v, 10/1) as eluent yielded the product as a slightly yellow viscous oil (470 mg, quantitative).

Synthesis of **4b**: 4,5-dichlorophthalic anhydride (2.17 g, 10 mmol) and 20 ml propionic acid was placed in a Schlenk flask under argon. Cyclohexylamine (1.72 ml, 15 mmol) was added dropwise with stirring. Then the mixture was heated to reflux for 3 h and allowed to gradually cool to room temperature. Colorless plate-like crystal was collected by filtration and washed with methanol. Further drying in vacuum yielded 2.85 g of **4b** (96%).

General procedure for the coupling reaction: In a heatgun-dried Schlenk flask, ortho-diamine (0.2 mmol), ortho-dichloride (0.24 mmol) and $Cs_2CO_3$ (163 mg, 0.5 mmol) were suspended in a mixture of 5 ml dry toluene and 1 ml dry tert-butanol. The mixture was purged with argon for 15 min followed by the addition of BrettPhos Pd G4 (9.2 mg, 5 mol%) and BrettPhos (5.4 mg, 5 mol%). After stirring at 100 °C for 1 d, the mixture was cooled to room temperature, and the solvent was removed *in vacuo*. The residue was purified by column chromatography on silica gel using a hexane/DCM solvent mixture. The obtained N,N'-dihydroazatetracene was quickly dissolved in 10 ml DCM and treated with $MnO_2$ (20 eq) due to the instability at ambient condition. After stirring at room temperature for 30 min, the mixture was filtered through Celite, and the solvent was removed *in vacuo*. The crude product was purified by flash column chromatography on silica gel using a hexane/DCM solvent mixture.

Synthesis of **5**: The GP was applied to **3a** (109 mg) and **4a** (55 mg). Column chromatography (hexane/DCM= 2:1 - 1:1) yielded **5** (113 mg, 81%) as dark blue solid.

Synthesis of **6**: The GP was applied to **3a** (109 mg) and **4b** (72 mg). Column chromatography (hexane/DCM= 2:1 – 1:1) yielded **6** (100 mg, 65%) as dark blue solid.

Synthesis of **7**: The GP was applied to **3b** (104 mg) and **4a** (55 mg). Column chromatography (hexane/DCM= 2:1 – 1:1) yielded **7** (101 mg, 75%) as dark blue solid.

Synthesis of **8**: The GP was applied to **3b** (104 mg) and **4b** (72 mg). Column chromatography (hexane/DCM= 2:1 – 1:1) yielded **8** (115 mg, 77%) as dark blue solid.

## 6.3 Results and discussion

### 6.3.1 Characterization

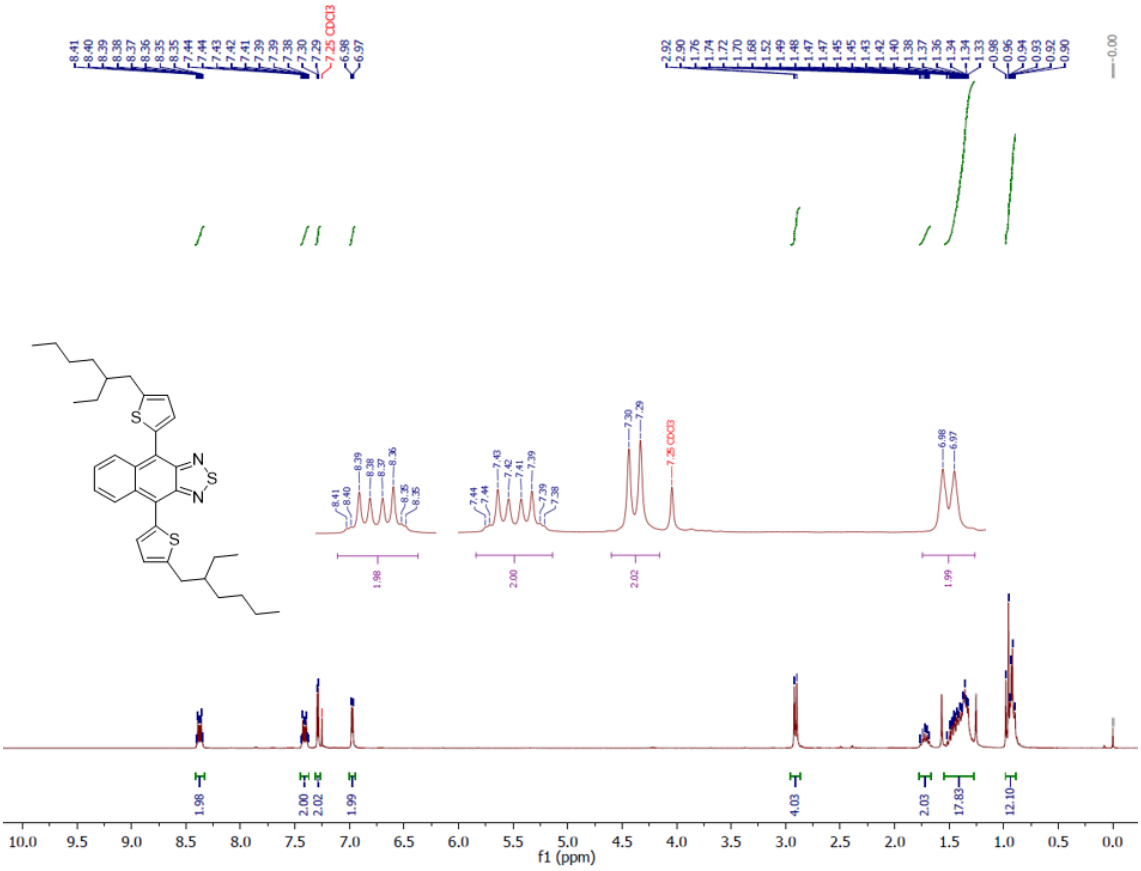


**Figure 6.3.1** $^{1}$H NMR spectrum of **2** in $CDCl_3$.

$^{1}$H NMR (300 MHz, $CDCl_3$) δ 8.41 – 8.33 (m, 2H), 7.45 – 7.37 (m, 2H), 7.29 (d, J = 3.5 Hz, 2H), 6.98 (d, J = 3.5 Hz, 2H), 2.91 (d, J = 6.7 Hz, 4H), 1.77 – 1.67 (m, 2H), 1.54 – 1.27 (m, 18H), 0.99 – 0.89 (m, 12H).

The peak area matches with the total number of H atoms in **2**. The result is in good accordance with the predicted spectrum.

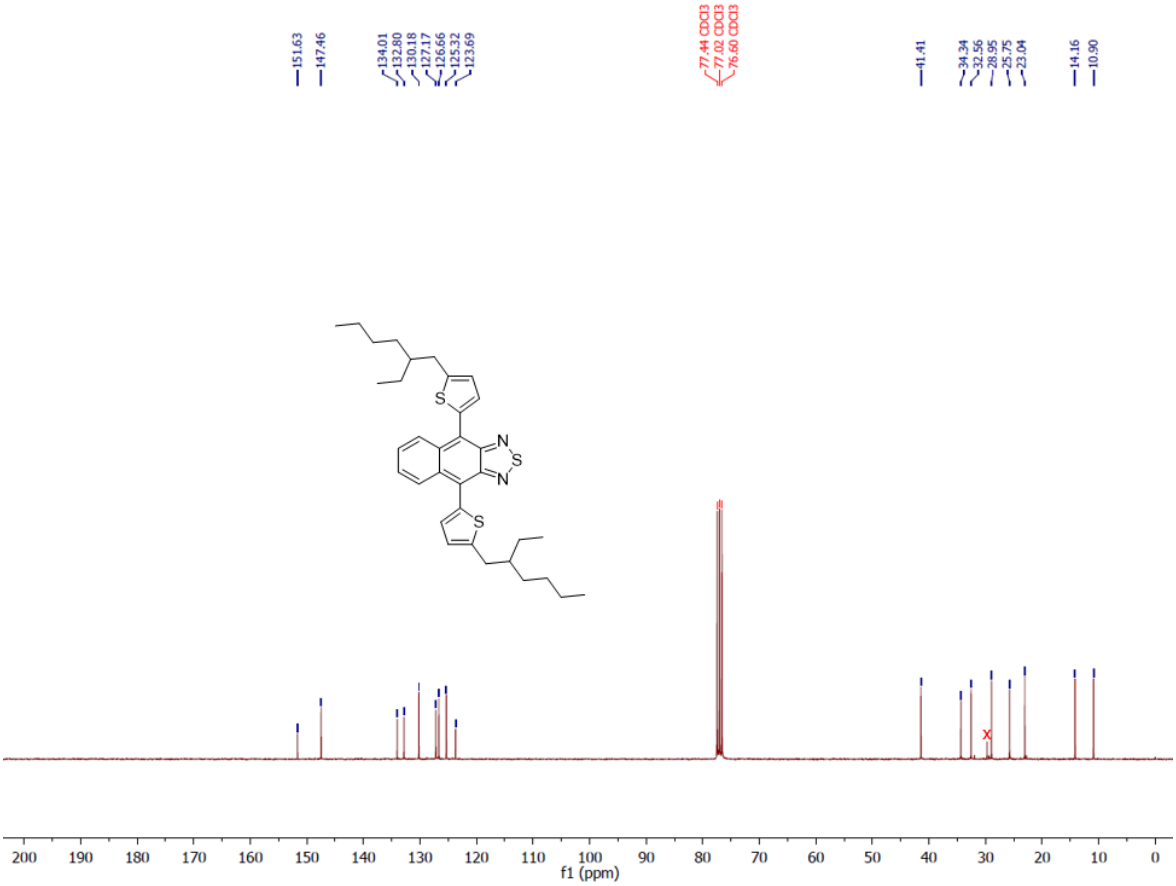


**Figure 6.3.2** $^{13}C$ NMR spectrum of **2** in $CDCl_3$.

$^{13}C$ NMR (75 MHz, $CDCl_3$) δ 151.63, 147.46, 134.01, 132.80, 130.18, 127.17, 126.66, 125.32, 123.69, 41.41, 34.34, 32.56, 28.95, 25.75, 23.04, 14.16, 10.90.

X at 29.7 ppm denotes the solvent residue. There are 17 peaks in the spectrum, which represents the 17 kinds of carbon atoms in **2**. The result is in good accordance with the predicted spectrum.

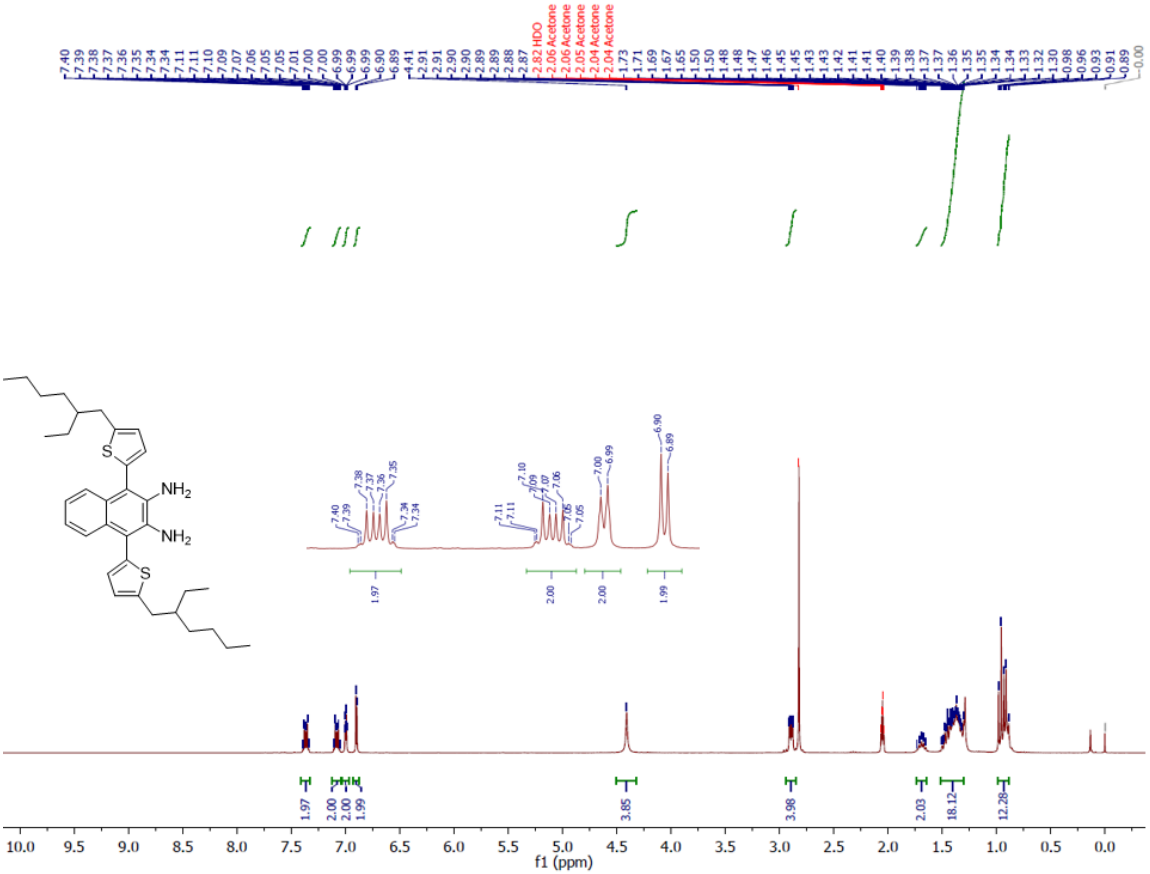


**Figure 6.3.3** $^{1}$H NMR spectrum of **3** in Acetone-$d_6$.

$^{1}$H NMR (300 MHz, Acetone-$d_6$) δ 7.41 – 7.33 (m, 2H), 7.12 – 7.04 (m, 2H), 7.00 (d, J = 3.3 Hz, 2H), 6.90 (d, J = 3.3 Hz, 2H), 4.41 (s, 4H), 2.94 – 2.85 (m, 4H), 1.74 – 1.64 (m, 2H), 1.51 – 1.30 (m, 18H), 0.99 – 0.88 (m, 12H).

The single peak at 4.41 ppm corresponds to amine protons. The peak area matches with the total number of H atoms in **3**. The result is in good accordance with the predicted spectrum.

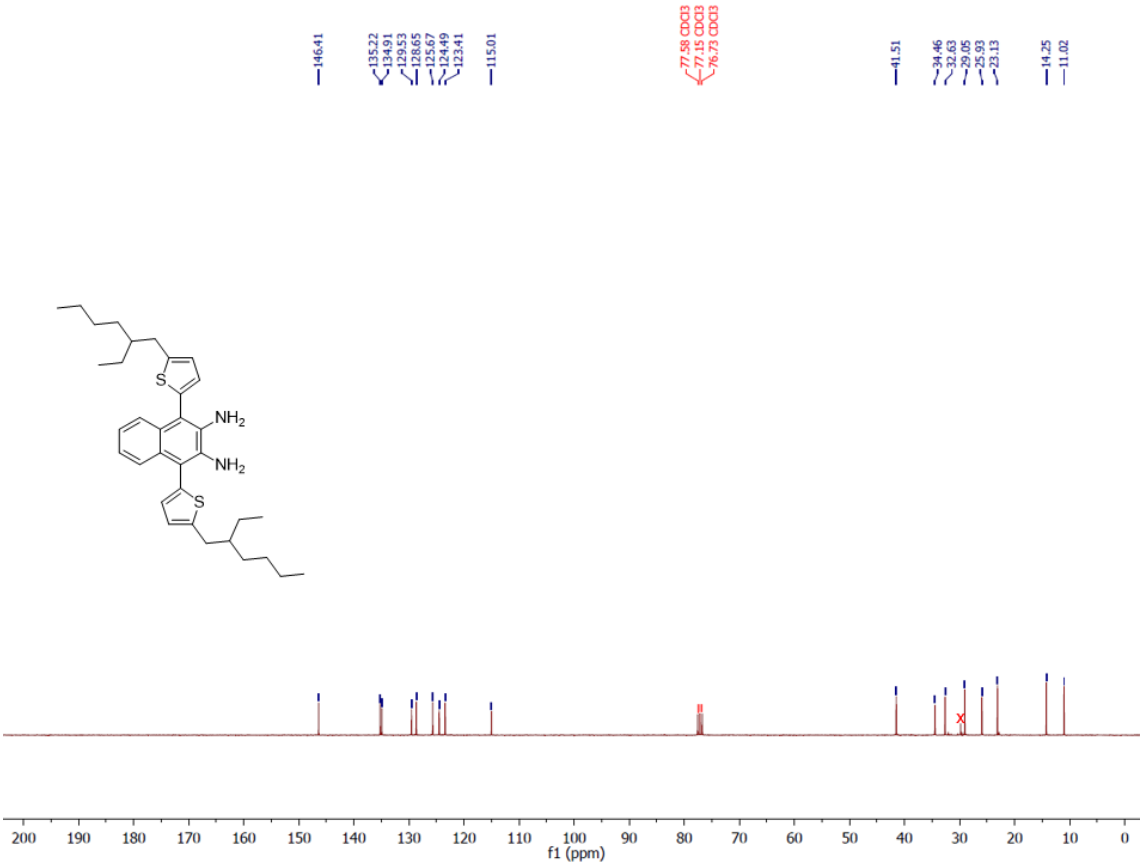


**Figure 6.3.4** $^{13}C$ NMR spectrum of **3** in $CDCl_3$.

$^{13}C$ NMR (75 MHz, $CDCl_3$) δ 146.41, 135.22, 134.91, 129.53, 128.65, 125.67, 124.49, 123.41, 115.01, 41.51, 34.46, 32.63, 29.05, 25.93, 23.13, 14.25, 11.02.

X at 29.7 ppm denotes the solvent residue. There are 17 peaks in the spectrum, which represents the 17 kinds of carbon atoms in **3**. The result is in good accordance with the predicted spectrum.

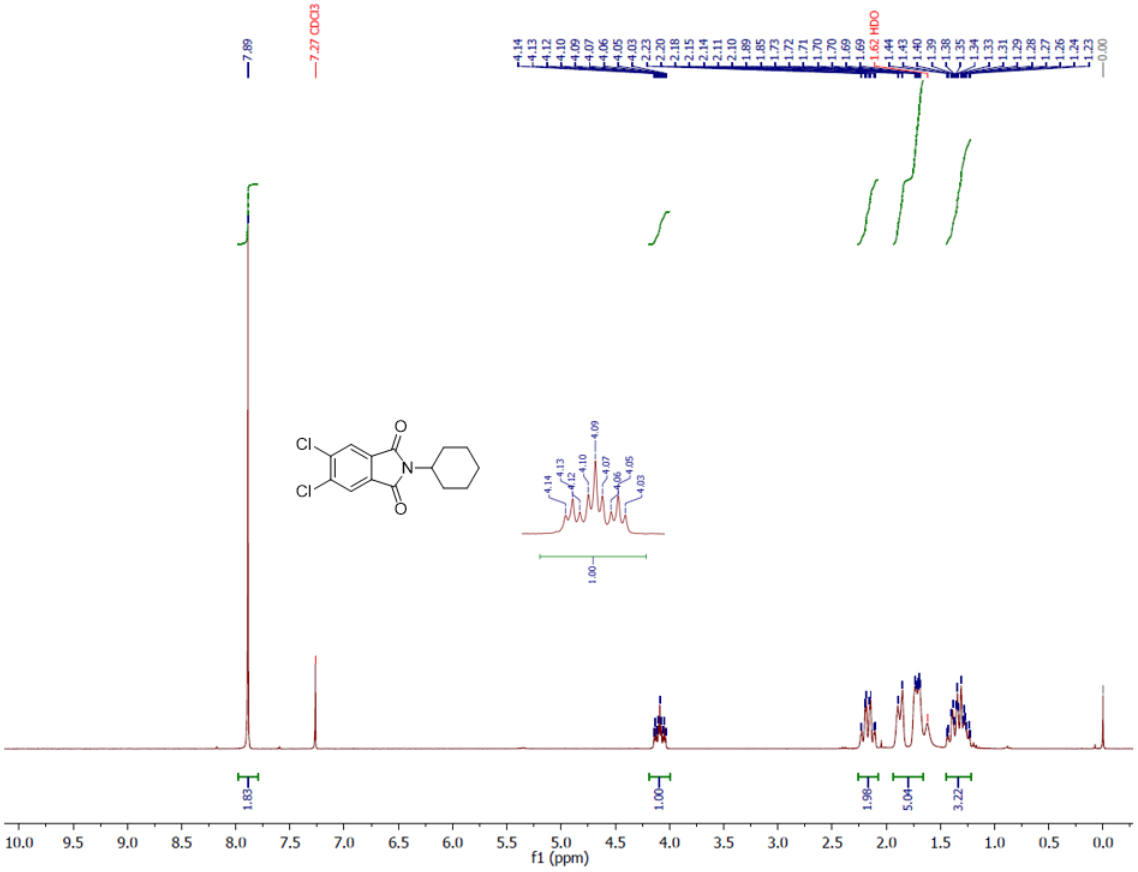


**Figure 6.3.5** $^{1}$H NMR spectrum of **4b** in $CDCl_3$.

$^{1}$H NMR (300 MHz, $CDCl_3$) δ 7.89 (s, 2H), 4.09 (tt, J = 12.4, 3.9 Hz, 1H), 2.26 – 2.08 (m, 2H), 1.94 – 1.66 (m, 5H), 1.45 – 1.22 (m, 3H).

The peak area matches with the total number of H atoms in **4b**. The result is in good accordance with the predicted spectrum.

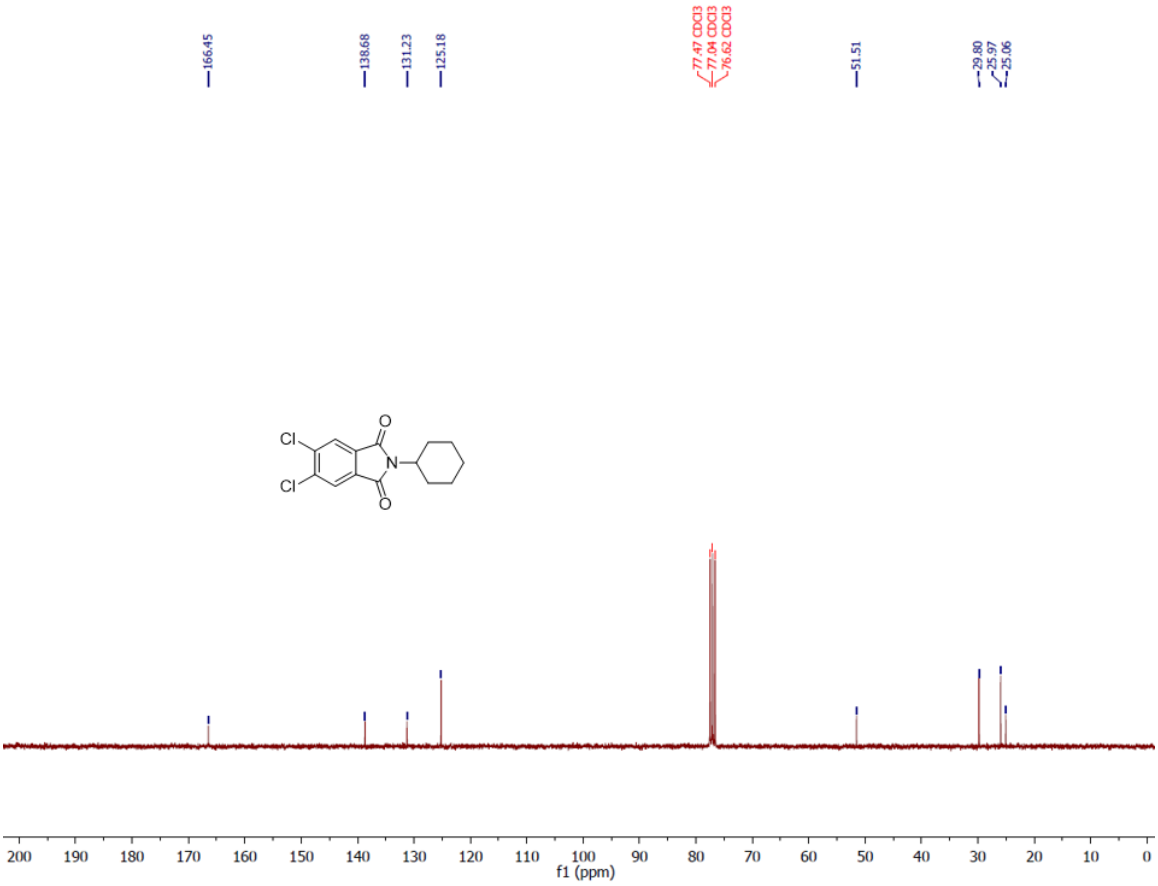


**Figure 6.3.6** $^{13}$C NMR spectrum of **4b** in $CDCl_3$.

$^{13}$C NMR (75 MHz, $CDCl_3$) δ 166.45, 138.68, 131.23, 125.18, 51.51, 29.80, 25.97, 25.06. There are 8 peaks in the spectrum, which represents the 8 kinds of carbon atoms in **3**. The result is in good accordance with the predicted spectrum.

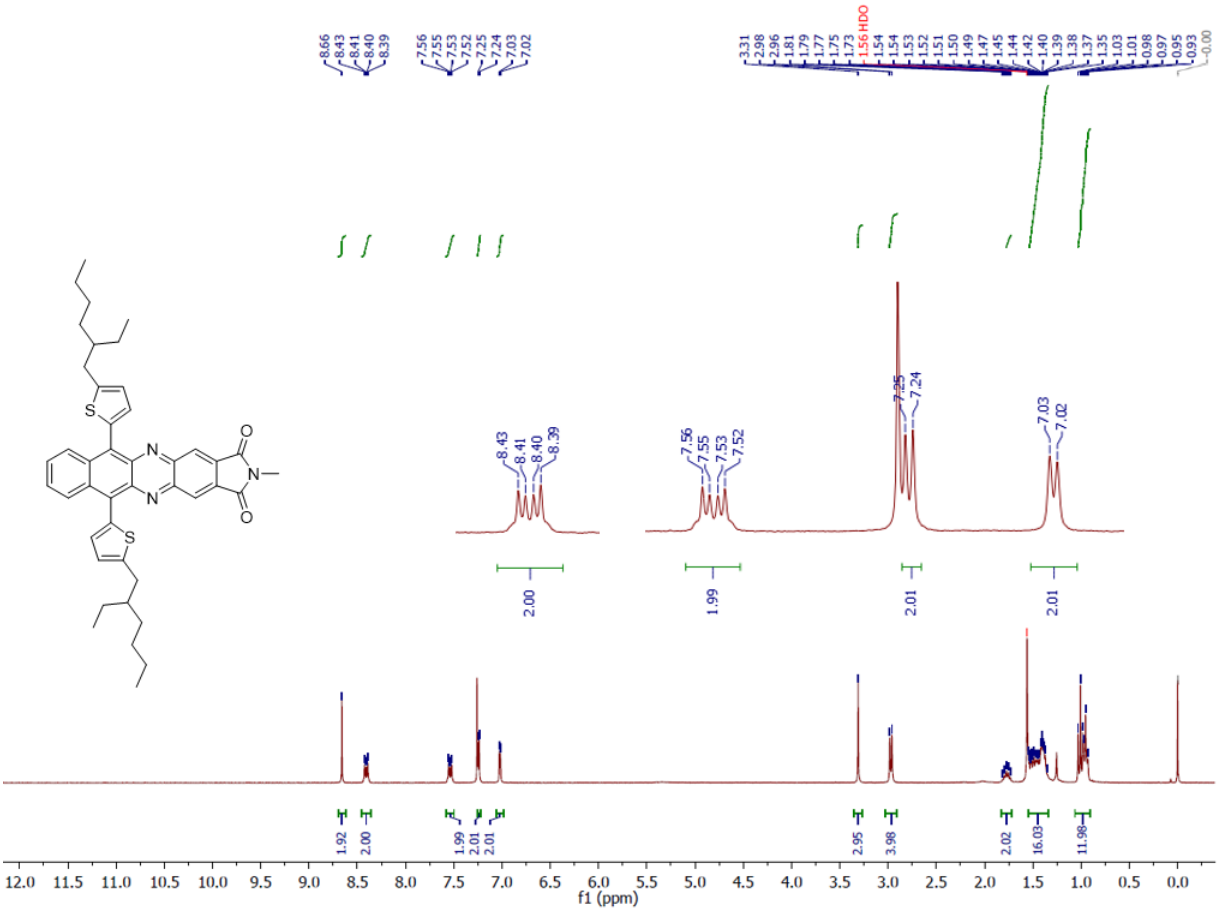


**Figure 6.3.7** $^{1}$H NMR spectrum of **5** in $CDCl_3$.

$^{1}$H NMR (300 MHz, $CDCl_3$) δ 8.66 (s, 2H), 8.46 – 8.36 (m, 2H), 7.59 – 7.49 (m, 2H), 7.24 (d, J = 3.5 Hz, 2H), 7.02 (d, J = 3.5 Hz, 2H), 3.31 (s, 3H), 2.97 (d, J = 6.8 Hz, 4H), 1.82 – 1.72 (m, 2H), 1.55 – 1.34 (m, 16H), 1.01 (t, J = 7.4 Hz, 6H), 0.95 (t, J = 7.2 Hz, 6H).

The single peak at 8.66 ppm belongs to the benzene next to the imide units. The two multiplets are characteristic of aromatic protons of naphthalene units. The doublets at 7.54 and 7.24 ppm correspond to the two protons of thiophene. The single peak at 3.31 ppm indicates the methyl group of the imide unit. The two methyl groups on the $C_8$ side chain show two triplets at 1.01 and 0.95 ppm. The peak area matches with the total number of H atoms in **5**. The result is in good accordance with the predicted spectrum.

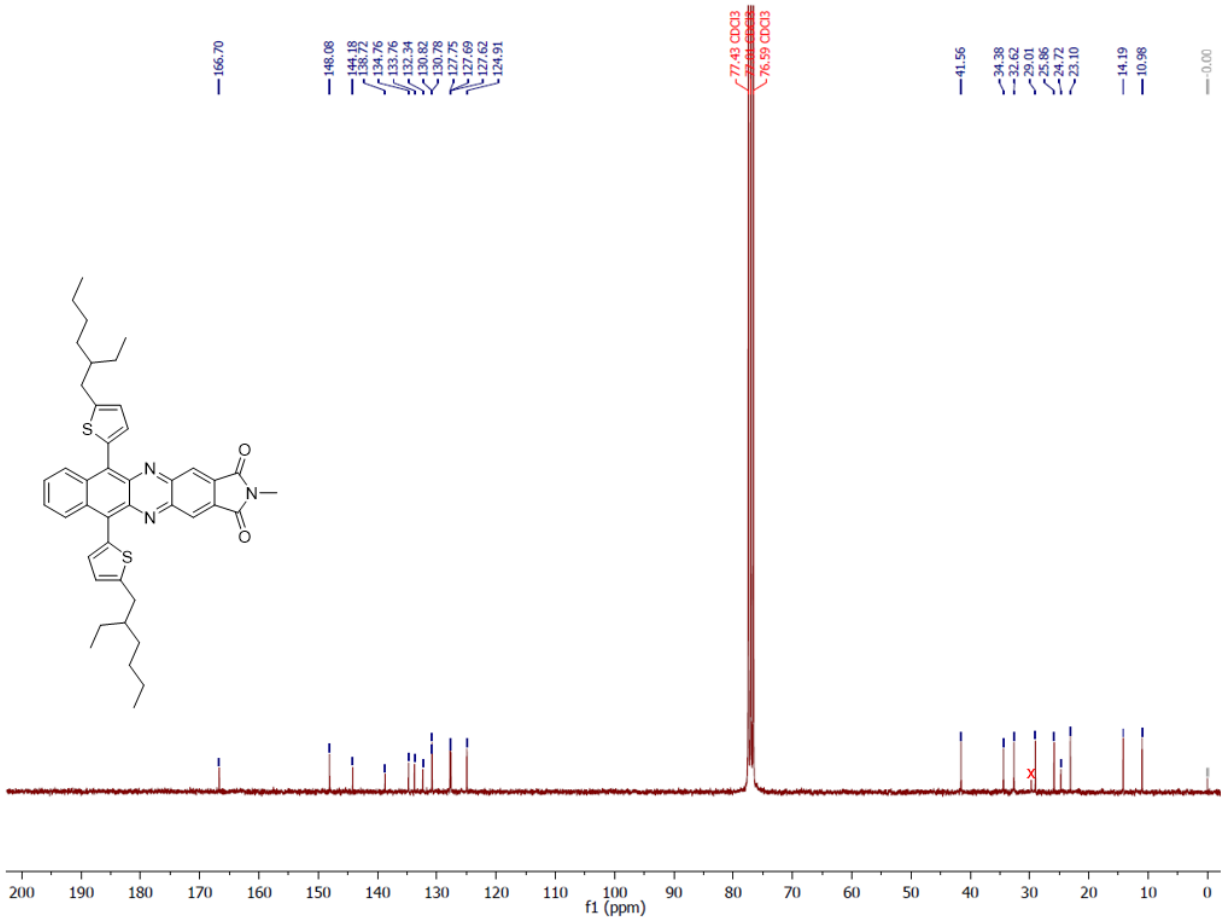


**Figure 6.3.8** $^{13}$C NMR spectrum of **5** in $CDCl_3$.

$^{13}$C NMR (75 MHz, $CDCl_3$) δ 166.70, 148.08, 144.18, 138.72, 134.76, 133.76, 132.34, 130.82, 130.78, 127.75, 127.69, 127.62, 124.91, 41.56, 34.38, 32.62, 29.01, 25.86, 24.72, 23.10, 14.19, 10.98.

X at 29.7 ppm denotes the solvent residue. The 8 peaks below 40 ppm belongs to $C_8$ alkyl chain. The peak at 41.56 ppm corresponds to methyl carbon of imide unit. The peak at 166.70 ppm indicate the carbonyl carbon of imide. There are 22 peaks in the spectrum, which represents the 22 kinds of carbon atoms in **5**. The result is in good accordance with the predicted spectrum.

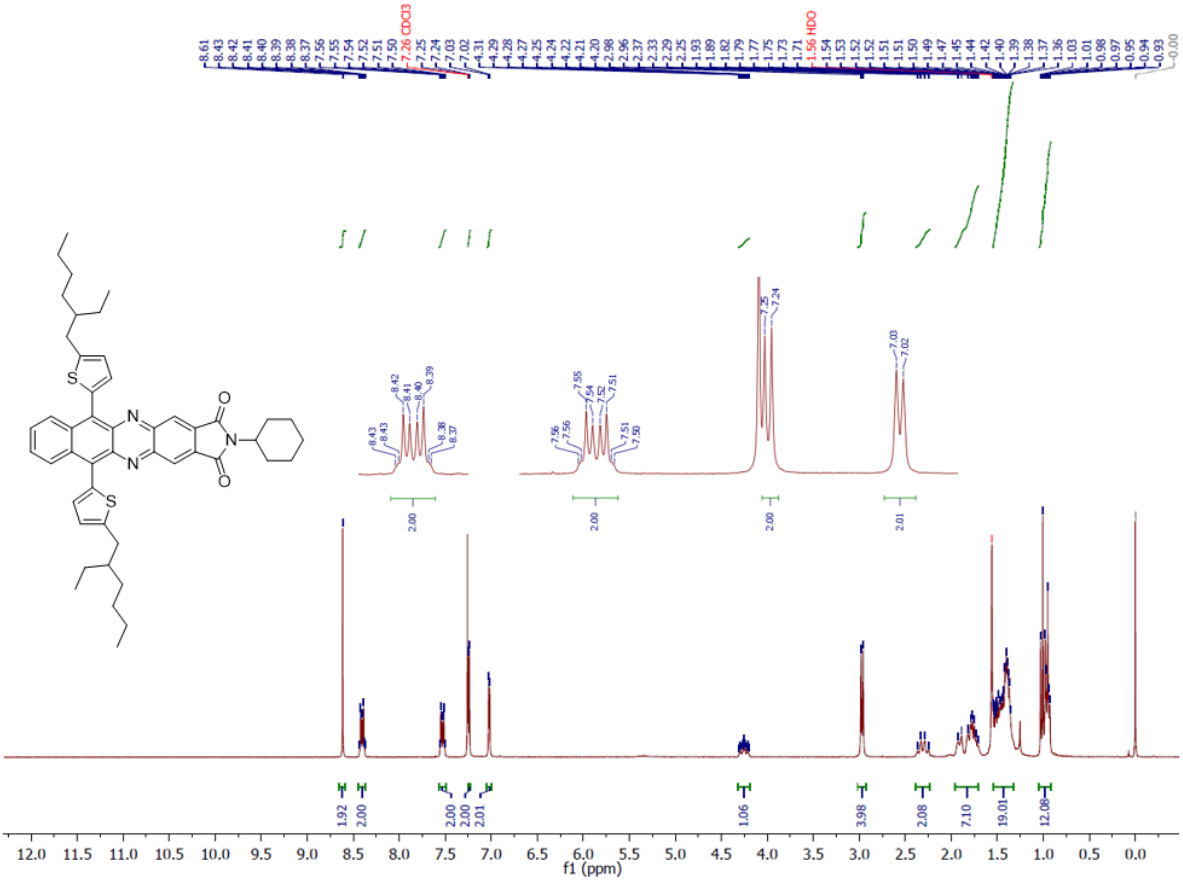


**Figure 6.3.9** $^{1}$H NMR spectrum of **6** in $CDCl_3$.

$^{1}$H NMR (300 MHz, $CDCl_3$) δ 8.61 (s, 2H), 8.44 – 8.37 (m, 2H), 7.57 – 7.49 (m, 2H), 7.24 (d, J = 3.5 Hz, 2H), 7.02 (d, J = 3.5 Hz, 2H), 4.26 (tt, J = 12.3, 3.7 Hz, 1H), 2.97 (d, J = 6.7 Hz, 4H), 2.39 – 2.23 (m, 2H), 1.96 – 1.70 (m, 7H), 1.55 – 1.33 (m, 19H), 1.06 – 0.89 (m, 12H).

The triple triplet at 4.26 ppm correspond to the hexyl proton which couples with two methylene groups. This is a good indication of the presence of hexyl group. The peak area matches with the total number of H atoms in **6**. The result is in good accordance with the predicted spectrum.

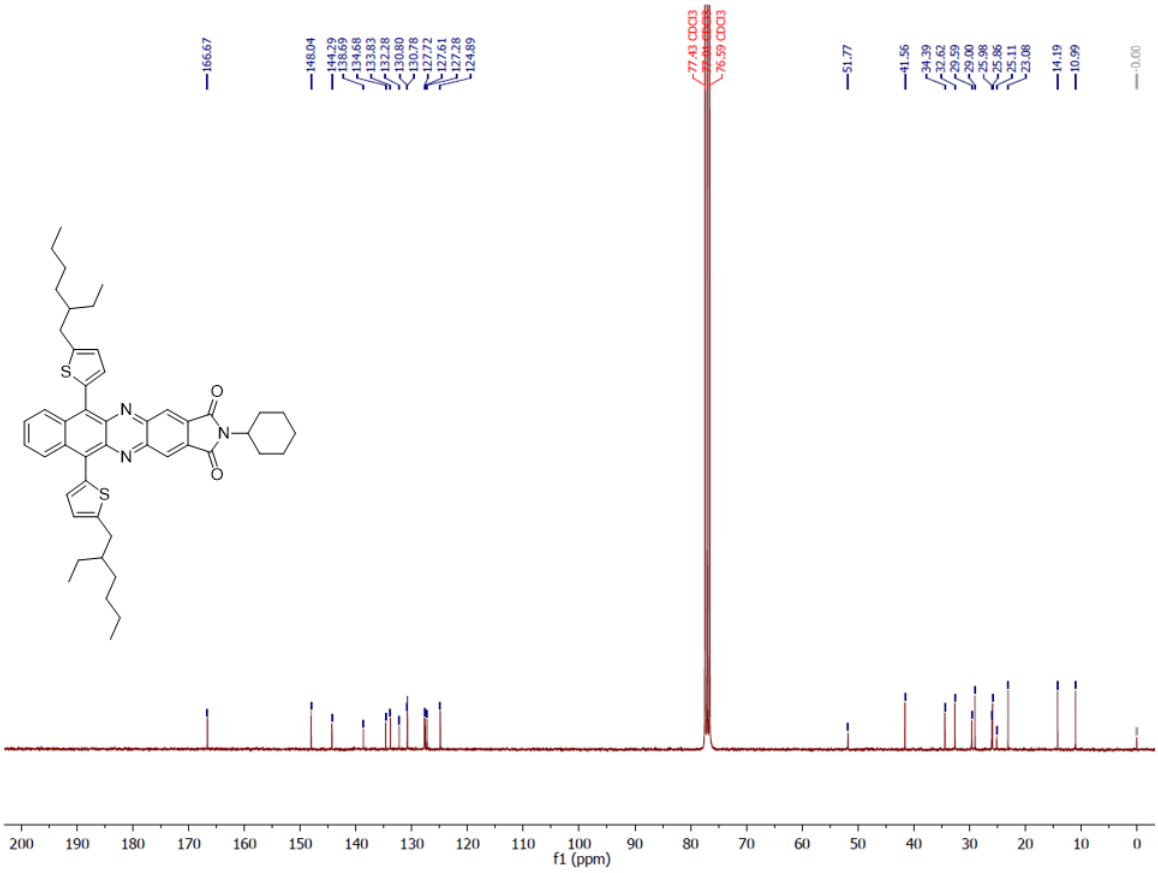


**Figure 6.3.10** $^{13}$C NMR spectrum of **6** in $CDCl_3$.

$^{13}$C NMR (75 MHz, $CDCl_3$) δ 166.67, 148.04, 144.29, 138.69, 134.68, 133.83, 132.28, 130.80, 130.78, 127.72, 127.61, 127.28, 124.89, 51.77, 41.56, 34.39, 32.62, 29.59, 29.00, 25.98, 25.86, 25.11, 23.08, 14.19, 10.99.

There are 12 peaks at upfield which consist of 4 hexyl peaks and 8 $C_8$ side chain peaks. Overall, there are 25 peaks in the spectrum, which represents the 25 kinds of carbon atoms in **6**. The result is in good accordance with the predicted spectrum.

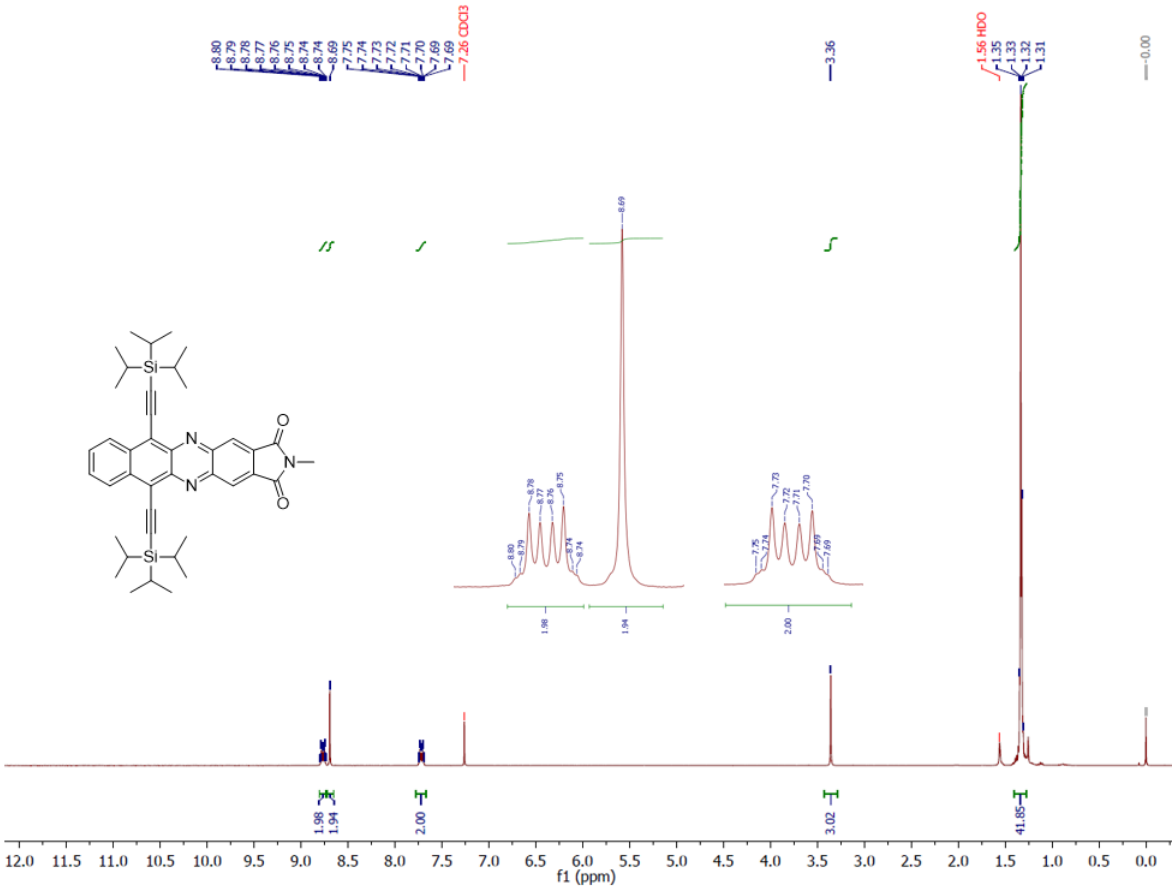


**Figure 6.3.11** $^{1}$H NMR spectrum of **7** in $CDCl_3$.

$^{1}$H NMR (300 MHz, $CDCl_3$) δ 8.80 – 8.73 (m, 2H), 8.69 (s, 2H), 7.77 – 7.67 (m, 2H), 3.36 (s, 3H), 1.33 (d, J = 3.5 Hz, 42H).

The replacement of electron-donating thiophene side chains with slightly electron-withdrawing TIPS groups results in downfield shift. The peak area matches with the total number of H atoms in **7**. The result is in good accordance with the predicted spectrum.

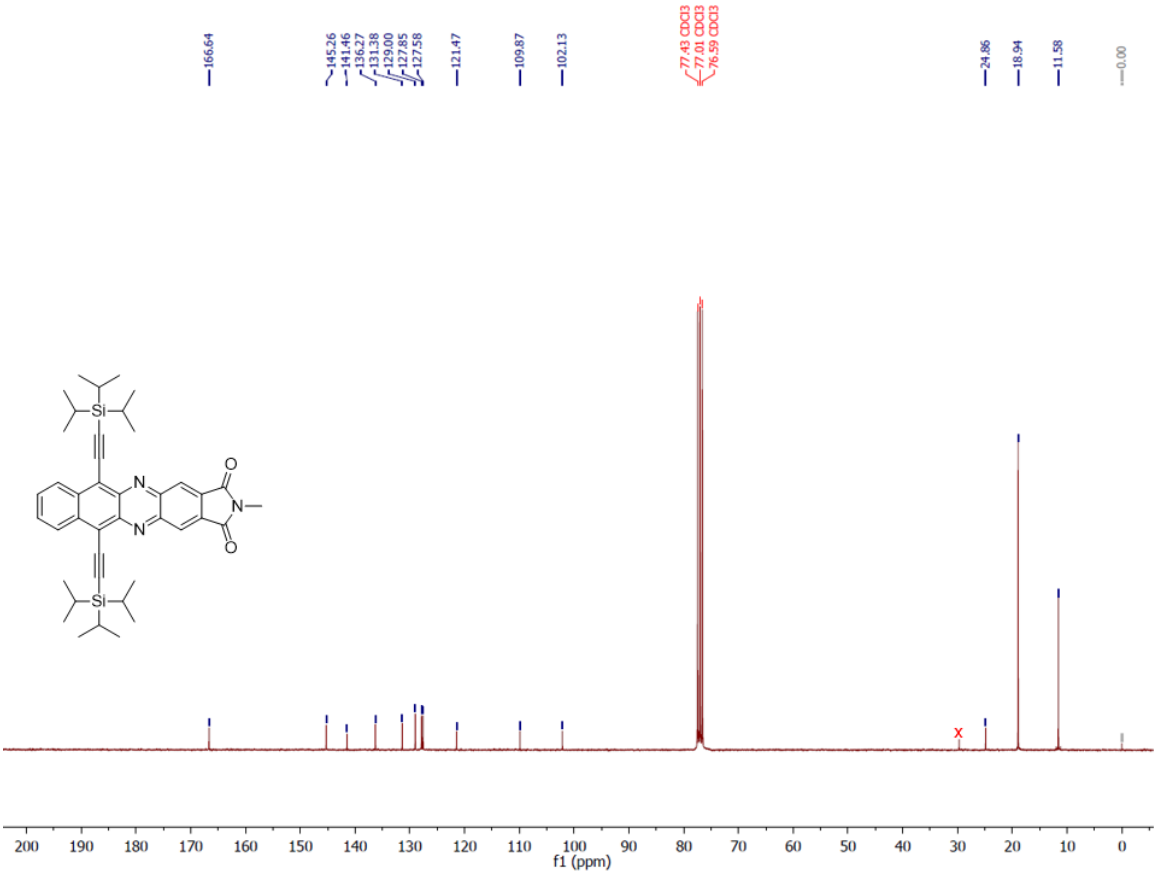


**Figure 6.3.12** $^{13}$C NMR spectrum of **7** in $CDCl_3$.

$^{13}$C NMR (75 MHz, $CDCl_3$) δ 166.64, 145.26, 141.46, 136.27, 131.38, 129.00, 127.85, 127.58, 121.47, 109.87, 102.13, 24.86, 18.94, 11.58.

X at 29.7 ppm denotes the solvent residue. There are 14 peaks in the spectrum, which represents the 14 kinds of carbon atoms in **7**. The result is in good accordance with the predicted spectrum.

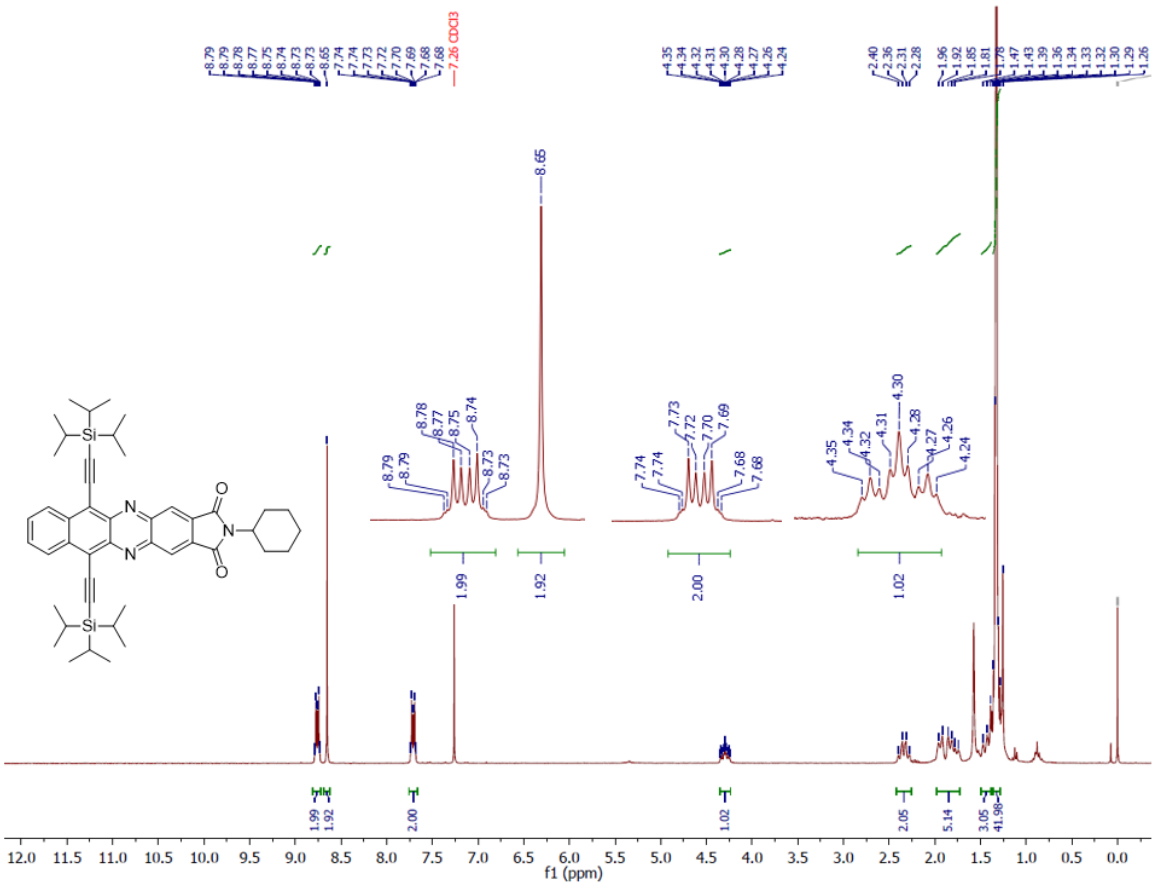


**Figure 6.3.13** $^{1}$H NMR spectrum of **8** in $CDCl_3$.

$^{1}$H NMR (300 MHz, $CDCl_3$) δ 8.81 – 8.72 (m, 2H), 8.65 (s, 2H), 7.76 – 7.67 (m, 2H), 4.30 (tt, J = 12.3, 3.6 Hz, 1H), 2.42 – 2.26 (m, 2H), 1.98 – 1.72 (m, 5H), 1.49 – 1.38 (m, 3H), 1.36 – 1.28 (m, 42H).

The peak area matches with the total number of H atoms in **8**. The result is in good accordance with the predicted spectrum.

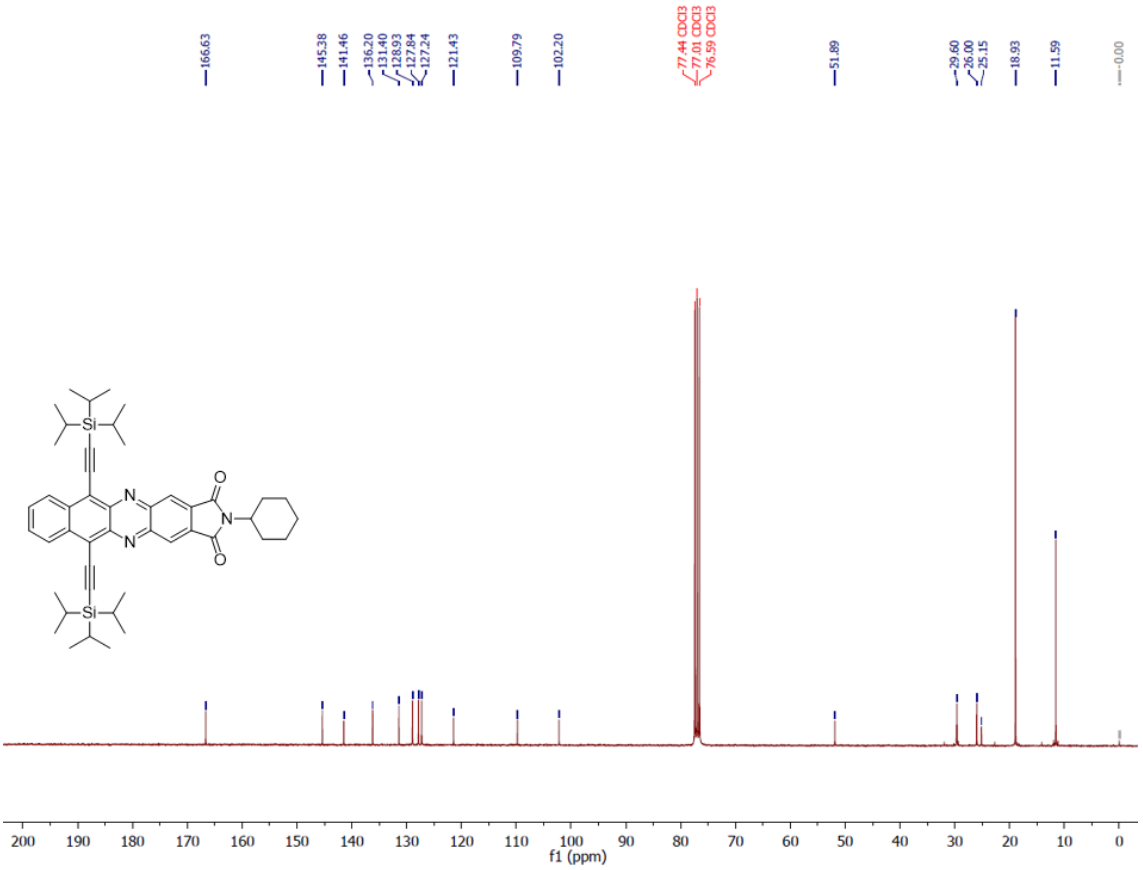


**Figure 6.3.14** $^{13}$C NMR spectrum of **8** in $CDCl_3$.

$^{13}$C NMR (75 MHz, $CDCl_3$) δ 166.63, 145.38, 141.46, 136.20, 131.40, 128.93, 127.84, 127.24, 121.43, 109.79, 102.20, 51.89, 29.60, 26.00, 25.15, 18.93, 11.59.

There are 17 peaks in the spectrum, which represents the 17 kinds of carbon atoms in **8**. The result is in good accordance with the predicted spectrum.

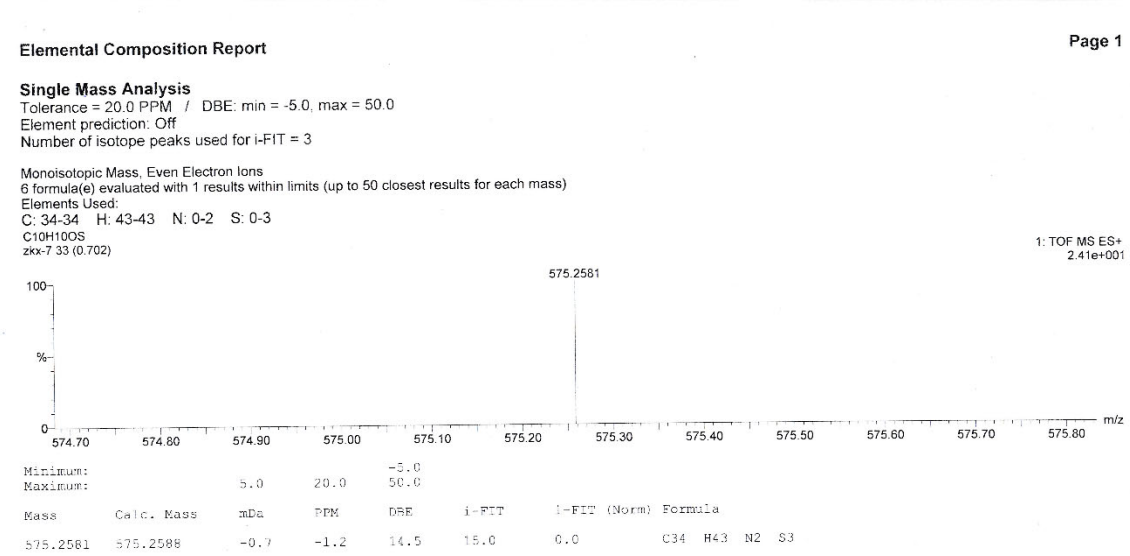


**Figure 6.3.15** HRMS spectrum of **2**.

HRMS, calcd for $C_{34}H_{43}N_2S_3$, 575.2588; found, 575.2581. The result is in good accordance with the exact mass of **2**.

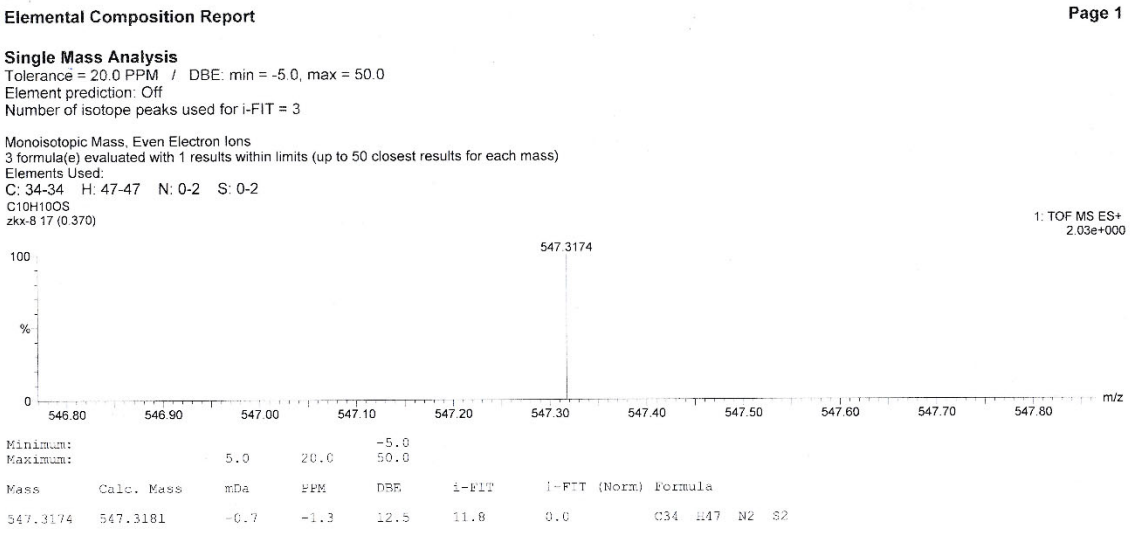


**Figure 6.3.16** HRMS spectrum of **3a**.

HRMS, calcd for $C_{34}H_{47}N_2S_2$, 547.3181; found, 547.3174. The result is in good accordance with the exact mass of **3**.

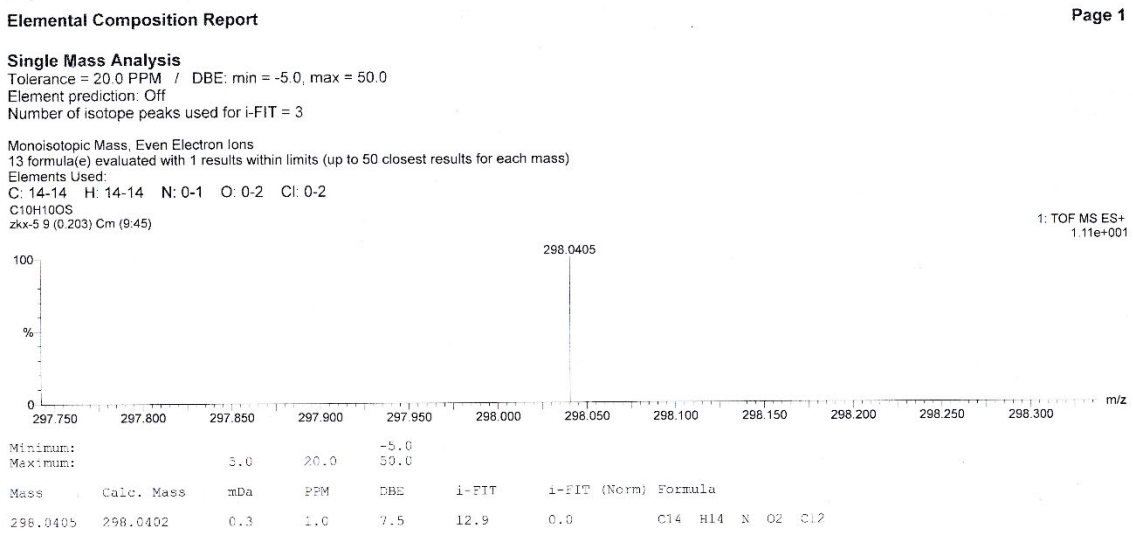


**Figure 6.3.17** HRMS spectrum of **4b**.

HRMS, calcd for $C_{14}H_{14}NO_2Cl_2$, 298.0402; found, 298.0405. The result is in good accordance with the exact mass of **4b**.

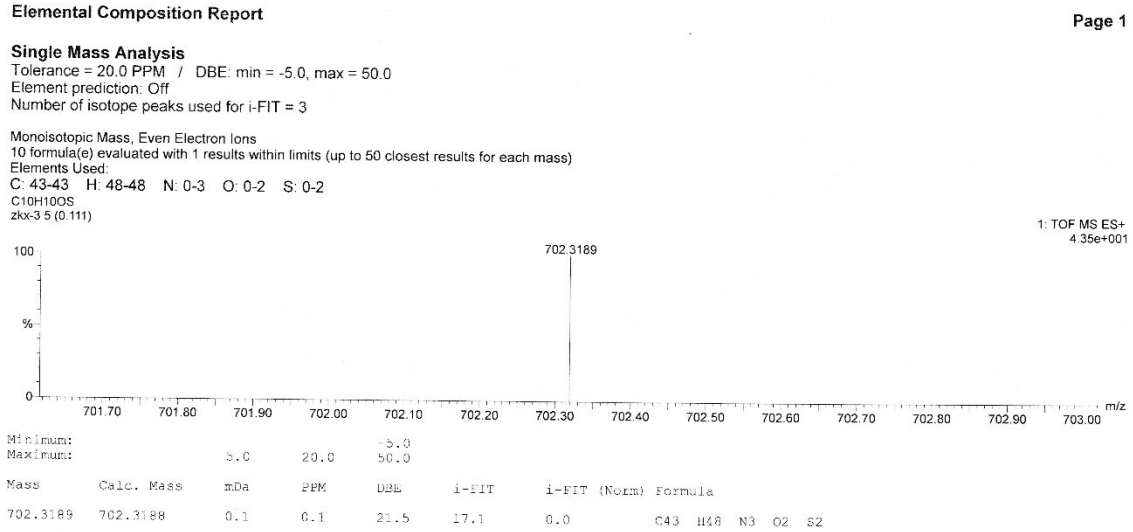


**Figure 6.3.18** HRMS spectrum of **5**.

HRMS, calcd for $C_{43}H_{48}N_3O_2S_2$, 702.3188; found, 702.3189. The result is in good accordance with the exact mass of **5**.

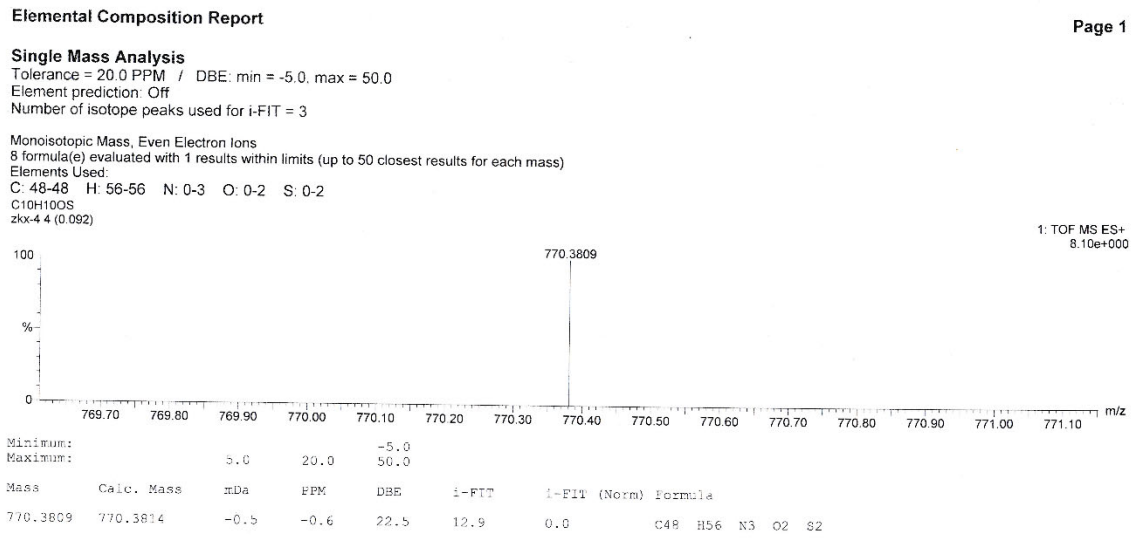


**Figure 6.3.19** HRMS spectrum of **6**.

HRMS, calcd for $C_{48}H_{56}N_3O_2S_2$, 770.3814; found, 770.3809. The result is in good accordance with the exact mass of **6**.

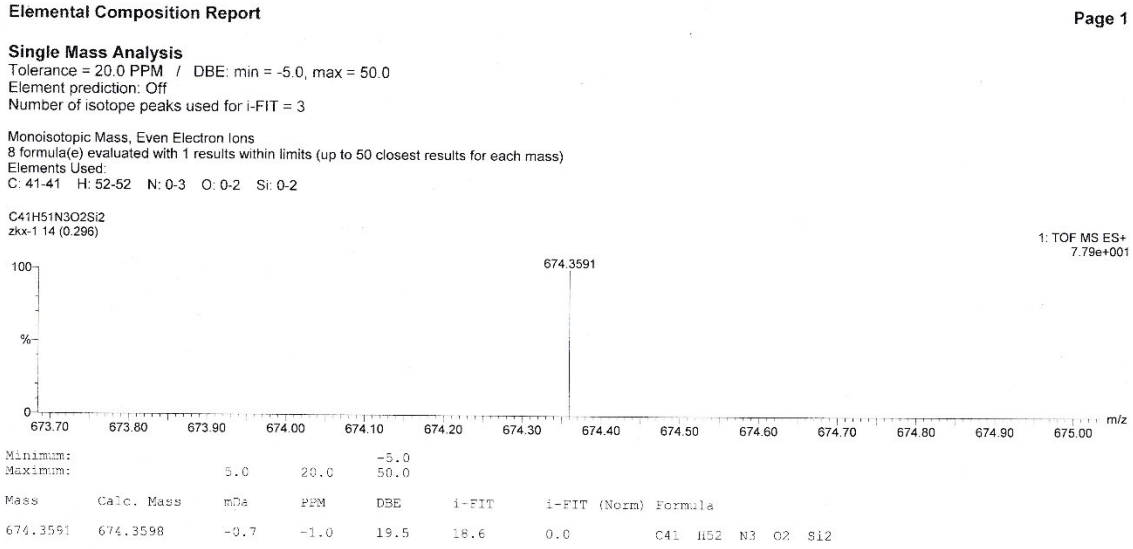


**Figure 6.3.20** HRMS spectrum of **7**.

HRMS, calcd for $C_{41}H_{52}N_3O_2Si_2$, 674.3598; found, 674.3591. The result is in good accordance with the exact mass of **7**.

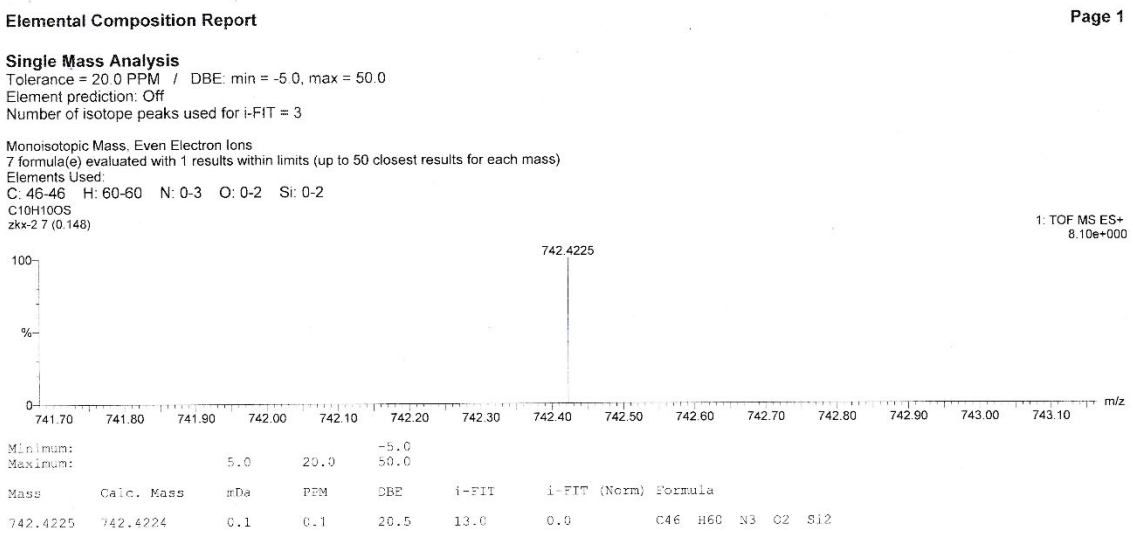


**Figure 6.3.21** HRMS spectrum of **8**.

HRMS, calcd for $C_{41}H_{52}N_3O_2Si_2$, 742.4224; found, 742.4225. The result is in good accordance with the exact mass of **8**.

### 6.3.2 Optical and electronic properties

The normalized absorption spectra of **6**, **8** and **9** in DCM are shown in Figure 6.3.20. $\lambda_{onset}$ of TIPS substituted tetracene imide **8** shows a significant redshift compared with **9**, which results in the narrower optical band gap of **8**. The difference between **6** and **9** in $\lambda_{onset}$ is even larger reaching 130 nm. Both **6** and **8** possess considerably redshifted $\lambda_{max}$ compared to **9**, which indicates size-dependent redshift in the absorption. The minute difference in $\lambda_{max}$ of **6** and **8**, on the other hand, is in good agreement with their identical conjugated backbone. Although **6** and **8** possess the same tetracene backbone, their photoluminescence properties are drastically different. **8** and **9** have strong red emission whereas **6** is non-emissive. The quenched fluorescence of **6** is caused by the intramolecular charge transfer from the thiophene unit to the pyrazine unit.

The optical and electronic properties of **5 - 9** are summarized in Table 6.3.1 and Table 6.3.2. As expected, the incorporation of imide segment to the diazatetracene backbone lead to a deeper LUMO (0.25 ev decrease for **8** and 0.19 ev decrease for **6**). The LUMO of **6** is

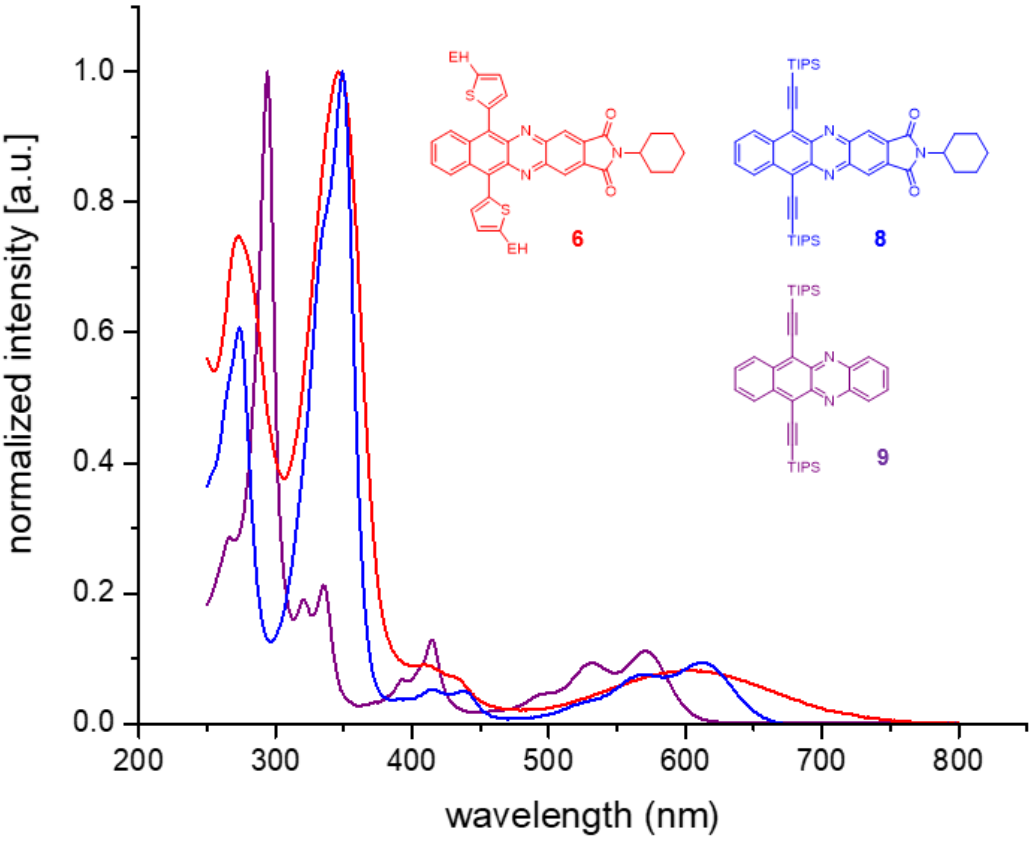


**Figure 6.3.22** Normalized absorption spectra of **6** and **8** in dichloromethane.

slightly shallower than that of **8** (0.6 ev), which is probably due to the attachment of electron-donating thiophene side chains to **6**.

**Table 6.3.1** Optical properties of compounds **5** - **9**.

| Compound | $\lambda_{max,\ abs.}$ [nm] | $\lambda_{onset}$ [nm] | $\lambda_{max,\ ems.}$ [nm] |
|---|---|---|---|
| **5** | 604 | 731 | --- |
| **6** | 604 | 730 | --- |
| **7** | 613 | 656 | 664 |
| **8** | 612 | 655 | 665 |
| **9** | 571 | 630 | 610 |

**Table 6.3.2** Electronic properties of compounds **5** - **9**.

| Compound | LUMO [ev] [a]meas./[b]calcd | HOMO [ev] [c]meas./[b]calcd | gap [ev] [d]meas./[b]calcd |
|---|---|---|---|
| **5** | -3.66/-3.12 | -5.36/-5.34 | 1.70/2.23 |
| **6** | -3.65/-3.09 | -5.34/-5.32 | 1.70/2.23 |
| **7** | -3.71/-3.37 | -5.60/-5.53 | 1.89/2.16 |
| **8** | -3.71/-3.35 | -5.60/-5.51 | 1.89/2.16 |
| **9** | -3.46/-3.29 | -5.67/-5.58 | 2.06/2.29 |

[a] $LUMO_{meas}$= - ($E_{red(onset)}$ + 4.8) (eV);

[b] DFT calculations (B3LYP/6-31G*) using Gaussian 09;

[c] $E_{HOMO}$=$E_{LUMO(CV)}$ - $E_{gap(opt)}$ (eV);

[d] $gap_{meas}$ was calculated from 1240nm/$\lambda_{onset}$.

Data for **9** is taken from reference [4a].

### 6.3.3 Single crystal X-ray structures

The crystals suitable for X-ray analysis were grown by slow diffusion of isopropanol into the chlorobenzene solutions of **5 – 8**. In the crystal of **7**, molecules form pairs through π–π stacking with a distance of 3.51 Å. The pairs are further held together by carbonyl–π interaction with a shorter distance of 3.38 Å, which forms a brick-wall motif. By changing the methyl group into cyclohexyl group, the crystal of **8** takes on a different packing motif. Due to the bulkiness of both TIPS group and cyclohexyl group, **8** is more twisted in the solid state and no π–π stacking is observed. Instead, the carbonyl–π interaction and CH-π interaction dominate the crystal of **8** with distances of 3.42 Å and 2.76 Å respectively. In order to overcome the steric hindrance, **8** shows a slipped one-dimensional packing. These stacks are so much offset that no brick-wall motif could form. For **6**, one-dimensional stacking is observed with antiparallel cofacial π–π stacking distances of 3.43 Å and 3.44 Å. Because of the less steric hindrance imposed by the thiophene side chains, there is a decrease in π–π stacking distance compared to **8**. From the crystal structures of **6** – **8**, it could be concluded that diazatetracene imides have strong tendency to form pairs in solid

state and adopt antiparallel cofacial packing mode. However, in the case of **8**, the steric hindrance is so prominent that the antiparallel cofacial packing is interrupted.

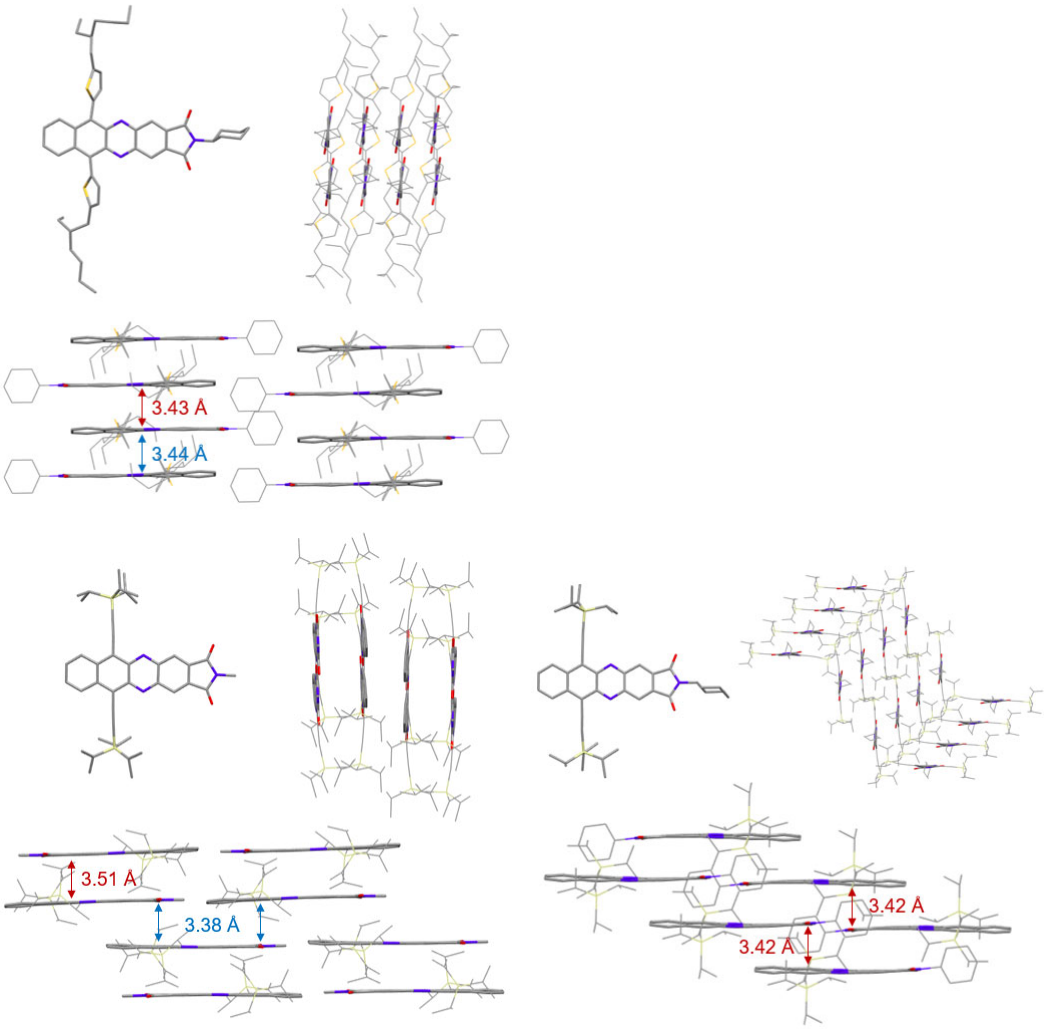


**Figure 6.3.23** Crystal structures and packing of **5** (top left), **7** (bottom left) and **8 (**bottom right).

## 6.4 Conclusion

In summary, a highly active palladium catalyst was selected to synthesize a series of novel imide-fused diazatetracenes. Its optical and electronic properties were investigated. The introduction of imide moiety successfully lowered the LUMO. Obviously redshifted absorption also indicates the extension of π-backbone. The effect of alkyl chains on solid state structures were also discussed. Besides π–π interaction, carbonyl–π interaction is also present in the crystal structure.

**References**

[1] a) J. E. Anthony, A. Facchetti, M. Heeney, S. R. Marder, X. Zhan, *Adv. Mater.* **2010**, *22*, 3876-3892; b) Q. Miao, *Adv. Mater.* **2014**, *26*, 5541-5549; c) J. Li, Q. Zhang, *ACS Appl. Mater. Interfaces* **2015**, *7*, 28049-28062.

[2] Q. Miao, T. Q. Nguyen, T. Someya, G. B. Blanchet, C. Nuckolls, *J. Am. Chem. Soc.* **2003**, *125*, 10284-10287.

[3] a) S. Miao, A. L. Appleton, N. Berger, S. Barlow, S. R. Marder, K. I. Hardcastle, U. H. F. Bunz, *Chem. Eur. J.* **2009**, *15*, 4990-4993; b) Z. Liang, Q. Tang, J. Xu, Q. Miao, *Adv. Mater.* **2011**, *23*, 1535-1539; c) O. Tverskoy, F. Rominger, A. Peters, H.-J. Himmel, U. H. F. Bunz, *Angew. Chem. Int. Ed.* **2011**, *50*, 3557-3560; d) G. Li, Y. C. Wu, J. K. Gao, C. Y. Wang, J. B. Li, H. C. Zhang, Y. Zhao, Y. L. Zhao, Q. C. Zhang, *J. Am. Chem. Soc.* **2012**, *134*, 20298-20301; e) J. U. Engelhart, B. D. Lindner, O. Tverskoy, F. Rominger, U. H. F. Bunz, *J. Org. Chem.* **2013**, *78*, 10832-10839; f) P. Biegger, O. Tverskoy, F. Rominger, U. H. F. Bunz, *Chem. Eur. J.* **2016**, *22*, 16315-16322; g) M. Chu, J.-X. Fan, S. Yang, D. Liu, C. F. Ng, H. Dong, A.-M. Ren, Q. Miao, *Adv. Mater.* **2018**, *30*, 1803467.

[4] a) B. D. Lindner, J. U. Engelhart, M. Märken, O. Tverskoy, A. L. Appleton, F. Rominger, K. I. Hardcastle, M. Enders, U. H. F. Bunz, *Chem. Eur. J.* **2012**, *18*, 4627-4633; b) X. Xu, B. Shan, S. Kalytchuk, M. Xie, S. Yang, D. Liu, S. V. Kershaw, Q. Miao, *Chem. Commun.* **2014**, *50*, 12828-12831; c) J. Li, F. Yan, J. Gao, P. Li, W.-W. Xiong, Y. Zhao, X. W. Sun, Q. Zhang, *Dyes and Pigments* **2015**, *112*, 93-98; d) S. Yang, B. Shan, X. Xu, Q. Miao, *Chem. Eur. J.* **2016**, *22*, 6637-6642; e) M. Müller, S. S. Beglaryan, S. Koser, S. Hahn, O. Tverskoy, F. Rominger, U. H. F. Bunz, *Chem. Eur. J.* **2017**, *23*, 7066-7073.

[5] a) H. Y. Chen, I. Chao, *Chemphyschem* **2006**, *7*, 2003-2007; b) M. Winkler, K. N. Houk, *J. Am. Chem. Soc.* **2007**, *129*, 1805-1815.

[6] Z. Wang, C. Kim, A. Facchetti, T. J. Marks, *J. Am. Chem. Soc.* **2007**, *129*, 13362-13363.

[7] a) P. Ruiz-Castillo, S. L. Buchwald, *Chem. Rev.* **2016**, *116*, 12564-12649; b) U. H. Bunz, J. U. Engelhart, *Chem. Eur. J.* **2016**, *22*, 4680-4689.

# Chapter 7

# Discussion and Future Work

*This chapter includes the unsuccessful attempts and implications of the previous three chapters. The extent to which the hypothesis was proven is also discussed. After concluding the thesis, new strategies towards unconventional azaarenes with nonlinear backbones or various functional groups could be obtained, which provides the opportunities for the synthesis of a wide range of novel azaarenes.*

## 7.1 General Discussion

### 7.1.1 Thiadiazole-fused star-shaped azaarene

Most star-shaped azaarenes are synthesized via two synthetic routes. First one is the condensation reaction of hexaketocyclohexane with various *o*-diamine compounds. The second one involves similar threefold condensation reaction between hexaaminobenzene and different kinds of *o*-diketones. However, the reactions between *o*-diamine and hexaketocyclohexane do not always furnish threefold-condensed star-shaped products. Instead, linear azaacenes with a central quinone segment could be obtained through twofold condensations.

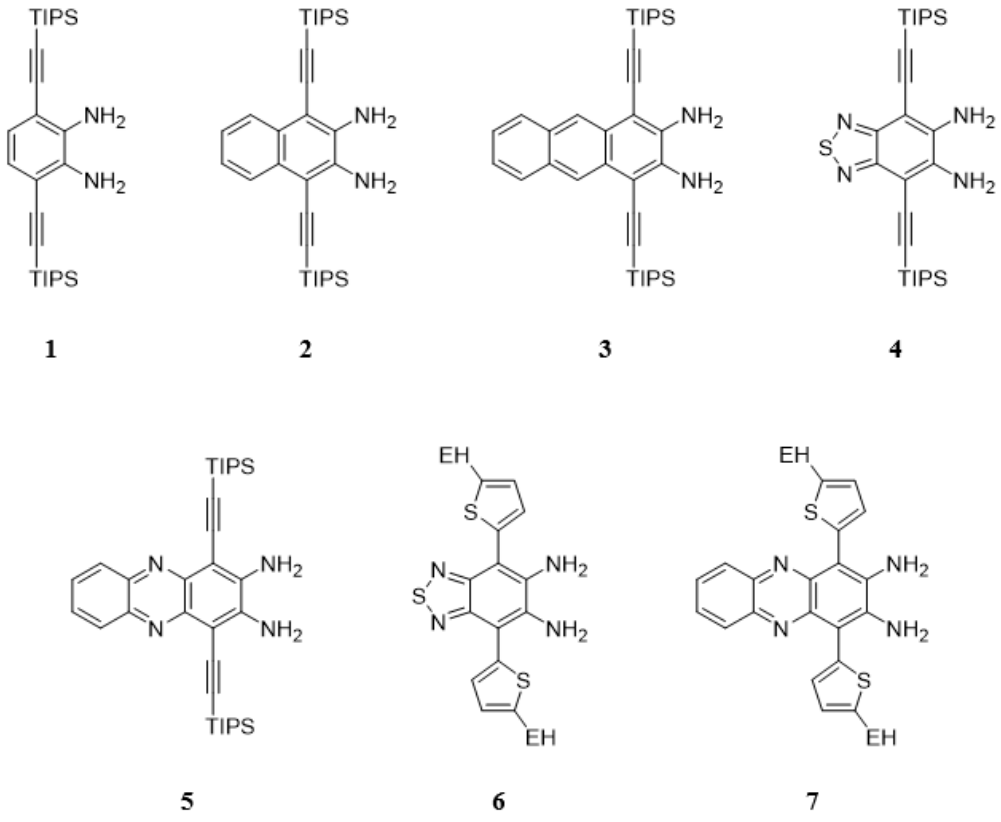


**Figure 7.1** Various alkylated *o*-diamines which have been used to react with hexaketocyclohexane.

Figure 7.1 shows various alkylated *o*-diamines which are used to react with hexaketocyclohexane.[1] Before the synthesis of HATNT, only **1** and **2** could give the desired star-shaped azaarenes, which is probably caused by the steric hindrance of alkyl chains. In order to synthesize the thiadiazole fused star-shaped azaarenes, TIPS groups were replaced with more flexible thiophene side chains. HATNT was then synthesized in 20 % yield.

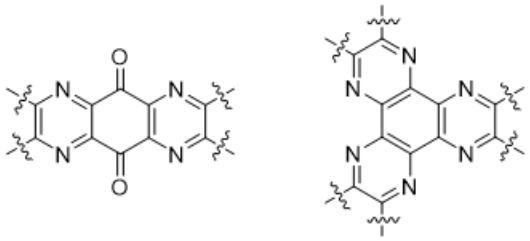

**Figure 7.2** Linear-fused quinone-containing twofold condensation product (left) and star-shaped threefold condensation product (right).

Following the successful synthesis of HATNT, thiophene-substituted phenazine *o*-diamine **7** was synthesized in a similar fashion to **5** and reacted with hexaketocyclohexane. The synthetic route is depicted in Figure 7.3. Starting from Boc protected phenazine diamine **8**, Stille reaction gave **9** in moderate yield. **7** was obtained in excellent yield via deprotection with trifluoroacetic acid in DCM.

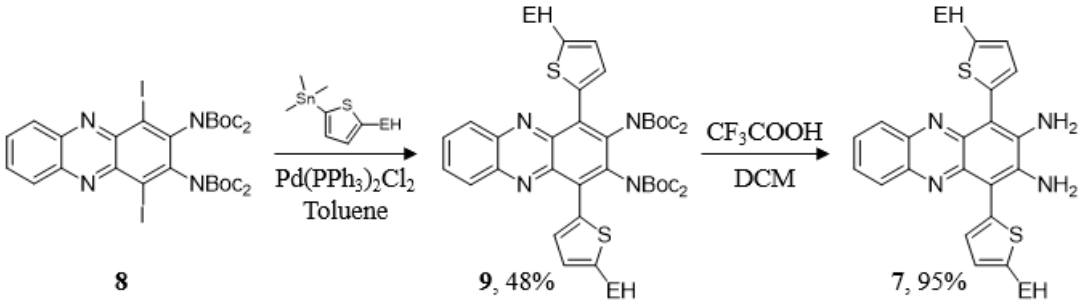


**Figure 7.3** Synthetic route towards **7**.

Much to our dismay, although flexible side chains were attached, no threefold condensation product was detected. Instead, only linear-fused product was obtained. Moreover, the linear product could not be converted into the fully oxidized form by *p*-chloranil. When stronger oxidizers, such as $MnO_2$, DDQ and $PbO_2$, were used, decomposition of **10** occurred. No obvious spots could be observed. Attempts to grow single crystals of **11** or **12** also failed.

The partially oxidized product turned out to be unstable in solution. After a few weeks, the initially green solution became yellow. The NMR spectra of **11** and **12** should have same number of peaks and protons. In addition, NH moiety do not couple with the nearby protons in either case. The only difference that could be acquired between **11** and **12** is the chemical shift of the NH moiety. But the chemical shift is a weak evidence. Thus, the configuration of the final product could not be ascertained.

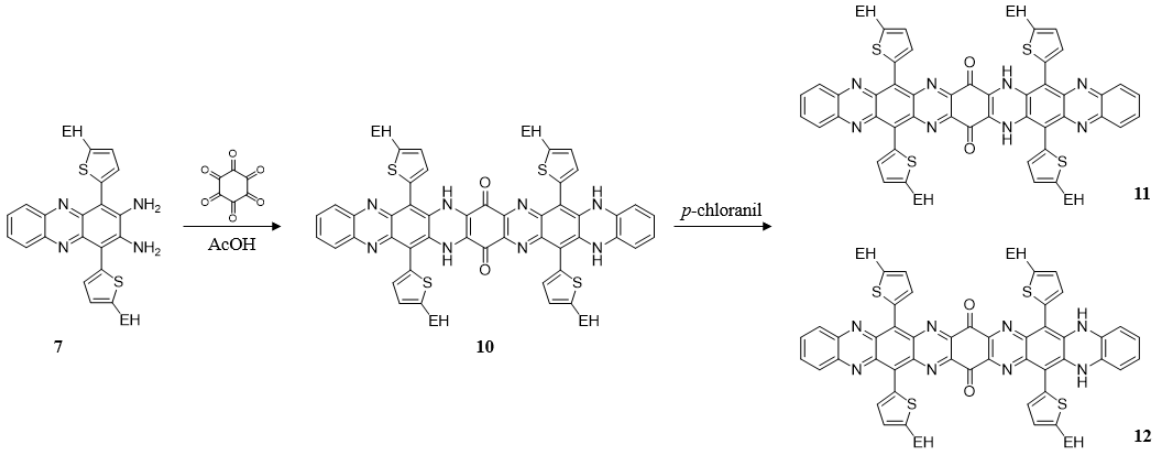


**Figure 7.4** Attempt to synthesize large star-shaped azaarenes.

Based on the successful synthesis of HATNT and unsuccessful synthesis of phenazine-branched star-shaped azaarene, it is postulated that the steric hindrance is not the only factor that governs the reaction. As the branch of the star becomes larger, the reactivity of *o*-diamine should increase accordingly in order to yield the star-shaped product since the linear-fused product is thermodynamically favored judging from the previous examples. In the case of **7**, although it has a similar steric hindrance to that of **6**, no trimer product was yielded due to the lack of increase in reactivity.

It might be difficult to further improve the reactivity of diamine **7**. Hence, it is not feasible to synthesize phenazine-branched star-shaped azaarene via direct condensation of **7** and hexaketocyclohexane. But there is another possible route. As shown in Figure 7.5, thiadiazole units of HATNT could be reduced to amino groups giving novel hexamine **13**. Further condensation of **13** and 1,2-benzoquinone yields the desired phenazine-branched star-shaped azaarenes **14**. Considering the poor stability of **11** or **12** in the presence of strong oxidizer, thiophene side chains could be replaced with phenyl side chains.

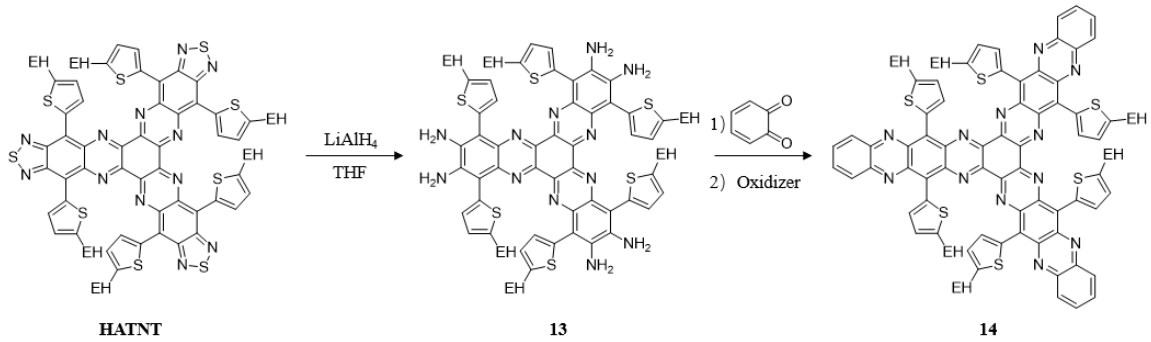


**Figure 7.5** Proposed synthetic route towards phenazine-branched star-shaped azaarenes.

The hexamine **13** could be a useful building block in the synthesis of even larger star-shaped azaarenes as well as fully conjugated COF (covalent organic framework).

To sum up, the star-shaped azaarene section, new ambipolar molecule HATNT was synthesized and showed great potential as electron transporting material in PSC. In addition, attempt to acquire larger star-shaped azaarene revealed that both steric hindrance and reactivity of *o*-diamine play important roles in the selectivity of condensation reaction.

### 7.1.2 U-shaped helical azaarenes

The lack of azaarenes which have non-linear shapes could be ascribed to the difficulty in synthesizing relevant *o*-quinones or dihalides. Star-shaped azaacenes could be acquired from commercially available hexaketocyclohexane and hexaaminobenzene. But for other non-linear azaarenes, the synthetic routes are not so straightforward. After extensive searching and reviewing of pertinent literatures, BSA (benzeneseleninic anhydride) was finally selected as oxidization reagent to obtain *o*-quinones.

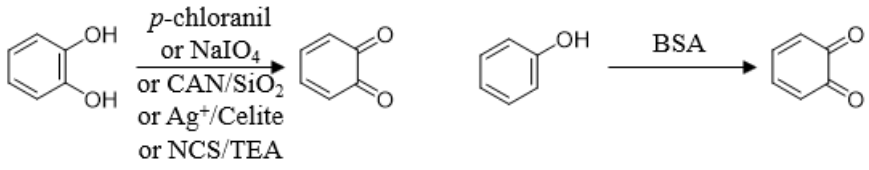


**Figure 7.6** Reported synthetic route towards *o*-quinones.

Figure 7.6 shows the reported methods of synthesizing *o*-quinones. Traditional methods require *o*-dihydroxy compounds as starting materials which are difficult to attain when the conjugated backbone is large. In contrast, monohydroxy compounds are easier to procure. Beside BSA, Fremy's salt could also be used to oxidize monohydroxy compounds.[2] However, Fremy's salt has poor selectivity towards *o*-quinones when the para position is not blocked. Apart from Fremy's salt, IBX is another candidate for oxidizing reagent.[3] It is quite useful when no electron-withdrawing moiety is attached. When electron-withdrawing groups are present, the oxidization could not proceed at all. As a result, phenols with more than one reaction site could not be fully oxidized by IBX. Therefore, BSA is deemed as the best oxidizing reagent for the synthesis of *o*-quinones.

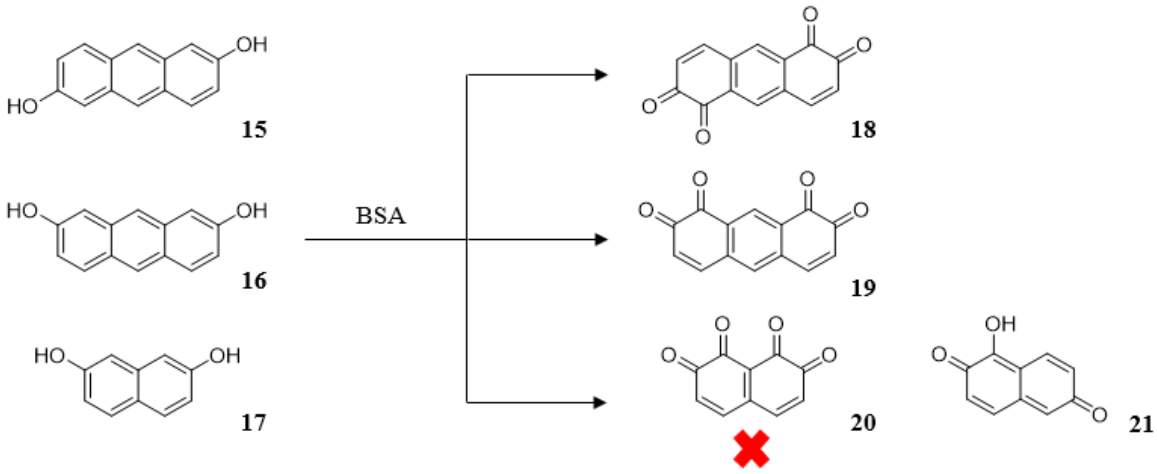


**Figure 7.7** Attempted syntheses of *o*-quinones using BSA.

As depicted in Figure 7.7, tetraketones **18** and **19** could be synthesized in good yields by reacting respective dihydroxy compounds with BSA. At first, the idea was to synthesize three groups of non-linear azaarenes centering ketones **18 - 20**. Unfortunately, **18** related Z-shaped azaarenes were reported right after my acquirement of **18**. So, **19** was then synthesized and reacted with *o*-diamines. Unlike **18**, tetraketone **19** cannot be recrystallized in 1,4-dioxane and shows worse solubility in common solvents even in THF. After the successful syntheses of U-shapes azaarenes, it was assumed that **17** could undergo the same oxidation giving naphthalene-1,2,7,8-tetraone **20**. To our surprise, **17** could not be fully oxidized to quinone form by BSA. Instead, hydroxyquinone **21** was obtained as major product. This compound has rather good solubility in common solvents such as methanol, DCM and DMSO. Although hydroxy groups in **17** do not have unoccupied para positions,

which means it is unlikely for **17** to produce *p*-quinones, the oxidation yielded **21** which is *p*-quinone but with extended conjugation through the naphthalene backbone. Due to the presence of this oxidation pathway, the target compound **20** could not be obtained from **17**. It is then proposed that blocking the 3,6 positions of **17** might inhibit the oxidation pathway.

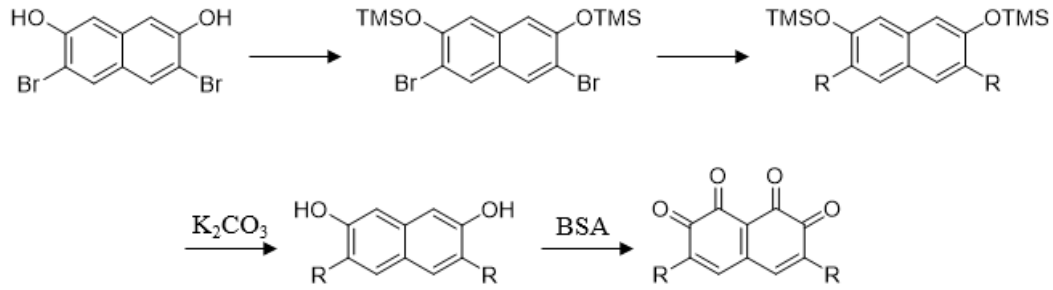


**Figure 7.8** Proposed new synthetic route towards naphthalene-1,2,7,8-tetraone using BSA.

The commercially available brominated dihydroxy naphthalene is first protected with TMS and then alkylated via Sonogashira coupling or Stille coupling. Further deprotection with potassium carbonate in methanol could afford the alkylated 2,7-dihydroxynaphthalene. After being oxidized with BSA, the desired alkylated naphthalene-1,2,7,8-tetraone could be obtained. This alkylated tetraone could react with *o*-diamines producing a new group of U-shaped azaarenes.

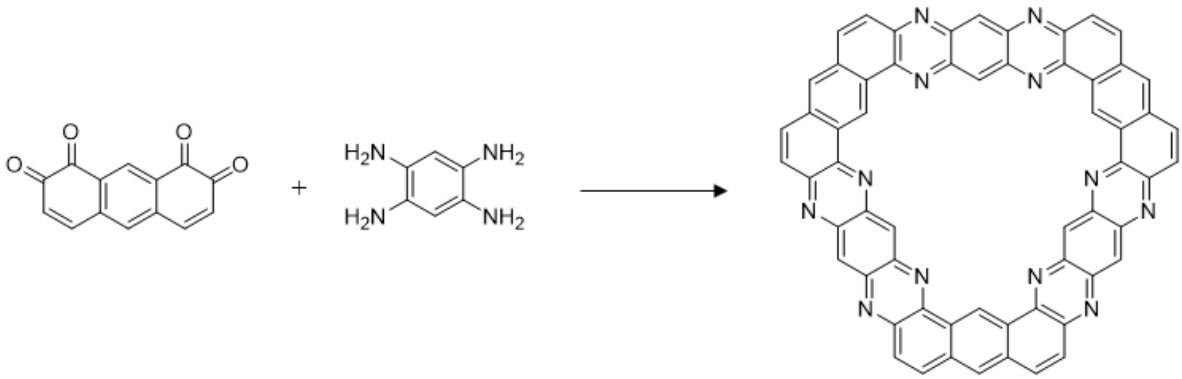


**Figure 7.9** Possible synthetic route towards large nitrogen-containing macrocycle.

In addition to the syntheses of U-shape azaacenes, anthracene-1,2,7,8-tetraone **19** is a potential building block for the synthesis of nitrogen-containing macrocycles. By reacting **19** with 1,2,4,5-tetraaminobenzene, macrocycle with twelve nitrogen atoms could be obtained (Figure 7.9). Apparently, the solubility of the proposed product should be very poor. Thus, alkylation of **19** is necessary in order to fully characterize the desired product.

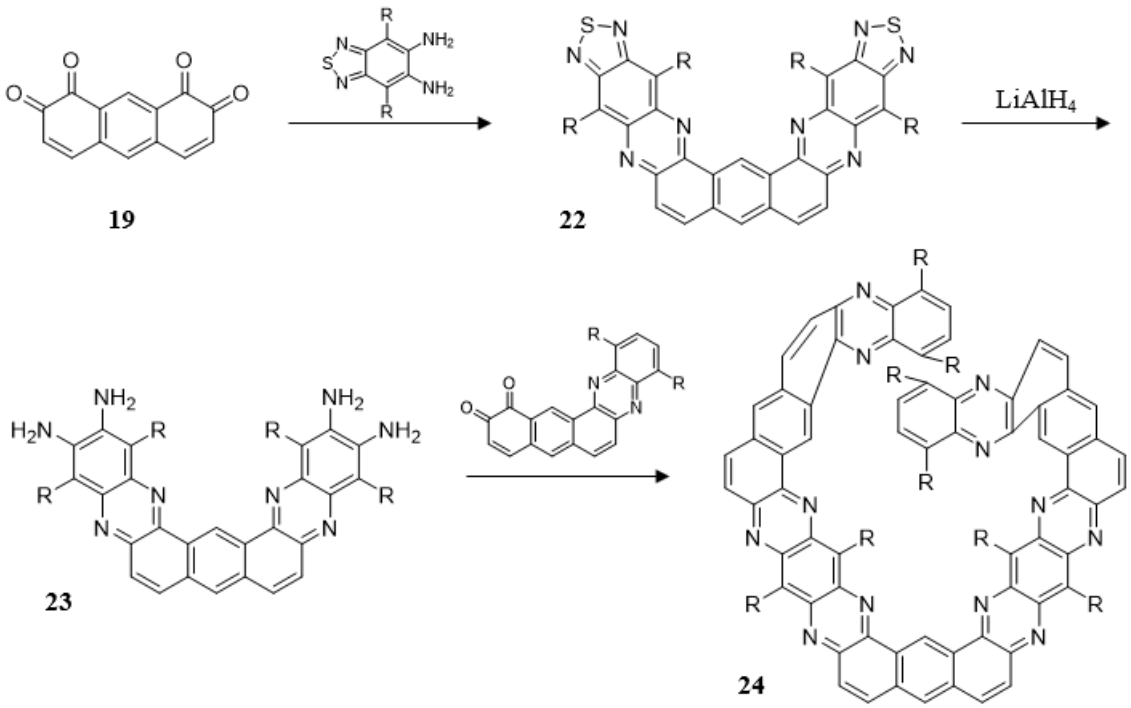


**Figure 7.10** Proposed synthetic route towards azaarene with multiple helicity.

From the U-shaped azaarenes, it is also possible to synthesize azaarenes with multiple helicity. By applying the benzothiadiazole diamine, thiadiazole-fused U-shaped azaarene **22** is acquired. Reduction by $LiAlH_4$ furnishes the tetraamine **23**. Further condensation with half-caped **19** gives the final product **24** with three helical centers. There would be isomers in the final step which could be isolated by preparative HPLC.

In conclusion, a new class of helical azaarenes were synthesized and their solid-state structures as well as electronic properties were investigated. Methods to synthesize the anthracene-1,2,7,8-tetraone **19** and its analogues were discussed. **19** also shows great potential as building block in making nitrogen-containing macrocycles and azahelicenes with multiple helicity.

### 7.1.3 Imide-fused Diazatetracene

The aim of this part is to investigate the syntheses and properties of imide-fused azaacenes. Diazatetracene is selected as the backbone where imide group would be attached. Initially, the traditional condensation reaction was considered to construct the azaacene backbone. However, it was later found that the synthetic route of this method would be lengthy and of low yield (Figure 7.11).

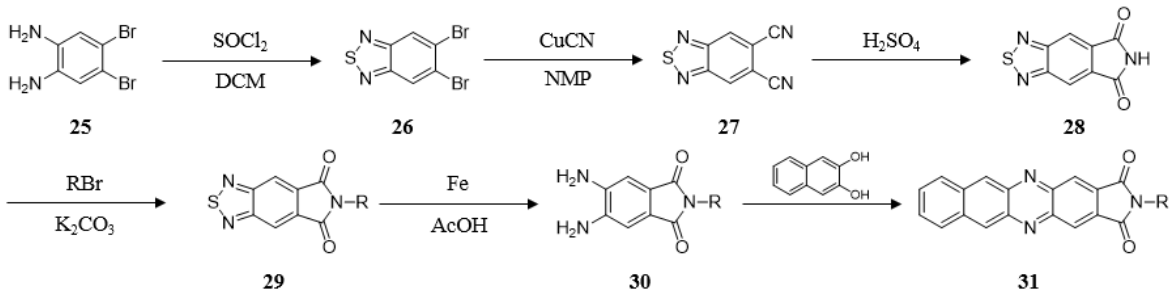


**Figure 7.11** Initially proposed synthetic route towards imide-fused diazatetracenes.

The palladium-catalyzed coupling was then chosen. As shown in Figure 7.12, the dichlorophthalimide **32** could be synthesized from commercially available dichlorophthalic anhydride in excellent yield. The coupling reactions between **31** and **32** gave **33** in good yields ranging from 65% - 81%.

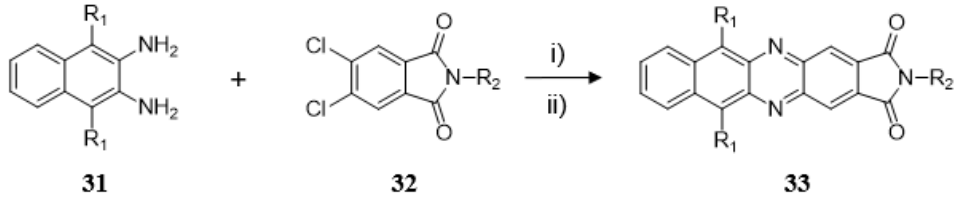


**Figure 7.12** Synthetic route towards imide-fused diazatetracenes. i) Pd Ruphos G4, $Cs_2CO_3$, toluene and *t*-BuOH; ii) Excessive $MnO_2$, DCM.

Because of the diminished reactivity of halogenated **32**, more potent catalyst was applied. *t*-BuOH was added as co-solvent in order to improve the solubility of $Cs_2CO_3$. Besides the diazatetracene backbone, tetraazatetracene backbone was also investigated. As depicted in Figure 7.13, using the same coupling condition, **36** could be obtained in yield above 90 % since the halogenated species **35** is highly reactive. Unfortunately, the oxidized **37** is unstable and very sensitive to moisture and protic solvents such as methanol and even

acetone. It is assumed that the instability of **37** is caused by the additional pyrazine ring which makes the imide moiety very electronegative and susceptible to hydrolysis.

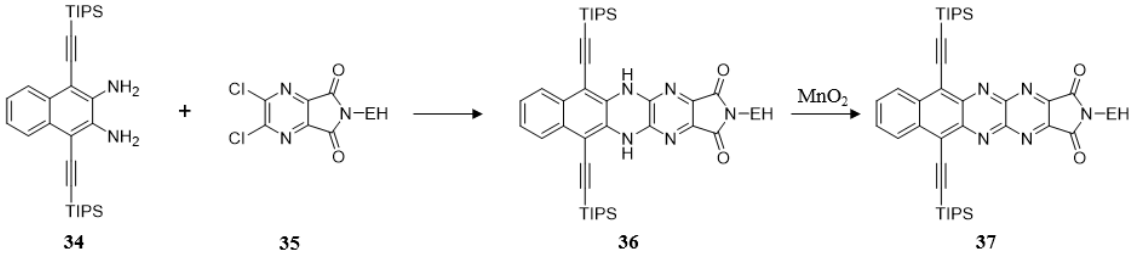


**Figure 7.13** Attempted synthesis of imide-fused tetraazatetracenes.

Although imide-fused diazatetracenes showed deeper LUMO level (-3.71 eV) than the pristine diazatetracene, the OFET devices of **33** did not show any performance at ambient condition. It is believed that when the LUMO is above -3.9 eV the electron-transporting behavior might be concealed in air.[4] Hence, it is necessary to further lower the LUMO of imide-fused diazatetracenes. There are several viable approaches. The first one is to change the side chain of imide to fluorinated species. Pei *et al.* reported that a 0.16 eV decrease in LUMO could be achieved by changing the alkyl chain of polycyclic imide from n-octyl to pentafluorophenyl.[5] Similar strategies have been widely used to synthesize NDIs and PDIs with low-lying LUMOs.[6]

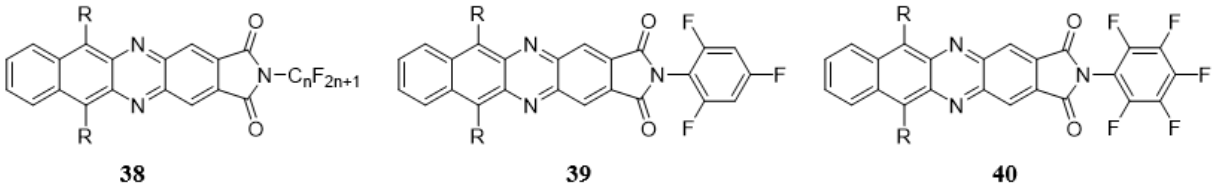


**Figure 7.14** Possible imide-fused diazatetracenes with deeper LUMO via side chain engineering.

Apart from the side chain engineering, more modification could be made over the imide moiety. By reacting with malononitrile, electron-withdrawing nitrile groups could be introduced which could significantly lower the LUMO.

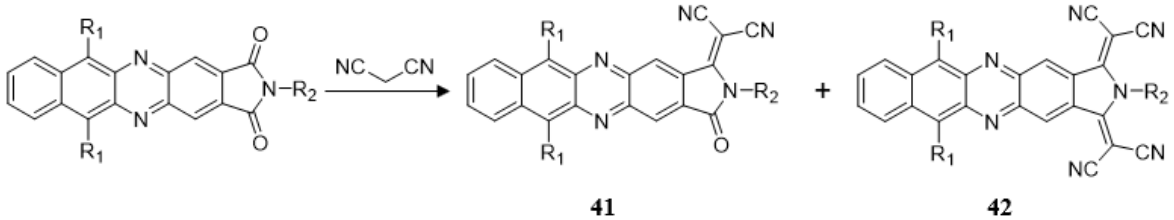


**Figure 7.15** Possible malononitrile containing diazatetracenes.

In addition to imide moiety, halogens could be attached to the naphthalene segment. The introduction of fluorine and nitrile would be beneficial for preventing the ingress of oxygen and moisture, hence improving the stability at ambient condition.

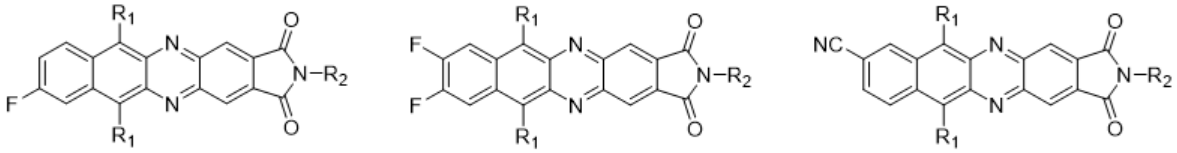


**Figure 7.16** Possible halogenated imide-fused diazatetracenes.

Moreover, larger π-backbone could also lead to deeper LUMO. Instead of naphthalene *o*-diamine, anthracene and phenazine *o*-diamines could be used to furnish imide-fused azapentacenes. Similarly, thiadiazole fused diaazatetracene analogue **48** could also be synthesized. However, more reactive dihalogen species is required for **47** and **48** since the phenazine and benzothiadiazole *o*-diamines have lower reactivity than naphthalene *o*-diamine.

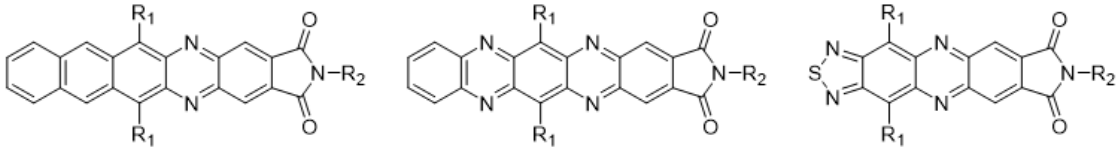


**Figure 7.17** Possible imide-fused azaacenes with different π-backbone.

In summary, a highly active palladium catalyst was selected to synthesize a series of novel imide-fused diazatetracenes. Its optical and electronic properties were investigated. The introduction of imide moiety successfully lowered the LUMO. Obviously redshifted absorption also indicates the extension of π-backbone. The effect of alkyl chains on solid-state structures were also discussed. Further modification over the structure could lead to imide-fused azaacenes with higher electron affinity and potential application in OFET devices.

## 7.2 Summary

The goal of this thesis is to explore the synthetic methods and properties of unconventional azaarenes with nonlinear shapes and novel functional groups. In the first result part, thiadiazole-fused star-shaped azaarene, HATNT, was synthesized. The synthetic approach towards star-shaped azaarenes using hexaketocyclohexane is also discussed. It is found that both steric hindrance and reactivity of *o*-diamine play important roles in the formation of star-shaped products. Strategy to synthesize larger star-shaped azaarenes has been proposed. Moreover, the application of HATNT in PSC as ETL has been investigated.

In the second result part, anthracene-1,2,7,8-tetraone was synthesized as the key building block to construct novel helical azaarenes. Various methods to oxidize phenols into quinones were evaluated. It is found that BSA could be a useful reagent in the synthesis of *o*-quinones. However, the synthesis of smaller analogue naphthalene-1,2,7,8-tetraone using BSA was unsuccessful. Due to the presence of oxidation pathway to naphthalene-2,6-dione, tetraone could not be formed unless the 3,6-positions are blocked. Strategies for future work centering the anthracene-1,2,7,8-tetraone and naphthalene-1,2,7,8-tetraone have been discussed. The electronic and optical properties were investigated and compared with Z-shaped counterpart.

In the third result part, a series of imide-fused diazatetracenes were synthesized. Because of the decreased reactivity of dichlorophthalimide, the previously reported conditions for C-N coupling was not applicable in this case. A more potent palladium source was then selected. *t*-BuOH was also added as co-solvent to accelerate the reaction. The yields range from 65% to 81%. Thus, a highly effective condition for the synthesis of pyrazine-containing azaarenes was obtained. Additionally, the LUMOs of imide-diazatetracenes could be further lowered via modifications at multiple sites.

In conclusion, the syntheses of non-linear star-shaped and U-shaped azaarenes were successfully achieved. The diazatetracenes with imide as functional group were also

obtained. These novel molecules were fully characterized, and their electronic and optical properties were investigated. The goal of thesis is fulfilled.

**References**

[1] a) S. Choudhary, C. Gozalvez, A. Higelin, I. Krossing, M. Melle-Franco, A. Mateo-Alonso, *Chem. Eur. J.* **2014**, *20*, 1525-1528; b) D. Cortizo-Lacalle, C. Gozalvez, M. Olano, X. Sun, M. Melle-Franco, L. E. Hueso, A. Mateo-Alonso, *Org. Lett.* **2015**, *17*, 5902-5905; c) J. Li, J. Miao, G. Long, J. Zhang, Y. Li, R. Ganguly, Y. Zhao, Y. Liu, B. Liu, Q. Zhang, *J. Mater. Chem. C* **2015**, *3*, 9877-9884; d) C. Wang, J. Zhang, G. Long, N. Aratani, H. Yamada, Y. Zhao, Q. Zhang, *Angew. Chem. Int. Ed.* **2015**, *54*, 6292-6296.

[2] S. Zippel, P. Boldt, *Synthesis* **1997**, *1997*, 173-175.

[3] D. Magdziak, A. A. Rodriguez, R. W. Van De Water, T. R. R. Pettus, *Org. Lett.* **2002**, *4*, 285-288.

[4] K. Zhou, H. Dong, H.-l. Zhang, W. Hu, *PCCP* **2014**, *16*, 22448-22457.

[5] L. Ding, H.-Z. Ying, Y. Zhou, T. Lei, J. Pei, *Org. Lett.* **2010**, *12*, 5522-5525.

[6] S. Kumar, J. Shukla, Y. Kumar, P. Mukhopadhyay, *Organic Chemistry Frontiers* **2018**, *5*, 2254-2276.

# APPENDIX

## A.1 Characterization methods

### NMR

$^{1}H$ NMR and $^{13}C$ NMR spectra were recorded on a Bruker Advance 300 NMR spectrometer at ambient temperature with tetramethylsilane (TMS) as internal standard.

### UV-Vis Spectroscopy

UV-Vis absorbance was recorded on UV-Vis-NIR spectrometer Cary 5000. Fluorescence was recoded on Shimadzu RF-5301.

### HRMS

High resolution mass spectrum (HRMS) was performed on a Waters Q-Tof premier mass spectrometer.

### CV

Cyclic voltammetry measurements were conducted on a CHI 604E electrochemical analyzer with glassy carbon (diameter: 1.6 mm; area: 0.02 $cm^2$) as a working electrode, and platinum wires as counter electrode and reference electrode, respectively. $Fc^+/Fc$ was used as an internal standard. Potentials were recorded versus $Fc^+/Fc$ in a solution of anhydrous dichloromethane (DCM) with 0.1 M tetrabutylammoniumhexafluorophosphate ($TBAPF_6$) as supporting electrolyte at a scan rate of 100 m $Vs^{-1}$. Employing empirical formulas $E_{LUMO/HOMO}$= -[4.8 - $E_{Fc}$ + $E_{re/ox}^{onset}$] eV, where $E_{Fc}$= 0.25 eV (measured in our setup), the value of HOMO or LUMO can be calculated.

### PCE Measurement

The current density-voltage (*J-V*) of the solar cells were measured using a Keithley 2400 source meter under simulated AM1.5 illumination (100 mW $cm^{-2}$) by a Xenon-lamp-based solar simulator (Solar Light Co. Inc., USA). The light intensity was calibrated using a Si-

reference cell certified by the National Renewable Energy Laboratory, with the mismatch factor less than 2%. A non-reflective mask (0.09 $cm^2$) was used for defining the cell area.

## A.2 Materials

### General

Analytical grade DCM, THF and AcOH were purchased from Merck. Analytical grade ethyl acetate, DMF, diethyl ether, methanol, isopropanol, toluene and chloroform were purchased from Fisher. Analytical grade DMSO and chlorobenzene were purchased from Sigma Aldrich. Deuterated chloroform, DMSO and acetone were purchased from Cambridge Isotope Laboratories. Deuterated THF was purchased from Merck. Technical grade DCM and hexane were purchased from Aik Moh. Sodium and calcium hydride were purchased from Sigma Aldrich. Anhydrous THF and DCM were prepared by drying over sodium metal and calcium hydride respectively, followed by distillation.

### Chapter 4

Hexaketocyclohexane octahydrate and 4,7-dibromobe-nzo[c][1,2,5]thiadiazole were purchased from Alfa Aesar. Thiophene, 2-ethylhexyl bromide, trimethyltin chloride and tetrachloro-1,4-benzoquinone (chloranil) were purchased from Sigma-Aldrich.

### Chapter 5

Boron tribromide, TIPS acetylene, 2,3-diaminophenazine, Iodine monochloride, 2,3-dichloride-1,4-naphquinone and anthrone were purchased from Sigma Aldrich. BSA was purchased from Acros. 4,7-dibromobe-nzo[c][1,2,5]thiadiazole was purchased from Alfa Aesar.

### Chapter 6

2,3-diaminonaphthalene, bromine, cyclohexylamine, tri(*o*-tolyl)phosphine, 2M $LiAlH_4$ in THF, $Cs_2CO_3$, activated manganese dioxide, tert-butanol, propionic acid, $Pd(dba)_2$, BrettPhos Pd G4 and BrettPhos were purchased from Sigma Aldrich. Thionyl chloride was purchased from Merck. 4,5-dichlorophthalic anhydride was purchased from TCI.

## A.3 Supplementary Data

### Chapter 4

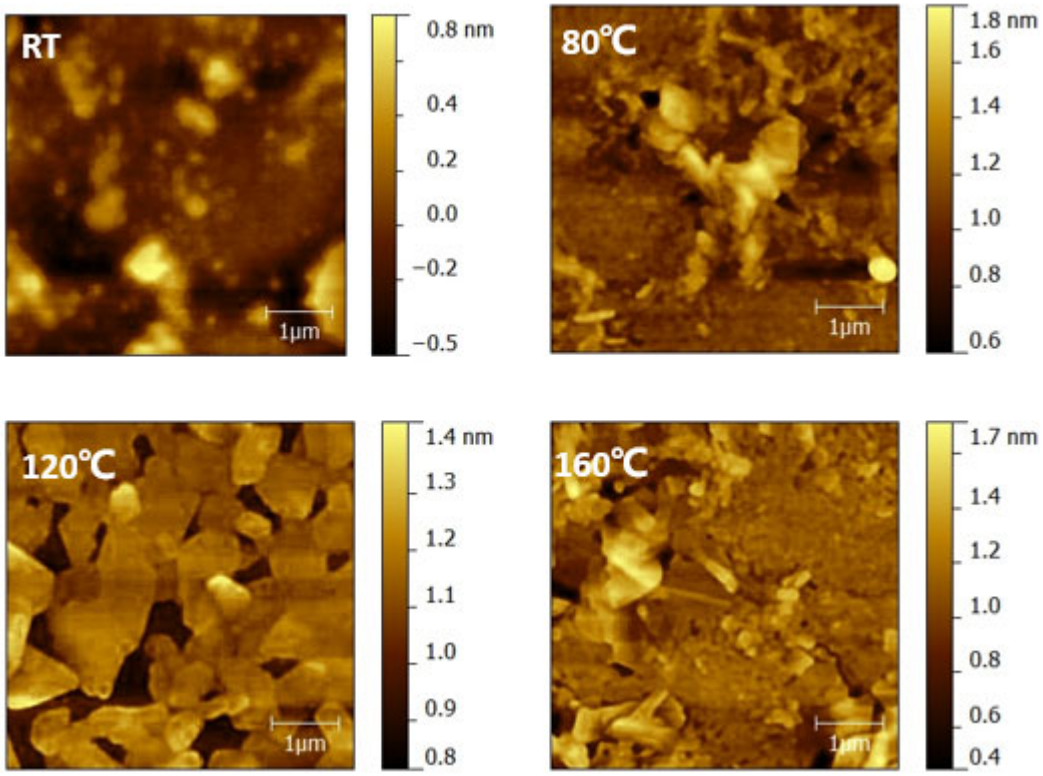


**Figure A.1** Atomic force microscope images of HATNT under different annealing temperatures.

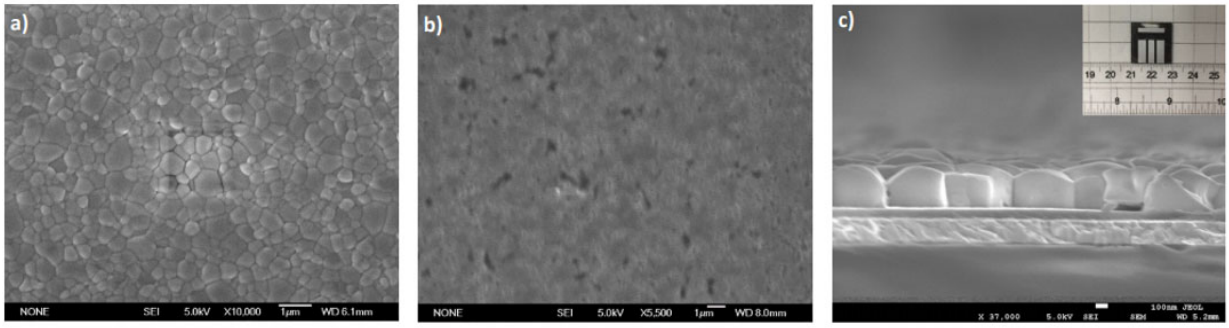


**Figure A.2** Scanning electron microscope images of the pure perovskite (a) and the bilayer perovskite/HATNT (55 nm) thin films (b). c) Cross-section image of the Glass/ITO/Perovskite, the inset shows the optical photograph of the device.

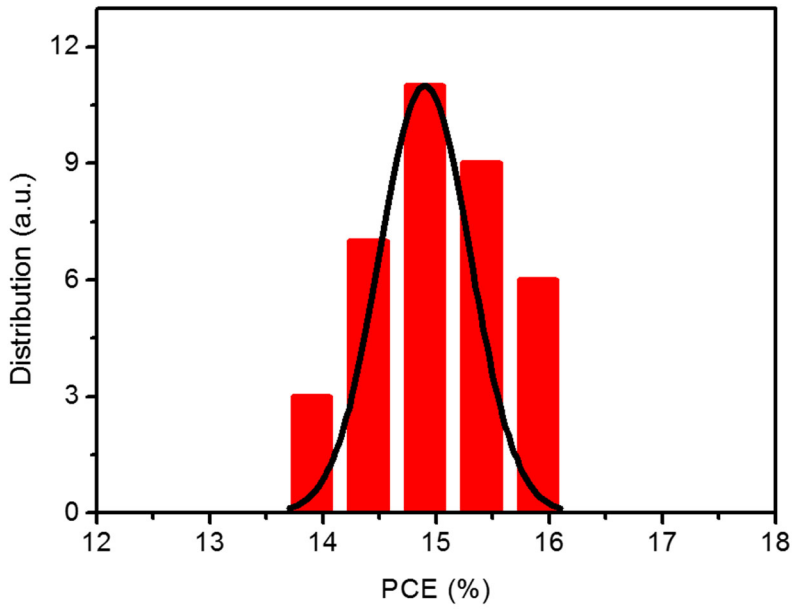


**Figure A.3** Device efficiency distribution characteristic of the 32 PCBM-based perovskite solar cells fabricated within on batch.

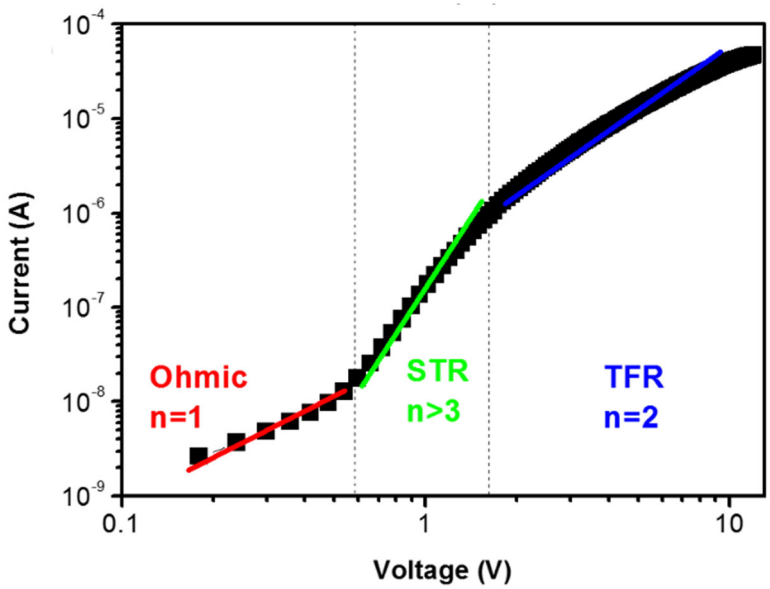


**Figure A.4** J-V curve for the electron-only device with a structure of glass/ITO/Cs2CO3/HATNT/Ca/Al.

**Table A.1** Material parameters for HATNT.

| Symbol | Unit | Description | HATNT |
|---|---|---|---|
| $L_T$ | nm | Thickness in device | 10-70 |
| $\mu_e$ | $cm^2.V^{-1}.s^{-1}$ | Electron mobility | $1.7\times10^{-2}$ |
| $\mu_h$ | $cm^2.V^{-1}.s^{-1}$ | Hole mobility | $1\times10^{-3}$ |
| $\tau_e$ | ns | Electron lifetime | 1000 |
| $\tau_h$ | ns | Hole lifetime | 1000 |
| $m_e$ | - | Electron effective mass | 0.02 |
| $m_h$ | - | Hole effective mass | 0.03 |
| $E_{CB}$ | eV | Conduction band/LUMO | 4.0 |
| $E_{VB}$ | eV | Valence band/HOMO | 5.62 |
| $E_g$ | eV | Band gap | 1.62 |
| $\varepsilon_r$ | - | Relative dielectric constant | 3.5 |

## Chapter 5

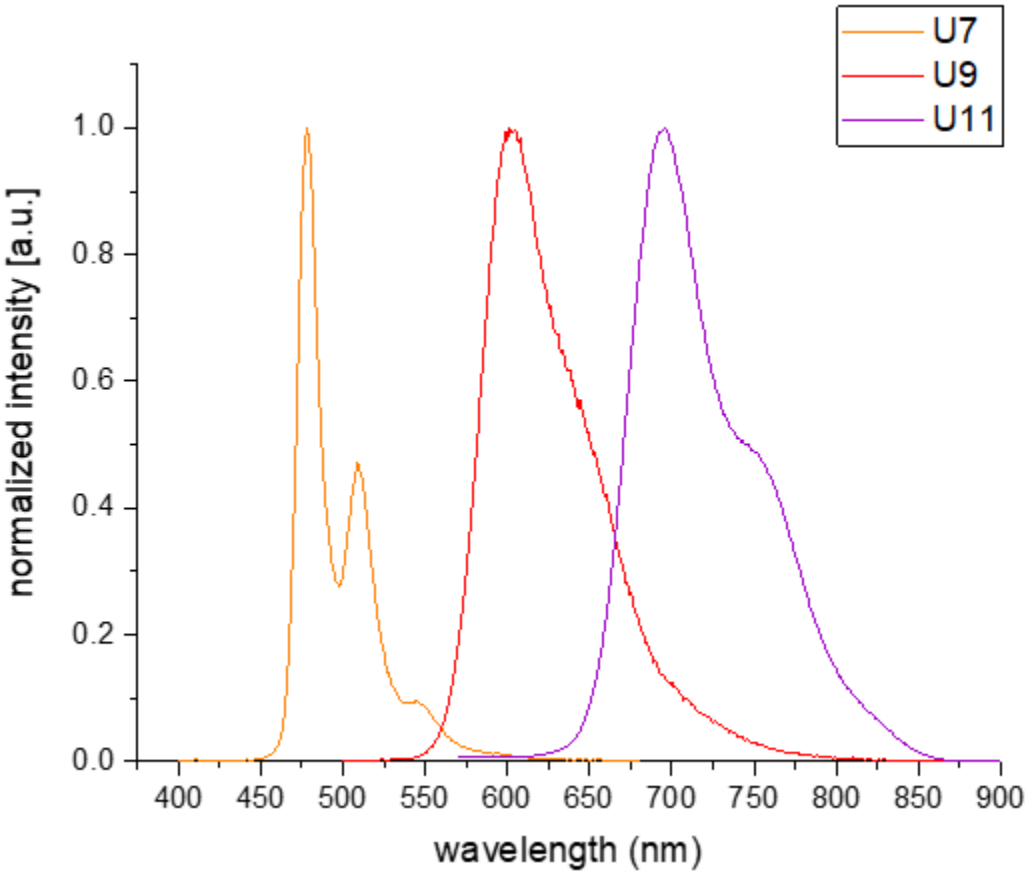


**Figure A.5** Normalized emission spectra of U7, U9 and U11 in DCM.

**Table A.2** Dihedral angles of U7, U9 and U11.

| Compound | Dihedral angles (°) | Sum (°) |
|---|---|---|
| U7 | φ1=5.69, φ2=1.67, φ3=13.99, φ4=4.53, φ5=3.57, φ6=14.43, φ7=1.11, φ8=7.76 | 52.66 |
| U9 | φ1=1.41, φ2=2.30, φ3=7.99, φ4=0.76, φ5=15.07, φ6=4.82, φ7=4.18, φ8=11.32, φ9=0.67, φ10=4.8, φ11=0.93, φ12=4.36 | 58.68 |
| U11 | φ1=0.57, φ2=1.90, φ3=3.21, φ4=7.47, φ5=5.84, φ6=1.95, φ7=13.64, φ8=2.52, φ9=7.58, φ10=13.97, φ11=2.62, φ12=8.19, φ13=5.94, φ14=3.39, φ15=2.02, φ16=1.18 | 81.99 |

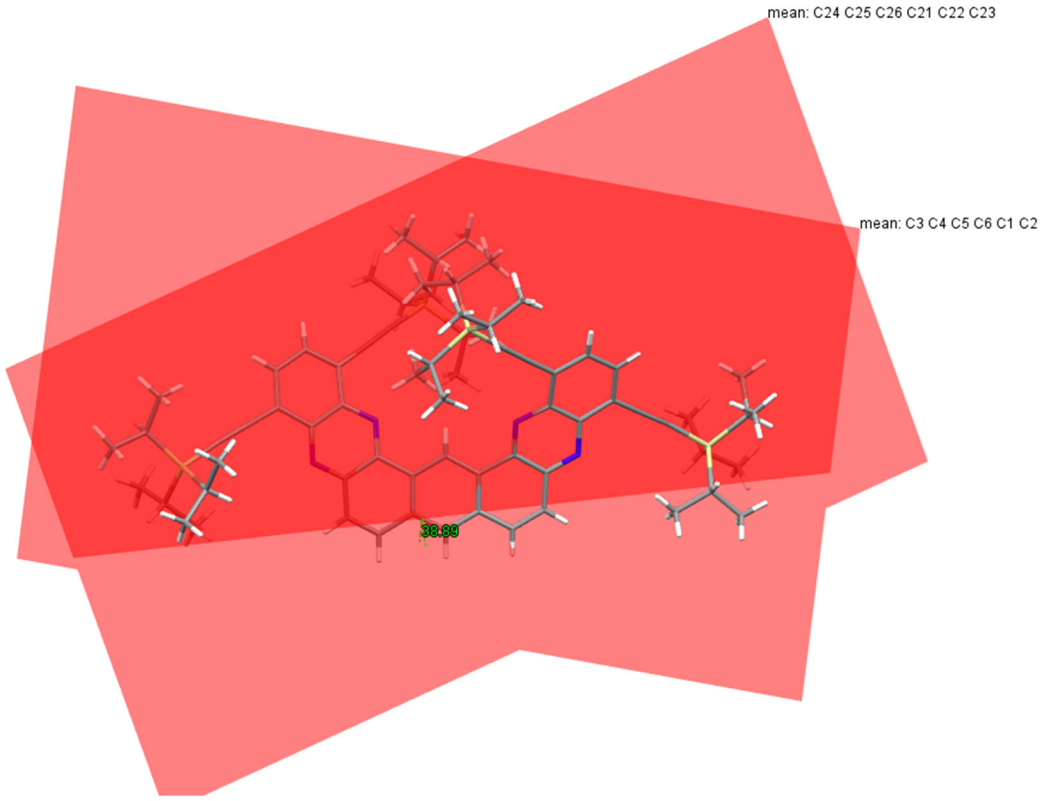


**Figure A.6** Interplane angle of U7.

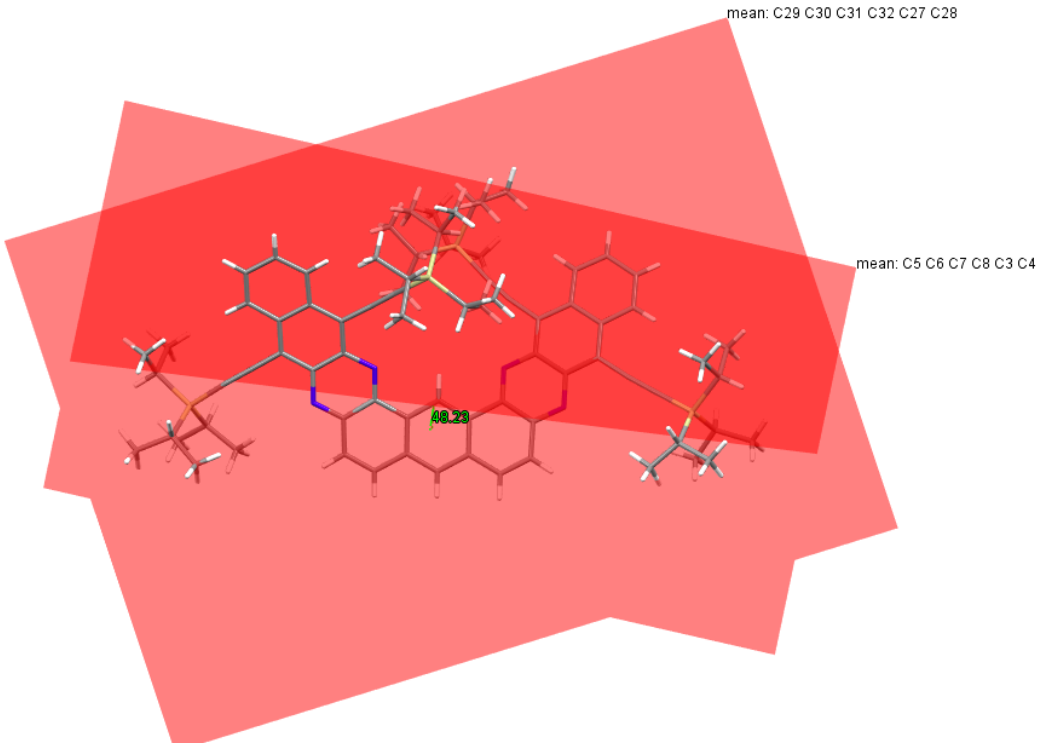


**Figure A.7** Interplane angle of U9.

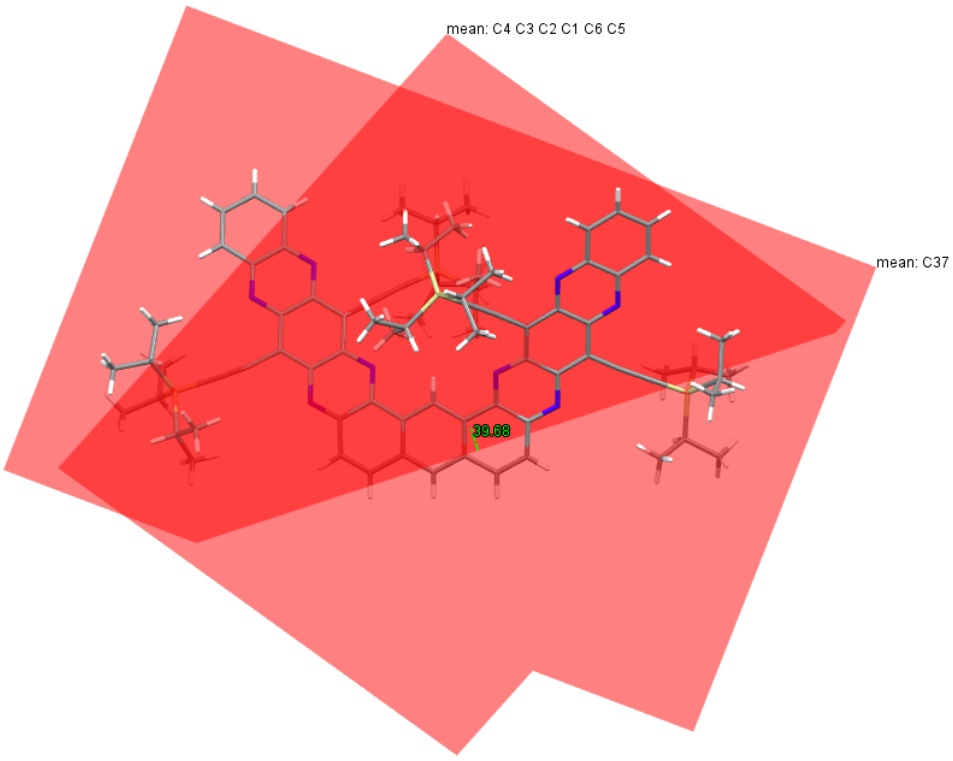


**Figure A.8** Interplane angle of U11.

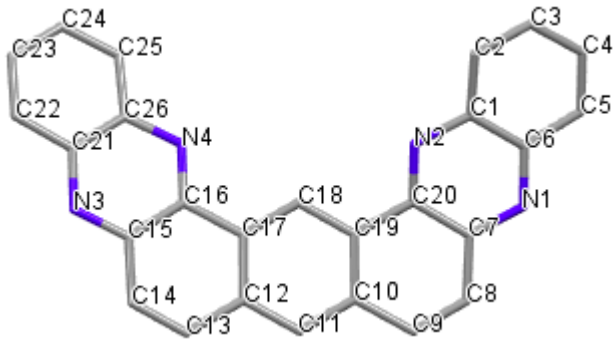


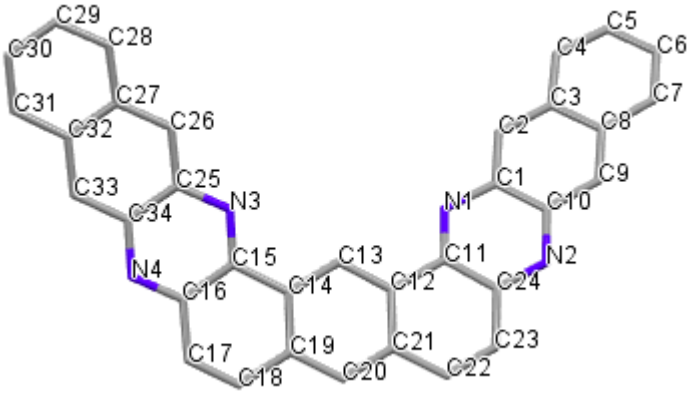

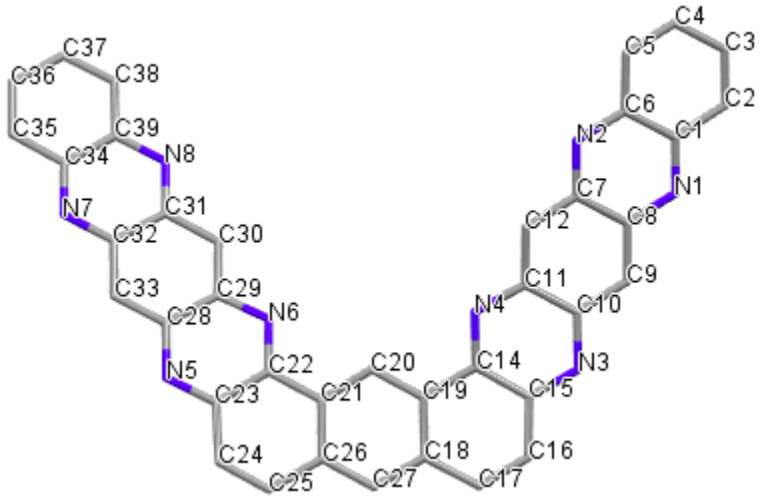


**Figure A.9** Atom labeling of U7, U9 and U11. The calculations of torsional angles of U7, U9 and U11 start from C2, C4 and C5 respectively.

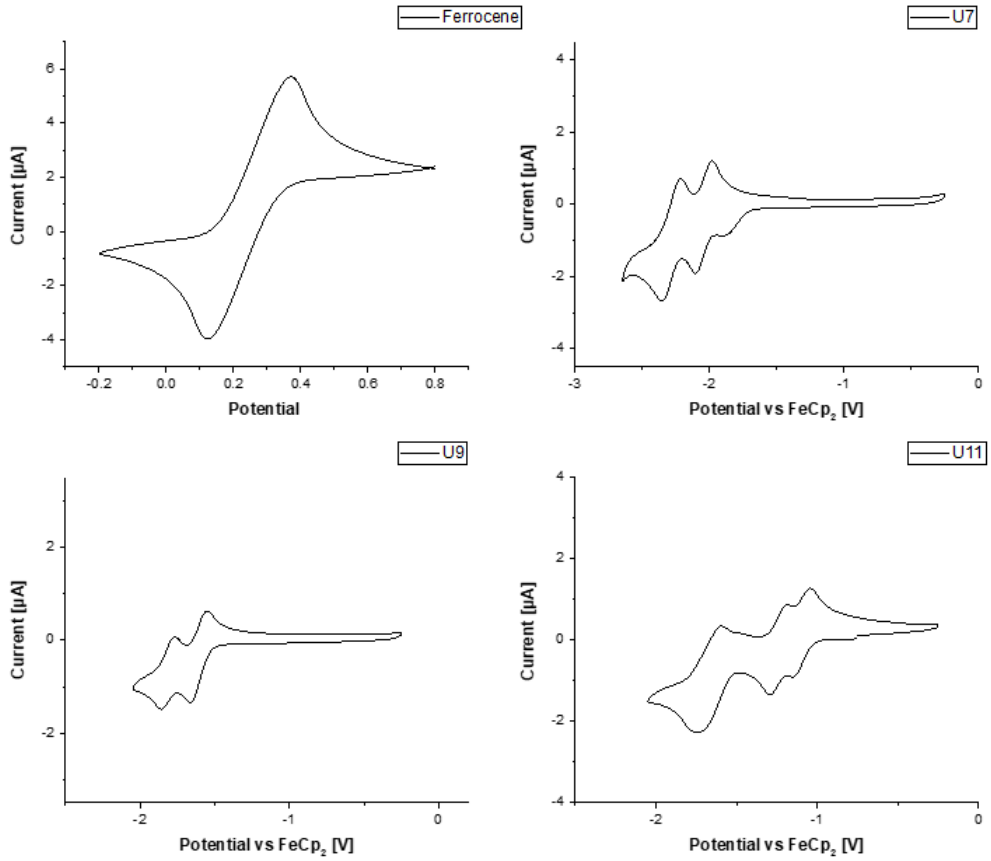


**Figure A.10** CV curves of Ferrocene, U7, U9 and U11.

Crystal data and refinement of U7:

| | | |
|---|---|---|
| Empirical formula | $C_{70}H_{94}N_4Si_4$ | |
| Formula weight | 1103.85 | |
| Temperature | 100 K | |
| Wavelength | 0.71073 Å | |
| Crystal system | Monoclinic | |
| Space group | $P2_{1/c}$ | |
| Unit cell dimensions | $a$ = 12.4305 (9) Å | $\alpha$ = 90° |
| | $b$ = 25.215 (2) Å | $\beta$ = 93.470 (3)° |
| | $c$ = 21.1193(19) Å | $\gamma$ = 90° |
| Volume | 6607.4 (9) Å$^3$ | |
| Z | 4 | |
| Absorption coefficient | 0.13 mm$^{-1}$ | |
| $F_{000}$ | 2392 | |
| Density(calculated) | 1.110 g/cm$^3$ | |
| Crystal size | 0.24 × 0.08 × 0.06 mm | |
| Crystal shape | needle | |
| Crystal color | yellow | |
| $\theta$ range for data collection | 2.5–26.5° | |
| Reflections collected | 76923 | |
| Independent reflections [$R_{int}$] | 15736 [0.149] | |
| Observed reflection [$I > 2\sigma(I)$] | 7723 | |
| Index ranges (h, k, l) | -16…16, -33…29, -27…27 | |
| Absorption correction | multi-scan SADABS-2016/2 | |
| Transmission factors: max, min | 0.99, 0.79 | |
| Refinement method | Full-matrix least-squares on F$^2$ | |
| Data/ restraint/ parameters | 15736/ 713/ 902 | |
| Goodness-of-fit on F$^2$ | 1.02 | |
| Final $R$ indices $R[F^2 > 2\sigma(F^2)]$, $wR(F^2)$ | 0.084, 0.257 | |
| Difference density: max, min | 0.91, -0.43 e Å$^{-3}$ | |

Crystal data and structure refinement of U9:

| | | |
|---|---|---|
| Empirical formula | $C_{78}H_{98}N_4Si_4$ | |
| Formula weight | 1203.96 | |
| Temperature | 200 K | |
| Wavelength | 0.71073 Å | |
| Crystal system | Triclinic | |
| Space group | $P\bar{1}$ | |
| Unit cell dimensions | $a$ = 15.2399 (7) Å | $\alpha$ = 101.9743 (18)° |
| | $b$ = 16.3922 (9) Å | $\beta$ = 113.9856 (15)° |
| | $c$ = 17.7725 (10) Å | $\gamma$ = 106.3678 (15)° |
| Volume | 3619.9 (3) Å$^3$ | |
| Z | 2 | |
| Absorption coefficient | 0.13 mm$^{-1}$ | |
| $F_{000}$ | 1300 | |
| Density (calculated) | 1.105 g/cm$^3$ | |
| Crystal size | 0.28 × 0.26 × 0.22 mm | |
| Crystal shape | block | |
| Crystal color | red | |
| $\theta$ range for data collection | 2.5–28.1° | |
| Reflections collected | 75860 | |
| Independent reflections [$R_{int}$] | 17902 [0.054] | |
| Observed reflection [$I > 2\sigma(I)$] | 11910 | |
| Index ranges (h, k, l) | -20…20, -21…21, -23…23 | |
| Absorption correction | multi-scan SADABS-2016/2 | |
| Transmission factors: max, min | 0.97, 0.91 | |
| Refinement method | Full-matrix least-squares on F$^2$ | |
| Data/ restraint/ parameters | 17902/ 117/ 799 | |
| Goodness-of-fit on F$^2$ | 1.03 | |
| Final $R$ indices $R[F^2 > 2\sigma(F^2)]$, $wR(F^2)$ | 0.063, 0.181 | |
| Difference density: max, min | 0.65, -0.45 e Å$^{-3}$ | |

Crystal data and structure refinement of U11.1.5 chlorobenzene:

| | | |
|---|---|---|
| Empirical formula | $C_{91}H_{105.5}Cl_{1.5}N_8Si_4$ | |
| Formula weight | 1476.86 | |
| Temperature | 100 K | |
| Wavelength | 0.71073 Å | |
| Crystal system | Triclinic | |
| Space group | $P\bar{1}$ | |
| Unit cell dimensions | $a$ = 12.6965 (13) Å | $\alpha$ = 78.420 (3)° |
| | $b$ = 17.3542 (18) Å | $\beta$ = 87.087 (3)° |
| | $c$ = 19.577 (2) Å | $\gamma$ = 80.742 (3)° |
| Volume | 4169.9 (7) $Å^3$ | |
| Z | 2 | |
| Absorption coefficient | 0.17 $mm^{-1}$ | |
| $F_{000}$ | 1578 | |
| Density (calculated) | 1.176 $g/cm^3$ | |
| Crystal size | 0.28 × 0.26 × 0.22 mm | |
| Crystal shape | block | |
| Crystal color | black | |
| $\theta$ range for data collection | 2.6–25.0° | |
| Reflections collected | 15223 | |
| Independent reflections [$R_{int}$] | 15223 [0.115] | |
| Observed reflection [$I > 2\sigma(I)$] | 8414 | |
| Index ranges (h, k, l) | -15…15, -20…20, -23…23 | |
| Absorption correction | multi-scan SADABS-2016/2 | |
| Refinement method | Full-matrix least-squares on $F^2$ | |
| Data/ restraint/ parameters | 15223/ 2916/ 1375 | |
| Goodness-of-fit on $F^2$ | 1.03 | |
| Final $R$ indices $R[F^2 > 2\sigma(F^2)]$, $wR(F^2)$ | 0.122, 0.379 | |
| Difference density: max, min | 0.96, -0.85 e $Å^{-3}$ | |

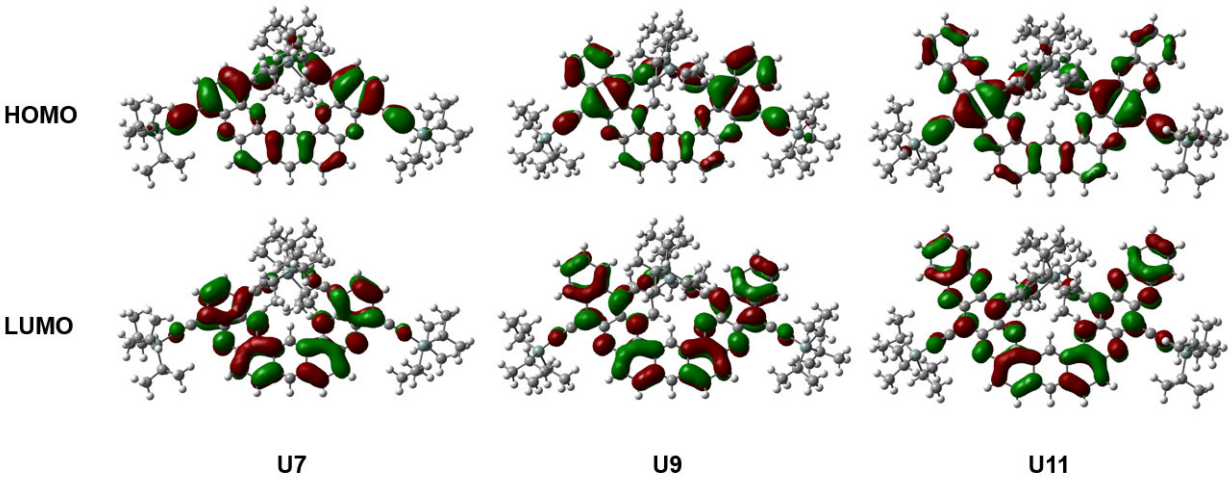


**Figure A.11** Quantum-chemical calculations of frontier molecular orbitals (FMOs).

## Chapter 6

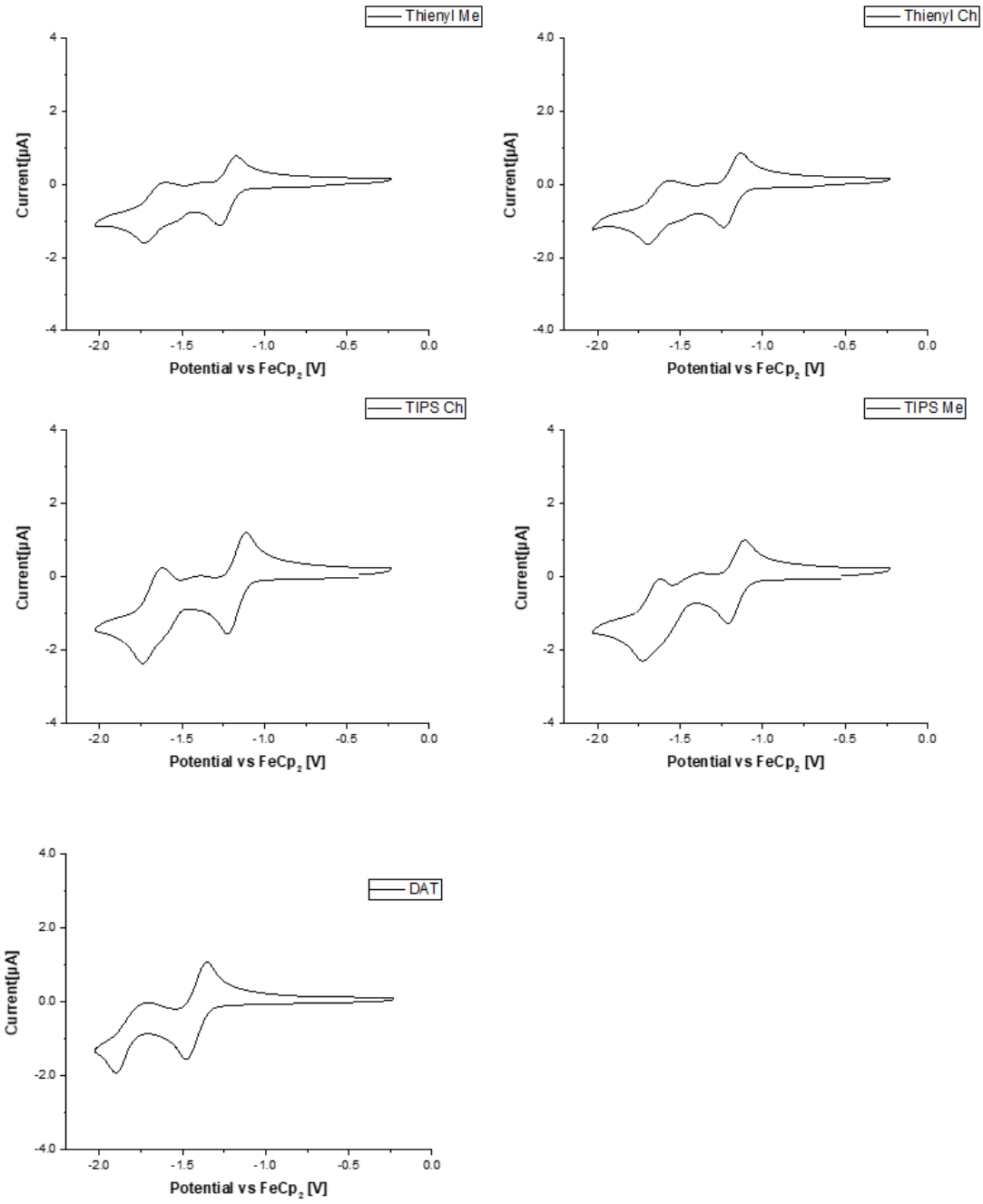


**Figure A.12** CV curves of imide-fused diazatetracenes and unmodified TIPS-DAT.

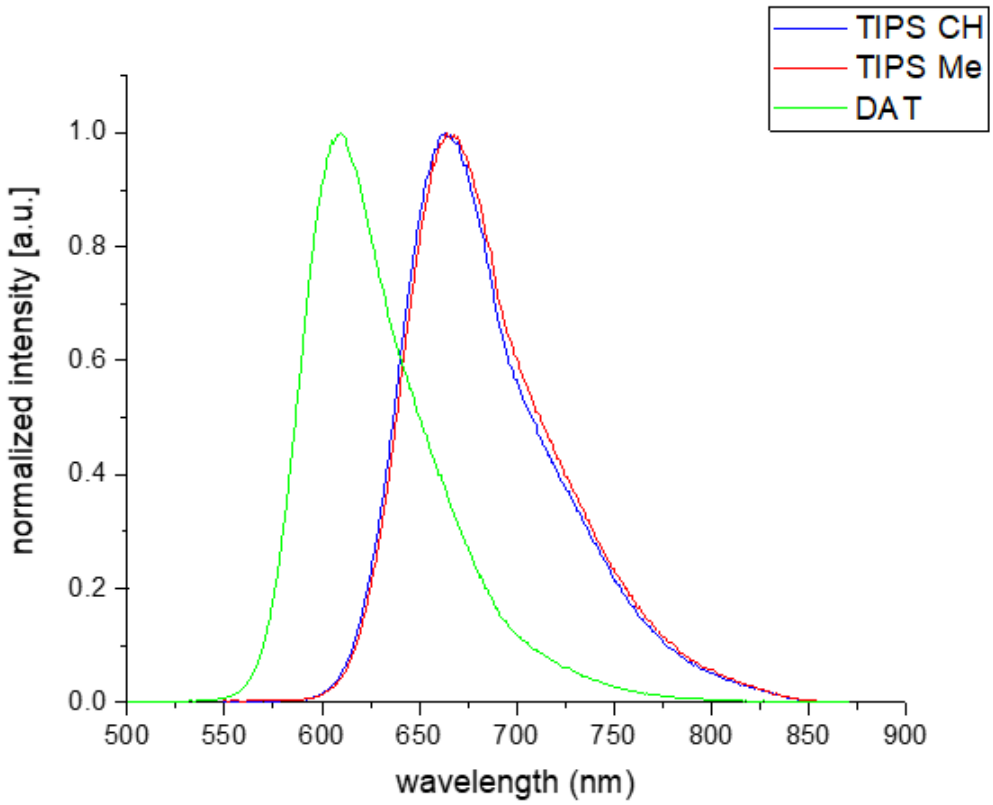


**Figure A.13** Normalized emission spectra of imide-fused TIPS-DATs and DAT in DCM.

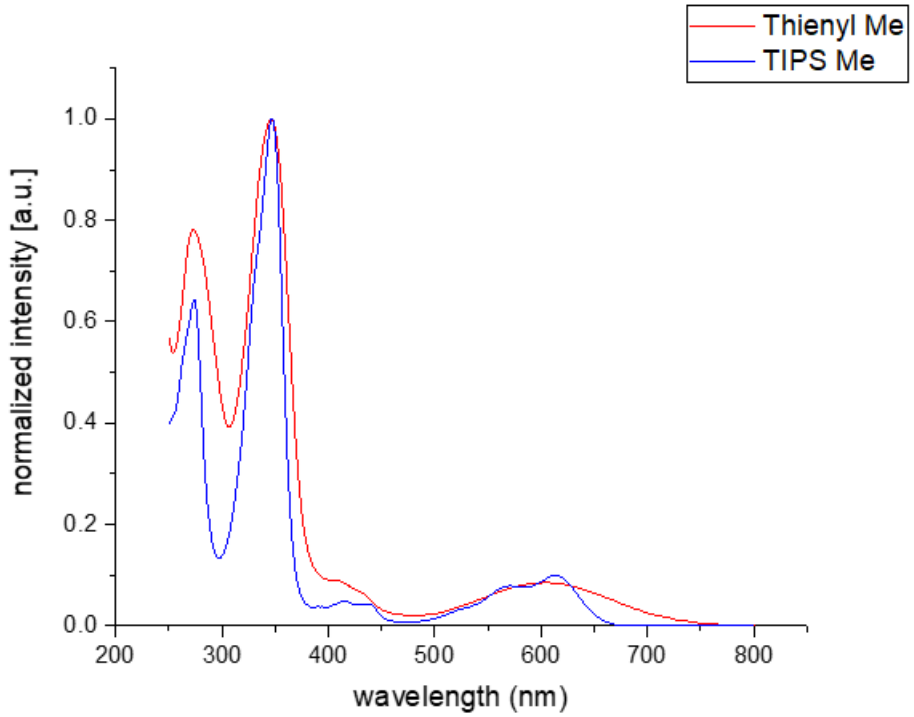


**Figure A.14** Normalized absorption spectra of N-methyl imide-fused DATs in DCM.

Crystal data and structure refinement of TIPS N-Me diazatetracene.

| | | |
|---|---|---|
| Empirical formula | $C_{41}H_{51}N_3O_2Si_2$ | |
| Formula weight | 674.02 | |
| Temperature | 296 K | |
| Wavelength | 0.71073 Å | |
| Crystal system | Monoclinic | |
| Space group | $P\ 2_1/c$ | |
| Unit cell dimensions | $a$ = 19.499 (4) Å | $\alpha$ = 90° |
| | $b$ = 14.079 (3) Å | $\beta$ = 112.835 (4)° |
| | $c$ = 15.710 (4) Å | $\gamma$ = 90° |
| Volume | 3974.9 (15) Å$^3$ | |
| Z | 4 | |
| Absorption coefficient | 0.13 mm$^{-1}$ | |
| $F_{000}$ | 1448 | |
| Density (calculated) | 1.126 g/cm$^3$ | |
| Crystal size | 0.20 × 0.20 × 0.15 mm | |
| Crystal shape | block | |
| Crystal color | dark blue | |
| $\theta$ range for data collection | 2.3–23.8° | |
| Reflections collected | 22385 | |
| Independent reflections [$R_{int}$] | 7014 [0.049] | |
| Observed reflection [$I > 2\sigma(I)$] | 3098 | |
| Index ranges (h, k, l) | -23…22, -16…16, -12…18 | |
| Absorption correction | multi-scan SADABS-2016/2 | |
| Transmission factors: max, min | 0.75, 0.62 | |
| Refinement method | Full-matrix least-squares on $F^2$ | |
| Data/ restraint/ parameters | 7014/ 149/ 444 | |
| Goodness-of-fit on $F^2$ | 1.05 | |
| Final $R$ indices $R[F^2 > 2\sigma(F^2)]$, $wR(F^2)$ | 0.121, 0.279 | |
| Difference density: max, min | 1.14, -0.63 e Å$^{-3}$ | |

Crystal data and structure refinement of TIPS N-Cyclohexyl diazatetracene.

| | | |
|---|---|---|
| Empirical formula | $C_{46}H_{59}N_3O_2Si_2$ | |
| Formula weight | 742.14 | |
| Temperature | 296 K | |
| Wavelength | 0.71073 Å | |
| Crystal system | Monoclinic | |
| Space group | $P\ 2_1/n$ | |
| Unit cell dimensions | $a$ = 8.699 (8) Å | $\alpha$ = 90° |
| | $b$ = 37.42 (3) Å | $\beta$ = 100.976 (12)° |
| | $c$ = 13.560 (12) Å | $\gamma$ = 90° |
| Volume | 4333 (7) Å$^3$ | |
| Z | 4 | |
| Absorption coefficient | 0.12 mm$^{-1}$ | |
| $F_{000}$ | 1600 | |
| Crystal shape | block | |
| Crystal color | dark blue | |
| $\theta$ range for data collection | 2.2–20.3° | |
| Reflections collected | 22837 | |
| Independent reflections [$R_{int}$] | 7617 [0.126] | |
| Observed reflection [$I > 2\sigma(I)$] | 2769 | |
| Index ranges (h, k, l) | -8…10, -36…44, -16…15 | |
| Absorption correction | multi-scan SADABS-2016/2 | |
| Refinement method | Full-matrix least-squares on F$^2$ | |
| Data/ restraint/ parameters | 7617/ 0/ 490 | |
| Goodness-of-fit on F$^2$ | 0.92 | |
| Final $R$ indices $R[F^2 > 2\sigma(F^2)]$, $wR(F^2)$ | 0.085, 0.302 | |
| Difference density: max, min | 0.31, -0.34 e Å$^{-3}$ | |

Crystal data and structure refinement of Thienyl N-Cyclohexyl diazatetracene.

| | | |
|---|---|---|
| Empirical formula | $C_{48}H_{55}N_3O_2S_2$ | |
| Formula weight | 770.07 | |
| Temperature | 100 K | |
| Wavelength | 1.54178 Å | |
| Crystal system | Triclinic | |
| Space group | $P\bar{1}$ | |
| Unit cell dimensions | $a$ = 6.9412 (5) Å | $\alpha$ = 100.756 (8)° |
| | $b$ = 16.4918 (16) Å | $\beta$ = 90.494 (7)° |
| | $c$ = 18.0439 (17) Å | $\gamma$ = 93.274 (7)° |
| Volume | 2015.5 (3) Å$^3$ | |
| Z | 2 | |
| Absorption coefficient | 1.52 mm$^{-1}$ | |
| $F_{000}$ | 1448 | |
| Density (calculated) | 1.263 g/cm$^3$ | |
| Crystal size | 0.22 × 0.02 × 0.01 mm | |
| Crystal shape | needle | |
| Crystal color | black | |
| $\theta$ range for data collection | 2.5–66.4° | |
| Reflections collected | 26740 | |
| Independent reflections [$R_{int}$] | 7120 [0.186] | |
| Observed reflection [$I > 2\sigma(I)$] | 3746 | |
| Index ranges (h, k, l) | -7…8, -19…19, -21…21 | |
| Absorption correction | multi-scan SADABS-2016/2 | |
| Transmission factors: max, min | 0.98, 0.64 | |
| Refinement method | Full-matrix least-squares on F$^2$ | |
| Data/ restraint/ parameters | 7120/ 1919/ 859 | |
| Goodness-of-fit on F$^2$ | 1.01 | |
| Final $R$ indices $R[F^2 > 2\sigma(F^2)]$, $wR(F^2)$ | 0.112, 0.296 | |
| Difference density: max, min | 0.40, -0.46 e Å$^{-3}$ | |

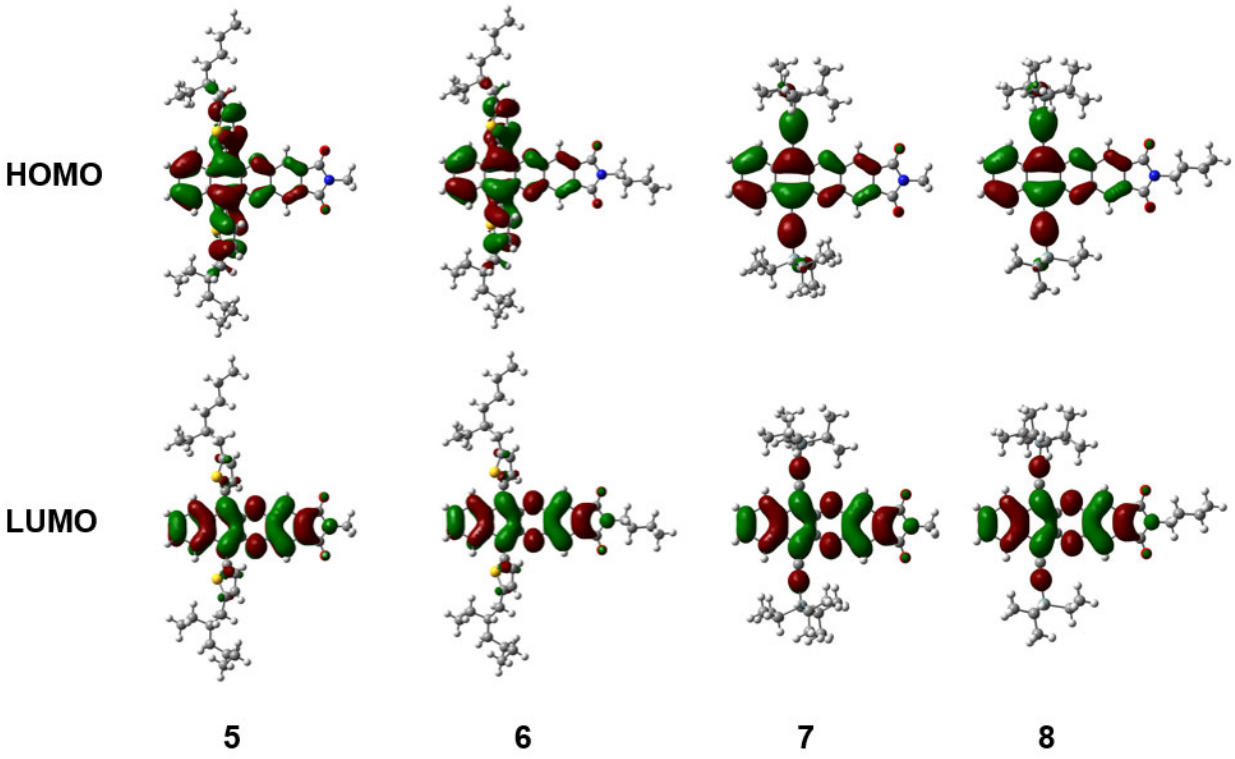


**Figure A.15** Quantum-chemical calculations of frontier molecular orbitals (FMOs)